

3-23-2018

SH-Wave Seismic Reflection Imaging and Inversion: An Analysis of Architectural and Physical Properties of a Near-Surface Point-Bar

Nathan William Benton

**SH-WAVE SEISMIC REFLECTION IMAGING AND INVERSION:
AN ANALYSIS OF ARCHITECTURAL AND PHYSICAL
PROPERTIES OF A NEAR-SURFACE POINT-BAR**

A Thesis

Submitted to the Graduate Faculty of the
Louisiana State University and
Agricultural and Mechanical College
in partial fulfillment of the
requirements for the degree of
Master of Science

in

The Department of Geology and Geophysics

by
Nathan William Benton
B.S., Baylor University, 2016
May 2018

In memory of Barrett Benton, Harley, and Dr. Cleve Brooks.

ACKNOWLEDGEMENTS

I thank Dr. Juan Lorenzo for providing your geological and geophysical insight for this research project. Also, I thank my committee members, Dr. Carol Wicks and Dr. Clinton Willson for guidance and involvement.

Thank-you to members of my research group for your contributions: Martial Morrison, Abah Omale, Blake Odom, Abby Maxwell, Trudy Watkins, and Adam Gostic.

Finally, thank-you to my family and friends.

TABLE OF CONTENTS

ACKNOWLEDGEMENTS	iii
ABSTRACT	viii
CHAPTER 1: INTRODUCTION & BACKGROUND INFORMATION.....	1
(1.1) Introduction.....	1
(1.2) Research Problems and Hypotheses	2
(1.3) Study Site	4
(1.4) Geological Background	4
(1.4.1) Overview of False River Geology & Development	4
(1.4.2) Ideal Point-Bar Complex Development & Architecture.....	5
(1.5) Previous Data.....	7
(1.5.1) EC Well-Log Data	7
(1.6) An Explanation and The Advantages of Shear-Waves.....	10
CHAPTER 2: METHODS	11
(2.1) Reconnaissance Study & Source Determination	11
(2.1.1) Target Exploration.....	11
(2.1.2) Seismic Source Determination.....	13
(2.2) Inline & Crossline Seismic Reflection Survey Details	18
(2.2.1) Field Acquisition Equipment.....	18
(2.2.2) Field Acquisition Site & Survey Geometry.....	19
(2.2.3) GPS Positioning of Shotpoints & Geophones	22
(2.3) Pre-Processing.....	22
(2.3.1) UTM Interpolation & Elevation Calculation.....	22
(2.3.2) Seismic Data Upload & Conversion	25
(2.4) Processing.....	25
(2.4.1) Polarity Reversal	25
(2.4.2) Shotgather Concatenation for Inline & Crossline Survey	27
(2.4.3) Shotgather Differencing	27
(2.4.4) Trace Repair	30
(2.4.5) Geometry & Sorting.....	32
(2.4.6) Elevation Statics Correction	32
(2.4.7) Top-Muting.....	35
(2.4.8) Velocity Analysis	37
(2.4.9) Residual Statics Correction.....	42
(2.4.10) Stack.....	43
(2.4.11) f-k Filter	46
(2.4.12) Phase Correction & Polarity Determination.....	47
(2.4.13) Seismic Amplitude Conditioning & Recovery	49
(2.4.14) A Case against Deconvolution & Migration	49
(2.5) Post-Processing	50
(2.5.1) Band-Limited Impedance (BLIMP) Inversion.....	50
(2.5.2) Time-to-Depth Conversion	54

CHAPTER 3: RESULTS & INTERPRETATIONS.....	57
(3.1) Results	57
(3.1.1) Seismic Cross-Sections	57
(3.1.2) SI Profiles.....	61
(3.1.3) SI Logs & EC Well-Logs.....	62
(3.2) Interpretations	69
(3.2.1) Seismic Cross-Sections & Sediment Package Architecture.....	69
(3.2.2) SI Profiles, EC Well-Logs, & Physical Properties of Sediment Packages.....	70
CHAPTER 4: ERROR ANALYSIS.....	71
(4.1) Error of Time-to-Depth Conversion.....	71
(4.2) Error of BLIMP Inversion & Sensitivity of Input Parameters	71
(4.2.1) Low-Cut Filter.....	72
(4.2.2) High-Cut Filter.....	77
(4.2.3) Low-Frequency Impedance Model.....	77
(4.2.4) Seismic Amplitudes.....	79
CHAPTER 5: DISCUSSION.....	81
(5.1) The Architecture of a Near-Surface Point-Bar: Confirmation of Ideal Models	81
(5.2) Comparison of SI Between Sand & Clay-Rich Sediment Packages: Compaction/Dewatering Model.....	81
(5.3) Dominant Causes & Implications of Well-Log Misalignments.....	84
CHAPTER 6: CONCLUSIONS & RECOMMENDATIONS	85
(6.1) Conclusions.....	85
(6.2) Recommendations.....	86
CHAPTER 7: REFERENCES.....	87
CHAPTER 8: APPENDIX	102
(8.1) List & Definition of Terms	102
(8.2) A Disclosure of Seismic Data Processing/Post-Processing & Image/Wiggle Plots.....	103
(8.3) Description & Effect of Clipping Seismic Data	103
(8.4) Zamin Directory Structure & Copying/Moving Data	104
(8.5) Seismic Data Upload & Conversion Workflow	105
(8.6) Main Seismic Data Output Files	105
(8.7) Non-Scripted Seismic Unix Commands for Processing/Post-Processing.....	106
(8.7.1) sustatic.....	106
(8.7.2) suphase	107
(8.7.3) sukeycount.....	107
(8.7.4) suwind.....	107
(8.7.5) sugain	110
(8.8) BASH Scripts.....	110
(8.8.1) ample_recov_2.sh & input_mod.awk	110

(8.8.2) depthing.sh	113
(8.8.3) kill_interp_repair.sh	114
(8.8.4) MNSatics.sh	117
(8.8.5) segy_to_su.sh	118
(8.8.6) header_input.sh	119
(8.8.7) su_to_segy.sh	120
(8.8.8) cat_oddOReven.sh	120
(8.8.9) suDiff.sh	121
(8.8.10) SET_p1_GEOM.sh	122
(8.8.11) SET_p2_GEOM.sh	123
(8.9) MATLAB	124
(8.9.1) MATLAB Subroutines	124
(8.9.1.1) wiggle.m	124
(8.9.1.2) vrms2vint.m	124
(8.9.1.3) Vint_populate.m	126
(8.9.1.4) model_builder.m	128
(8.9.1.5) vel_interp.m	131
(8.9.1.6) utm_interpolation.m	133
(8.9.1.7) blimp.m	135
(8.9.1.8) auto_blimp.m	138
(8.9.1.9) load_plot_seismic.m	140
(8.9.1.10) isalmost.m	140
(8.9.1.11) phase_estimator.m	142
(8.9.1.12) vmodel_avg.m	144
(8.9.1.13) imp_smoother.m	145
(8.9.1.14) gaussfilt.m	145
(8.9.2) SeisLab Commands	147
(8.9.2.1) s_convert	147
(8.9.2.2) write_segy_file	148
(8.9.2.3) read_segy_file_legacy	148
(8.9.2.4) s_phase_rotation	148
(8.9.2.5) read_las_file	148
(8.10) Perl Scripts	148
(8.10.1) Sseg2su	148
(8.10.2) Reverse_polarity.pl	148
(8.10.3) Suclean_geom.pl	148
(8.10.4) Make_cmp.pl	149
(8.10.5) iTop_Mute3 & iTop_Mute3.config	149
(8.10.6) Sumute2.pl	149
(8.10.7) iVA2 & iVA2.config	149
(8.10.8) suCatpar.pl	149
(8.10.9) Sustack.pl	149
(8.10.10) Sudipfilt & Sudipfilt.config	149
(8.10.11) estat_calc.pl	149
(8.11) Software	152
(8.11.1) Opendtect	152

(8.11.2) LasApps	152
VITA	153

ABSTRACT

Both architecture and physical properties of near-surface point-bar sediment packages have not been imaged or analyzed via SH-wave seismic reflection surveying, respectively. Point-bar architecture within near-surface environments characterized by conductive, saturated, and/or unconsolidated sediments cannot be well-imaged with other remote sensing methods compared to the SH-wave seismic reflection surveying method. The physical properties that distinguish different point-bar sediment packages are variably altered during early-stage diagenetic processes such as compaction and dewatering, thereby changing SH-wave seismic velocities and subsequently shear impedance of different sediment packages. This study accomplishes two objectives by acquiring, processing, and inverting seismic reflection data from two surveys as well as incorporating well-log data from previous studies. First, we successfully image and provide the first high-resolution images of a near-surface downstream point-bar via SH-wave seismic reflection surveying. Dipping seismic reflectors are seen on the survey oriented orthogonal to paleochannel, and mainly lateral seismic reflectors are present on the survey set parallel to paleochannel. These results confirm ideal downstream point-bar models, and thereby demonstrate the effectiveness of using SH-wave seismic reflection surveying compared to other remote sensing methods. Secondly, we use an early-stage diagenesis model to rationalize that compaction and dewatering are likely the primary causal mechanisms that develop the seismic shear impedance properties associated with different near-surface point-bar sediment packages. Overall, this study demonstrates the usefulness of SH-wave seismic reflection surveying and shear impedance inversion for near-surface seismic analyses.

CHAPTER 1: INTRODUCTION & BACKGROUND INFORMATION

(1.1) Introduction

Multiple studies have been conducted whereby the near-surface is analyzed by seismic reflection surveying (Bachrach et al., 2001; Bachrach et al., 1998c; B ker et al., 1998; Deidda et al., 2001; Guevara et al., 2010; Hasbrouck 1991; Miller et al., 1988; Missiaen et al., 2008; Sloan et al., 2016; Steeples 1998; Steeples et al., 1982; Steeples et al., 1995; Young et al., 2001). These studies present different workflows, objectives, and the complexity associated with acquiring, processing, and interpreting seismic reflection data collected from various near-surface environments. For this particular study, I image and quantitatively characterize near-surface (~9 – 30 m) downstream point-bar sediment packages via SH-wave seismic reflection surveying and band-limited impedance inversion. High-resolution seismic imagery and detailed inversion profiles from this study confirm ideal fluvial downstream point-bar models as well as rationalize how early-diagenetic processes such as compaction and dewatering are likely the primary casual mechanisms that develop the seismic impedance properties associated with different downstream point-bars sediment packages.

Conventionally, longitudinal waves (or P-waves) are used for reflection imaging and characterizing the subsurface (Deidda et al., 2001). Transverse-waves (or S-waves) are also employed, however, data acquisition and processing are usually more labor intensive (Deidda et al., 2001; Haines et al., 2010; Pugin et al., 2002; Pugin et al., 2004; Wolz 2003a). In particular, horizontally-polarized S-waves (SH-waves) are used for near-surface surveying (Cardarelli et al., 2014; Guy 2006; Hasbrouck 1991; Krawczyk et al., 2013a; Michaels 1996; Wang et al., 2000; Xia et al., 2002; Zhang 1990).

Near-surface point-bar architecture has been imaged with seismic and ground-penetrating radar (GPR) methods on small and large-scale surveys (Bachrach et al., 1998a; Bridge et al., 1995b; Corbeau et al., 2004; Gawthorpe et al., 1993; R. G. et al., 2007). To date, only P-wave and GPR surveying are successively employed for the objective of imaging a point-bar. Despite the surveying methods used in previous studies for subsurface imaging, ideal point-bar architecture is usually shown. Overall, ideal point-bar architecture includes dipping sediment packages towards paleochannel thalweg and relatively lateral sediment packages parallel to paleochannel (R. G. et al., 2007). For GPR surveying, electromagnetic attenuation is an overwhelming issue that severely limits the imaging capabilities for fluid-saturated conductive sediments (i.e. wet clays), which usually comprise multiple sections of fluvial point-bars (Frazier et al., 1961; McCann et al., 1988; Nanson 1980). As for P-waves, resolution capabilities are inherently limited relative to S-waves, especially in unconsolidated and/or saturated sediments (Beilecke et al., 2016; Young et al., 2001). Part of this study aims to provide high-resolution imagery of architectural features associated with a near-surface downstream point-bar, thereby demonstrating that using S-waves is advantageous relative to other geophysical remote sensing methods as the subsurface at our study site is characterized mainly by unconsolidated sediments, a shallow (~6.5 m) water table, and the presence of multiple clay-rich sediment packages (Fisk 1944; Lechnowskyj 2015).

Inversion of near-surface seismic reflection data is a relatively uncommon task (Vardy et al., 2015). This shortcoming results from the fact that an overwhelming number of shallow subsurface seismic research is designated for only imaging near-surface targets (Monrigal et al., 2016). For this study, a band-limited impedance inversion algorithm is used to deterministically calculate seismic shear-impedance (SI) of sand and clay-rich sediment packages associated with a near-surface downstream point-bar from SH-wave seismic reflection data.

The presence of clay and sand either in mixture or isolation subsequently results in different seismic velocities for each sediment package (Avseth et al., 2005b). For sand- and clay-rich sediments that have undergone early-stage diagenetic processes such as compaction and dewatering, there is a subsequent effect of an increase of rigidity corresponding to clays more so compared to sands (Englehardt 1977; Holland 1980). Also, for saturated and unconsolidated sand-rich sediments that that have experienced little to no diagenesis, grain contacts retain low a rigidity (Avseth et al., 2005a). The overall increase of clay rigidity results in a higher SH-wave seismic velocity compared to sand-rich sediments, which also translates to a comparatively greater SI magnitude for clay.

A near-surface downstream point bar is analyzed via SH-waves, and seismic data are subsequently inverted for SI, thereby providing both a high-resolution image of architectural features and physical properties associated with sediment packages that comprise a near-surface downstream point-bar, respectively. The architectural features of an ideal downstream point-bar model in terms of dipping and non-dipping sediment packages are verified via seismic sections. Particularly, a survey situated approximately parallel to the paleomeander channel provides a new and improved perspective of point-bar architecture. Moreover, in terms of physical properties, alternating sand- and clay-rich sediment packages that comprise a downstream point-bar are studied via seismic SI. Inversion results indicate that clay-rich sediments retain a comparatively greater SI magnitude compared to sand-rich sediments due to early-stage diagenetic processes.

The study area for this research project is located at the southern end of False River (Pointe Coupee Parish, Louisiana). Along with seismic data acquired for this study, existing data from the survey area includes two electrical conductivity (EC) well-logs. Both processed seismic sections, SI profiles, and well-log data are incorporated together to facilitate a detailed analysis of a near-surface downstream point-bar.

(1.2) Research Problems and Hypotheses

Characteristic architecture of fluvial point-bars models include dipping and non-dipping strata associated with alternating sand and clay-rich sediment packages (Fustic et al., 2012; Labrecque et al., 2011). Research shows for GPR and seismic surveys set approximately parallel to paleochannel, there is little to no dip of sediment packages (Corbeanu et al., 2004; Ielpi et al., 2014). However, for surveys oriented orthogonal to paleochannel, there is an associated dip of point-bar sediment packages towards channel thalweg (Ghinassi et al., 2016). Although GPR and P-wave seismic imaging are used in previous research, each surveying method comes with an associated disadvantage. Namely, near-surface GPR surveying capabilities can be extremely limited in conductive subsurface conditions (i.e. clays) due to electromagnetic

attenuation, and P-wave seismic imaging is inherently constrained by resolution capabilities relative to S-waves, especially in saturated and unconsolidated sediments (Carr et al., 1998; Gawthorpe et al., 1993; Hildebrand et al., 2002).

Physical properties associated with alternating subsurface point-bar sand- and clay-rich sediment packages develop and change over time as diagenesis occurs (Burst 1976; Englehardt 1977; Holland 1980). Some notable physical properties of near-surface sediment packages include pressure, grain size, density, packing, porosity, pore shape, pore pressure, pore fluid, volumetric water content, permeability, and rigidity (Bachrach et al., 1998d; Grote et al., 2003; Jarvis et al., 2002; Pelton 2005; Santamarina et al., 2001; Santamarina et al., 2005; Yilmaz 1987). Most of these physical properties can be significantly altered and affect one another during early-stage diagenesis via mechanical processes such as compaction and dewatering (Andrade et al., 2011; Englehardt 1977; Holland 1980). Consequently, such developments and their corresponding variable effect over time and space largely affects an important dependent physical property – seismic shear impedance (or SI) (Cha et al., 2014a; Knight et al., 2005; L’Heureux et al., 2017; Latimer et al., 2000).

In sand- and clay-rich sediments, the initial packing of grains facilitates different compaction behavior over time as early-stage diagenesis occurs (Holland 1980). Indeed, for clay-rich sediment packages, initial packing results in a rapid and continual drop of porosity in the near-surface (~1 – 30 m) relative to sand-rich sediment packages as compaction occurs (Holland 1980). Moreover, sand-rich sediments that have undergone little to no diagenesis – especially those that are saturated and unconsolidated – retain a low rigidity at grain contacts (Avseth et al., 2005a). The reduction of clay porosity from compaction and the corresponding increase of pressure results in clay-rich sediments retaining a greater rigidity compared to sand-rich sediments (Englehardt 1977; Holland 1980).

As compaction occurs, dewatering facilitates the reduction of fluid volumetric water content in different sediments (Lambe et al., 1969). Overall, the result of dewatering can further increase clay rigidity (Cha et al., 2014b; Mainsant et al., 2012; Odum et al., 2004).

In summary, compaction and dewatering of clay-rich sediments results in a porosity and water content reduction, both of which develop greater rigidity of near-surface clay-rich sediment packages relative to sand-rich sediment packages. Higher rigidity manifests itself as a comparatively greater SH-wave seismic velocity in clay-rich sediments, which also translates to a relatively greater SI.

The first objective of this study is to confirm the dipping and non-dipping architecture associated with ideal fluvial downstream point-bar models via high-resolution SH-wave seismic reflection imaging and thereby demonstrate that using this particular remote surveying method is superior to others in near-surface environments characterized by conductive, saturated, and/or unconsolidated sediments. To date, no study has successfully imaged a near-surface point-bar with SH-waves.

In addition, this study seeks to verify that clay-rich sediment packages associated near-surface fluvial point-bars can retain comparatively greater seismic SI magnitudes compared to sand-rich sediments mainly due to compaction and dewatering. Incorporating an early-stage diagenetic model to explain the differing SI magnitudes associated with near-surface point-bar sediment packages has not previously been

used and may serve to improve the quantitative characterization of fluvial point-bar models.

(1.3) Study Site

I conduct two seismic reflection surveys near the southern end of an oxbow lake called False River (Pointe Coupee Parish, Louisiana) (Figure 1.1).



Figure 1.1. The United States and all state boundaries therein are illustrated with an inset superimposed. The inset is a satellite image of the False River area with a red box inclosing the approximate area this study investigates (Google, 2017).

(1.4) Geological Background

(1.4.1) Overview of False River Geology & Development

False River is an oxbow lake (Figure 1.1 & 1.2) located approximately 30 km north of Baton Rouge and slightly west of the Mississippi River (Farrell 1987). The avulsion event that facilitated the cut-off and development of the False River area occurred in the early 1700's (Simons et al., 1974; Sternberg 1956). The sediments that comprise the lower to mid (<40 m) subsurface stratigraphy of this area are Pleistocene gravels and Holocene sands (Figure 1.2) (Saucier 1969). Upper sections of the near-surface (1 – 30 m) and floodplain are composed of sand and clay-rich deposits (Morrison 2017; Wolman et al., 1957). The near-surface and subaerially-exposed sections of False River are comprised of multiple point-bar complexes and scroll-bars, respectively.

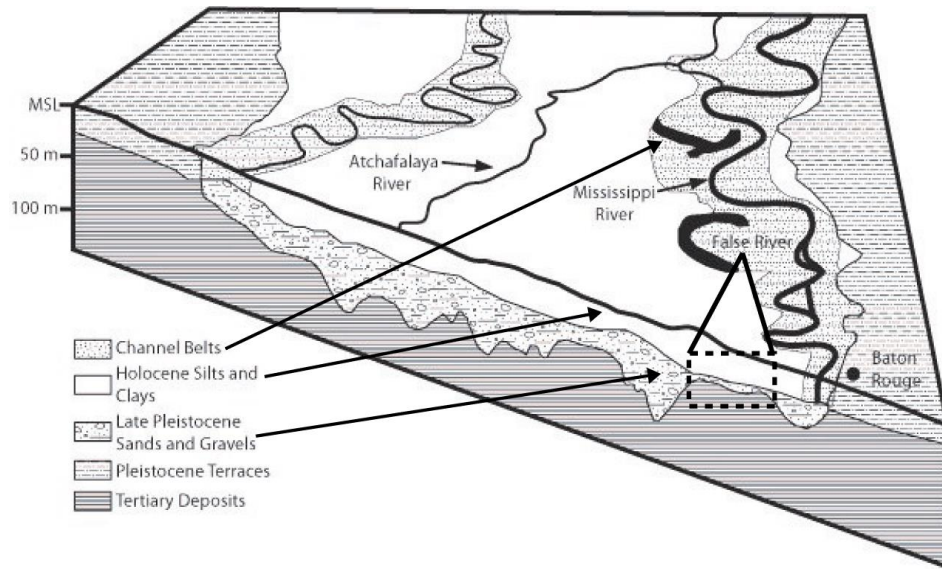


Figure 1.2. Overview of False River area geology (Fisk 1944). The geology enclosed within the dashed box is projected to the survey site at a southern section of the False River area.

(1.4.2) Ideal Point-Bar Complex Development & Architecture

Point-bars progressively form through lateral accretion as well as continual erosion and deposition along convex banks of meandering river bends (Davies 1966; Fustic et al., 2012; Harms et al., 1982; Mowbray 1983). Point-bar complexes may be divided into three sections: upper, central, and downstream (Figure 1.3) (Ghinassi et al., 2015). The development of point-bars favors the preservation of downstream sections (Ghinassi et al., 2016). Although central point-bars are often preserved, they are comparatively less so with respect to downstream point-bars. Upstream point-bar deposits are highly eroded and are rarely preserved (Ghinassi et al., 2015).

Downstream flow conditions along convex channel bends are dominated by relatively slower flow velocity and secondary circulation (Kasvi et al., 2013). These conditions deliver a relatively low-energy environment whereby finer-grained sediments such as silt and clay settle on the inner (convex) bank further downstream and mainly on the shallower sections of a given point-bar complex (Davidson 1985; Ghinassi et al., 2016; Julien 2002).

Ideal point-bar models oriented orthogonal to flow exhibit internal architecture made of sediment packages that dip towards channel thalweg (Figure 1.3 & 1.4). (Pranter et al., 2007). However, for models showing point-bar architecture situated parallel to channel flow, there is little to no dip associated with sediment packages (Figure 1.3 & 1.4) (Noah et al., 1992).

The False River area is comprised of multiple point-bar complexes. For each area of a given complex in this area (upstream, midstream, and downstream), the overall architecture and physical properties of point-bar sediment packages are different (Clift 2016; Ghinassi et al., 2016). This study seismically examines a downstream point-bar and the sediment packages that comprise it.

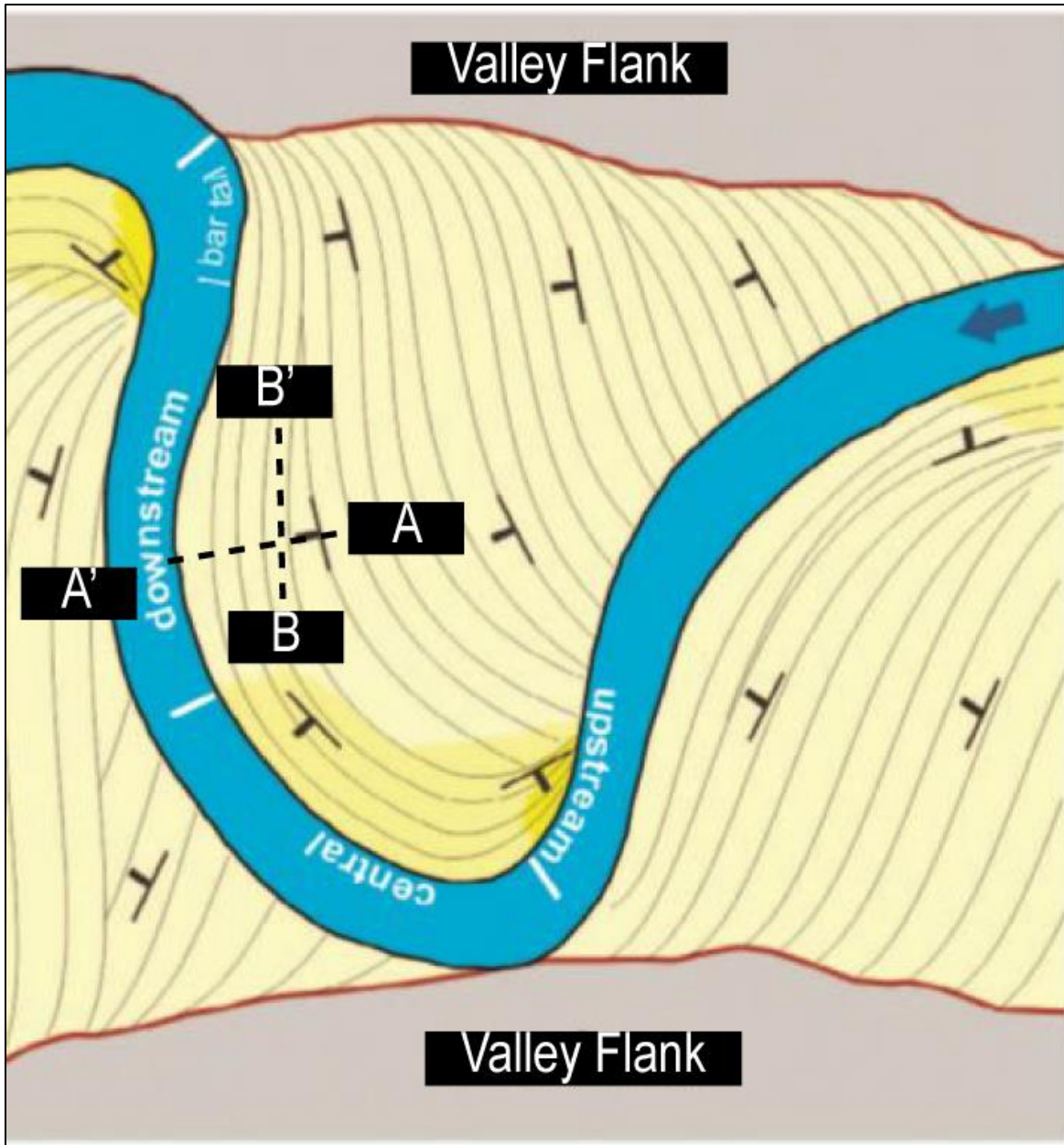


Figure 1.3. Meandering river bend and overall point-bar complex development from aerial perspective adapted from Ghinassi et al. (2015). The three sections of a point-bar complex are imaged here: upstream, central, and downstream. The dashed line within the downstream point-bar area is approximately orthogonal to the channel (A – A'). The B – B' line is parallel to channel flow. With respect to Figure 1.2, the valley flank illustrated here may be generalized to the Pleistocene terrace adjacent to the Mississippi River.

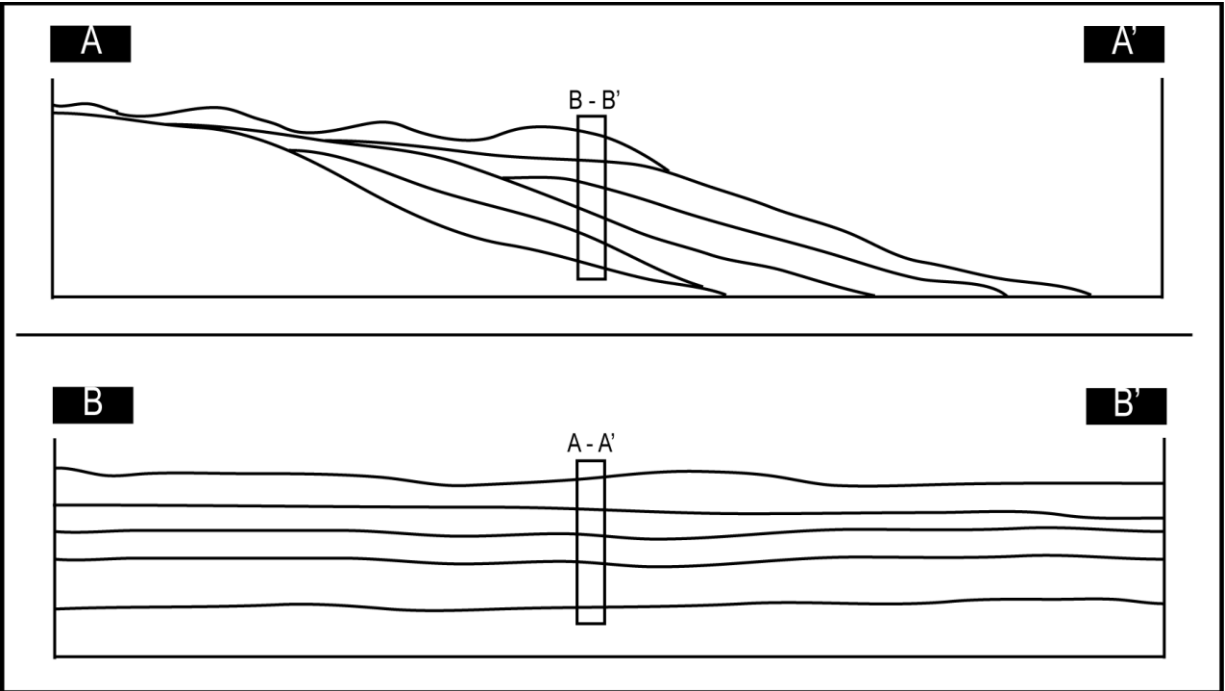


Figure 1.4. A 2-D cross-section view of the A – A' line from Figure 1.3 is illustrated here (top). The architecture from left to right is indicative of the dipping point-bar sediment packages towards channel thalweg, which flows into the page. The AX denotation near the middle shows the location where the B – B' intersects (bottom). Specifically, B goes out of the page, and B' goes into the page (parallel to channel flow). Sediment packages illustrated here undulate slightly but do not necessarily dip relative to the top cross-section (A – A'). The BX is the position of B – B' that intersects with AX. Overall, the A – A' and B – B' sections are orthogonal to one another. This ideal model of a downstream point-bar is adapted from Pranter et al. (2007).

(1.5) Previous Data

Well-log data is available for this study from previous research at the survey site (Figure 1.5) (Lechnowskyj 2015). Specifically, I incorporate two electrical conductivity (EC) well-logs.

(1.5.1) EC Well-Log Data

The EC logs I use for this study are from W5 (Figure 1.6[[left](#)]) and W7 (Figure 1.6[[right](#)]). Each of these wells lie directly within the study site (Table 1.1 & Figure 1.5).

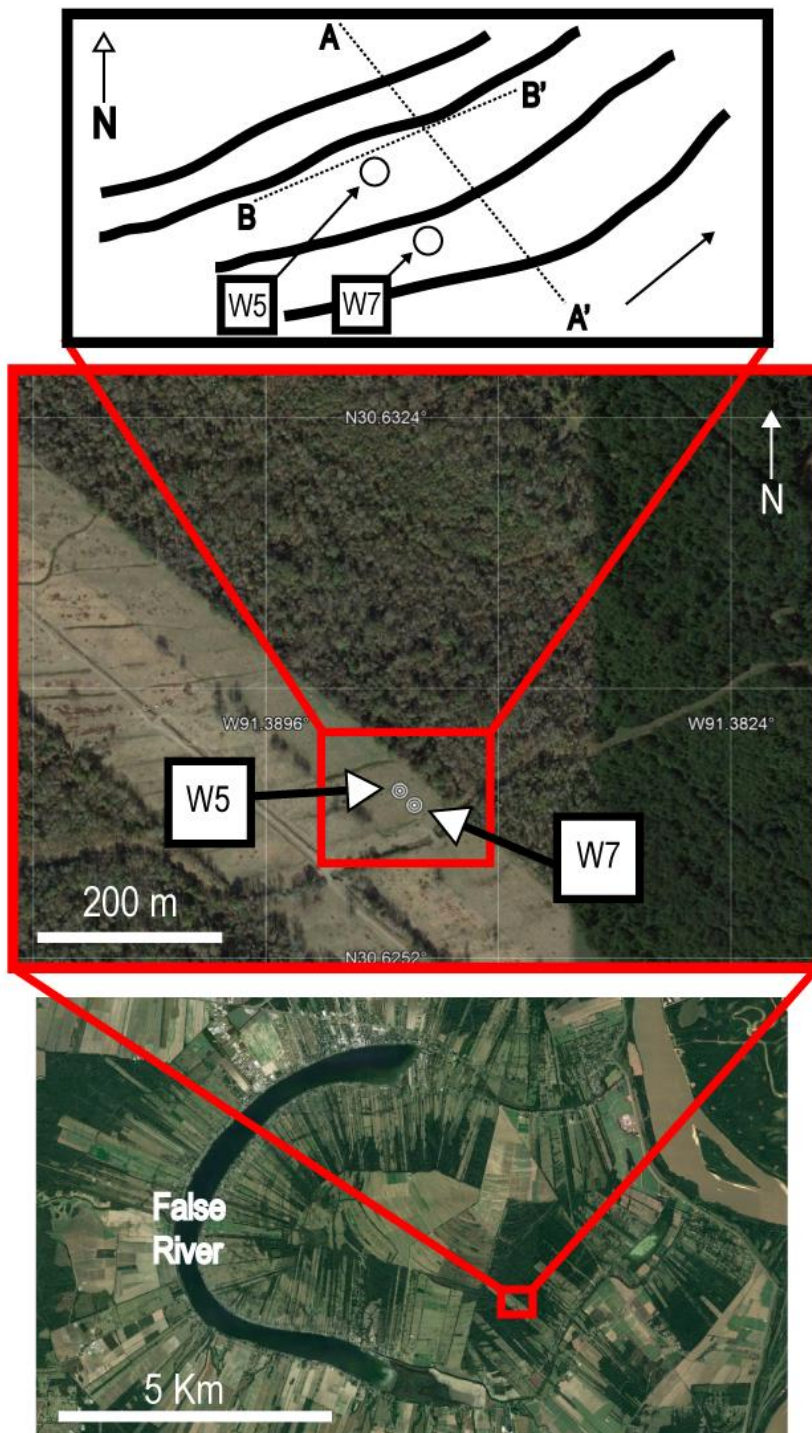


Figure 1.5. The first inset above is identical to the inset of Figure 1.1. This inset displays a closer satellite image of the study site (Google, 2017). The approximate locations (Table 1.1) of W5 and W7 are shown. The second inset (top) shows an illustration which incorporates the aerial view of an ideal downstream point-bar model (Figure 1.3) with respect to the study site along with well locations as well as the A – A' and B – B' lines superimposed. The arrow in the bottom right corner indicates paleochannel flow.

Interpolations of certain increases of EC from W5 to W7 based on previous research present evidence of different point-bar sediment packages dipping from ~NW to ~SE (Lechnowskyj 2015). Collectively, W5 and W7 are approximately parallel to A – A'. As such, these well-log data confirm dipping sediment packages associated with a downstream point-bar. As for B – B', there are no wells parallel to this line. Despite this data limitation, there should be comparatively little to no lateral change of point-bar sediment package architecture or physical properties parallel (B – B') to paleochannel flow.

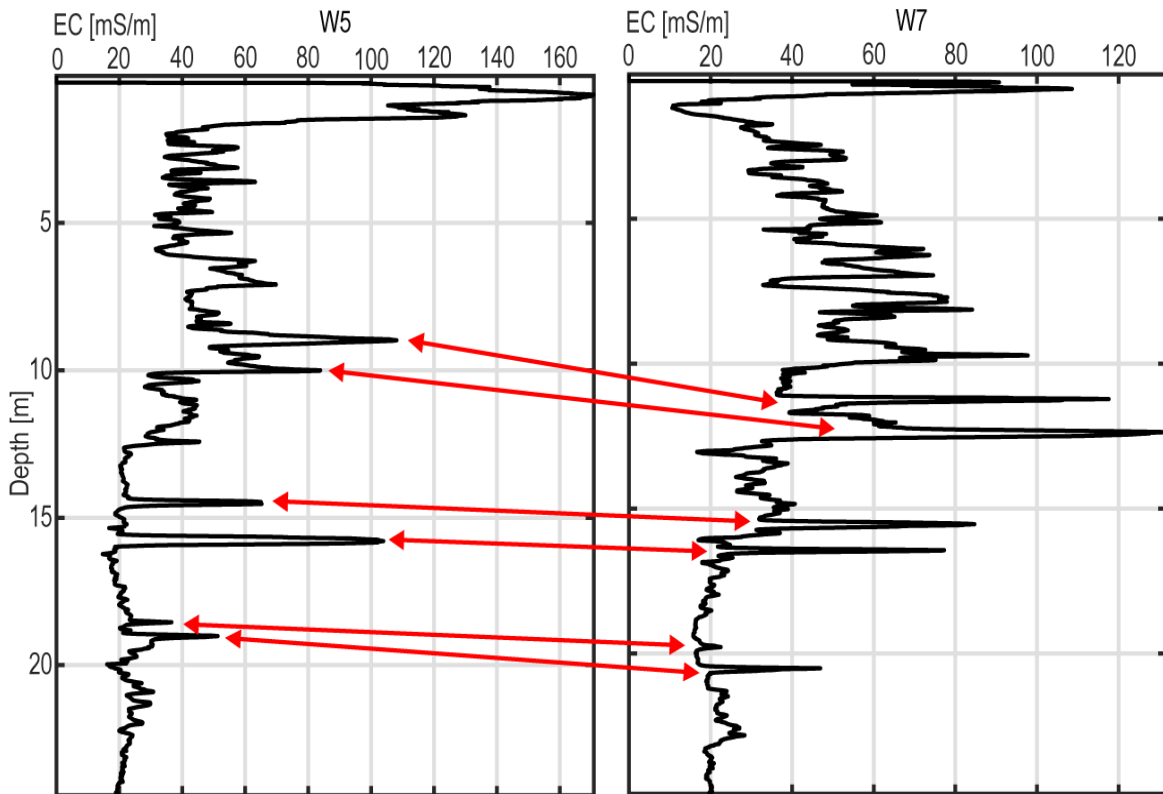


Figure 1.6. EC measurements for W5 (left). Certain increases of EC are interpolated to W7 (right), which is positioned further ~SE relative to W5. The distance from W5 to W7 is ~31 m. Interpolation of certain EC increases are selected only deeper than ~9 m because I cannot seismically image any shallower near-surface targets.

Values associated with each interpolated EC increase shows some degree of lateral and vertical change from W5 to W7. Indeed, although the dipping architecture associated with a given sediment package may remain relatively unchanging, its physical properties may change.

Table 1.1. Latitude and longitude of W5 and W7 locations. Error associated with each GPS measurement is ± 10 m.

EC Wells	Latitude [Degrees]	Longitude [Degrees]
W5	30.627429	-91.387522
W7	30.627237	-91.387296

(1.6) An Explanation and The Advantages of Shear-Waves

Shear-waves (S-waves) propagate as a function of subsurface soil or rock matrix stiffness (shear-modulus) and are essentially unaffected by the presence of fluids relative to P-waves (Krawczyk et al., 2013b; Veeken et al., 2004; Wolz 2003b). Therefore, S-waves are ideal for analyzing saturated near-surface environments, especially in conditions such as a shallow water-table or gas-rich sediments (Hasbrouck 1991; Krawczyk et al., 2013b; Missiaen et al., 2008; Santamarina et al., 2005; Wang et al., 2000). Unconsolidated and saturated sediments characterize the near-surface environment that this study analyzes. The water table is relatively shallow (~6.4 m) at our survey site (Lechnowskyj 2015). We assume pore spaces are partially saturated by primarily air and water.

A horizontally-polarized S-wave (SH) particle motion displaces into/out of the page (Figure 1.7). In addition to the details above, surface seismic reflection surveying with SH-waves provide other advantages. Specifically, no mode conversion occurs upon reflection and transmission at the interface separating parallel interfaces (Aki et al., 1980). This scenario only occurs so long as the survey surface and interface are parallel to one another (Xia et al., 2002). For both obliquely incident P- and vertically-polarized (SV) waves, mode conversions occur, which complicates the resulting wavefield and comparatively reduces the amplitude of the reflected/transmitted propagating seismic wavefront (Young et al., 2001). Another advantageous feature of SH-waves is their relative stability at pre-critical reflection angles (Simmons et al., 2001). Also, S-waves experience less attenuation in the upper near-surface (~5 – 10 m) relative to P-waves in unconsolidated sediments (Krohn et al., 2016). Lastly, near-surface SV-waves are susceptible to generating pronounced surface ghosts (Krohn et al., 2016).

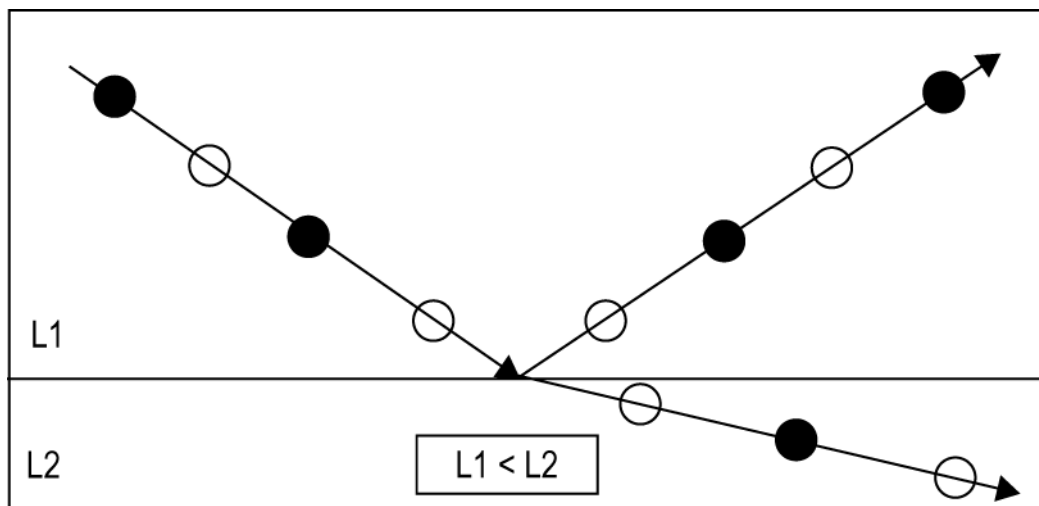


Figure 1.7. SH-wave reflecting off and transmitting through an interface that divides two differing constant velocity media. The velocity associated with L1 is greater than L2. Filled black dots indicate particle motion out of page, and empty circles indicate particle motion into page. This illustration is modified from Liner (2004).

CHAPTER 2: METHODS

(2.1) Reconnaissance Study & Source Determination

Before planning and conducting a seismic survey, it is necessary to perform reconnaissance work for two critical reasons (Büker et al., 1998; Miller et al., 1989; Steeples et al., 1998; Stone 1998). The first is to evaluate if there is any detectable subsurface target that may be seismically image (Steeples et al., 1998). The second is to determine which seismic energy source provides optimal spectral characteristics at the proposed survey site (Miller et al., 1986).

(2.1.1) Target Exploration

Acquisition parameters are set prior to any data acquisition for this study (Table 2.1). I detect multiple seismic reflectors from pseudo walk-away (Figure 2.1) shotgathers (Figure 2.2). This 2-D survey geometry requires geophones to remain stationary between successive shots, which are moved and positioned with respect to the maximum-receiver-offset (Spikes et al., 2005).

Table 2.1. Details of the pseudo walk-way survey. See Figure 2.1 for a pseudo walk-away survey layout. WASP is an abbreviation for walk-away shot-point.

Pseudo Walk-Away Survey Date	02/11/2017
Seismograph	24-Channel, 24-Bit Resolution, R-24 Geometrics Strataview
Sensors	24, Mark Products, 30-Hz SH-geophones
Channels	24
Delay Recording Time	-0.010 s
Total Sampling Time	4.010 s
Sampling Interval	0.0005 s
Nyquist Frequency	1000 Hz
Survey Orientation	301° NW
Survey Location (WASP-1)	Latitude: 30.627452°, Longitude: -91.387908°
Sources	Shear-Gun and Hammer
Group Interval (WASP-1, WASP-2, and WASP-3)	1 m
WASP-1 Minimum/Maximum Source-to-Receiver Offset	1 m / 25 m
WASP-2 Minimum/Maximum Source-to-Receiver Offset	25 m / 49 m
WASP-3 Minimum/Maximum Source-to-Receiver Offset	49 m / 73 m

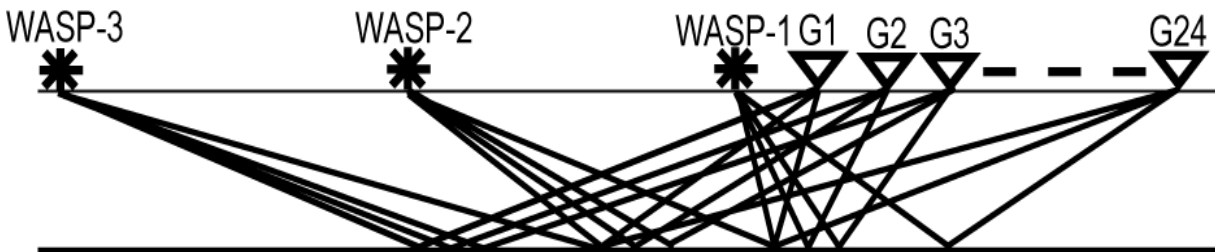


Figure 2.1. 2-D cross-section illustrates the acquisition geometry and ray paths associated with the pseudo walk-away reflection survey. G1 – G24 denote geophone number and positions for each shotgather (WASP-1 – WASP-3).

Near-surface seismic reflectors are mainly concentrated within an optimal window (Figure 2.2). This *window* is defined as a variable space-time section within a given shotgather that retains only reflection events with little to no coherent noise interference (i.e. direct, air-blast, guided, refracted, ground-roll, and Love-waves) (Hunter et al., 1984).

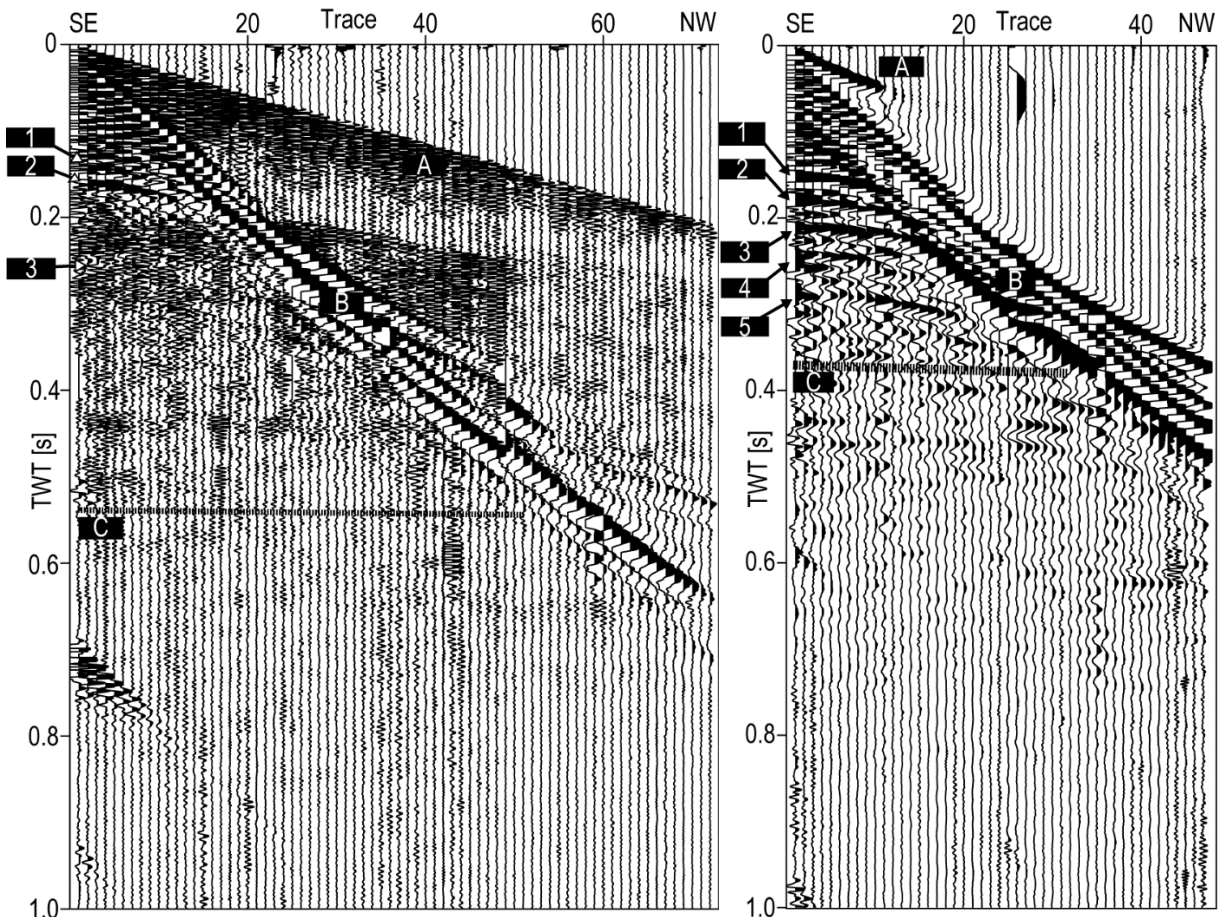


Figure 2.2. Comparatively higher frequencies (left) are present as a result of using the shear-gun as the seismic source. Features A, B, and C correspond to the air-blast, Love-wave, and optimal window, respectively. Features 1 and 2 are reflections. Feature 3 corresponds to a high frequency packet that exhibits an overall hyperbolic moveout that is discernable in and out of the optimal window. The seismic data imaged here are clipped (0.5). Also, no gaining or filtering are applied. Trace spacing is 1 m. Seismic data are from WASP-1, WASP-2, and WASP-3. Comparatively lower frequency content dominates this shotgather (right), which corresponds to the hammer source. Features A, B, and C are the air-blast, Love-wave, and optimal window, respectively. The presence of the air-blast is comparatively minimal. Also, more reflection events (Features 1 – 5) are visible as a result of using the hammer as the seismic energy source. No gaining or filtering has been applied, however the data are clipped (0.5). Trace spacing is 1 m. Seismic data are from WASP-1 and WASP-2.

(2.1.2) Seismic Source Determination

The hammer/shear-plate (Figure 2.3[right] & 2.4) is selected as the optimal seismic source instead of the shear-gun (Figure 2.3[left]) for three reasons: safety, cost, and superiority in terms of spectral properties. This source is comprised of two components: a shear-plate and hammer. The hammer is used to manually strike the shear-plate from both the left and right directions by a user, thereby inducing two opposite polarity shear-impulses into the earth that are subsequently recorded as left and right-shotgathers, respectively. This type of seismic source is successfully used by previous shear-wave studies (Pugin et al., 2002).

Despite the shear-gun source generating comparatively higher frequencies, I choose the hammer as the primary seismic source for this study. This ruling is based not only on the reasons listed above and below, but also on the fact that higher frequency content does not necessarily provide or guarantee the means for greater resolution (Bleistein et al., 2001).

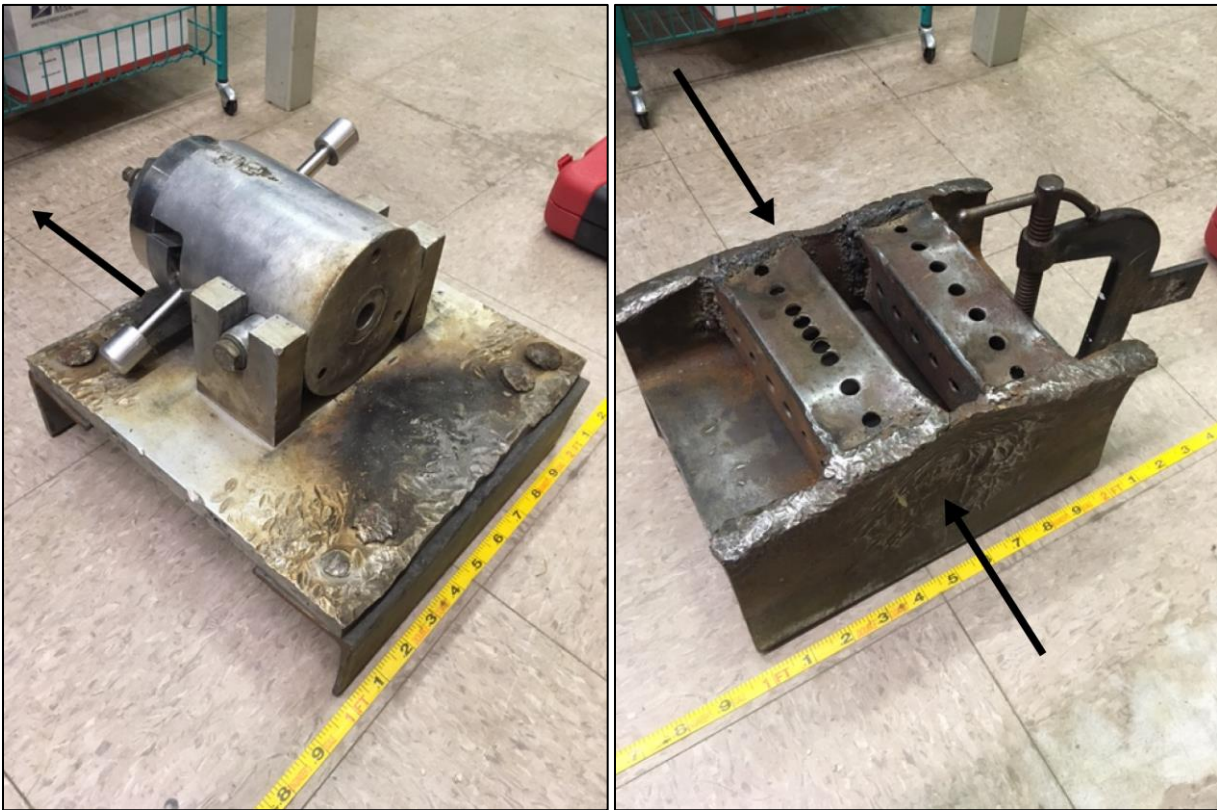


Figure 2.3. The shear-gun source (left). As it is positioned for this image, the initial force generated from an explosion displaces the entire apparatus in the direction indicated by the arrow. Units of the yellow measuring tape adjacent to the plate are inches. Black arrows on the shear-plate (right) indicate the direction and position of a left/right strike with the hammer. Units of the yellow measuring tape adjacent to the plate are inches. The weight of the shear-plate is ~13.6 kg.



Figure 2.4. This is the hammer. A user stands atop the shear-plate and manually applies a force to the shear-plate by striking the left/right side of the plate. This action generates and transmits a shear-impulse into the earth. The weight of the hammer is ~4.22 kg.

We use shotgathers corresponding to both the shear-gun and hammer sources from the first shotpoints of the pseudo walk-away survey (WASP-1) to evaluate the power-frequency characteristics and distribution of each seismic source (Figure 2.5). Using f-x and power spectra analyses, the optimal source is selected. The first three traces of both the shear-gun and hammer shotgathers from WASP-1 are used to provide a near-field estimate the spectral properties corresponding to each seismic source. Also, all traces of each shotgather from WASP-1 are used to examine amplitude-frequency distribution with offset.

Seismic sources are evaluated according to safety, cost, portability, efficiency, and repeatability in terms of both power and phase characteristics (Burger 1992; Hanahen 1948; Miller et al., 1989; Pugin et al., 2002; Wiederhold 2006). A hammer source is naturally safer than one that requires explosives (Hanahen 1948). Also, a hammer source requires minimal maintenance and overall cost relative to a seismic source that requires explosives. The phase of both the shear-gun and hammer sources is not examined as analyses of spectral properties of near-surface land seismic sources conventionally focus on only assessing power-frequency content (Mestan 2015; Miller et al., 1989; Miller et al., 1986). However, the phase of processed seismic data will be discussed later (Section 2.4.12).

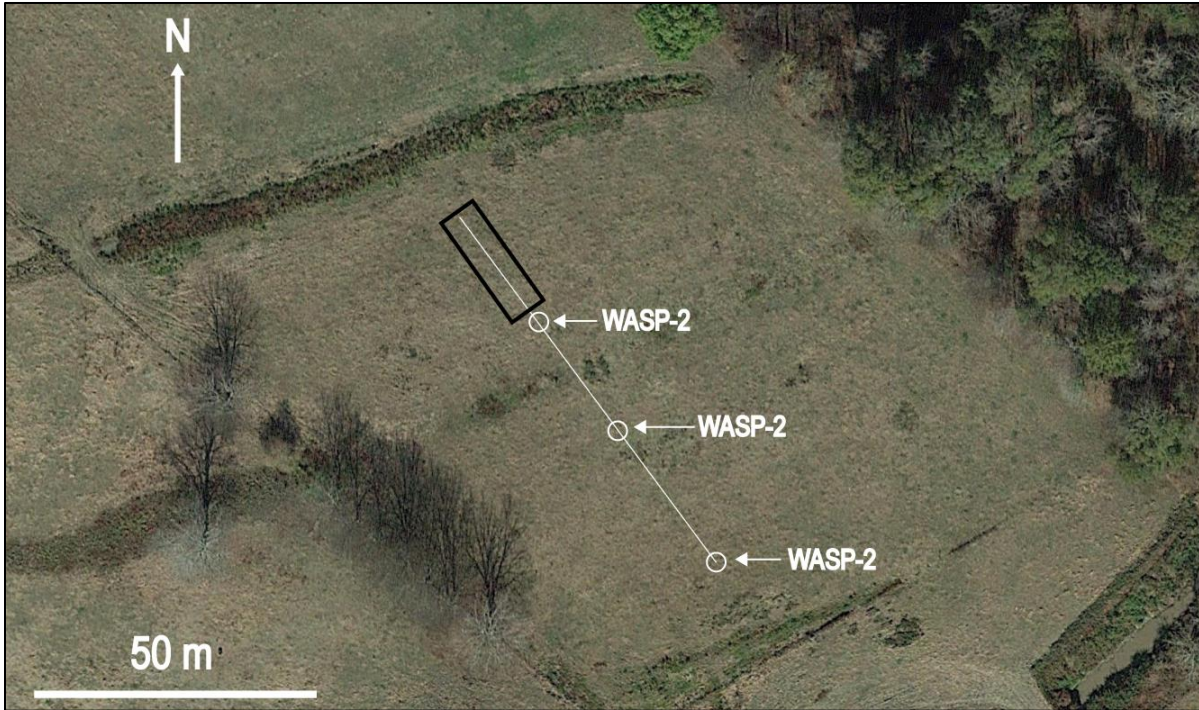


Figure 2.5. A satellite image that shows the pseudo walk-away survey (Google, 2017). WASP is an abbreviation for walk-away shotpoint. The shotpoint locations corresponding to the walk-away shotgather for the shear-gun source includes WASP-1, WASP-2, and WASP-3. We use only two shotpoints for the hammer seismic source (WASP-1 and WASP-2). The rectangular box at the northwestern end of the pseudo walk-away survey encloses the area where twenty-four geophones are positioned for the entirety of the walk-away survey.

Overall, the shear-gun generates higher frequencies (+100 Hz) and amplitude content that is unevenly distributed with offset relative to the hammer source (Figure 2.6). Also, the near-field estimate shows multiple notches with periodic behavior (Figure 2.7). The result of these notches is an uneven power spectrum, which is undesirable for a seismic source (Miller et al., 1989; Yilmaz 1987). The periodicity of the notches appears similar to ghost notches that are often observed in marine seismic data (Moldoveanu et al., 2006). Power corresponding to ~38, ~58 – 75, and ~90 – 100 Hz is either absent or highly attenuated. The cause of these notches are unknown. A possible reason for the notched normalized power spectrum is post-explosion reverberations generated by the shear-gun source.

Normalized power spectra and f-x data corresponding to the hammer source present relatively more uniformity in terms of frequency and amplitude distribution with offset as well as a flatter bandwidth from the near-field estimate (Figure 2.8). This spectral behavior is preferable because I seek to preserve as much evenly consolidated power and frequency content as possible for imaging and inversion purposes (Arya et al., 1978; Becquey et al., 1979; Widess 1973). Also, more frequency and power content are present below 20 Hz relative to the shear-gun source (Figure 2.7 & 2.9). Retaining comparatively more frequency and power content at and below this range (>15 – 20 Hz) is critical for seismic inversion (Cooke et al., 2010).

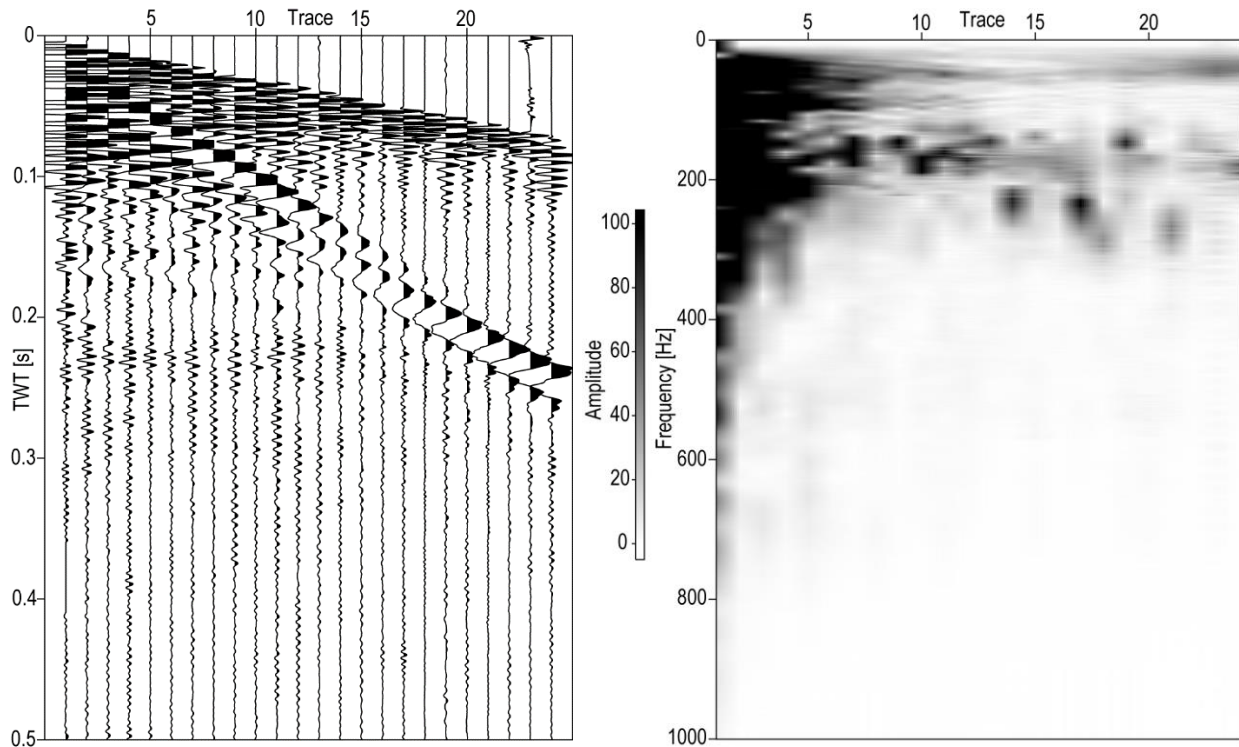


Figure 2.6. Shotgather (left) from WASP-1 corresponding to the shear-gun source. Time range of 0.0 – 0.5 s is used and the seismic data are clipped (perc=95). Also, no gaining or filtering are applied. Trace spacing is 1 m. Calculated f-x spectrum (right) of data displayed in Figure 2.6[left]. This type of display shows amplitude and frequency variations with offset. Amplitude is highest in traces 1 – 6, and the approximate bandwidth ranges 15 – 380 Hz.

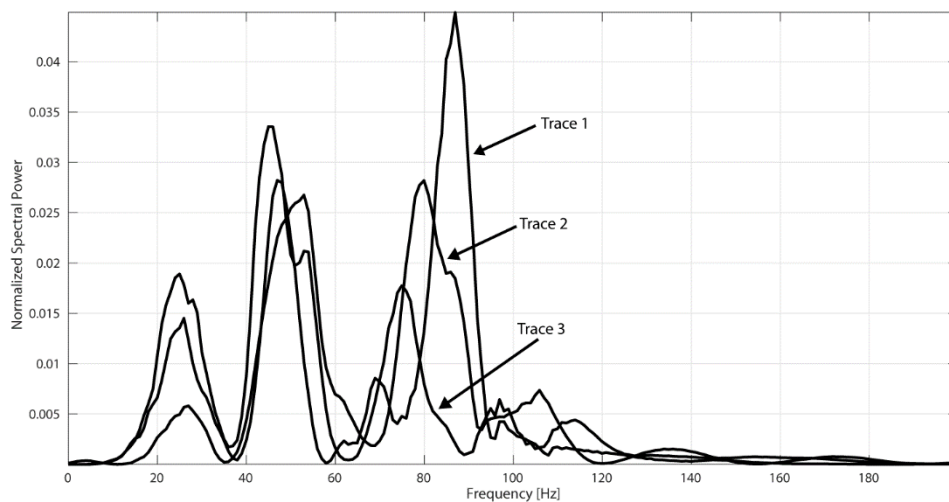


Figure 2.7. Amplitude spectra (0 – 200 Hz) of traces 1 – 3 of the shear-gun source. The overall bandwidth is uneven in terms of power and frequency. Also, multiple periodic notches appear throughout for each trace.

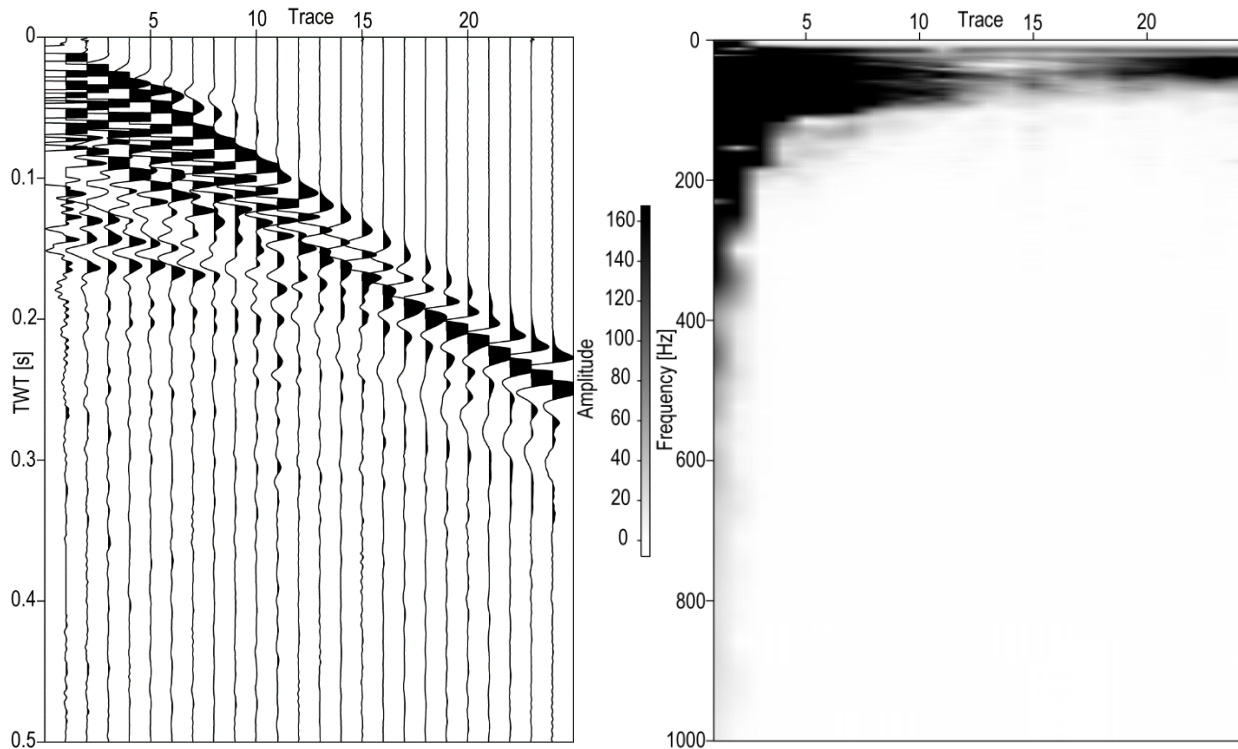


Figure 2.8. The first shotgather of the hammer source (left) from WASP-1 (Figure xxx). No gaining or filtering is used. Seismic data are clipped (perc=95), and the trace spacing is 1 m. The f-x graph (right) corresponding to the hammer source, which is different compared to the shear-gun source in that a greater concentration and more evenly distributed level of amplitude is present at greater offsets. Most energy resides from traces 1 – 11 with a bandwidth of 0 – 280 Hz.

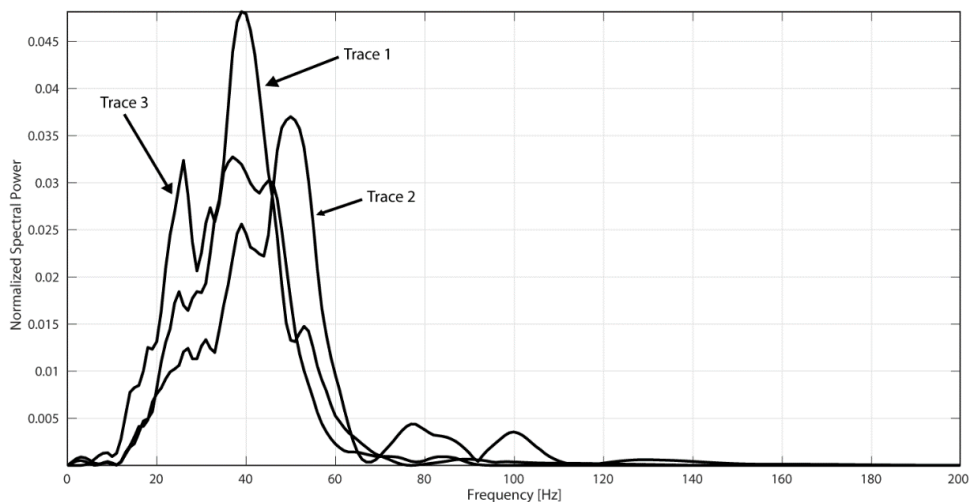


Figure 2.9. The first three traces of the first shotgather from WASP-1 are used to estimate the near-field power spectra characteristics of the hammer source. Small notches are also present for these data. The largest reduction of power here is ~ 0.01 (Trace 3). For the shear-gun source, power reduction ranges from $\sim 0.005 - 0.04$.

(2.2) Inline & Crossline Seismic Reflection Survey Details

Two separate seismic reflection surveys are conducted for this study (Table 2.2).

Table 2.2. Technical characteristics of the source, recording instrumentation, as well as acquisition positioning and geometry of both the inline and crossline seismic reflection surveys. The error associated with the position of each shotpoint is ± 5.0 m.

Inline Crossline Seismic Reflection Survey Dates	Inline: 02/17/2017, 02/18/2017, 03/03/2017 Crossline: 03/17/2017, 03/22/2017
Seismograph	24-Channel, 24-Bit Resolution, R-24 Geometrics Strataview
Source	Hammer
Sensors	48, Mark Products, 30-Hz SH-geophones
Channels	24
Delay Recording Time	-0.010 s
Total Sampling Time	2.0475 s
Sampling Interval	0.0005 s
Nyquist Frequency	1000 Hz
Minimum Source-to-Receiver Offset	1 m
Maximum Source-to-Receiver Offset	25 m
Geophone Interval	1 m
Shotpoint Interval	1 m
Inline (Magnetic) Azimuth	141°
Crossline (Magnetic) Azimuth	223°
Inline GPS Position of First/Last Shotpoint	Shotpoint 1: 30.627756°,-91.387653° / Shotpoint 104: 30.627043°,-91.386903°
Crossline GPS Position of First/Last Shotpoint	Shotpoint 1: 30.627561°,-91.387218° / Shotpoint 48: 30.627413°,-91.387658°

(2.2.1) Field Acquisition Equipment

All seismic data are recorded with a Geometrics R-24 Strataview (Figure 2.10[left]). Two twenty-four channel take-out cables are connected to one another. Each channel is connected to a separate geophone (Figure 2.10[middle]). Altogether, the forty-eight channel cable is connected to the rota-long-switch (Figure 2.10[right] & 2.11), which is also connected to the Geometrics R-24 Strataview for recording.



Figure 2.10. I use the Geometrics R-24 Strataview (left) to set the sampling rate, file structure, and record all seismic data for this study (Figure 2.12). A single Mark Products, 30-Hz, geophone (middle). As the geophone is situated for this image, it detects motion into and out of the page. The rota-long-switch (right) is connected to both the 48-channel take-out cable and Geometrics R-24 Strataview. The rota-long-switch allows for successive reconfiguration of channels for each shotpoint

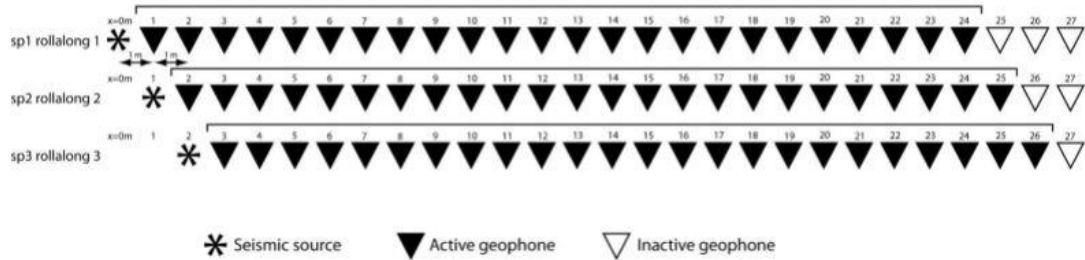


Figure 2.11. At each new shotpoint, the rota-long-switch is used to reconfigure all channels so that each shotgather maintains a full twenty-four traces. This optimizes seismic data acquisition. This figure is adapted from Morrison (2017).

(2.2.2) Field Acquisition Site & Survey Geometry

Two seismic reflection surveys are conducted at a southern section of an oxbow lake called False River (Figure 1.5 & 2.12). The initial A – A' is now replaced by IL – IL'. The IL is an abbreviation for inline as this particular survey is oriented approximately parallel to both W5 and W7. As for B – B', this line is now referred to as crossline (CL – CL') as this survey is situated orthogonal to the inline survey and the well locations (Figure 2.12).

I collect 104 inline shotgathers starting from the northwestern section at shotpoint 1 (IL) and ending in the southeastern end at shotpoint 104 (IL'). IL is equivalent to ILSP1, which is the first shotpoint of the inline survey. Likewise, IL' is equivalent to ILSP104 as this is the last shotpoint corresponding to the inline survey (Figure 2.12 & 2.13[left]).

I acquire 48 shotgathers for the crossline survey. The starting point of the crossline survey is located at the northeastern section of the line segment set perpendicular to the inline survey. From the first crossline shotpoint (CL' or CLSP1) in the northeastern end, I acquire data towards the southwest section until shotpoint 48 (CL or CLSP48) (Figure 2.12 & 2.13[right]).

The overall geometry of the inline and crossline surveys are configured for two-dimensional (2-D) common-mid-point (CMP) seismic reflection profiling (Mauring et al., 1995; Mayne 1962). From IL to IL', the inline survey length is ~104.0 m. For the crossline survey, the distance between CL' and CL is ~48.0 m. I use the end-on method for seismic data acquisition (Figure 2.14) (Yilmaz 1987).

The field acquisition geometry for the inline and crossline surveys is identical except for the final section of the inline survey. Specifically, from ILSP82 to ILSP104, each shotgather incrementally loses a trace due to progression up to the final shotpoint (Figure 2.15).

The topography of the southeastern section of the inline survey is characterized by a small elevation increase (Figure 2.12 & 2.13[left]) followed by a sharp elevation decrease into a channel (Figure 2.12 & 2.15). We do not deploy sensors into the channelized area. I accommodate for the lack of geophones by a special modification of the acquisition geometry for the inline survey. I correct for the geometry configuration and CMP sorting for trace headers in Section 2.4.5.

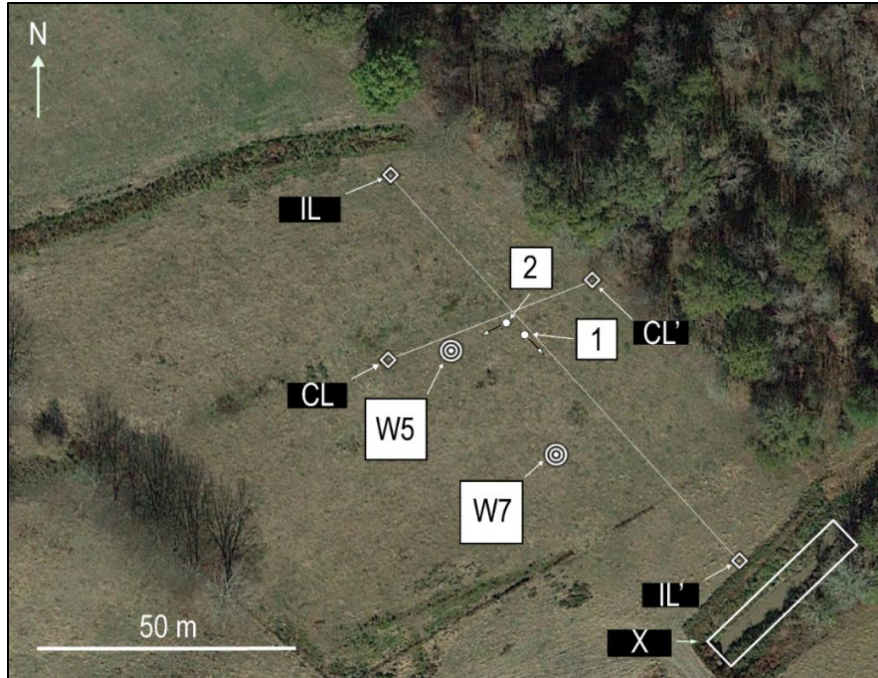


Figure 2.12. The position and orientation of the inline (IL – IL') and crossline (CL' – CL) surveys (Google, 2017). Also, the location of the two EC wells I use for this survey are shown (W5 & W7). IL – IL' represents the inline survey. CL – CL' represents the crossline survey. Feature X encloses a topographic low that is characterized by a channelized area. Ground perspective images from positions 1 and 2 are provided in Figure 2.13.



Figure 2.13. The inline survey ground perspective (left) from position 1 (Figure 2.12). The solid black line represents the position and orientation of the inline survey. The dashed box at the middle partially encloses a topographic high immediately before the topographic low area (Figure 2.12). Position 2 (Figure 2.12) captures part of the crossline survey (right). The black arrows on either side of the geophone indicate the primary ground motion that is measured during data acquisition.

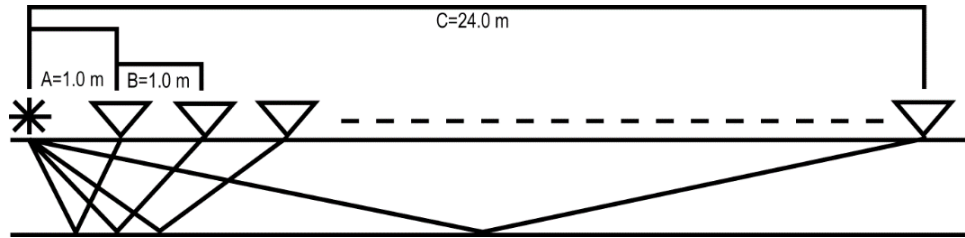


Figure 2.14. I use the end-on acquisition method for both the inline and crossline survey. The asterisk symbol at the left denotes the seismic source, and triangle icons represent individual receivers and channels. The distance that encloses A is the minimum source-to-receiver offset (1.0 m). B represents the group interval (receiver spacing), which is also 1.0 m. The distance of C is the maximum source-to-receiver offset (24.0 m). Line segments extending from the source to different receivers indicates ray paths.

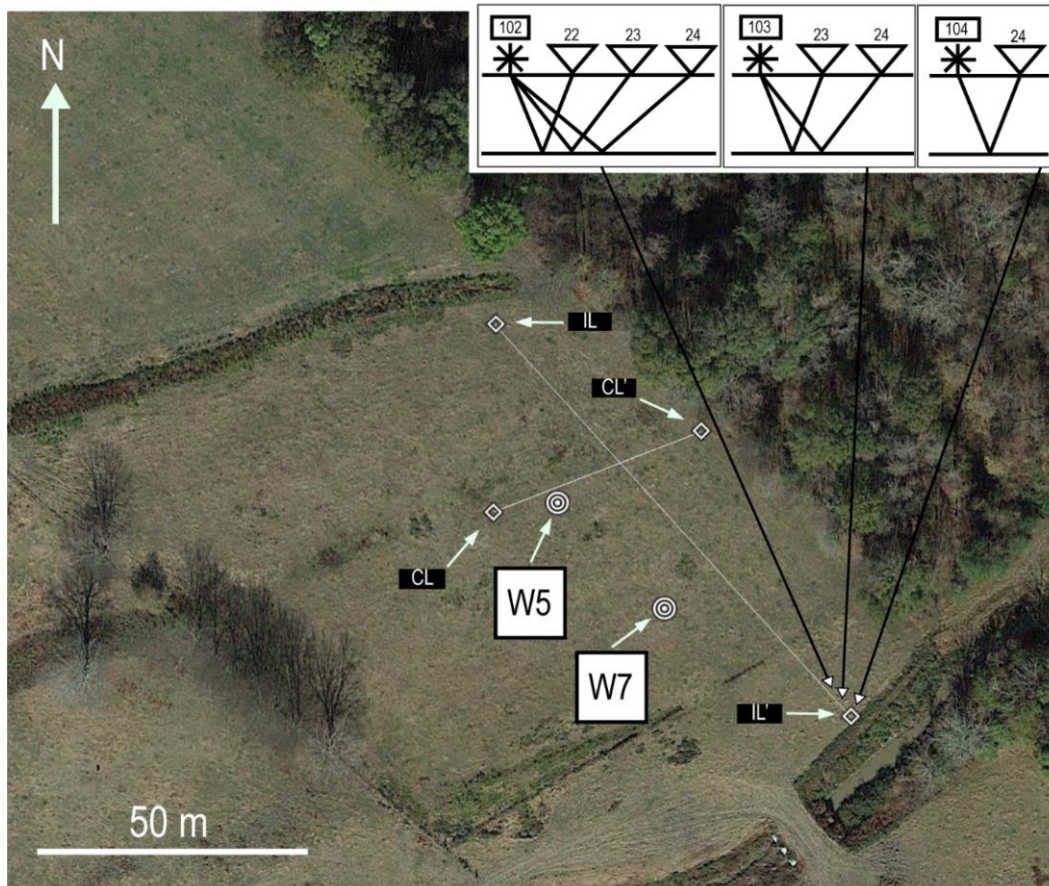


Figure 2.15. The three end-on common-shotgathers above the satellite image of the survey area represent the final three shotgathers collected for the inline survey (ILSP 102 – ILSP104) (Google, 2017). The number within the box above the asterisk (seismic source) indicates the shotpoint number. The number above each triangle (geophone) indicates geophone number. Each successive shotgather loses a trace (or geophone), and the source is subsequently positioned where that given geophone previously was. Although this pattern is only demonstrated for ILSP102 – 104, it is identical for ILSP82 – ILSP101 but with more geophones.

(2.2.3) GPS Positioning of Shotpoints & Geophones

A global positioning system (GPS) device calculates the approximate location of the first shotpoint and last geophone position of each acquisition day (Table 2.3, 2.4, 2.5, & 2.6). All GPS measurements are recorded in universal transverse mercator (UTM, z=15) format. Error for all GPS measurements is ± 10 m.

Table 2.3. The first shotpoint location of each acquisition day is acquired via GPS. These UTM data correspond to the inline survey.

ACQUISITION DAY	DATE	SHOTPOINT	NORTHING [m]	EASTING [m]
1.0	02/17/2017	1.0	3389457.0	654529.0
2.0	02/18/2017	36.0	3389432.0	654556.0
3.0	03/03/2017	65.0	3389410.0	654576.0

Table 2.4. The last geophone (L.G.) of each acquisition day is acquired via GPS. These UTM data correspond to the inline survey.

ACQUISITION DAY	DATE	L.G. NORTHING [m]	L.G. EASTING [m]
1.0	02/17/2017	3389414.0	654571.0
2.0	02/18/2017	3389392.0	654590.0
3.0	03/03/2017	3389378.0	654603.0

Table 2.5. Same as Table 2.3, however, these data correspond to the crossline survey.

ACQUISITION DAY	DATE	SHOTPOINT	NORTHING [m]	EASTING [m]
1.0	03/17/2017	1.0	3389436.0	654571.0
2.0	03/22/2017	25.0	3389428.0	654549.0

Table 2.6. Same as Table 2.4, however, these data correspond to the crossline survey.

ACQUISITION DAY	DATE	L.G. NORTHING [m]	L.G. EASTING [m]
1.0	03/17/2017	3389419.0	654529.0
2.0	03/22/2017	3389408.0	654507.0

(2.3) Pre-Processing

Before processing all acquired seismic data, we conduct two pre-processing steps. The first step is the interpolation of UTM information between the first shotpoint and last geophone position for a given day. Each interpolated position retains a unique UTM coordinate. With each UTM coordinate, we estimate elevation. Lastly, seismic data upload and conversion from SEG-2 to SU format are the final steps of pre-processing.

(2.3.1) UTM Interpolation & Elevation Calculation

The approximate UTM coordinates between each first shotpoint and last geophone pair of a given acquisition day are estimated via linear interpolation of UTM coordinates. Interpolation is performed with `utm_interpolation.m` (Section 8.9.1.6). Inline and crossline UTM coordinates are interpolated separately for each acquisition day (Figure 2.16, 2.17, & 2.18) and subsequently concatenated (Figure 2.19). The process of interpolation is identical for both the inline and crossline survey.

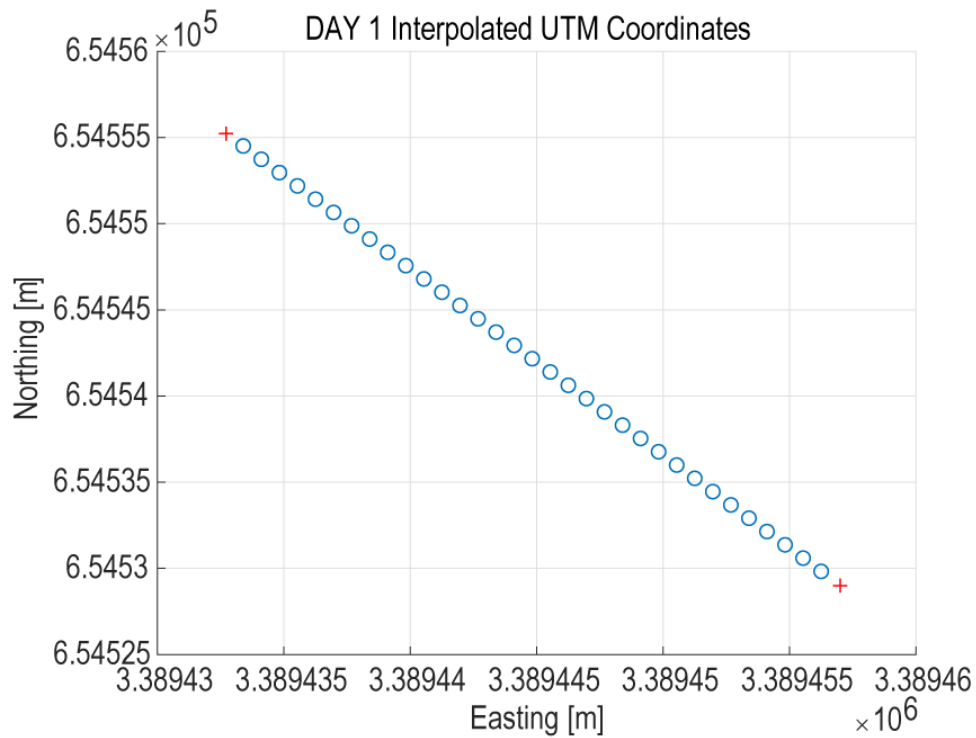


Figure 2.16. Interpolated locations (circles) between the first shotpoint and last geophone of the first acquisition day (02/17/2017) for the inline survey. The crosses indicate the anchor positions where GPS measurements are recorded.

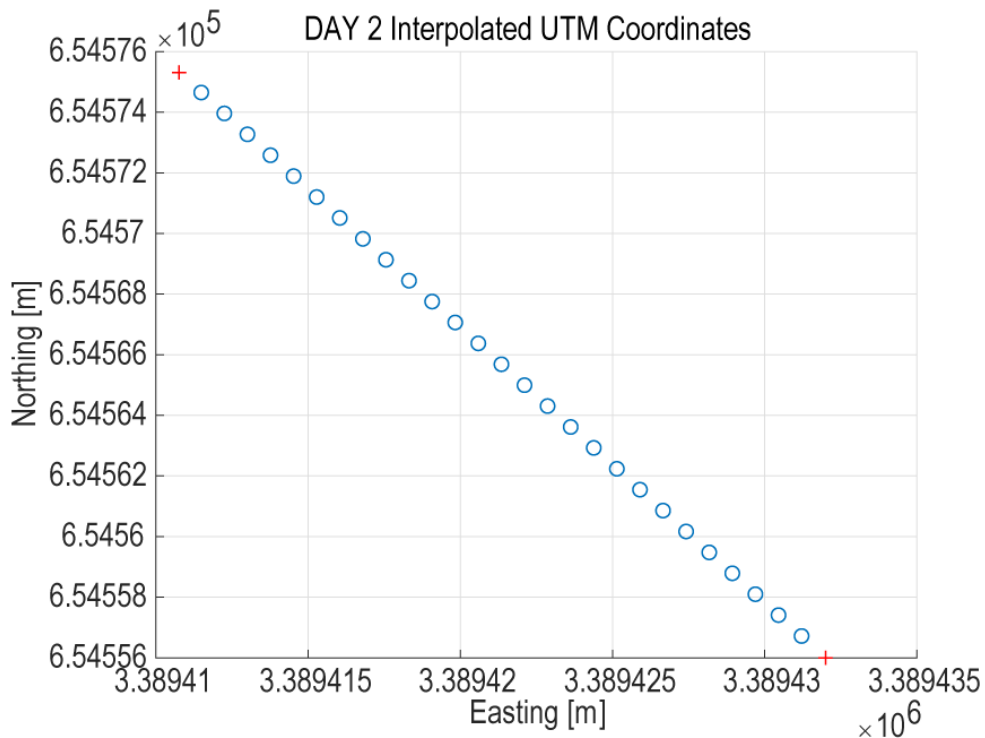


Figure 2.17. Same as Figure 2.16, however, these data are from the second acquisition day of the inline survey (02/18/2017).

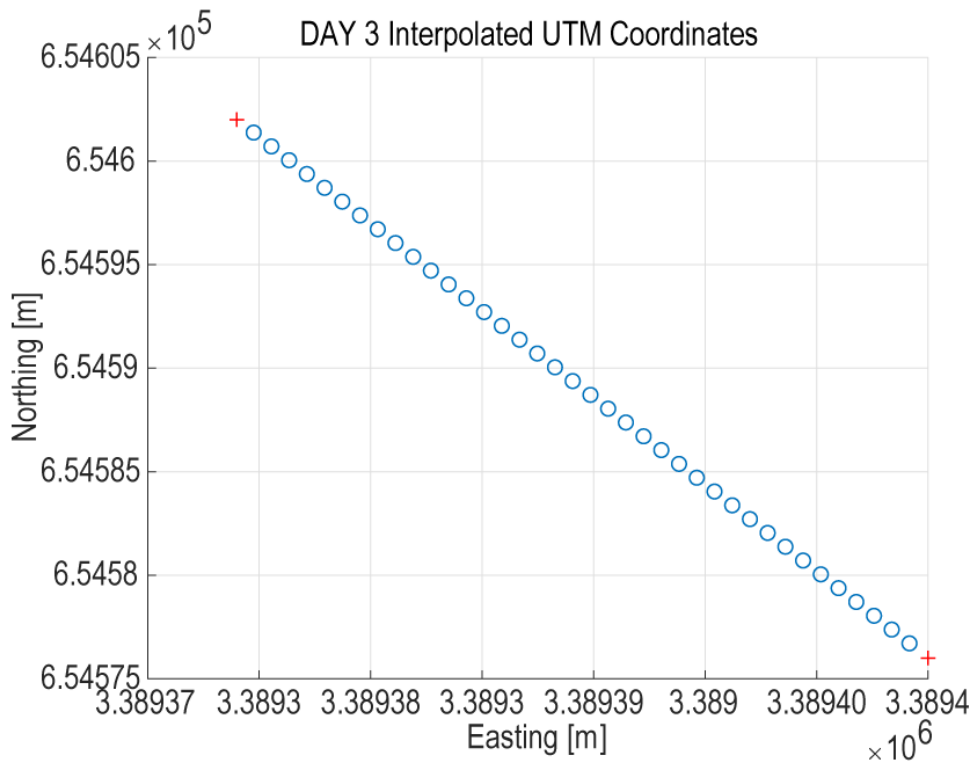


Figure 2.18. Same as Figure 2.16 and 2.17, however, these data correspond to the third acquisition day for the inline survey (03/03/2017).

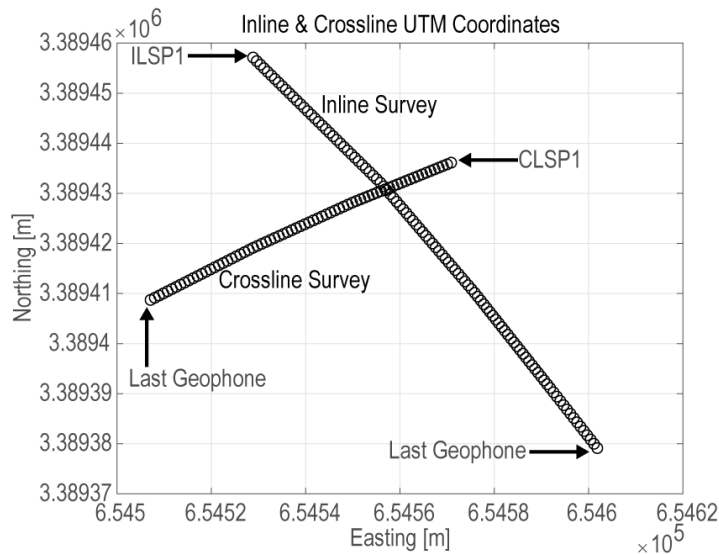


Figure 2.19. All inline and crossline UTM coordinates (circles). ILSP1 corresponds to data from acquisition day 1 (Table 2.3) of the inline survey. The last geophone position of the inline survey corresponds to data from acquisition day 3 (Table 2.4). Likewise, CLSP1 correlates to data from acquisition day 1 (Table 2.5) of the crossline survey. The last geophone position of the crossline survey corresponds to data from acquisition day 2 (Table 2.6). UTM coordinates for a given survey may be accessed via the gx and gy trace headers associated with each processed seismic section.

We use software to estimate the elevation profile for the inline and crossline surveys (Figure 2.20). The northing and easting values of each interpolated UTM position is provided as input to the software. The output is the estimated elevation value at each UTM coordinate. The software uses two datum sets for elevation calculation. The horizontal datum is NAD83 (GR580), and the vertical datum is NAVD88 (GEOID99). Error associated with the vertical datum (elevation) is ± 0.5 m. Elevation data is acquired from LiDAR (Light Detection and Ranging) (<http://www.atlas.lsu.edu/>) data (Atlas, 2001).

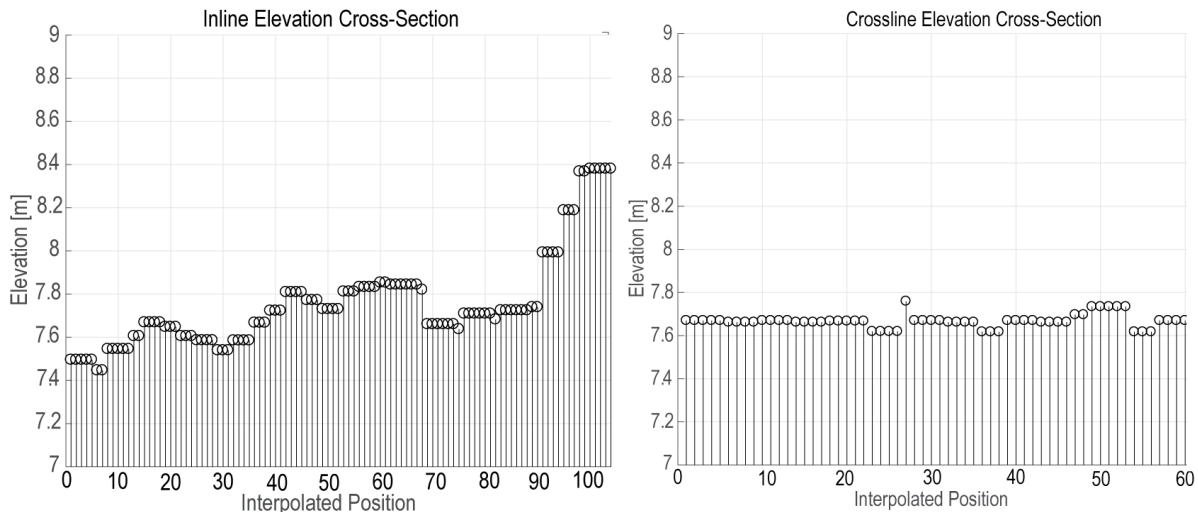


Figure 2.20. The inline elevation profile (left) is shown here. Past interpolated position 90, there is a relatively sharp elevation increase (IL=1 & IL'=104). The elevation profile (right) of the crossline survey, which is basically flat (CL'=1 & CL=60).

(2.3.2) Seismic Data Upload & Conversion

Seismic data acquired for this study are originally recorded in SEG-2 format by the Geometrics R-24. After each acquisition day, all seismic data are transferred and copied to an external memory device (Section 8.5). Data residing on the external memory device is subsequently copied to the main processing machine (Section 8.4) and converted to SU format via Sseg2su (Section 8.10.1).

(2.4) Processing

I process seismic data to generate a picture of the subsurface and condition amplitudes for seismic inversion. The overall process involves fifteen steps (Figure 2.21).

(2.4.1) Polarity Reversal

Because of miswiring in the rota-long-switch, traces 13 – 24 of each shotgather are 180° out-of-phase relative to traces 1 – 12 (Figure 2.22[left]). This issue is fixed by multiplying all samples for traces 13 – 24 by a unitary scalar (-1) via Reverse_polarity.pl (Section 8.10.2). The outcome of this processing step is a fixed shotgather where traces 1 – 24 are in-phase (Figure 2.22[right]).

To quality control (QC) the polarity reversal process, three seismic arrivals (air-blast, Love-waves, and a single seismic reflection event) of a given shotgather are selected and compared between the uncorrected (Figure 2.22[left]) and corrected shotgathers (Figure 2.22[right]).

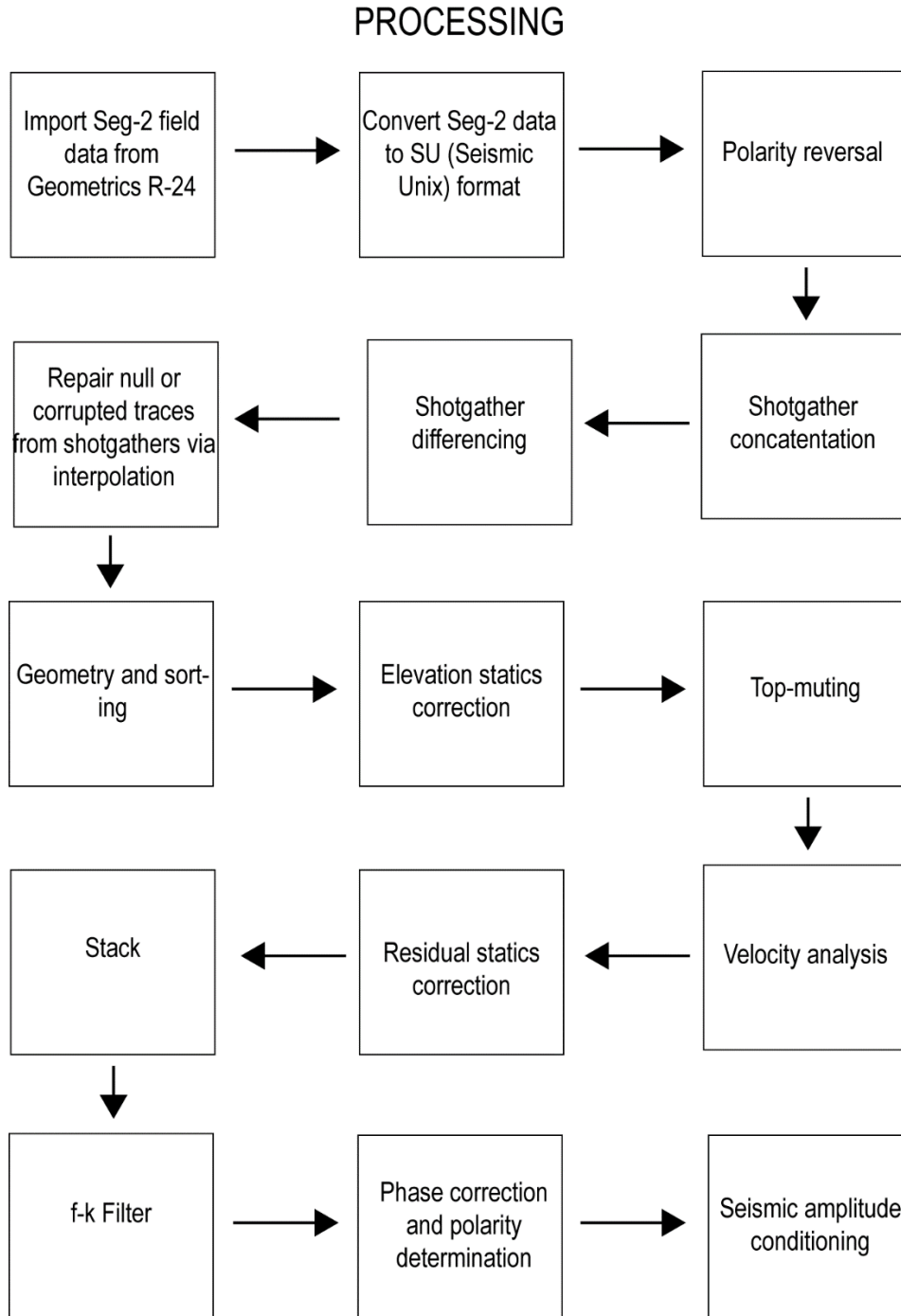


Figure 2.21. Workflow chart summarizes each section of seismic data processing.

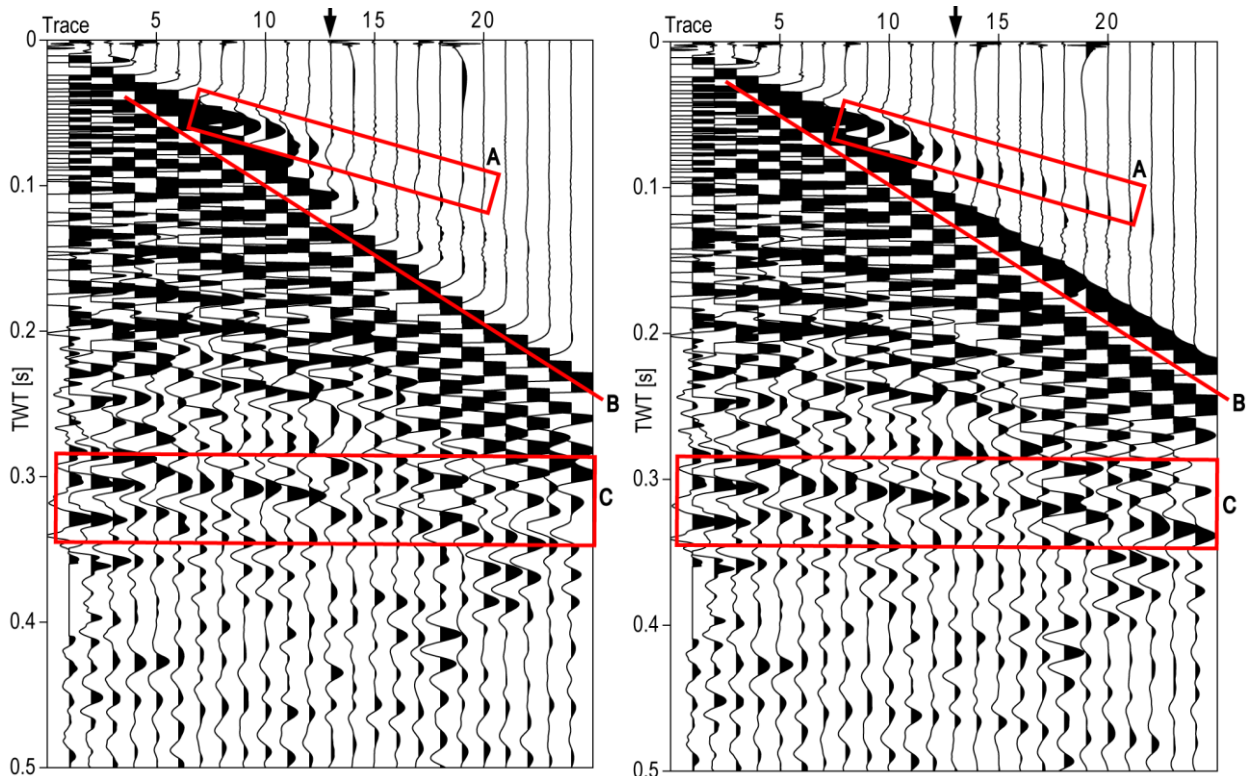


Figure 2.22. Polarity reversal is not applied (left) to these seismic data. Features A, B, and C are the air-blast, Love-wave, and single reflection event, respectively. The arrow points to trace 13, which is the first trace that is polarity-reversed. Features A – C present seismic arrivals that confirm traces 13 – 24 are 180° out-of-phase relative to traces 1 – 12. Seismic data displayed here correspond to ILSP20 of the inline survey. No gaining or filtered is applied, however, these seismic data are clipped (0.5). Trace spacing is 1 m. The polarity of traces 13 – 24 (right) of this shotgather is reversed. As a result of polarity-reversal, the continuity of seismic arrivals corresponding to features A – C is improved. No gaining or filtered are applied, however, these seismic data are clipped (0.5). Trace spacing is 1 m.

(2.4.2) Shotgather Concatenation for Inline & Crossline Survey

The inline and crossline surveys are composed of separate, unconnected shotgathers. For the inline survey, 104 individual shotgathers that correspond to 104 unique shotpoints. Likewise, the crossline survey retains 48 separate shotgathers from 48 shotpoints. In order to connect (or concatenate) each of these shotgathers according to their respective survey and shotpoint order, I use `cat_oddOReven.sh` (Section 8.8.8). Altogether, the result of shotgather concatenation results in two SU files for each survey. One file corresponds to all *left* hits (Section 8.1), and the other file corresponds to all *right* hits (Section 8.1).

(2.4.3) Shotgather Differencing

Differencing (or polarity subtraction) is a conventional processing step in S-wave seismic surveying (Waters 1981). S-wave seismic analyses report that differencing is

necessary and conducting this processing step improves SNR by enhancing SH-wave reflections and reducing signal that corresponds to mode-converted P-waves (Hasbrouck 1991; Wolz 2003a; Young et al., 2001).

A simple model provides an ideal example of how differencing amplifies signal that corresponds to SH-waves (Figure 2.23 & 2.24). I separately perform shotgather differencing for inline and crossline surveys (Figure 2.25, 2.26, & 2.27).

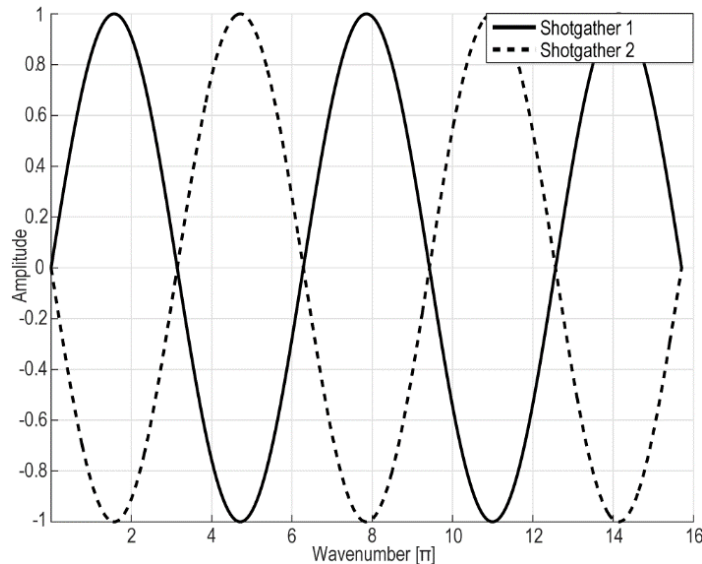


Figure 2.23. Assume each wavefield generated from separate sources results in two reflected, upcoming SH-waves that are 180° out-of-phase. Ideally, this scenario is desirable and assumed prior to shotgather differencing. This ideal model does not include any random and/or coherent noise that is inevitably present in any seismic wavefield.

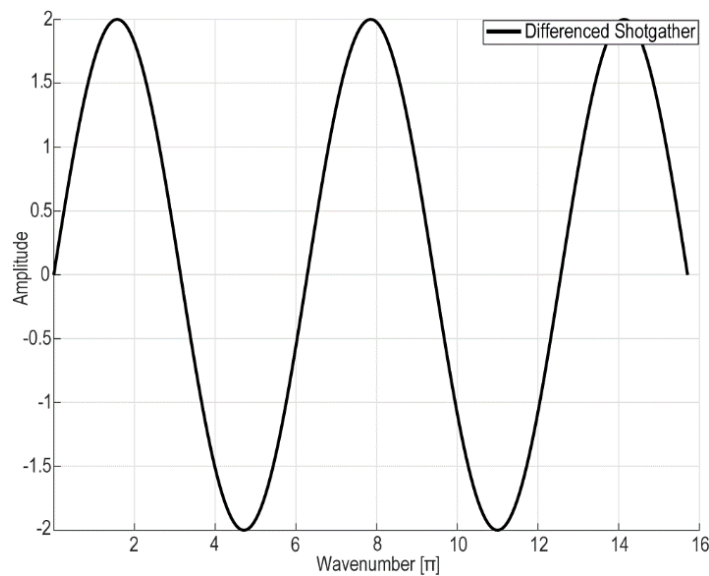


Figure 2.24. The right image displays the result of differencing both shotgathers. Overall, the SH-wave reflection signal has increased.

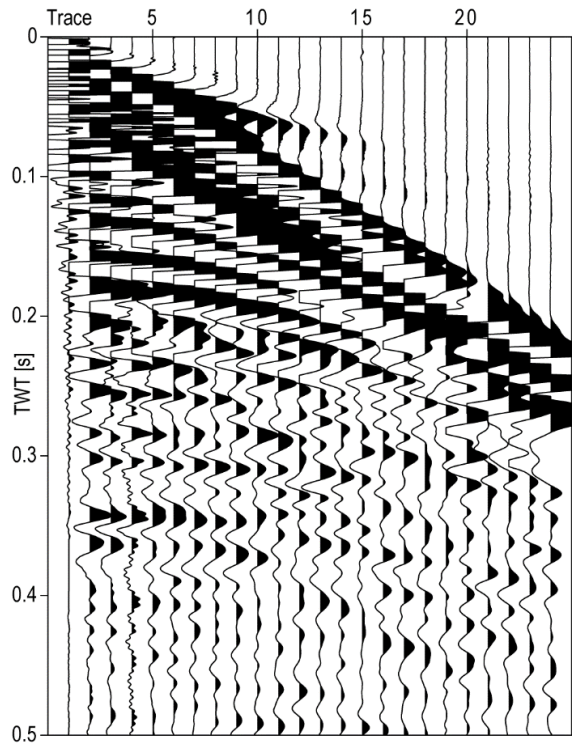


Figure 2.25. The left-hit shotgather from CLSP25. Seismic data are clipped (0.5) with no gaining or filtering applied. Trace spacing is 1 m.

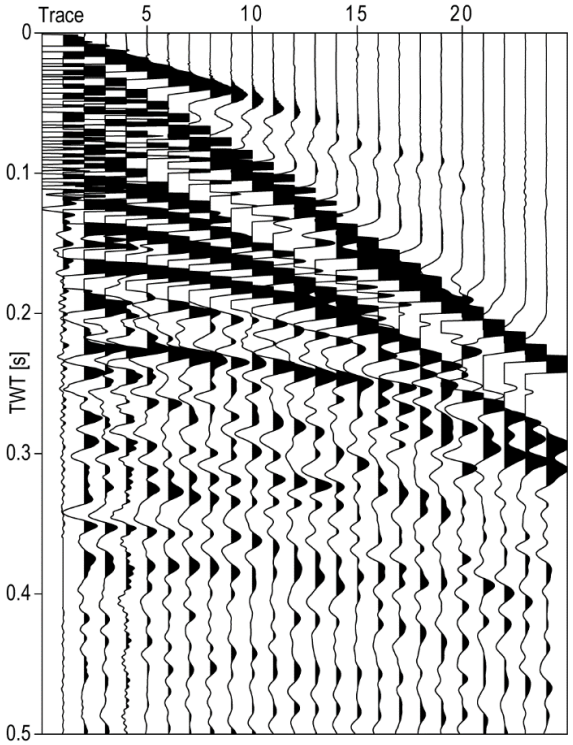


Figure 2.26. The right-hit shotgather from CLSP25. Seismic data are clipped (0.5) with no gaining or filtering. Ideally, all polarized seismic events are ideally 180° out-of-phase relative to seismic data displayed by Figure 2.25. Trace spacing is 1 m.

The left and right-hit SU files corresponding to both the inline and crossline survey are supplied and differenced separately via `suDiff.sh` (Section 8.8.9). As a result, a single SU file for each survey represents the differenced seismic data (Figure 2.27).

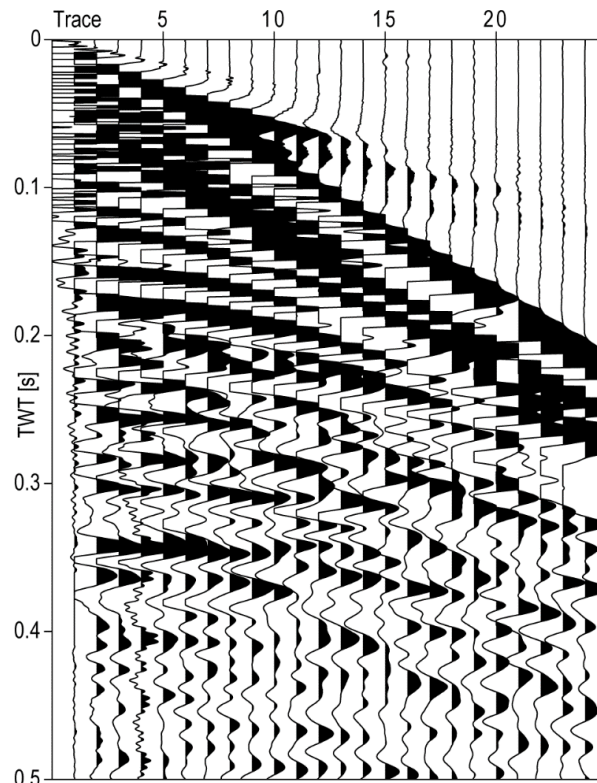


Figure 2.27. The shotgater generated from differencing both seismic data from left and right-hit shotgathers corresponding to CLSP25. Seismic data are clipped (0.5) with no filtering or gaining. Trace spacing is 1 m.

(2.4.4) Trace Repair

Corrupted traces are a common outcome of faulty acquisition equipment (Sheriff 1981; Yilmaz 1987).

We identify and null undesirable traces for each shotgater of each shotpoint. Subsequently, the removed trace is replaced by interpolation of traces on either side. Many shotgathers retain a large number (~4.0 – 25.0%) of corrupted traces (Figure 2.28[left]). To counter this loss of seismic data, I conducted interpolation via `kill_interp_repair.sh` (Section 8.8.3) to repair corrupted traces, thereby reducing the overall loss of data. This processing step is achievable and practical due to the comparatively small-scale size of both seismic surveys.

The interpolated shotgater (Figure 2.28[right]) shows improvement in some sections relative to the raw shotgater. There remain limitations of the improvement that results from interpolation. These limitations manifest themselves as spiky noise and misaligned of seismic reflectors. Trace interpolation does not significantly alter the power-frequency characteristics of each shotgater (Figure 2.29 & 2.30).

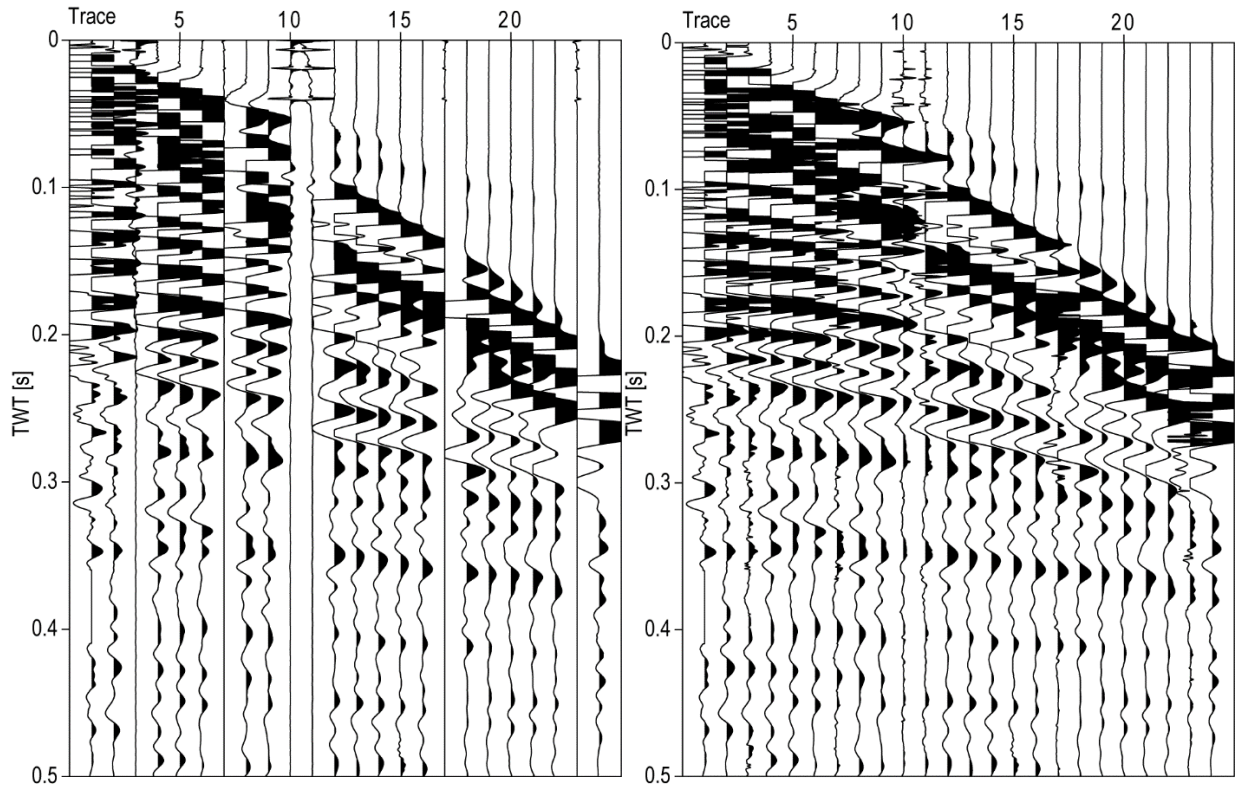


Figure 2.28. Traces 3, 8, 10, 11, 17, and 23 (left) are corrupted. Seismic shotgather is from CLSP47. Also, data is clipped (clip=0.5) and bandpass filtered (f=0,5,100,120 | amps=0,1,1,0). Trace spacing is 1 m. Repaired shotgather (right) from Figure 2.28[left]. All traces have been repaired – some better than others. Shallower events (0.05 – 0.20 s) results in spikier noise while deeper ones (0.25 – 0.50 s) are smoother. Traces 10 and 11 provide an example of the limitations associated with trace interpolation. Specifically, from ~0.14 – 0.19 s, there is severe misalignment of some seismic reflectors. The cause of these misalignments is unknown. Seismic data shown here are also clipped (0.5) and bandpass filtered (f=0,5,100,120 | amps=0,1,1,0). Trace spacing is 1 m.

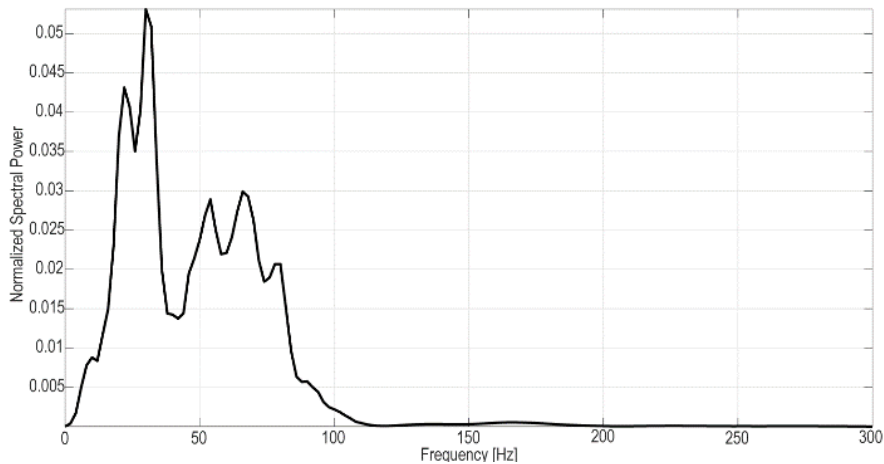


Figure 2.29. Normalized power-frequency spectrum for the non-interpolated seismic data corresponding to Figure 2.28[left].

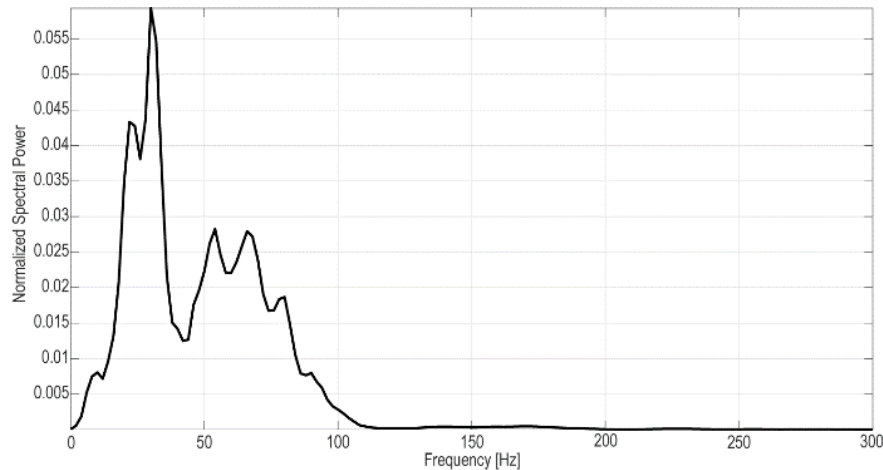


Figure 2.30. Normalized power-frequency spectrum of interpolated seismic data from Figure 2.28[right]. Both Figure 2.29 and 2.30 are highly similar. The relatively minor differences between the two figures can be seen at ~20 – 30 Hz. The notch that lies within this band (~20 – 30 Hz) is reduced as a result of interpolation.

(2.4.5) Geometry & Sorting

Seismic trace headers are set according to field notes recorded for each acquisition day. The field geometry is initially set with `Suclean_geom.pl` (Section 8.10.3) for inline and crossline surveys. Subsequently, CMP sorting is initially conducted via `Make_cmpl.pl` (Section 8.10.4).

From ILSP1 – ILSP 81, the geometry configuration workflow is identical relative to the crossline survey. However, the geometry set for trace headers from ILSP82 – ILSP104 is processed differently in terms all other shotgathers from both the inline and crossline survey. We apply special geometry modifications to inline survey trace headers via `SET_p1_GEOM.sh` (Section 8.8.10) and `SET_p2_GEOM.sh` (8.8.11).

Interpolated UTM coordinates and calculated elevation values are also assigned to trace headers for the inline and crossline surveys for subsequent processing (Section 2.4.6).

(2.4.6) Elevation Statics Correction

For most near-surface seismic analyses, applying some form of a static correction is imperative for recovering and maintaining the seismic fidelity of near-surface reflectors (Büker et al., 1998; Sloan et al., 2016). This is especially true for S-wave studies due to comparatively smaller wavelengths relative to P-waves (Cox 1999; Haines et al., 2010).

There are two primary assumptions associated with this elevation statics correction method. The first is that the velocity characteristics of the near-surface at and above the seismic reference datum (SRD) (7.0 m) remains constant. The second is that all recorded seismic signals is the result of only downgoing and upcoming vertical raypaths (Ronen et al., 1985).

We apply a simple elevation statics correction in two steps for the inline and crossline surveys in the shotgather domain (Figure 2.31). The first step involves

calculating a statics correction text file via `estat_calc.pl` (Section 8.10.11). The second (and last) stage involves applying the static corrections supplied by the output text file (Section 8.7.1). The position and elevation of the source and all sensors of each shotgather are acquired from interpolated UTM coordinates. The constant value assigned to the velocity model is estimated from the velocity of the Love-wave (Figure 2.31 & Equation 2.1). Each elevation static correction is calculated with respect to the elevation of the seismic source, geophone, and accompanied near-surface constant velocity model (Figure 2.31 & Equation 2.2). The SRD we use for the velocity model is flat and set slightly beneath the lowest elevation of the inline profile (Burger 1992). The lowest elevation is ~ 7.4 m, so we established the SRD at 7.0 m (Figure 2.32 & 2.33). The topographic gradient along the crossline survey is minor relative to the inline survey, especially for elevation points greater than ~ 90 of the inline survey.

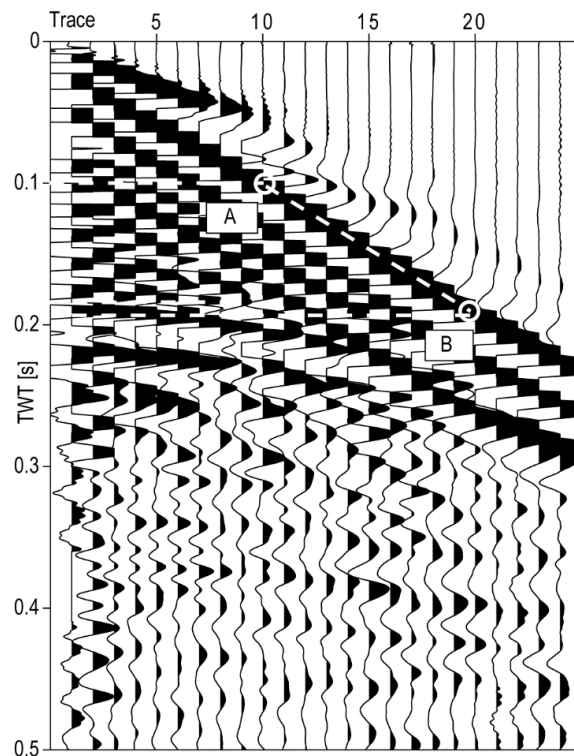


Figure 2.31. Shotgather from ILSP71. Boxes A and B are adjacent to circles enclosing points. The point adjacent to Box A is at trace 10 (TWT= ~ 0.1 s), and the point adjacent to Box B is at trace 20 (TWT= ~ 0.195 s). The dashed slope connecting Box A and B is reciprocated to provide an estimate of the Love-wave velocity, which is used for both the inline and crossline elevation models (Equation 2.1 & 2.2). Seismic data are clipped (0.5) with no gaining or filtering. Trace spacing is 1 m.

$$\frac{dt}{dx} = \frac{0.195 \text{ s} - 0.100 \text{ s}}{20.00 \text{ m} - 10.00 \text{ m}} = \frac{0.095 \text{ s}}{10.00 \text{ m}} = 0.0095 \frac{\text{s}}{\text{m}} = \frac{1}{\frac{dt}{dx}} = \sim 105.26 \frac{\text{m}}{\text{s}}$$

Equation 2.1. Using two points from shown by Figure 51, the group velocity is calculated (dt=change of time, dx=change of distance). Note that the distance between the two points (i.e. trace 10 – 20) is 10 m, which is in accordance with the group interval.

$$TWT_{\text{STATIC}} = \frac{E_s + E_R}{V}$$

Equation 2.2. With both the source (E_s) and receiver (E_R) elevation value as well as the calculated velocity (V), I use this equation to evaluate the static value (E_{TWT}) assigned to each trace of each shotgather.

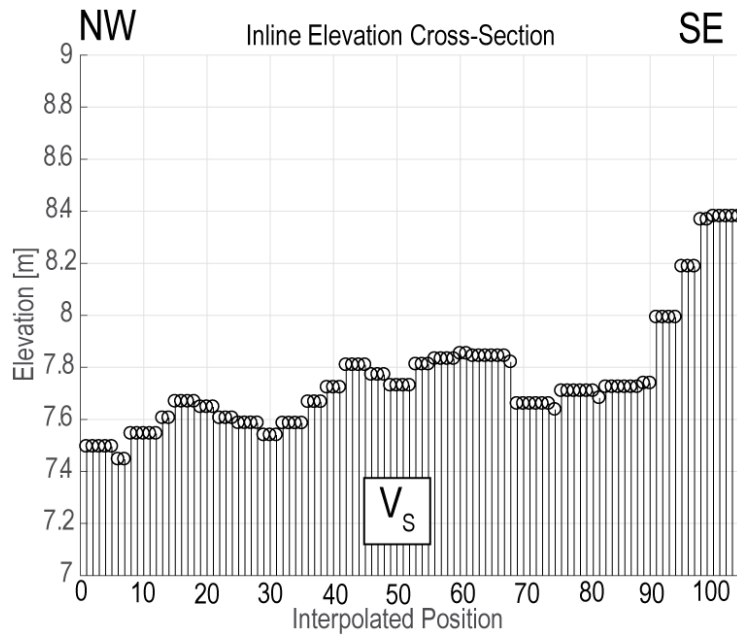


Figure 2.32. Same as Figure 2.20[left]. The elevation scale is exaggerated (x52) to display the topographic gradient for different GPS locations. The V_s variable within the stemmed plot area represents the constant velocity value assigned to all points greater than or equal to 7.0 m.

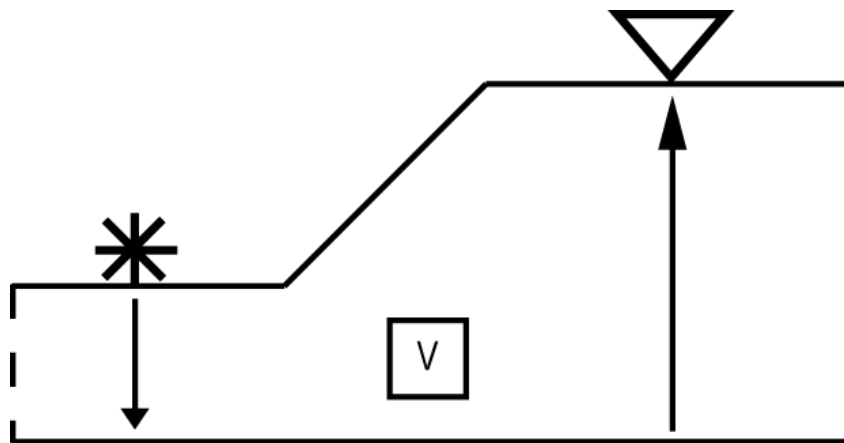


Figure 2.33. Cross-section schematic illustrates the purpose and assumptions associated with the elevation static correction I apply for the inline and crossline surveys. The normal ray relative to the source (asterisk) represents the downgoing wavefront, and the ray normal to the receiver (triangle) represents the upcoming wavefront. Our elevation static correction compensates for elevation changes relative to the SRD

Elevation static corrections do not noticeably improve our data (Figure 2.34). Most misalignment of distinct seismic arrivals are likely attributable to weathering layer effects, which we do not account for (Robinson et al., ; Sloan et al., 2016).

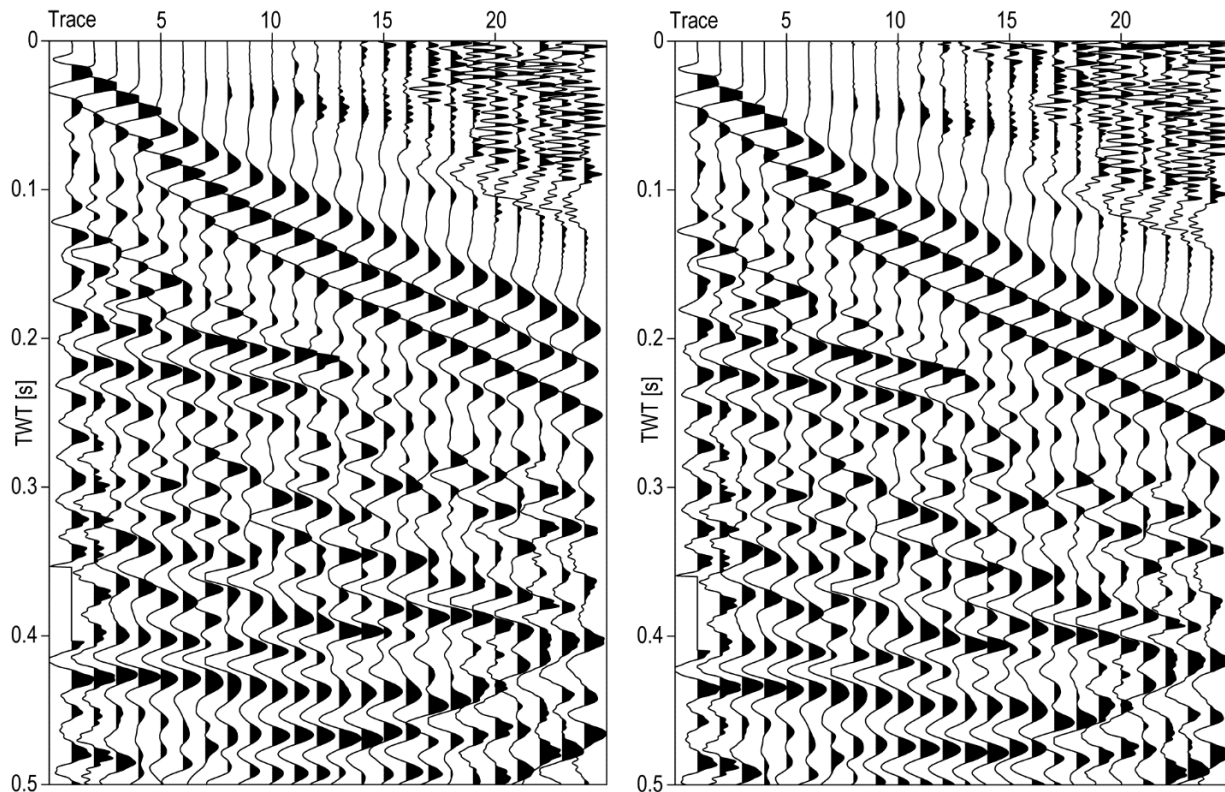


Figure 2.34. Shotpoint 81 (left) from the inline survey. No static corrections are applied. Seismic data are clipped (perc=97) with no gaining or filtering. Trace spacing is 1 m. Elevation static corrections applied (right) to seismic data displayed in Figure 2.34[left]. No significant change and/or improvement is noticeable. The minimum static shift is ~ 0.006 s, and the maximum is ~ 0.017 s. Seismic data are clipped (perc=99) and have automatic gained controlled (AGC) (wagc=0.08 s) applied. Trace spacing is 1 m.

(2.4.7) Top-Muting

Muting is an effective processing method to eliminate coherent forms of seismic noise such as ground-roll, Love-waves, air-blasts, refractions, and guided waves (Roth et al., 1998; Sloan et al., 2008).

For this study, the primary source of coherent noise is Love-waves. I only use top-muting as all forms of coherent noise mainly reside outside and above the optimal window. An analysis of image and wiggle plots displaying automatic-AGC seismic data in the shotgather domain determines the optimal TWT-offset picks to establish the top-muting path (Figure 2.35).

The process of establishing the optimal TWT-offset path for the top-mute function with the methods introduced above requires a combination of balancing SNR as well as identifying Love-waves and earliest reflection events. After properly gaining a selected shotgather and identifying noise from reflection signal, a path is selected across the

entire gather. All seismic data at and above this path is muted with a 10 sample (0.005 s) accompanied taper to minimize edge effects that may arise during subsequent processing and post-processing stages (Figure 2.36) (Yilmaz 2001). The muting path is selected via `iTop_Mute3` (Section 8.10.5). Subsequently, all samples at and above the defined path are zeroed out with a pre-defined taper via `Sumute2.pl` (Section 8.10.6).

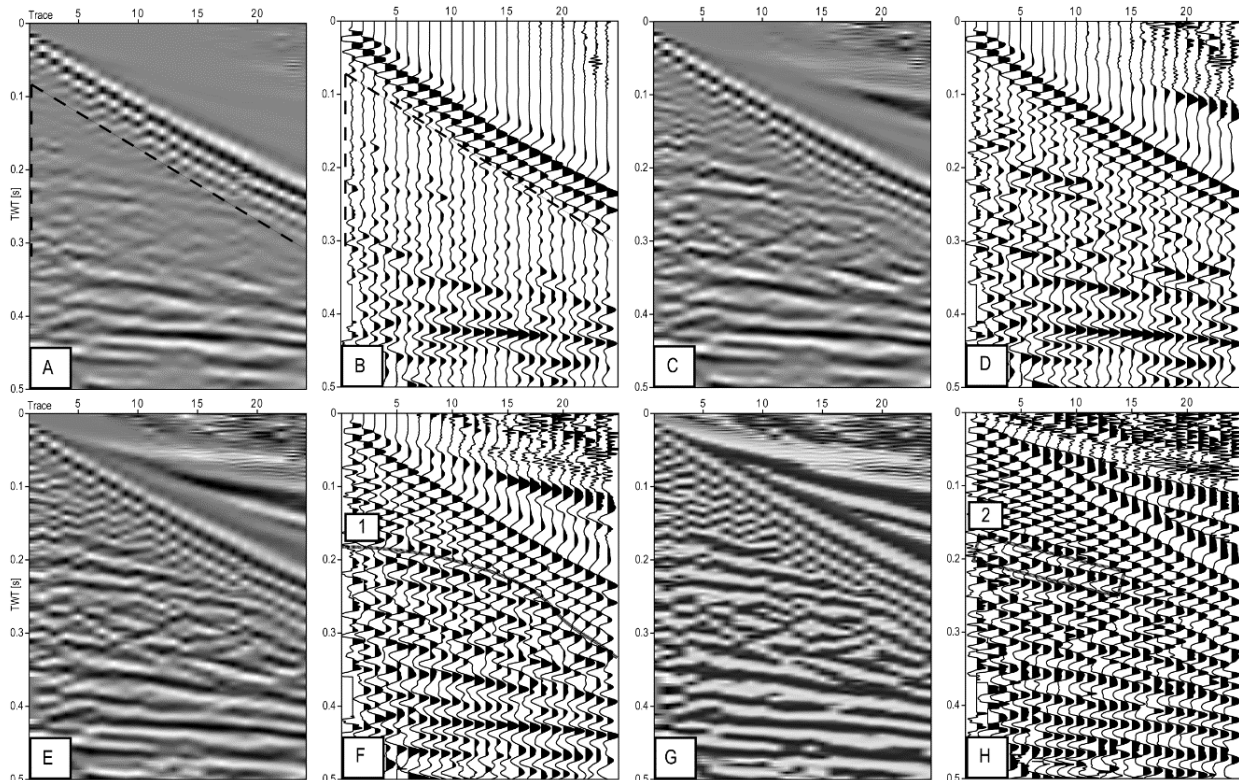


Figure 2.35. ILSP75 shotgathers with different AGC parameters applied. From top to bottom, each row retains an image and wiggle plot that displays results from a different AGC window. The triangular area indicated by dashed lines of A and B represents the optimal window [A – B]. A – B display poor AGC results as a consequence of using too large a window ($w_{agc}=0.2$ s). Most early reflection events within the optimal zone have been extinguished due to the improper AGC application. C – D present improvements from more visible reflection events using a smaller AGC window ($w_{agc}=0.1$ s). Images E – F display optimal results in terms of maintaining SNR and yielding the most well-defined reflection events ($w_{agc}=0.05$ s). Images G – H retains the smallest window for AGC ($w_{agc}=0.008$ s) and the lowest SNR. There is evidence of a reflection event at ~ 0.8 s (Box 2), however, Love-wave energy interference is too severe. The dashed line adjacent to Box 1 of image F presents the TWT-offset path selected for the muting function. All seismic data at and above the selected path are muted. All seismic data are clipped ($perc=99$). Trace spacing is ~ 1 m.

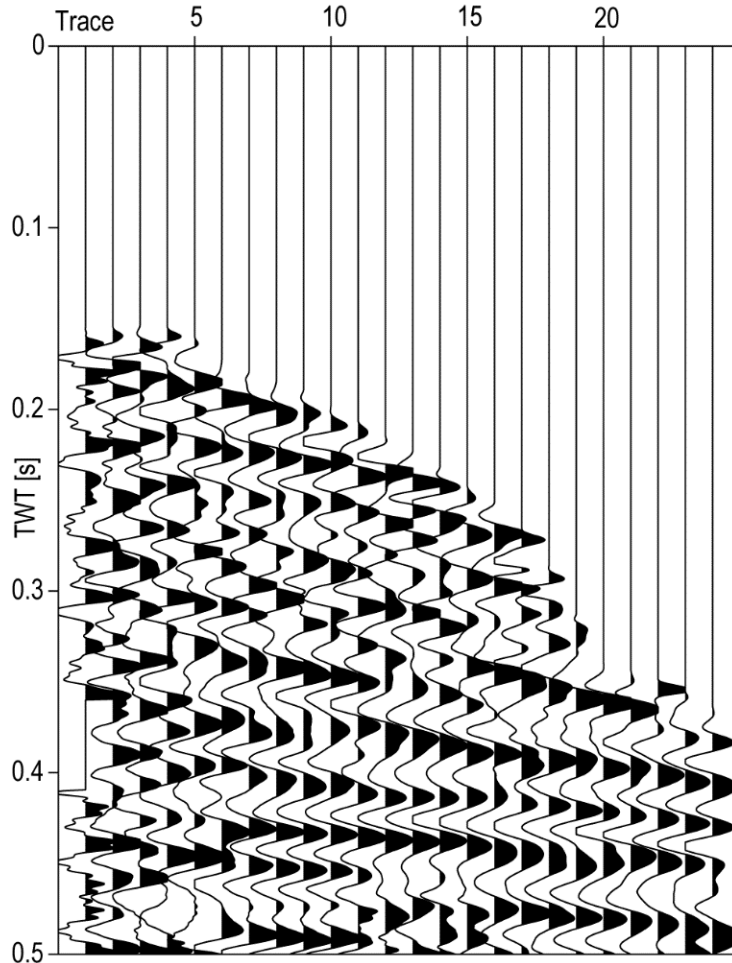


Figure 2.36. The results of apply top-muting along the defined path displayed in Figure 2.46[F]. The process has mostly if not altogether removed Love-waves. Seismic data displayed here are from ILSP75. AGC is applied (wagc=0.05 s) with a perc of 97.

(2.4.8) Velocity Analysis

We correct for seismic reflector normal moveout (NMO) associated with inline and crossline CMP gathers via velocity analysis (Yilmaz 1987). The velocity spectrum corresponding to a given CMP (Figure 2.37[left]) is calculated via semblance and subsequently displayed as a contour plot (Figure 2.37[right]). Optimal TWT-velocity pairs retain relatively high values of semblance. Error associated with each TWT-velocity pick is approximately $\pm 10\%$.

I interactively choose these high-value pairs (Table 2.7) to correct for and flatten the hyperbolic behavior (Figure 2.37[left]) associated with seismic reflectors of individual CMP gathers iVA2 (Section 8.10.7) and suCatpar.pl (Section 8.10.8). The result of applying the user-selected TWT-velocity pairs corrects for NMO, thereby flattening the seismic reflector(s) (Figure 2.38). The overall process of velocity analysis is performed for each CMP gather from both the inline and crossline survey (Figure 2.39, Table 2.8, & Figure 2.40). The minimum fold is 1, and the maximum fold is 24 (Figure 2.41).

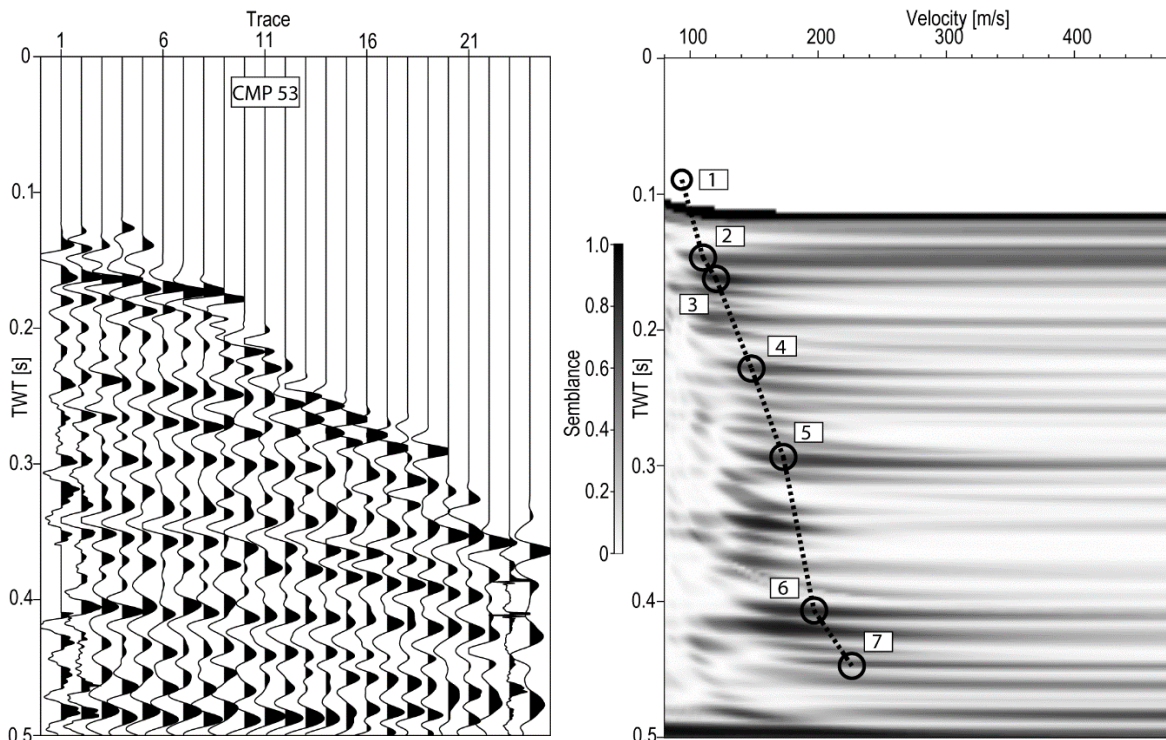


Figure 2.37. CMP 53 of the inline survey (left) with no NMO correction applied. Multiple seismic reflection events appear from ~0.16 – 0.49 s. Seismic data are gained ($wagc=0.08$ s) and clipped ($perc=99$). Trace spacing is ~1 m. Velocity spectrum (right) as a contour plot calculated via semblance of seismic data displayed in Figure 2.37[left] with respect to the velocity analysis parameters listed below. Boxes 1 – 7 are TWT-velocity pairs interactively selected by a user (Table 2.7). Velocity analysis parameters are first velocity set as 80 m/s, velocity increment as 2 m/s, and number of velocities as 200. Semblance values are clipped ($perc=99$).

Table 2.7. TWT-velocity pairs selected from data corresponding Figure 2.37[right]. These data are supplied as pairs for each pick to the NMO correction equation to flatten hyperbolic seismic reflectors.

Pick	TWT [s]	V_{RMS} [m/s]
1	0.09	95
2	0.147	108
3	0.162	127
4	0.23	160
5	0.297	191
6	0.409	229
7	0.446	250

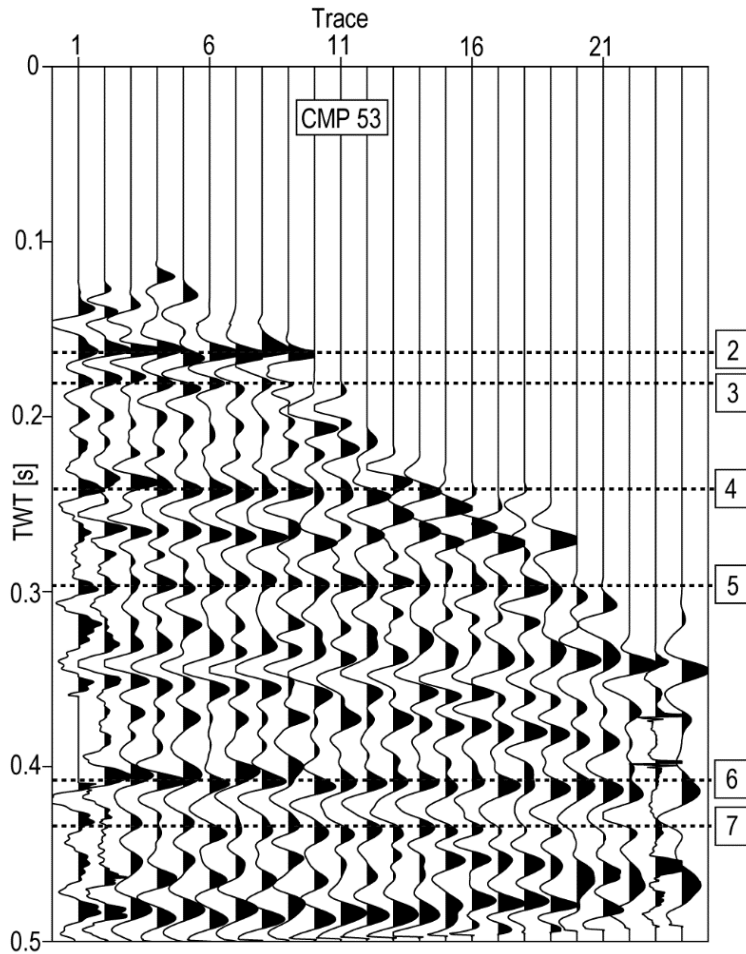


Figure 2.38. NMO-corrected CMP 53 of the inline survey. Interpreted primary reflection events have been flattened. Boxes 2 – 7 correlate to TWT-velocity picks from Table 2.7. Deviations of main lobes from the horizontal lines indicated by boxes 2 – 7 may be primarily attributed to effects of near-surface velocity heterogeneity (Sloan et al., 2016). Seismic data are gained ($wagc=0.08$ s) and clipped ($perc=99$). Trace spacing is ~ 1 m.

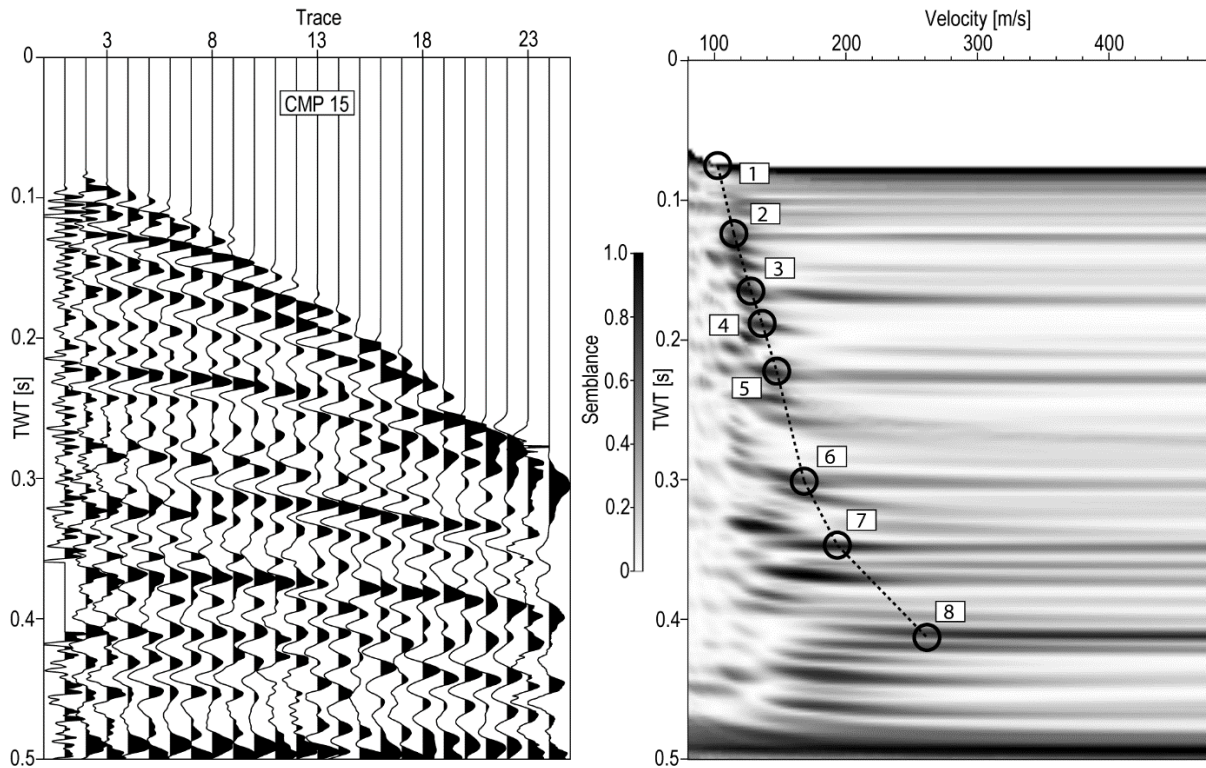


Figure 2.39. CMP 15 (left) from the crossline survey with no NMO correction applied. Seismic data are gained ($wagc=0.08$ s) and clipped ($perc=99$). Trace spacing is ~ 1 m. Velocity spectrum (right) as a contour plot calculated via semblance of seismic data displayed in Figure 2.39[left] with respect to the velocity analysis parameters listed below. Boxes 1 – 8 are TWT-velocity pairs interactively selected by a user (Table 2.8). Velocity analysis parameters are first velocity set as 80 m/s, velocity increment as 2 m/s, and number of velocities as 200. Semblance values are clipped ($perc=99$).

Table 2.8. Same as Table 2.7, however, these data are selected for CMP 15 (Figure 2.52). These data are supplied as pairs for each pick to the NMO correction equation to flatten hyperbolic seismic reflectors.

Pick	TWT [s]	V_{RMS} [m/s]
1	0.075	101
2	0.123	115
3	0.168	130
4	0.19	138
5	0.226	150
6	0.3	171
7	0.347	192
8	0.408	244

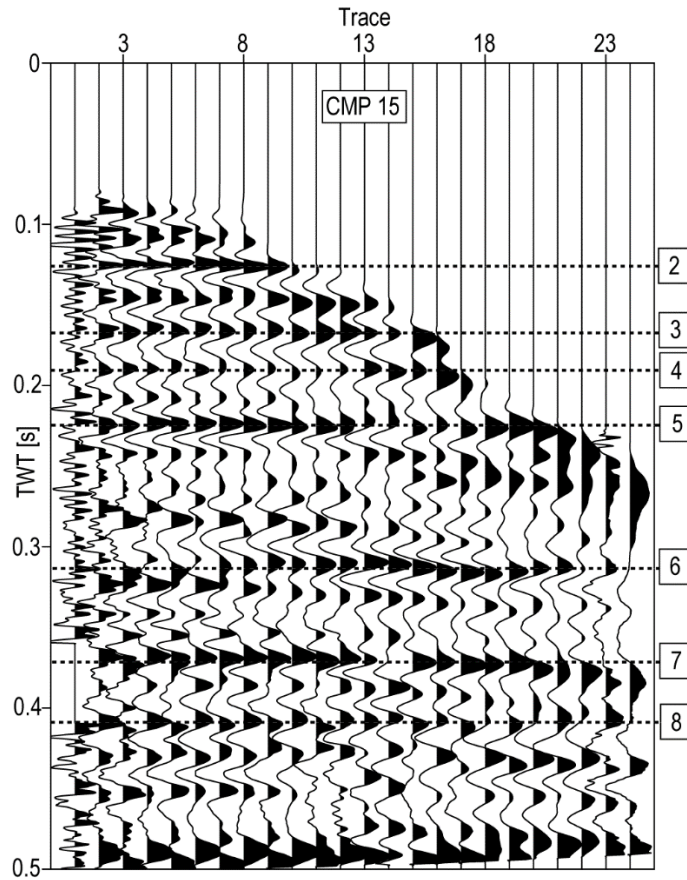


Figure 2.40. NMO-corrected data for CMP 15 of the crossline survey. Boxes 2 – 8 correlate to TWT-velocity pairs in Table 2.8. Seismic data are gained (wagc=0.08 s) and clipped (perc=99). Trace spacing is ~1 m.

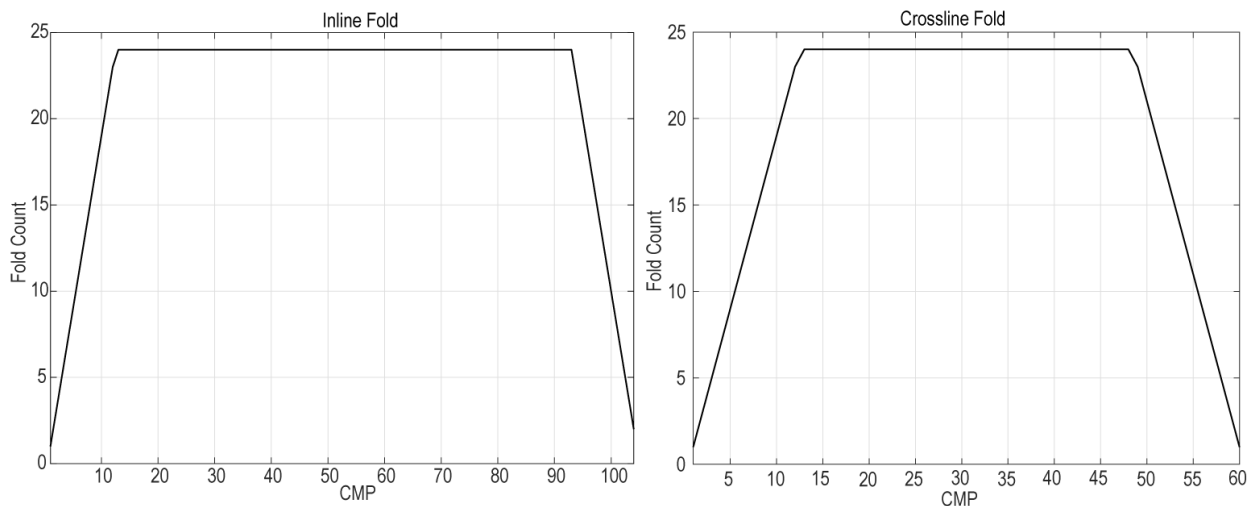


Figure 2.41. Fold count calculated for each CMP for the inline survey (left) via sukeycount (Section 8.7.3). Total fold count ranges from CMP 1 – 104. Maximum fold is 24, and minimum fold is 1. Crossline fold count from CMP 1 – 60 (right) for the crossline survey.

(2.4.9) Residual Statics Correction

Short wavelength misalignments of flattened seismic reflectors generated from elevation statics correction, velocity analysis, and near-surface velocity heterogeneity may be mitigated via residual statics corrections (Cox 1999; Sheriff 1981).

We use surface-consistent residual statics estimation by stack-power maximization for improving the final stack for both inline and crossline surveys (Figure 2.42 & 2.43) (Ronen et al., 1985). Residual statics correction are calculated via MNSatics.sh (Section 8.8.4) and subsequently applied with sustatic (Section 8.7.1).

Similar to the elevation statics, residual statics correction does not noticeably change the alignment of distinct seismic events.

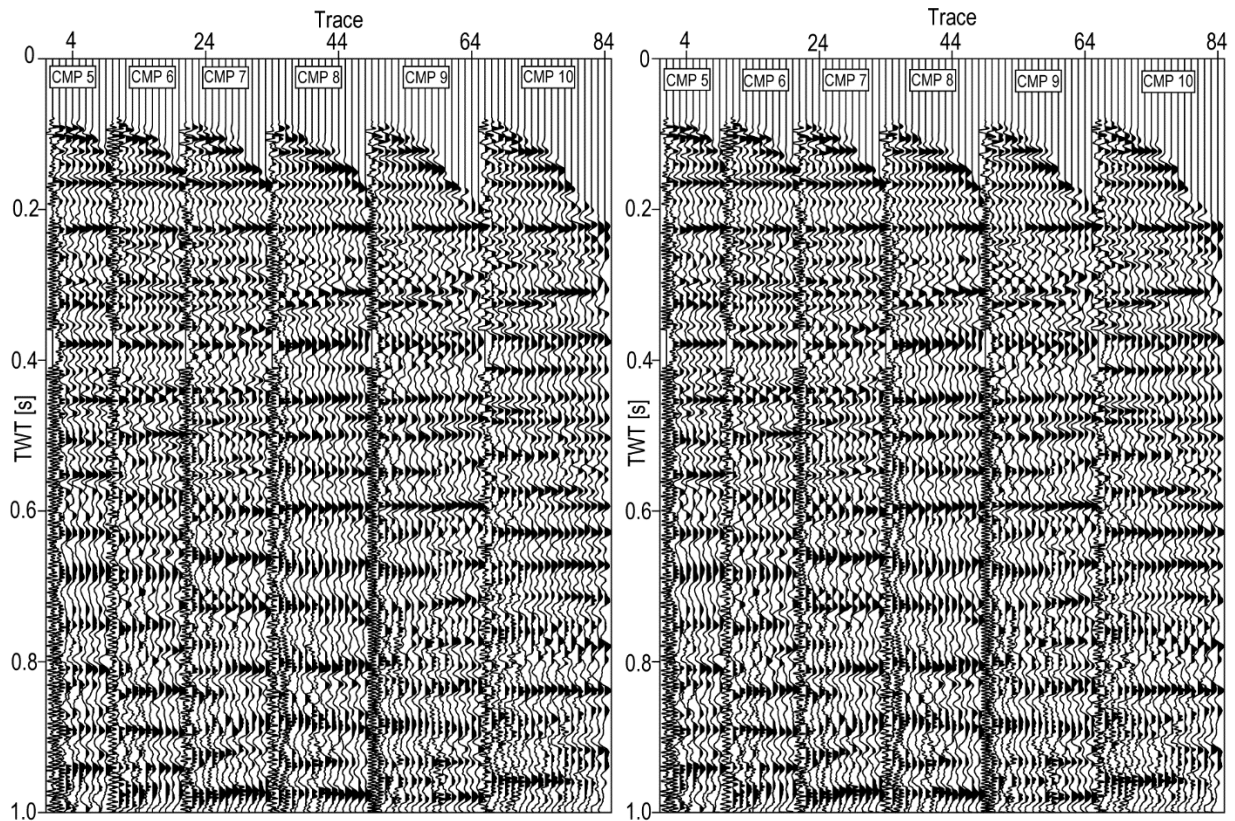


Figure 2.42. CMP 5 – 10 (left) of the crossline survey. No residual static corrections are applied. Seismic data are clipped (perc=99), gained (AGC, wagc=0.08 s). Trace spacing is ~1 m. Residual statics corrections (right) are applied. Compared to Figure 2.42[left], there is no discernable difference or improvement of seismic reflectors. All residual static corrections range 0 – 1 ms. Seismic data are clipped (perc=99), gained (AGC, wagc=0.08 s). Trace spacing is ~1 m.

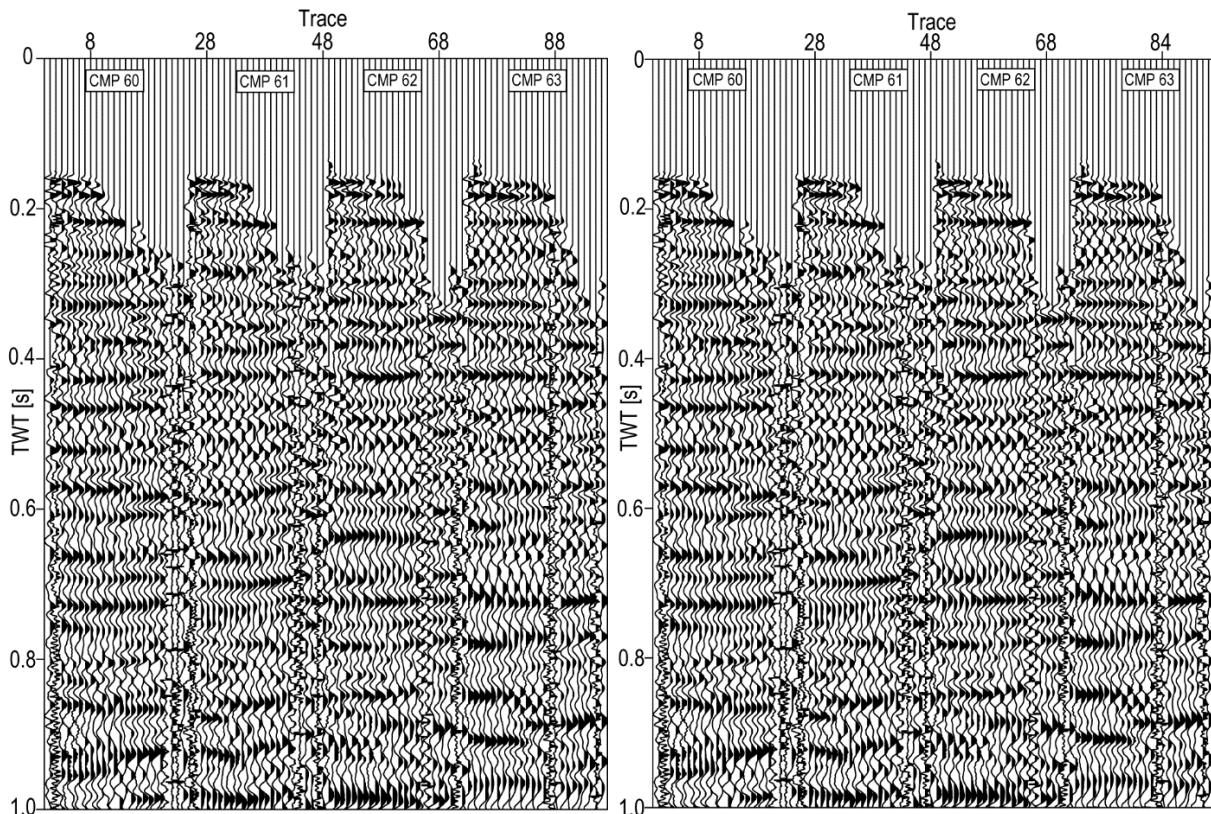


Figure 2.43. CMP 60 – 63 of the inline survey (left) with no residual static corrections applied. Seismic data are clipped (perc=99), gained (AGC, wagg=0.08 s). Trace spacing is ~1 m. Static corrections (right) to data displayed in Figure 2.43[left]. There is no discernible change and/or improvement to CMP gathers. All residual statics corrections range -1 – 2 ms. Seismic data are clipped (perc=99), gained (AGC, wagg=0.08 s). Trace spacing is ~1 m.

(2.4.10) Stack

The process of stacking involves cumulative summation of all traces associated with a given CMP gather (Sheriff 1991). Overall, the optimal result of a stack is improved SNR (Yilmaz 1987). Each stacked trace theoretically represents a zero-offset section (Figure 2.44) (Liner 2004; Yilmaz 1987). Stacked traces and the seismic cross-sections that consist of them allow for each trace to be represented with the convolutional model (Robinson 1999). This theoretical context serves as the fundamental infrastructure of subsequent post-processing and inversion calculations (Bleistein et al., 2001).

All traces of a given CMP gather are cumulatively summed to generate a single trace (Figure 2.45). There are 104 CMP gathers for the inline survey, therefore, 104 traces comprise the stacked section (Figure 2.46). Likewise, the crossline survey, which retains 60 CMP gathers, generates a 60-trace stacked seismic section (Figure 2.47). I apply stacking and subsequently generate a seismic cross-section via `Sustack.pl` (Section 8.10.9).

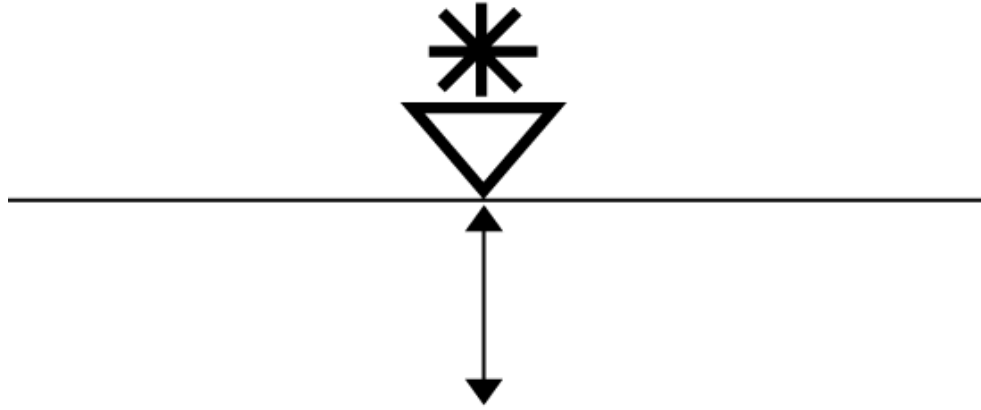


Figure 2.44. A theoretical representation of a zero-offset receiver and source. Specifically, the source (asterisk) and receiver (triangle) are perfectly coincident with one another. The normally-incident upgoing and downgoing ray-path is illustrated by the arrow-capped line segment.

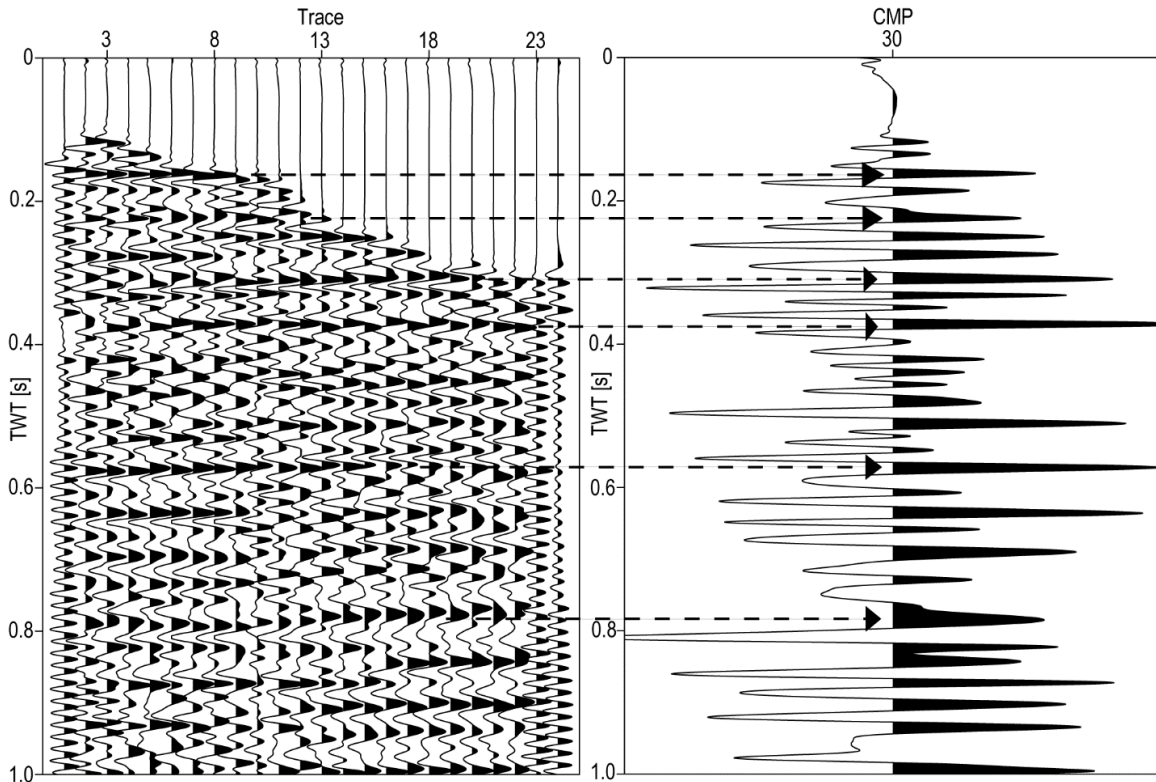


Figure 2.45. CMP 30 (left) from the inline survey. Seismic data are clipped (perc=99), gained (AGC, wagc=0.08 s), and band-passed filtered (f=5, 15, 70, 100 | amps=0, 1, 1, 0). Trace spacing is ~1 m. Single trace (right) generated from stacking (or summing) all traces from CMP 30 of the inline survey. The arrows emanating from Figure 2.45[left] and pointing to certain local amplitude peaks in the stacked trace indicate the regions that correspond to interpreted reflection events.

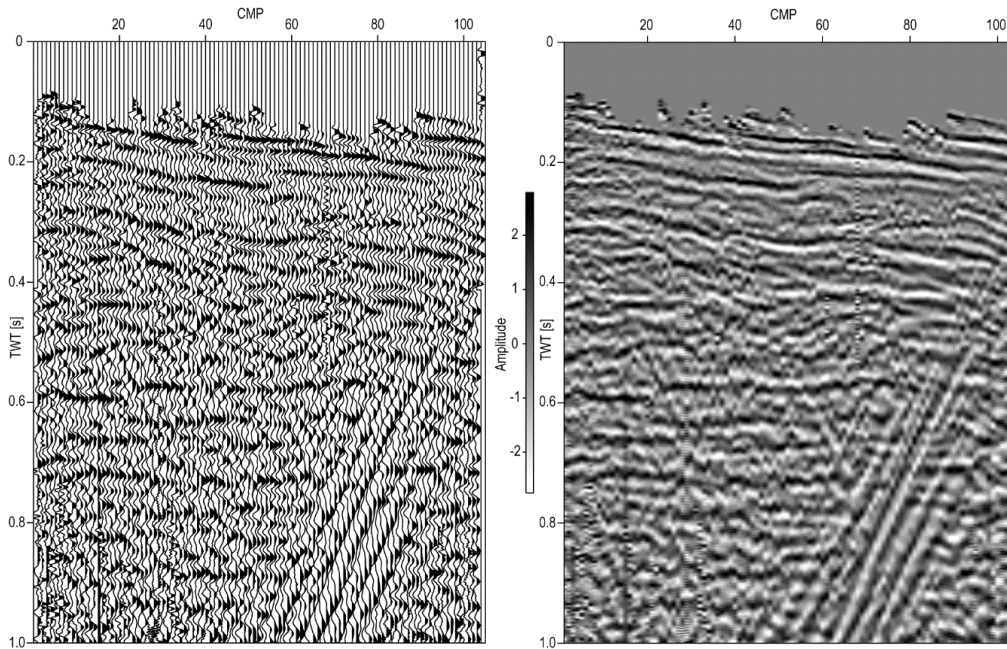


Figure 2.46. Wiggle plot (left) of stacked cross-section of the inline survey. Seismic data here are gained (AGC, $wagc=0.08$ s) and clipped (perc=99). Trace spacing is ~ 1 m. Image plot (right) of the inline seismic cross-section. Side-scattered energy is subsequently filtered out (Section 2.4.11). Seismic data are gained (AGC, $wagc=0.08$ s) and clipped (perc=99). Trace spacing is ~ 1 m.

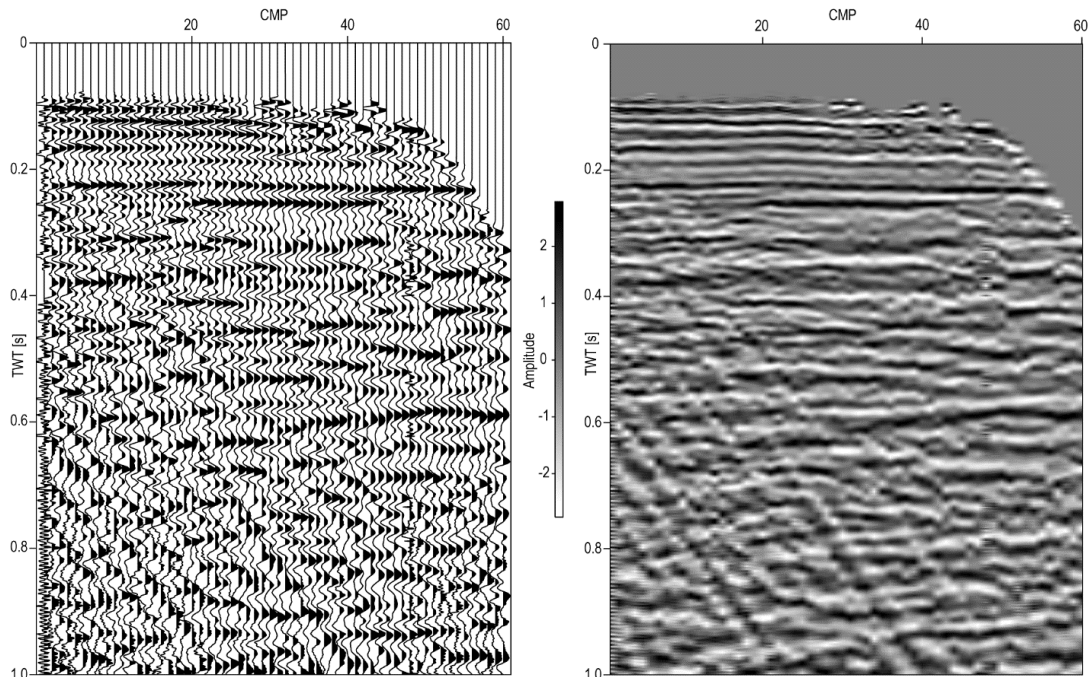


Figure 2.47. Wiggle plots (left) of cross-section corresponding to the crossline survey. Seismic data here is gained (AGC, $wagc=0.08$ s) and clipped (perc=99). Trace spacing is ~ 1 m. Image plot (right) of crossline cross-section. Side-scattered energy is subsequently filtered out (Section 2.4.11). Seismic data are gained (AGC, $wagc=0.08$ s) and clipped (perc=99). Trace spacing is ~ 1 m.

(2.4.11) f-k Filter

F-k filtering is an effective processing method whereby pre or post-stack seismic arrivals are decomposed into planar wavefield components by both frequency and wavenumber and subsequently filtered out via filtering parameters (Ikelle et al., 2005a; Yilmaz 1987).

We apply f-k filtering to post-stack data to remove side-scattered energy via Sudipfilt (Section 8.10.10). The process of frequency-wavenumber (f-k) filtering removes linear side-scattered energy associated with both the inline and crossline cross-sections.

The inline cross-section displays distinct side-scattered energy that dips from right to left with comparatively minor side-scattered energy dipping right to left (Figure 2.46). The crossline section displays distinct side-scattered energy that dips from left to right with comparatively minor side-scattered energy dipping right to left (Figure 2.47). I apply both a positive and negative dip filter to remove the linear coherent noise (i.e. side-scattered seismic energy) associated with both seismic sections (Figure 2.48 & 2.49).

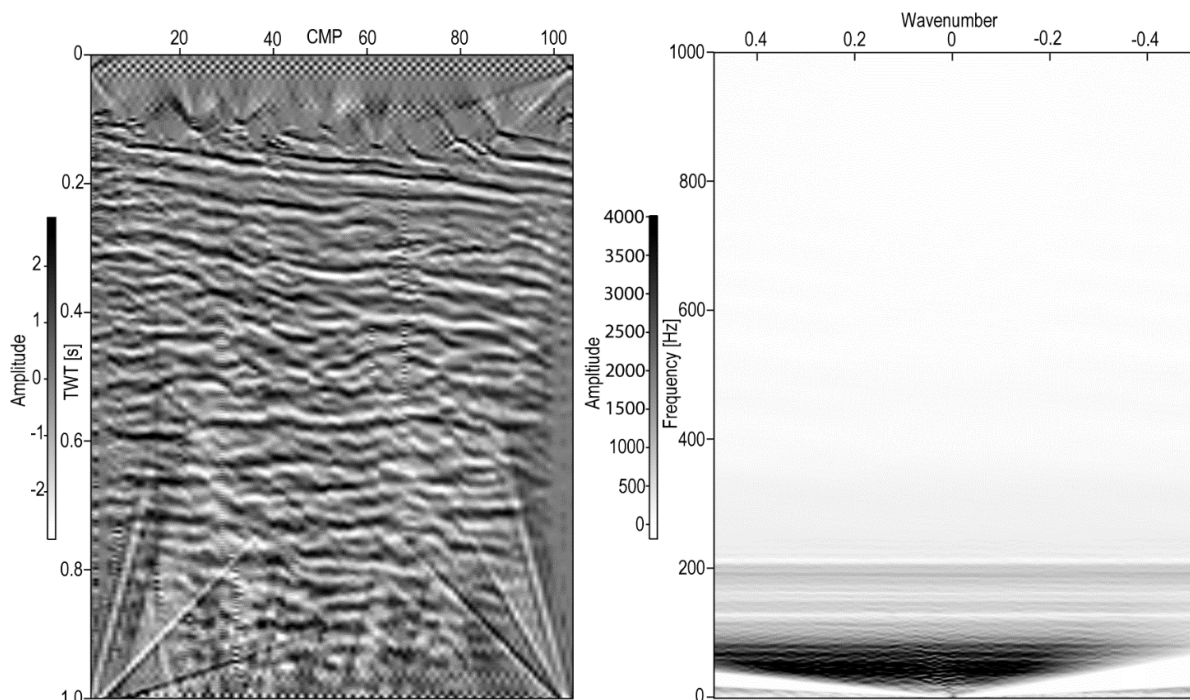


Figure 2.48. F-k filtered (left) inline cross-section. While most side-scattered energy is effectively removed, multiple processing artifacts are introduced in the top and bottom sections of the filtered cross-section. The artifacts at the top are removed via manual top muting and those at the bottom are ignored by windowing the cross-section from 0.1 – 0.7 s. Seismic data are gained (AGC, wagg=0.08 s), clipped (perc=99), and band-passed filtered (f=5,50,120,200 | amps=0,1,1,0). Trace spacing is ~ 1 m. F-k plot (right) calculated from data displayed in Figure 2.48[left]. Triangular-shaped white zones near the wave number axis on both the positive and negative quadrant represents frequency-wavenumber pairs that are selected and zeroed out to remove the side-scattered energy. Data are clipped (perc=99).

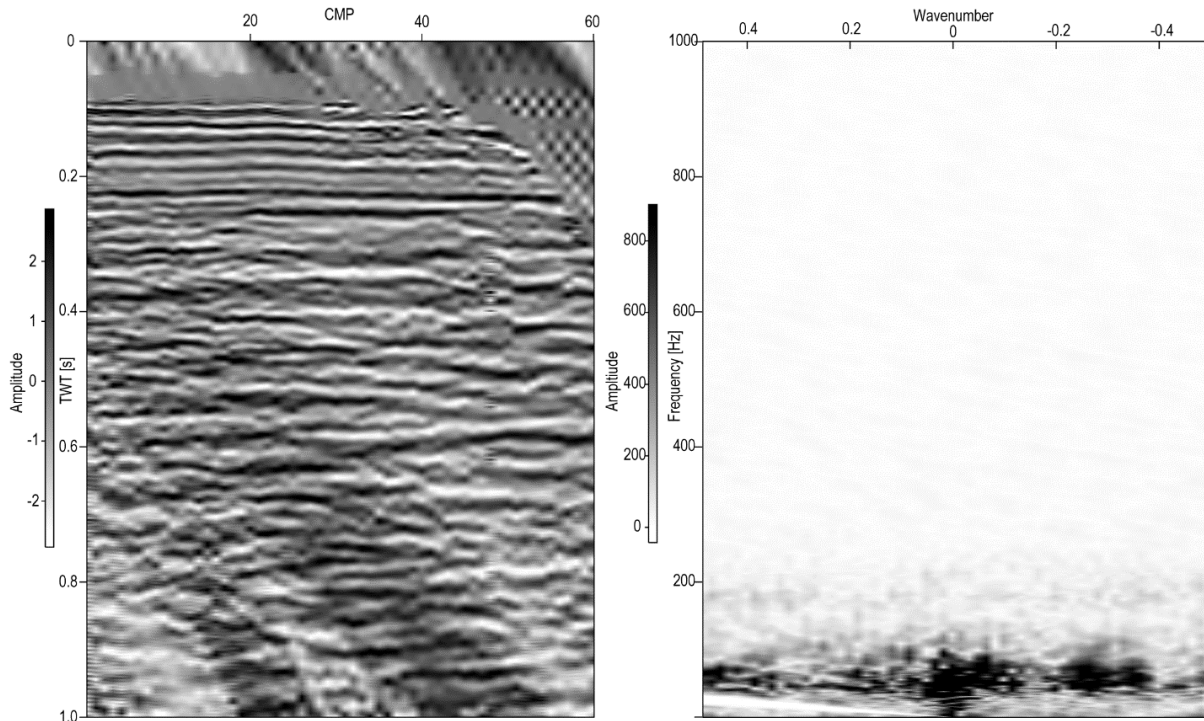


Figure 2.49. F-k filtered (left) crossline cross-section. Side-scattered energy is mostly removed with the introduction of minor processing artifacts in the top and bottom sections of the cross-section. These artifacts are subsequently removed via top-muting artifacts and windowing out the bottom section for subsequent processing and post-processing (0.1 – 0.7 s). Seismic data are gained (AGC, wagg=0.08s), clipped (perc=99), and (f=5,50,120,200 | amps=0,1,1,0). Trace spacing is ~1 m. F-k spectrum (right) corresponding to the filtered crossline section. The narrow white zone near the wavenumber axis in the positive quadrant indicates the frequency-wavenumber pairs that are selected to remove the side-scattered energy. F-k data here is clipped (perc=99).

(2.4.12) Phase Correction & Polarity Determination

For accurate post-processing and interpretation of stacked seismic data, it is critical to evaluate the phase and polarity of processed cross-sections (Brown 2001; Simm et al., 2002). The method I use to determine and correct for phase delay as well as assign polarity involves iterative constant phase (10° increment) rotations and cumulative amplitude summation along a single continuous seismic reflector for a given cross-section (Roden et al., 1999).

I use `phase_estimator.m` (Section 8.9.1.11) to estimate which constant phase rotation yields the greatest cumulative seismic amplitude summation (Figure 2.50 & 2.51). After this process, the optimal phase angle is applied (Figure 2.52) to the inline and crossline sections via `supphase` (Section 8.7.2).

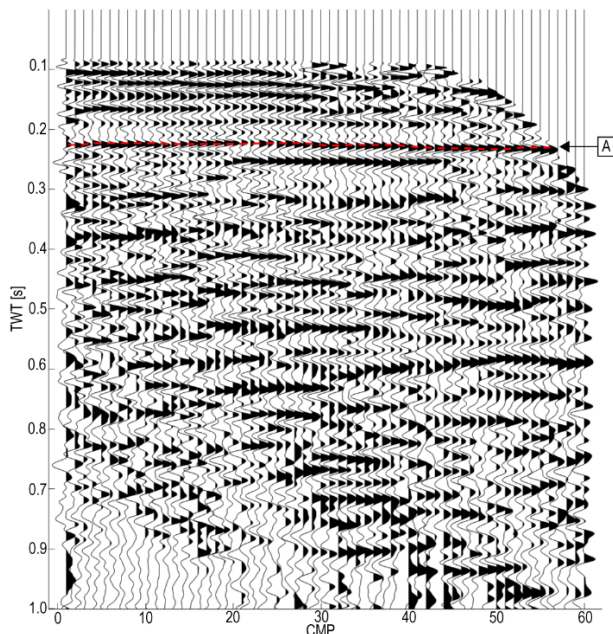


Figure 2.50. Crossline cross-section before phase rotation. A single seismic reflection event at ~0.23 s (Box A) is selected to establish a 1-D gate along its lateral extent. Amplitudes are cumulatively summed across the entire gate for each phase rotation. Seismic data are gained (AGC, $wagc=0.08$ s) and clipped (perc=99). Trace spacing is ~1 m. This wiggle plot is generate via wiggle.m (Section 8.9.1.1).

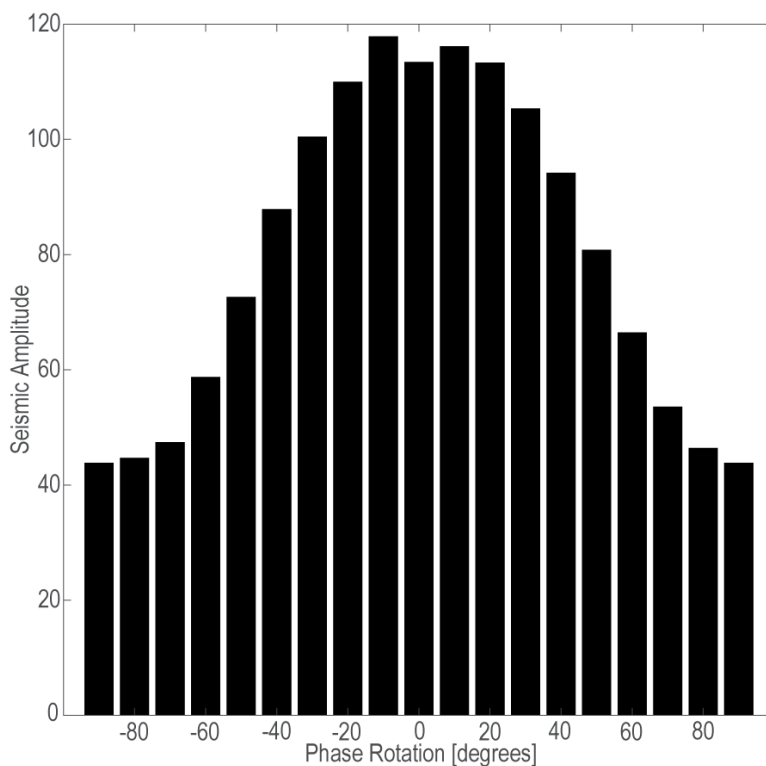


Figure 2.51. Each bar corresponds to the total amplitude summation associated to a given phase rotation. Phase rotation 0 indicates the initial phase of the crossline cross-section. The greatest seismic amplitude summation is reached at approximately -10° .

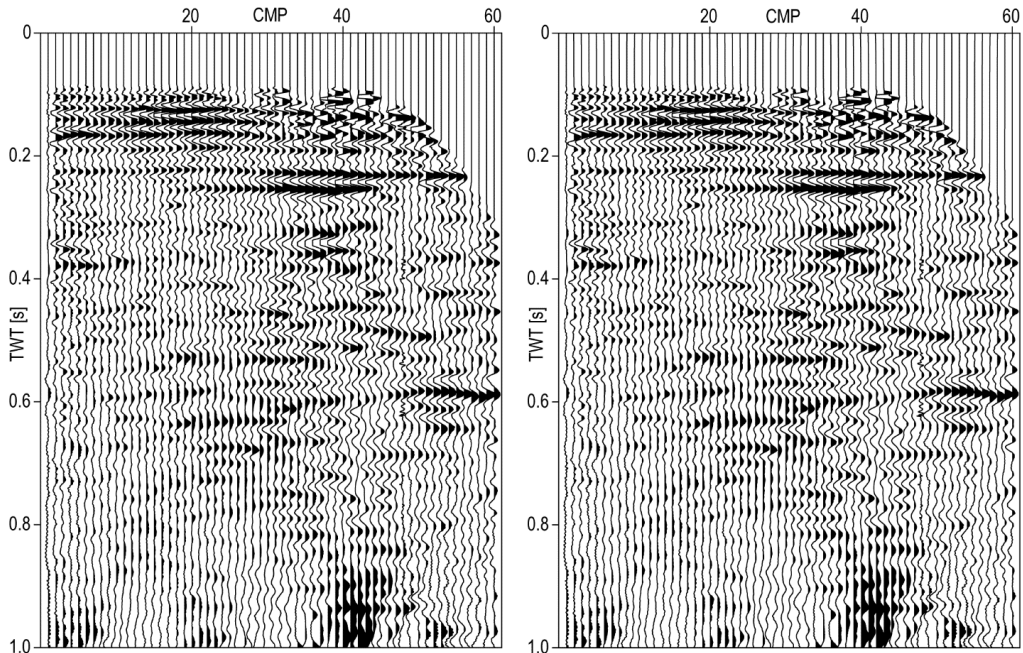


Figure 2.52. Same as Figure 2.50, however, the 1-D summation gate (left) is removed and these seismic data are gained (tpow=1.8) and clipped (perc=99). Trace spacing is ~1 m. Phase-rotated crossline (right) cross-section. All traces are constant phase-rotated by -10° . Seismic data are gained (tpow=1.8) and clipped (perc=99). Trace spacing is ~1 m.

We determine that our seismic data is approximately $\sim 10^\circ$ out-of-phase (Figure 2.50), thus applying a -10° phase constant rotation yields an approximate zero-phase seismic cross-section (Roden et al., 1999). After phase-rotation, the polarity of all seismic data after phase rotation is set as American standard (Brown 2001; Simm et al., 2002). The constant phase rotation is applied to both the inline and crossline sections.

(2.4.13) Seismic Amplitude Conditioning & Recovery

It is critical to preserve both the true seismic amplitude and frequency characteristics throughout data processing for the purposes of inversion (Becquey et al., 1979; Lloyd 2013). True amplitude conditioning and recovery are vital to properly condition seismic amplitudes for the purposes of inversion (Berteussen et al., 1983). I apply a wave equation-based divergence correction via `ample_recov_2.sh` to condition and recover seismic amplitudes (Section 8.8.1).

(2.4.14) A Case against Deconvolution & Migration

In both the pre and post-stack domains, gapped and non-gapped deconvolution significantly reduced SNR of seismic data corresponding to both the inline and crossline surveys. Indeed, deconvolution is regularly known to perform poorly on shallow subsurface seismic data and is therefore usually not applied (Sloan et al., 2007; Steeples et al., 1998; Steeples et al., 1995; Young et al., 2001). As a result, no form of deconvolution is applied to our seismic data.

No form of migration is applied to our seismic data for three reasons. First, migration inevitably alters the phase and amplitude of seismic data (Gray 1997). Alteration of the waveform is detrimental for seismic inversion results (Lavergne et al., 1977; Lindseth 1976). Secondly, it is unnecessary for the reason that interpreted dipping reflectors – mainly from the inline cross-section – exhibit no more than an 8° dip. This decision is based on the V_{NMO}/V ratio of ~ 1.0 for dips $1 - 10^\circ$ (Yilmaz 1987). The difference of velocities from a flat reflector relative to those corresponding to a dipping reflector is negligible and therefore does not warrant seismic migration. Lastly, we choose to not apply migration because no diffractions are observed on both the inline and crossline sections.

(2.5) Post-Processing

The post-processing section involves building various velocity models, low-frequency impedance models, performing band-limited impedance (BLIMP) inversion, and depth-conversion of both crossline and inline seismic cross-sections and inverted SI profiles.

(2.5.1) Band-Limited Impedance (BLIMP) Inversion

BLIMP is a post-stack impedance inversion algorithm (Ferguson et al., 1997). Previous studies provide the infrastructure and theoretical framework for BLIMP inversion (Becquey et al., 1979; Lavergne et al., 1977; Peterson et al., 1955; Waters 1981). Conventionally, BLIMP inverts for acoustic impedance (AI), however, I use it to calculate shear impedance (or SI).

Two inputs are required for the BLIMP inversion process. The first is uploading processed seismic data via `load_plot_seismic.m` (Section 8.9.1.9). I possess this input for the inline and crossline cross-sections as it is the output of the final stage of seismic data processing (Figure 2.53). The next and final data component required for BLIMP inversion is a low-frequency impedance model. The low frequency content of seismic data, which ranges approximately from $\sim 1 - 15$ Hz and is usually absent, is supplied via the a low-frequency impedance model (Lindseth 1979; Lloyd 2013). Each low-frequency impedance log that comprises the low-frequency impedance model is generated from one section of seismic data processing and post-processing. The first stage is the calculation of a low-frequency velocity log (Lavergne et al., 1977). I acquire a low-frequency velocity log from performing velocity analysis for each CMP gather (Section 2.4.8) (Berteussen et al., 1983). For our purposes, the low-frequency velocity model is initially V_{RMS} (Figure 2.54[*left*]) but subsequently converted to V_{INT} (Figure 2.54[*right*]) during post-processing via `model_builder.m` and `vrms2vint.m`, respectively (Section 8.9.1.4 & 8.9.1.2). This process is conducted for both the inline and crossline models (Figure 2.55). Altogether, each (V_{INT}) low-frequency velocity log is multiplied with unitary bulk density to supply a low-frequency impedance log and altogether concatenated to build an impedance model, which is also equivalent to a V_{INT} model (Jarvis et al., 2002). We concatenate each impedance log to build a low-frequency impedance model (Figure 2.56), thereby supplying the last necessary data component for BLIMP inversion.

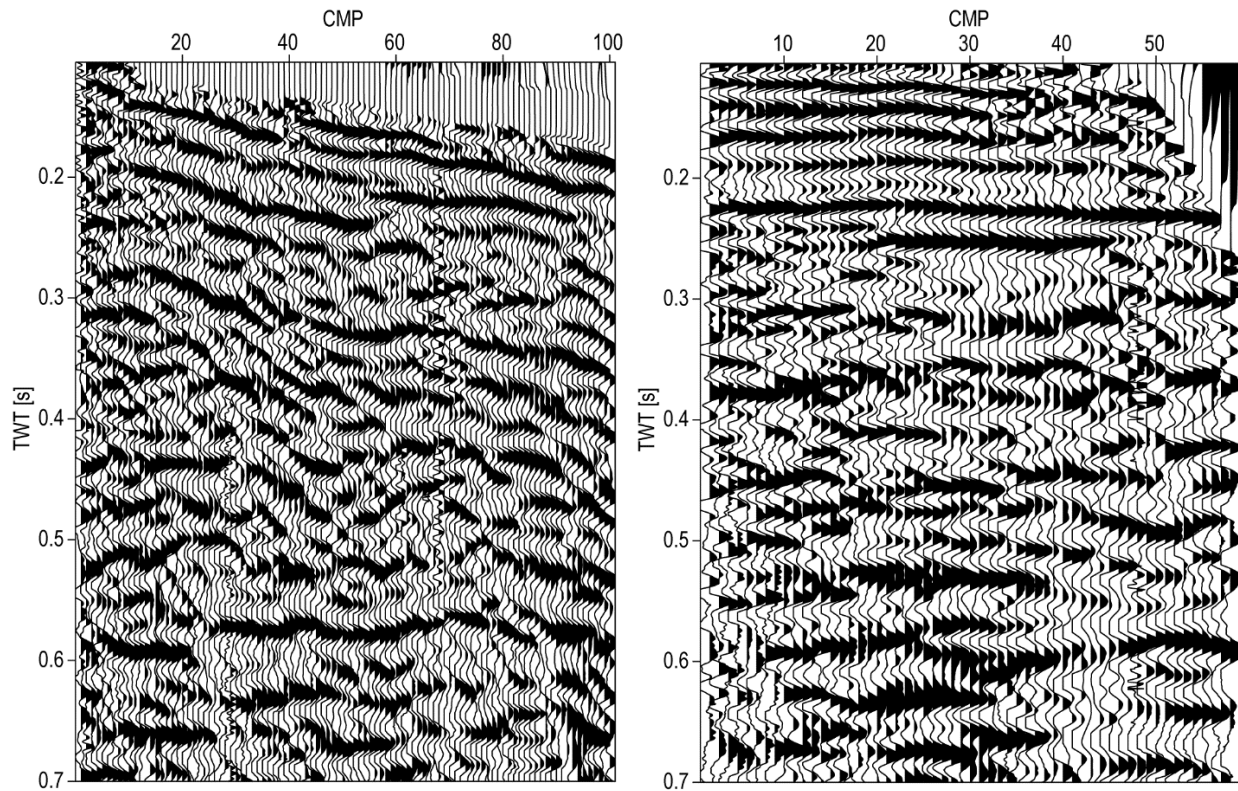


Figure 2.53. Processed inline (left) seismic cross-section. Seismic data are gained (AGC, $w_{agc}=0.08$ s) and clipped ($clip=1.5$). CMP spacing is ~ 1 m. Processed crossline seismic cross-section (right). Seismic data are gained (AGC, $w_{agc}=0.08$ s) and clipped ($clip=1.5$). CMP spacing is ~ 1 m.

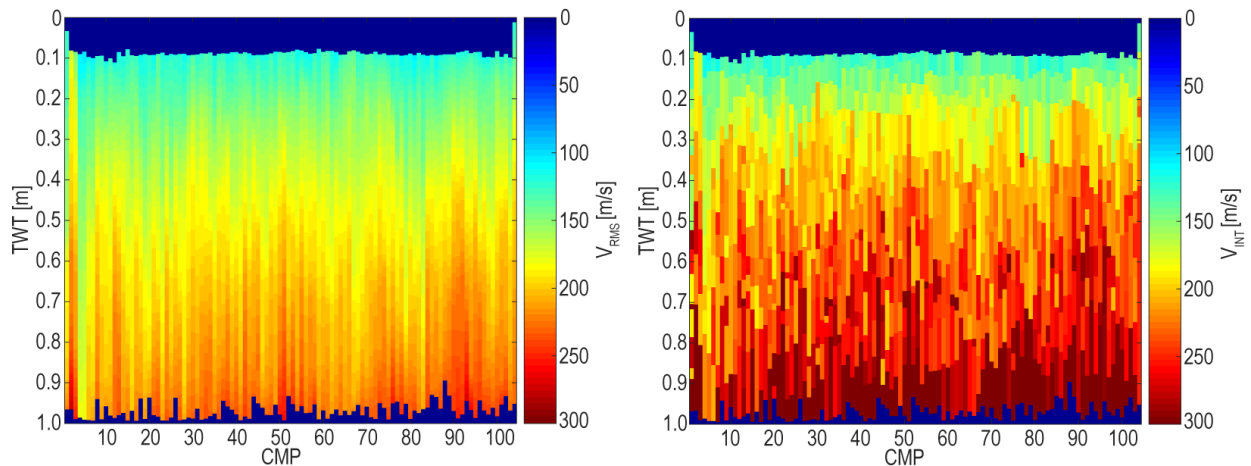


Figure 2.54. The inline V_{RMS} model (left) and the calculated inline V_{INT} model (right). For subsequent stages in post-processing and inversion, I use data from 0.105 – 0.7 s from CMP 1 - 100.

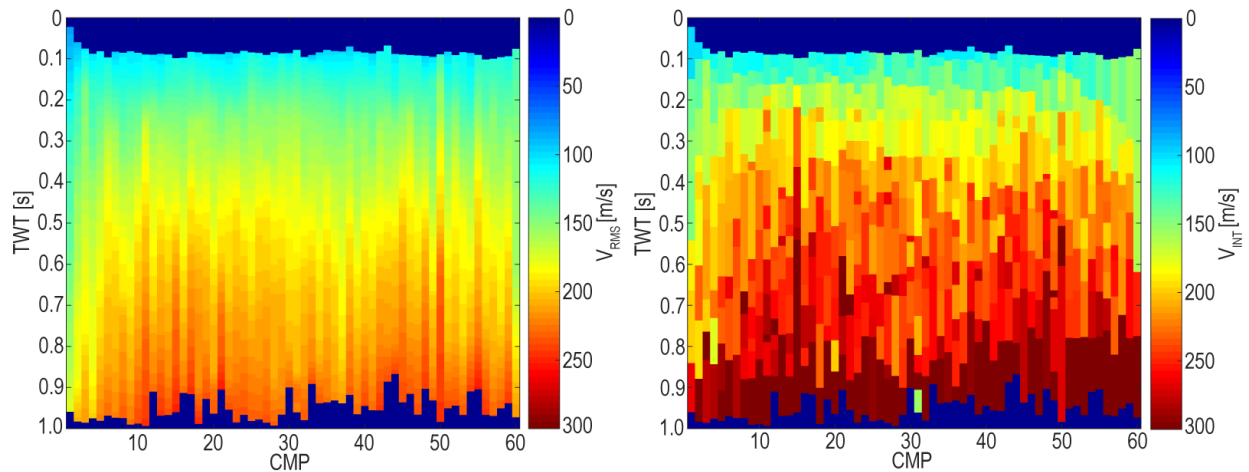


Figure 2.55. The crossline V_{RMS} model (left) and the calculated crossline V_{INT} model (right). For subsequent stages in post-processing and inversion, I use data from 0.105 – 0.7 s from CMP 2 – 58.

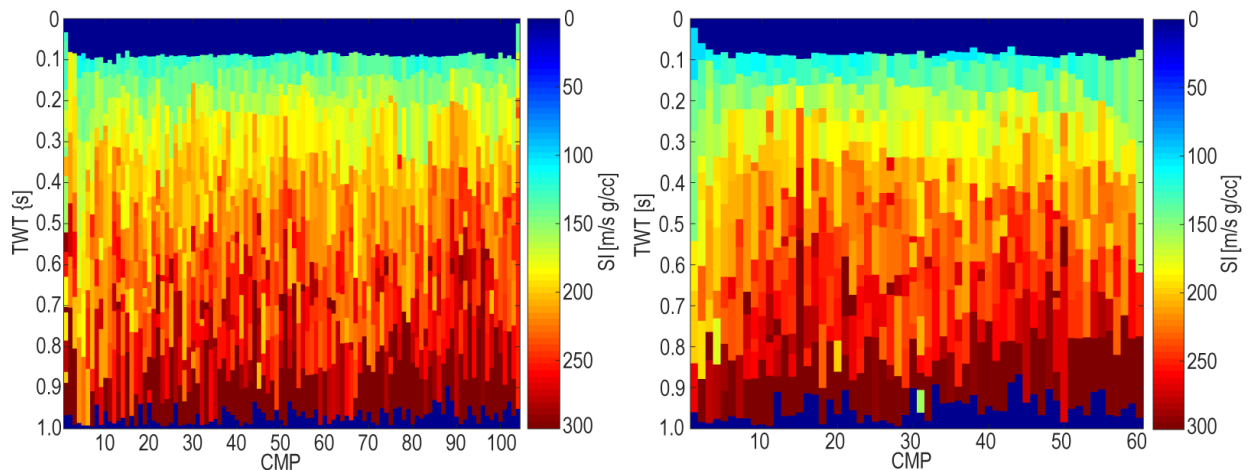


Figure 2.56. The raw inline low-frequency impedance model (left), which is identical to data displayed in Figure 2.54[right]. The raw crossline low-frequency impedance model (right). Data displayed here is identical to Figure 2.55[right]

BLIMP inversion is performed trace-by-trace via `auto_blimp.m` (Section 8.9.1.8) in ten stages (Ferguson et al., 1997; Lloyd 2013). Stages 1 – 10 are performed for each trace and corresponding low-frequency impedance log (Table 2.9). Stage 3 and Stage 7 apply user-supplied filtering parameters. For the low-cut filter, I use 15 Hz (Stage 3). For the high-pass filter (Stage 7), I use 90 Hz. Each of these filters are accompanied by a default roll-off Gaussian filter. The following ten stages cover the entire BLIMP inversion process for a single trace with its accompanied low-frequency impedance log. After inversion of each trace, the raw SI profile (Figure 2.57) is Gaussian-smoothed (1σ) via `imp_smoother.m` (Figure 2.58) (Section 8.9.1.13).

Table 2.9. A single iteration of BLIMP performs stages 1 – 10 to invert one trace.

Stage	Process
1	Remove and save linear trend of low-frequency impedance log
2	Calculate the Fourier spectra of the differenced low-frequency impedance log
3	Low-cut filter the seismic trace corresponding the impedance log
4	Integrate and exponentiate the filtered seismic trace to transform the trace into a pseudo-impedance log (Lloyd 2013)
5	Calculate the Fourier spectra of the pseudo-impedance log
6	Scale and match the spectra of both the pseudo-impedance log and the differenced low-frequency impedance log
7	High-cut filter the differenced and scaled low-frequency impedance log
8	Sum the filtered and scaled pseudo-impedance log spectra to the differenced, scaled, and filtered low-frequency impedance log spectra
9	Calculate the inverse Fourier transform of the summed result of Stage 8
10	Add the saved linear trend (Stage 1) to the result of Stage 9. The result of Stage 10 is a single SI log.

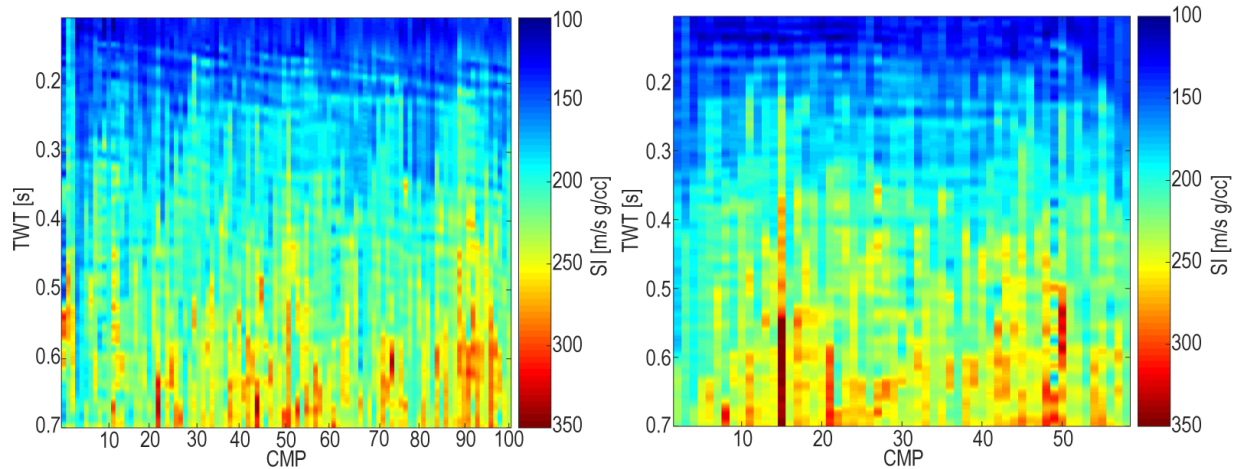


Figure 2.57. Raw result (left) from BLIMP inversion for the inline SI profile. To remove the blocky character of this result, we apply a Gaussian filter (1σ) for smoothing purposes. Raw BLIMP inversion result (right) for the crossline SI profile. I apply the same Gaussian filter (1σ) from the inline inversion result to the crossline profile.

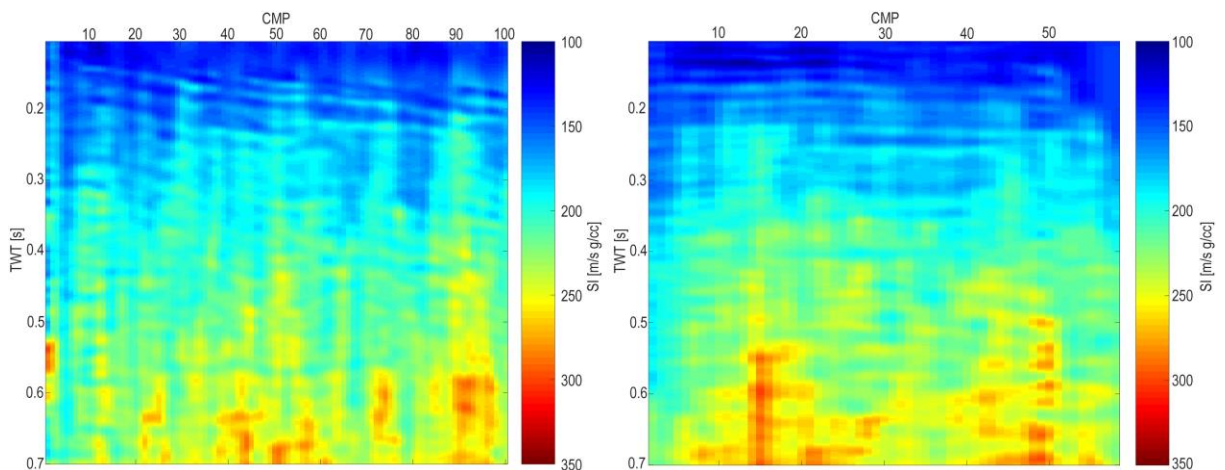


Figure 2.58. Gaussian-smoothed inline (left) SI profile, and the Gaussian-smoothed crossline (right) SI profile.

(2.5.2) Time-to-Depth Conversion

I depth-convert the time-domain seismic cross-sections and SI profiles in order to compare them to EC well-log measurements.

The process of depth-converting seismic cross-sections is slightly different than depth-converting SI profiles (Table 2.10). I use the same velocity model for depth-conversion of both the inline cross-section and SI profile. Likewise, I also use the same velocity model for depth-converting the crossline cross-section and SI profile. Instead of using the raw V_{INT} models, I calculate arithmetic mean of both the inline and crossline V_{INT} models to generate corresponding averaged velocity models (Figure 2.59). This process is necessary because the Seismic Unix model `suttoz` within `depthing.sh` (Section 8.8.2) module cannot accept unequal TWT/ V_{INT} pairs for each trace.

I use the averaged inline V_{INT} to convert TWT seismic sections into depth (m) (Figure 2.60[left]). Likewise, I use the averaged crossline V_{INT} to convert TWT seismic sections into depth (m) (Figure 2.60[right]).

Table 2.10. The overall process of converting time-domain seismic cross-sections or SI profiles to depth and transferring files. Steps 1 – 4 exclusively apply to time-domain SI profiles. To convert seismic cross-sections to depth, I only use steps 5 – 6. Depth-conversion of SI profiles requires steps 1 – 6.

Step	Task	Tool
1	Convert SI Matrix to Structure Data Type	s_convert (Section 8.9.2.1)
2	Convert SI Structure to SEG-Y Format	write_seg_y_file (Section 8.9.2.2)
3	Import Converted SEG-Y File to Zamin	(Section 8.4)
4	Convert SEG-Y File to Seismic Unix (.su) Format	seg_y_to_su.sh (Section 8.8.5)
5	Average V_{INT} model and Format Data to Strings	vmodel_avg.m (Section 8.9.1.12)
6	Copy Strings data from Step(5) to depthing.sh (Section 8.8.2)	Any text editor
7	Convert Selected SI Profile or Seismic Cross-Section to Depth	depthing.sh (Section 8.8.2)
8	Window Depth-Converted File	(Section 8.7.4)
9	Convert Depth-Converted and Windowed Data to SEG-Y Format	su_to_seg_y.sh (Section 8.8.7)
10	Transfer Converted SEG-Y File from Zamin	(Section 8.4)

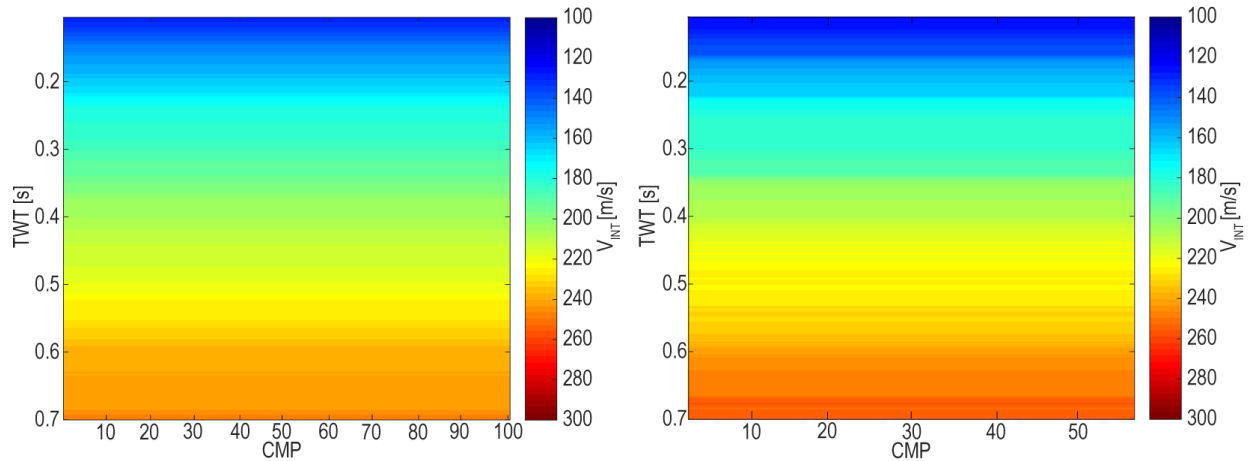


Figure 2.59. Averaged inline V_{INT} model (left) I use for depth-converting the inline cross-section and SI profile. I calculate the arithmetic mean of each row corresponding to the raw V_{INT} model. Averaged crossline V_{INT} model (right) I use for depth-converting the crossline cross-section and SI profile. I calculate the arithmetic mean of each row corresponding to the raw V_{INT} model.

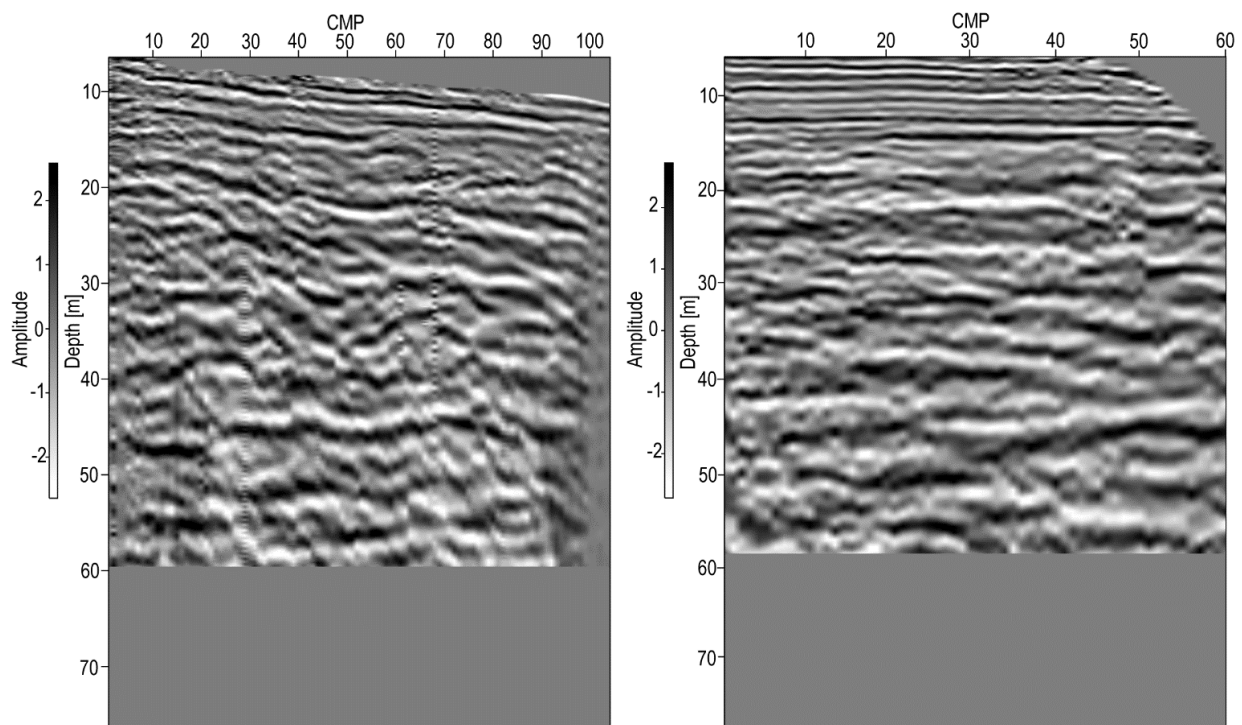


Figure 2.60. Depth-converted (left) inline seismic cross-section. The grey region at the bottom is windowed out for results section using Step 8 of Table 2.10. Depth-converted crossline (right) seismic cross-section. The grey region at the bottom is windowed out for results section using Step 8 of Table 2.9.

CHAPTER 3: RESULTS & INTERPRETATIONS

(3.1) Results

(3.1.1) Seismic Cross-Sections

Multiple continuous seismic reflectors are observed on both the inline and crossline cross-sections (Figure 3.1). All seismic horizons I select for mapping are of positive amplitudes.

The inline cross-section exhibits two continuous and dipping ($\sim 7.0 \pm 1^\circ$) seismic horizons (IL2 & IL8) (Figure 3.2[right]). A few localized and semi-continuous dipping seismic horizons (IL1, IL3, IL4, IL5, & IL6) are also present. A continuous reflection event is deeper and relatively flatter (IL8) than all other reflectors above it. The approximate amplitude range of all mapped seismic reflectors except for IL3 & IL6 is $\sim 1.0 - 2.5$. Horizons IL3 and IL6 retain a comparatively lower amplitude range of $\sim 0.1 - 0.8$.

The crossline cross-section displays numerous continuous seismic horizons that show little to no dip ($\sim 1.0 - 2^\circ$) (Figure 3.3). Seismic amplitudes for horizons CL1 – CL3 from CMP $\sim 30 - 55$ are discontinuous and somewhat chaotic due to comparatively greater presence of Love-wave during data acquisition. Lack of data quality in this section of the crossline seismic section negatively affects inversion results. CL4 is flat and continuous across the length of the section. CL5 is relatively continuous from \sim CMP 5 – 45. The amplitude along CL5 is highly variant laterally where the leftmost and rightmost zones are comparatively low ($\sim 0.0 - 0.25$) while the center is significantly higher ($\sim 2.0 - 2.2$). The bottom horizon (CL6) undulates laterally from \sim CMP 22 – CMP 60.

2-D seismic sections from the processed inline and crossline surveys provide high-resolution imagery of a downstream point-bar from different orientations. Each mapped horizon are spatially identified according to CMP and TWT. In order to display how each mapped horizon from both the inline and crossline sections correlate, we superimpose each cross-sections in 3-D space to view which inline horizons matches to a given crossline horizon, and vice versa (Figure 3.4).

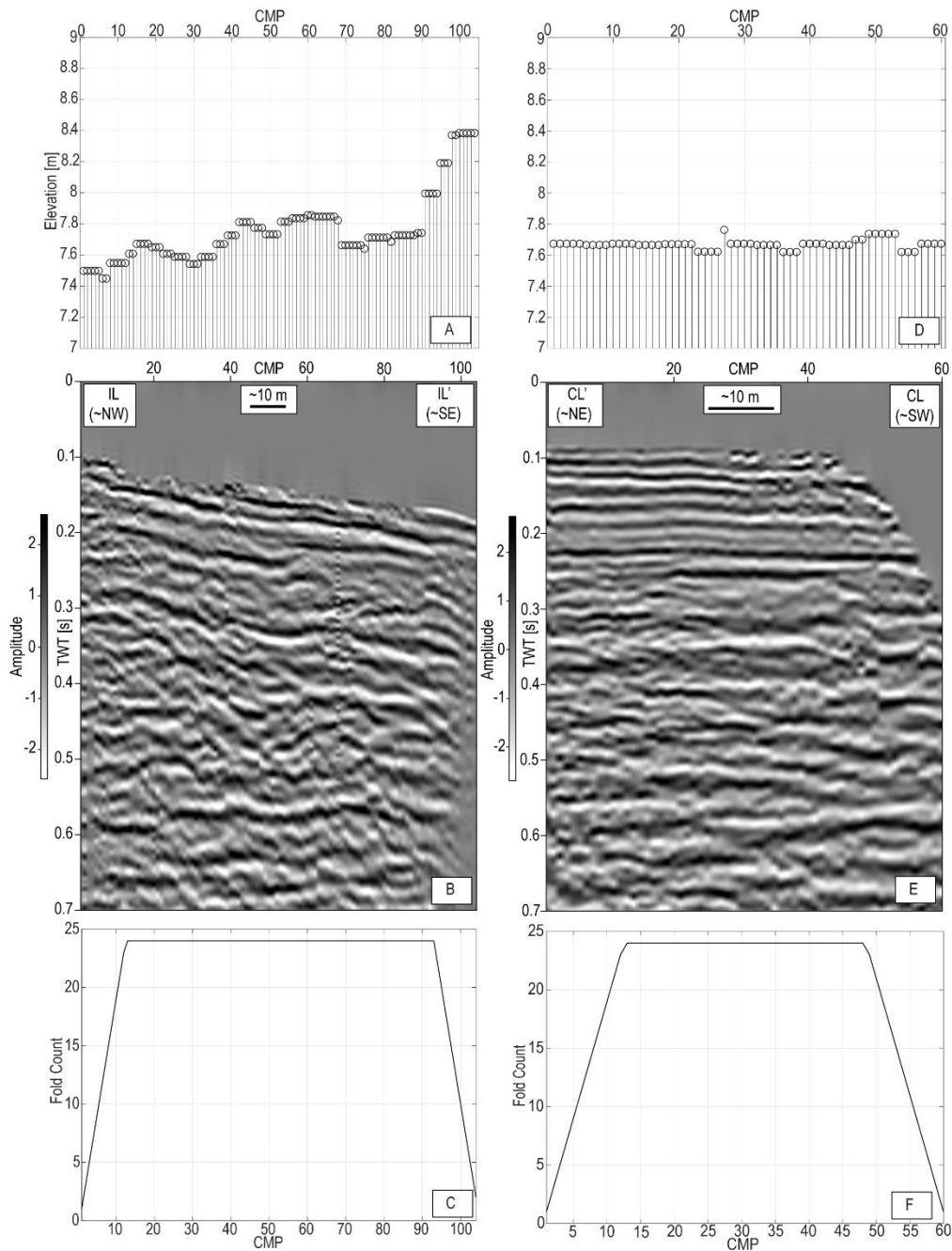


Figure 3.1. Plot A is the elevation profile corresponding to the inline cross-section. Image B is the processed inline cross-section. Seismic data are clipped (perc=99) and gained (AGC, wagg=0.08 s). CMP spacing is ~1 m. Plot C is the fold count of the inline cross-section. Minimum fold is 1, and maximum fold is 24. Plot D is the elevation profile of the crossline cross-section. Image E is processed crossline cross-section. Seismic data are clipped (perc=99), gained (AGC, wagg=0.08 s), and band-pass filtered (f=0,15,100,130 | amps=0,1,1,0). CMP spacing is ~1 m. Plot F is the fold count of crossline cross-section. Minimum fold is 2, and maximum fold is 24.

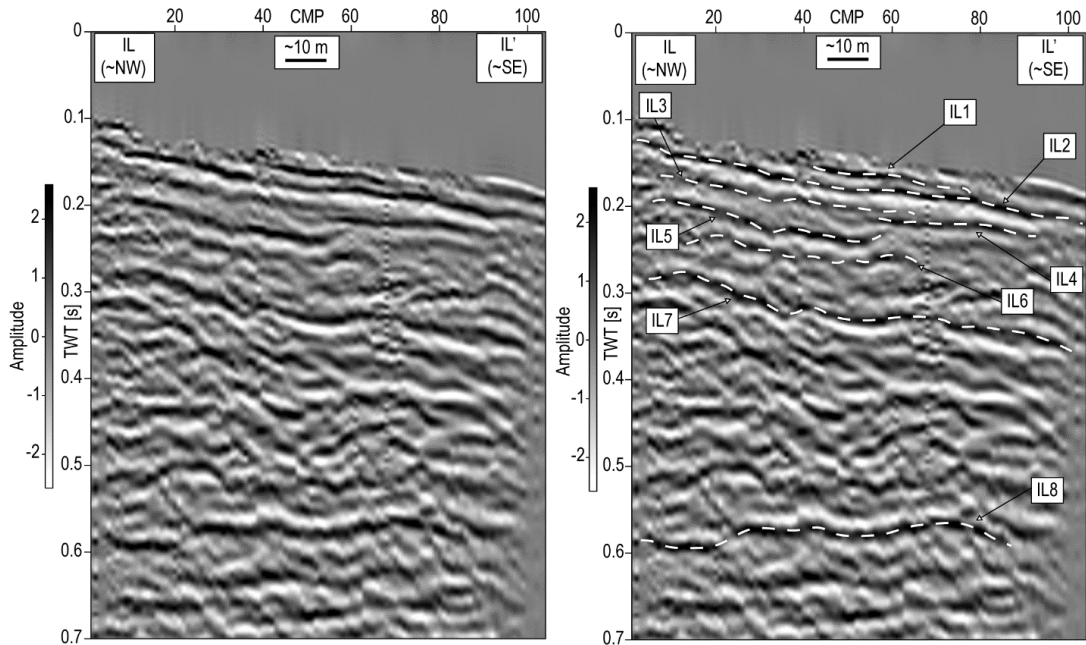


Figure 3.2. Same as Figure 3.1[B] (left). Windowed (0.0 – 0.7 s) and interpreted inline cross-section (right). Horizons 1 – 2 correspond to dipping ($\sim 7.0 \pm 1^\circ$) seismic reflectors. All interpreted horizons (IL1 – IL8) are positive seismic reflectors (i.e. black events). Seismic data imaged here are gained (AGC, $w_{agc}=0.08$ s), clipped (perc=99), and band-pass filtered ($f=0,15,100,130$ | $amps=0,1,1,0$). CMP spacing is ~ 1 m.

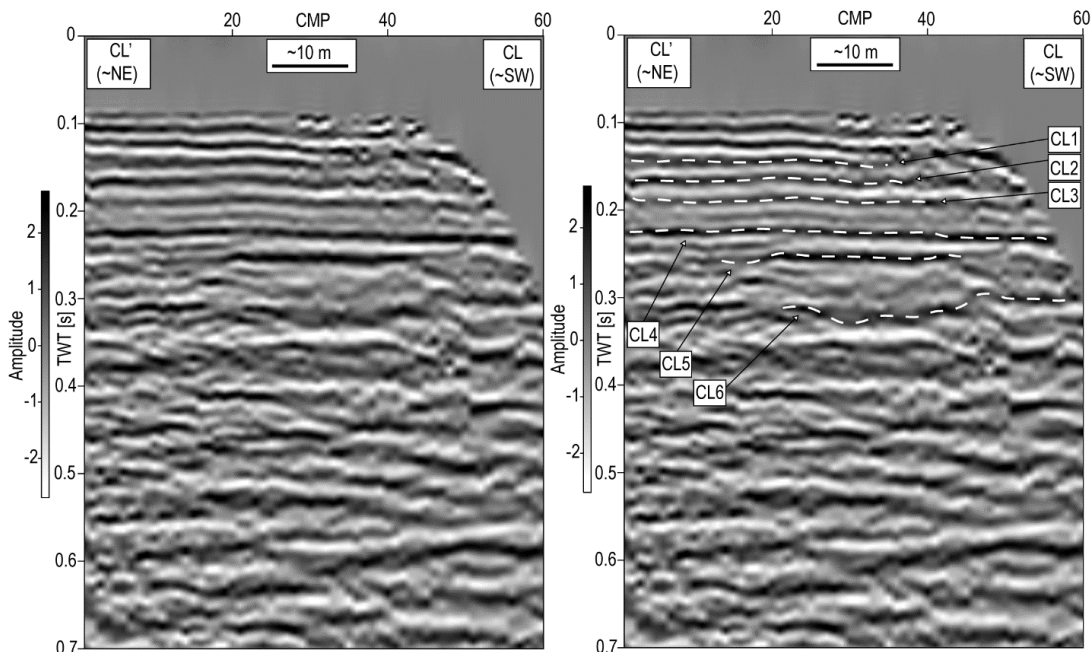


Figure 3.3. Same as Figure 3.1[E] (left). Windowed (0.0 – 0.7 s) and interpreted crossline cross-section (right). CL1 – CL6 correspond to six separately interpreted and mapped primary reflections. Seismic data are gained (AGC, $w_{agc}=0.08$ s), clipped (perc=99), and band-pass filtered ($f=0,15,100,130$ | $amps=0,1,1,0$). CMP spacing is ~ 1 m.

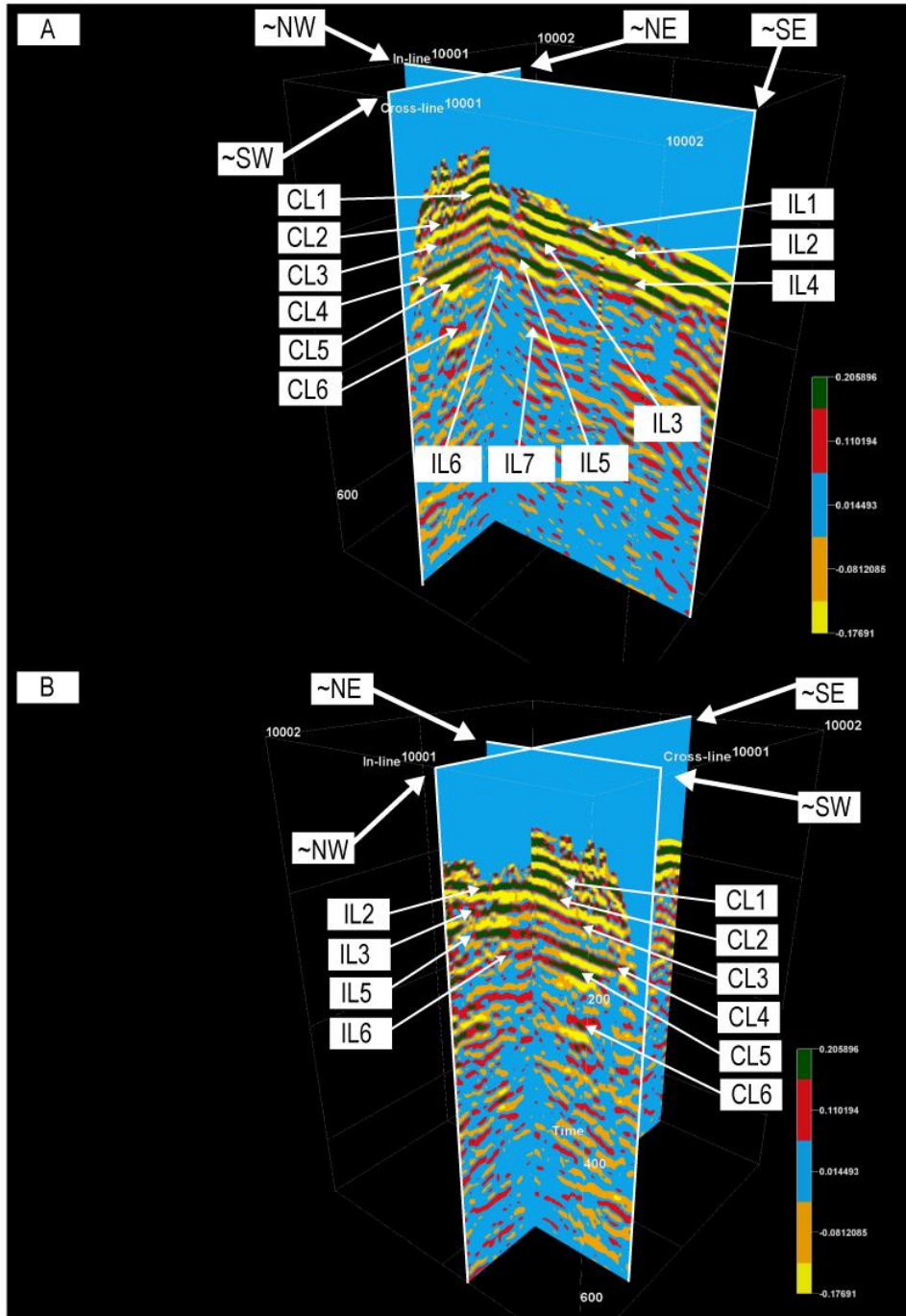


Figure 3.4. Inline and crossline seismic sections superimposed displayed from two perspectives [A & B]. Seismic horizons IL1 and CL1 are possibly the same (i.e. IL1=CL1). Likewise, IL2 =CL2, IL3=CL3, IL5=CL4, and IL6=CL5. IL4 does not correlate to any horizon on the crossline section because it pinches out before the intersection with the crossline section. IL7 and CL6 possibly correlate, however, I am unable to confidently align or image both horizons relative to earlier horizons. For IL8, I am unable to locate a matching horizon on the crossline section.

(3.1.2) SI Profiles

We invert windowed (0.105 – 0.7 s) time-domain seismic data for SI. Most interpreted seismic horizons from the inline (IL1 – IL5) and all from the crossline section also appear in their respective SI profiles.

The inline SI profile shows four horizons (IL1 – IL6) that correlate well with their respective interpreted seismic amplitudes (Figure 3.5). Two horizons (IL7 & IL8) that are interpreted on the inline cross-section are not correlated to the inline SI profile as they are not distinguishable relative to others identified on the profile. I observe that positive seismic amplitudes map to relative increases in SI for the inline profile. Likewise, relative decreases of seismic amplitudes map to decrease of SI.

All interpreted seismic horizons from the crossline cross-section are observed as their SI equivalent on the crossline profile (Figure 3.6). Similar to the inline results, we observe that positive seismic amplitudes corresponding to the crossline section correlate to relative increases of SI. Likewise, negative seismic amplitudes correspond to relative decreases of SI.

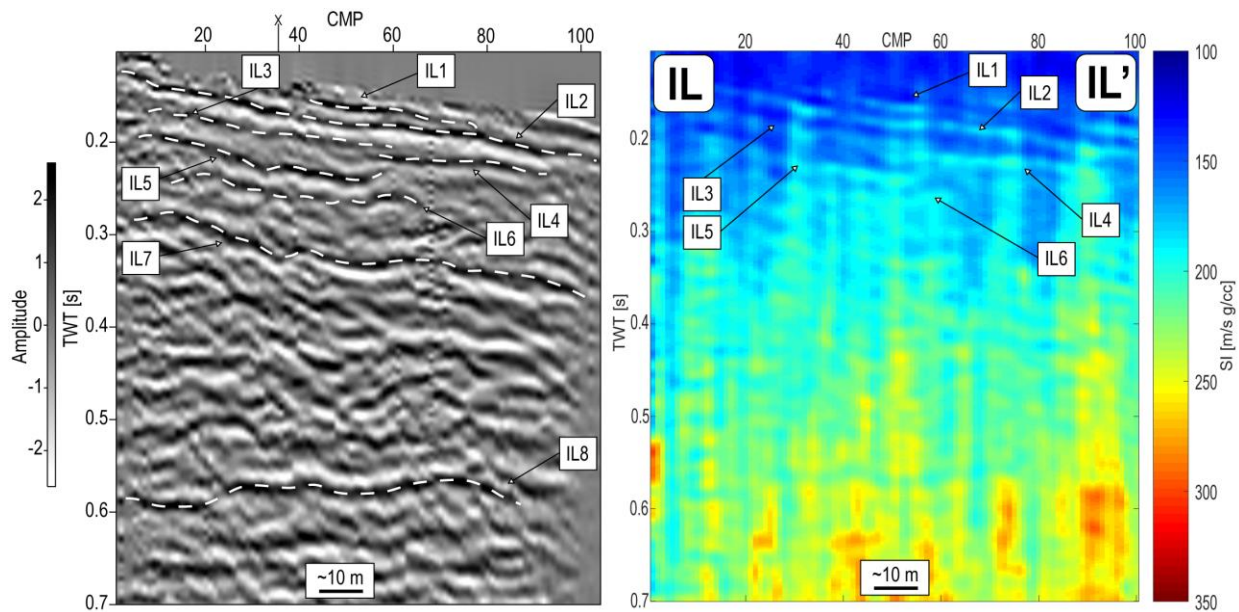


Figure 3.5. Same as Figure 3.2[left] (left). The x at ~CMP 37 is approximately where the crossline section intersects with CL' going into the page, and CL coming out of the page. The SI inline profile (right). Compared to Figure 3.5[left], we only identify six (IL1 – IL6) of the eight horizons interpreted for the inline cross-section. Each interpreted positive seismic horizon (IL1 – IL6) correlates to a relative increase of SI.

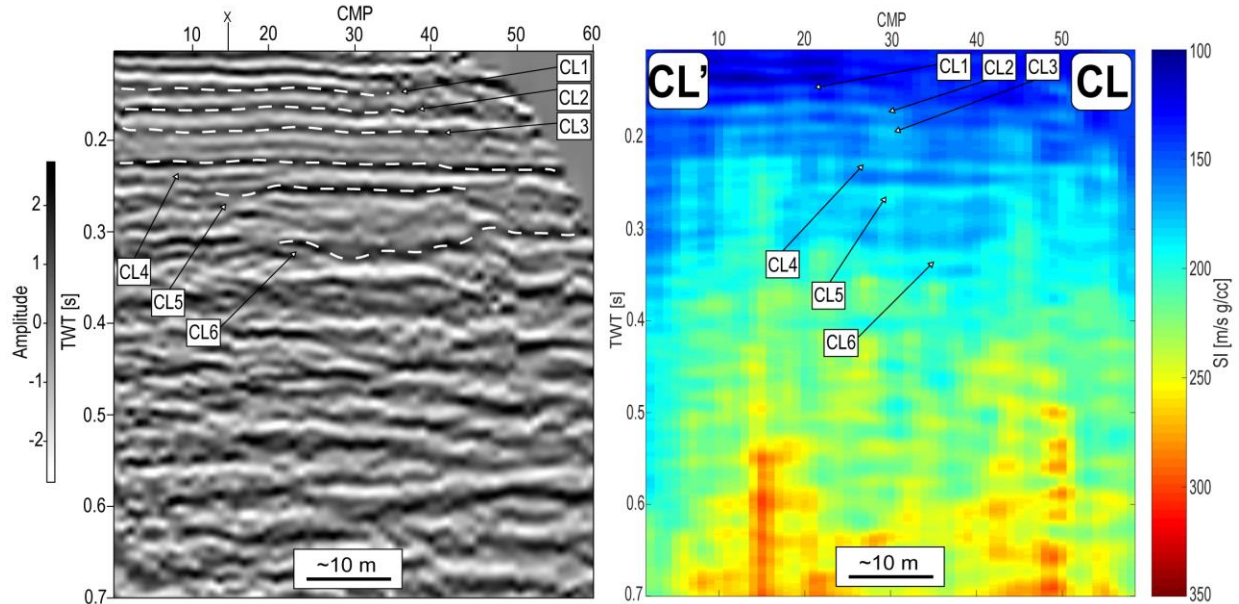


Figure 3.6. Same as Figure 3.3[left] (left). The x at ~CMP 16 is approximately where the inline section intersects with IL' going into the page, and IL coming out of the page. The SI crossline profile (right). We correlate all interpreted seismic horizons from their SI equivalent. Similar to results shown in Figure 3.5, positive seismic horizons correlate to relative increases of SI in the profile. SI horizons CL1 – CL3 become blurred past ~CMP 35 – 40.

(3.1.3) SI Logs & EC Well-Logs

Sets of SI curves from the depth-converted inline and crossline profile (Figure 3.7) are compared to both unfiltered and filtered EC well-logs from W5 and W7. I filter the W5 and W7 EC well-logs via convolution with a Gaussian wavelet via `gaussfilt.m` (Section 8.9.1.14) to approximately match the power spectrum corresponding to SI logs. Both unfiltered and filtered W5 (Figure 3.8, 3.9, 3.10, & 3.11) measurements are compared to inline SI logs 35 – 40. Also, unfiltered and filtered W7 EC well-logs are compared to inline SI logs 65 – 70 (Figure 3.12, 3.13, 3.14, & 3.15). Lastly, both unfiltered and filtered W5 well-logs are compared to the SI logs 35 – 40 corresponding to the crossline profile (Figure 3.16, 3.17, 3.18, & 3.19).

Generally, increases of SI correspond to increases of unfiltered EC. Conversely, decreases of SI usually correlate to relative decreases of unfiltered EC. Some increases and decreases of EC apparently do not match with some SI curves. This observation is later addressed and explained discussion (Section 5.3).

Lower frequencies (~5 – 25 Hz) of filtered EC logs are of higher spectral power relative to SI logs. However, the mid to high frequency range more closely matches the SI log power spectra, especially compared to unfiltered EC well-logs. Despite the power spectra of both filtered EC and SI logs not exactly matching, effective comparisons can still be made.

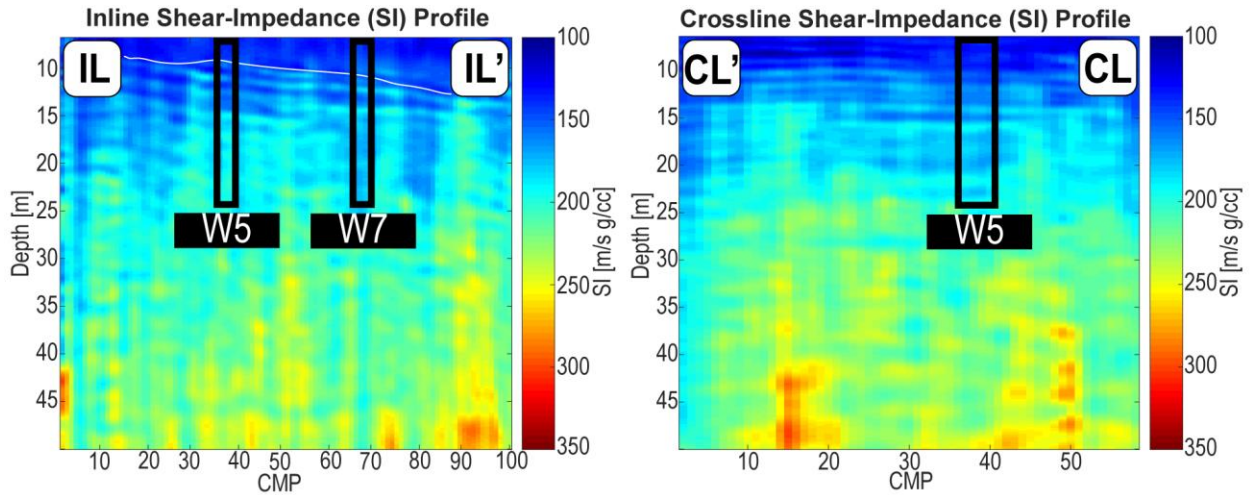


Figure 3.7. W5 EC measurements are projected to CMP 35 – 40 for the inline profile (left). W7 EC measurements are projected to CMP 65 – 70 (left). The aforementioned range of CMPs is also referred to SI logs. SI data is windowed from 8 to 50 m. The W5 EC well-log is projected to CMP 35 – 40 (right). The aforementioned range of CMPs is also referred to SI logs. SI data is windowed from 8 to 50 m.

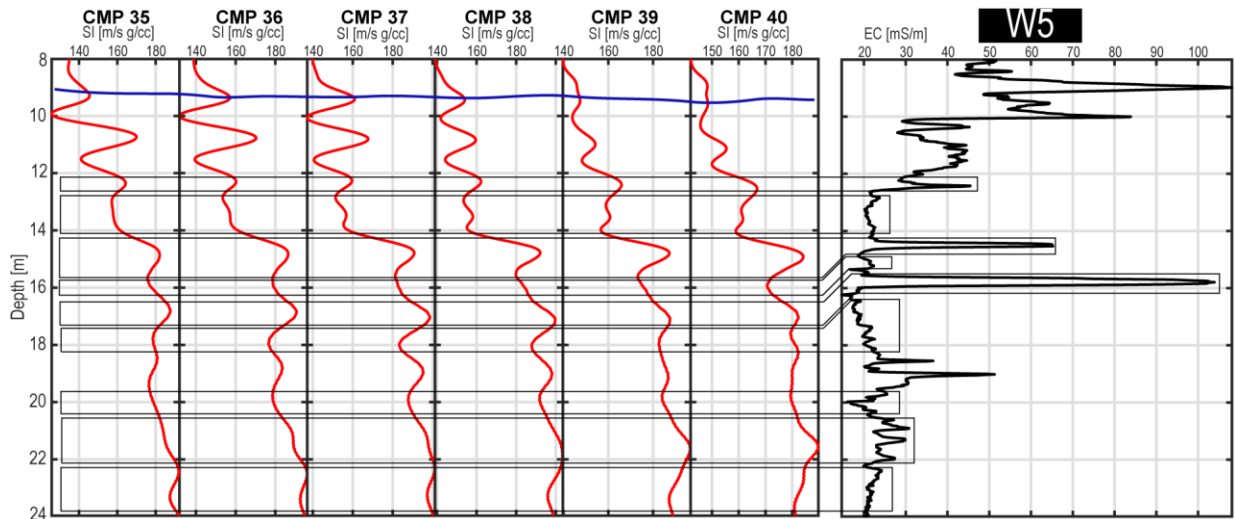


Figure 3.8. SI logs 35 – 40 (CMP 35 – 40) of the inline SI profile juxtaposed to the unfiltered W5 EC well-log.

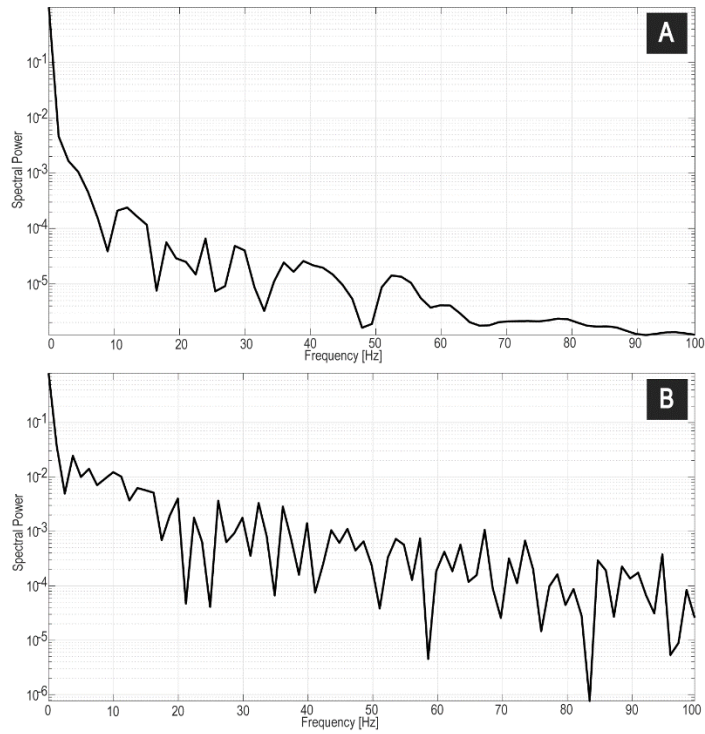


Figure 3.9. Plot A displays power spectra corresponding SI logs 35 – 40 from the inline profile. Plot B shows power spectra properties of unfiltered EC log from W5.

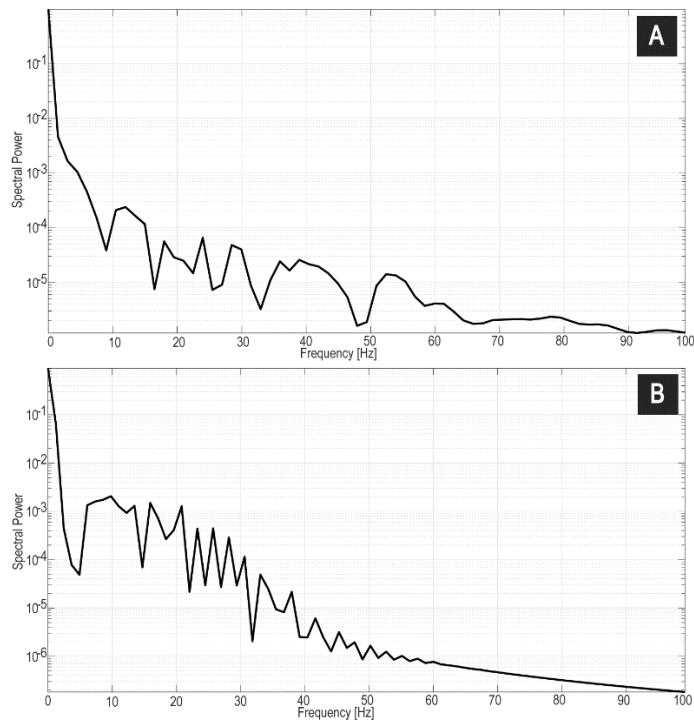


Figure 3.10. Plot A displays power spectra corresponding SI logs 35 – 40 from the inline profile. Plot B shows power spectra properties of filtered EC log from W5.

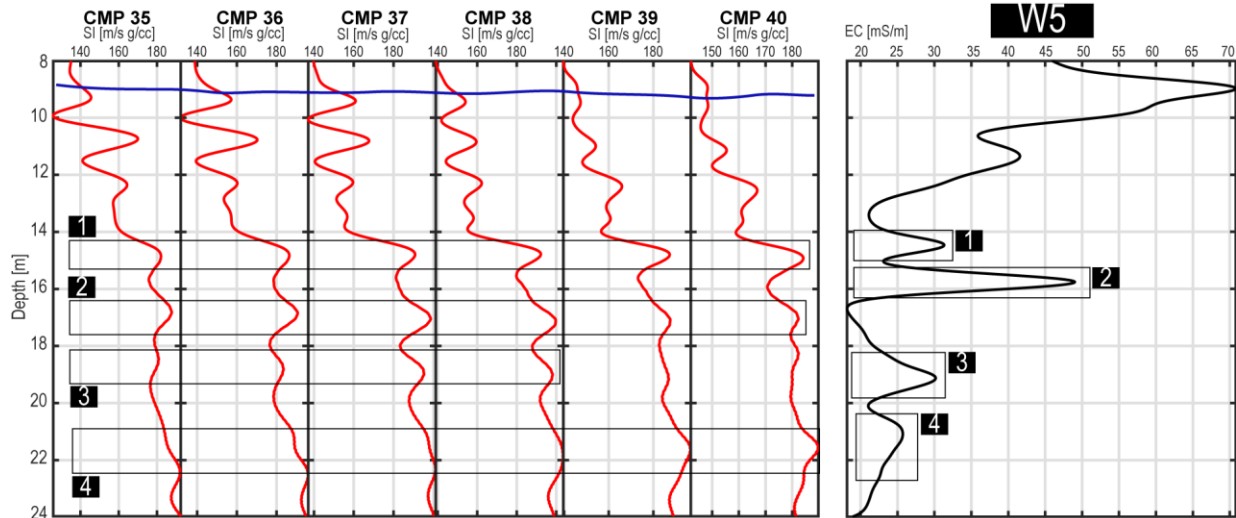


Figure 3.11. In-line SI logs 35 – 40 (CMP 35 – 40) compared to the filtered W5 EC well-log. Comparisons 1 – 4 show relative increases of SI closely matching increases of filtered EC. All data at and above the solid blue corresponds to top-muted seismic data, therefore, there should be no similarity between SI and EC.

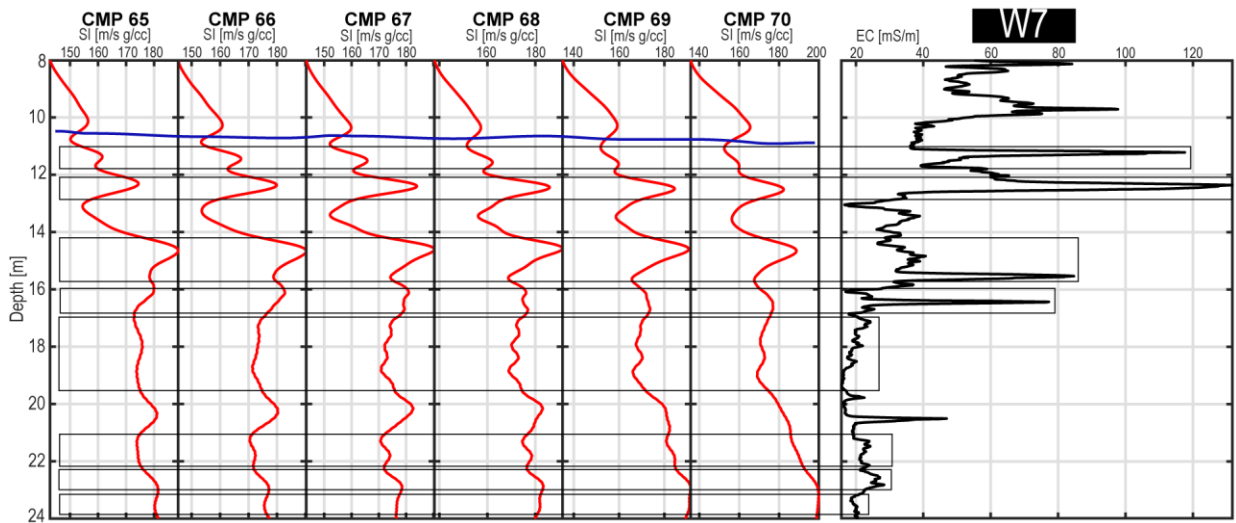


Figure 3.12. SI logs 65 – 70 (CMP 65 – 70) of the inline SI profile juxtaposed to the W7 unfiltered EC well-log measurements. Similarities are shown between the SI curves and unfiltered EC log. Relative increases of SI usually correspond to increases of EC. No correlation exists between EC and SI above the solid blue line because these SI measurements correspond to the inline cross-section muted zone.

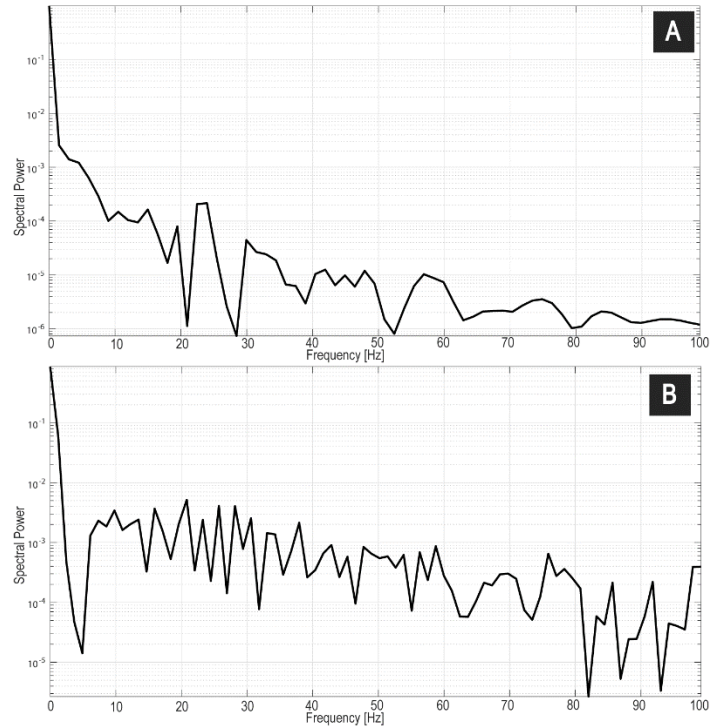


Figure 3.13. Plot A displays power spectra corresponding inline SI logs 65 – 70. Plot B shows power spectra properties of the unfiltered EC log from W7.

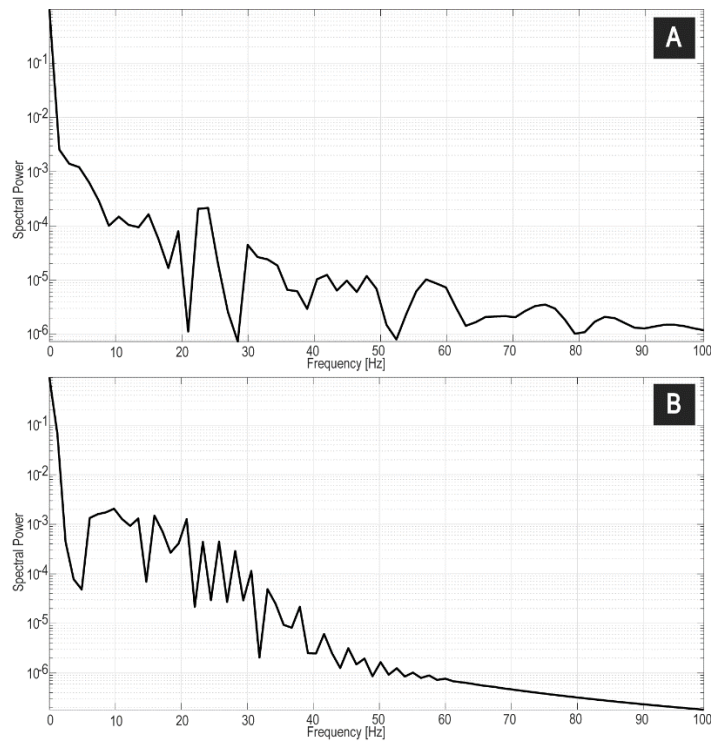


Figure 3.14. Plot A displays power spectra corresponding SI logs 65 – 70 from the inline profile. Plot B shows power spectra properties of filtered EC well-log from W7.

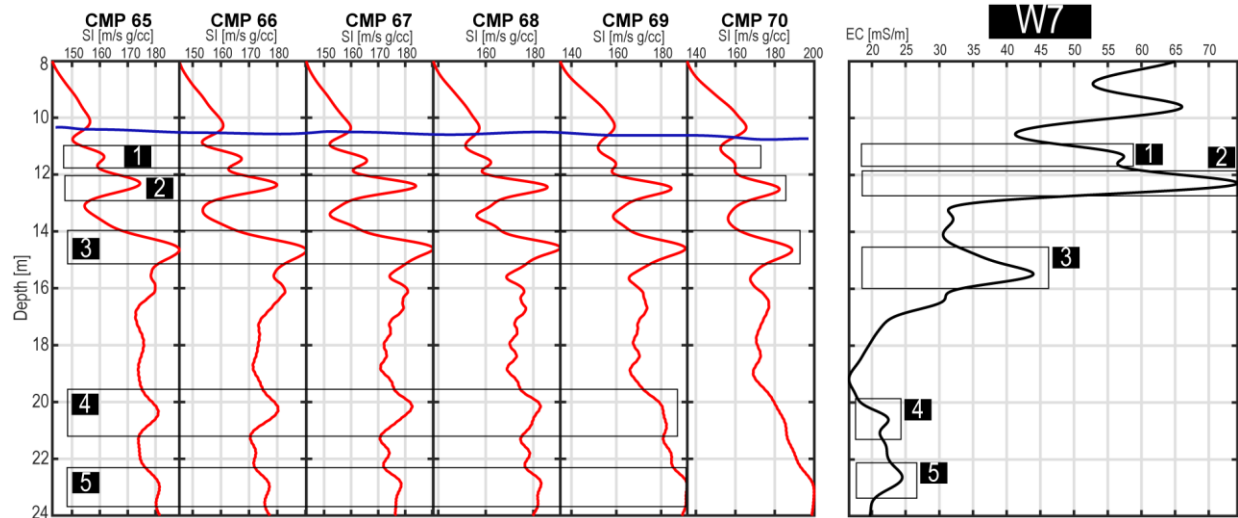


Figure 3.15. Filtered EC well-log juxtaposed to inline SI logs 65 – 70. Comparisons 1 – 4 shown relative increases of SI closely matching increases of filtered EC. All data at and above the solid blue corresponds to top-muted seismic data, therefore, there should be no similarity between SI and EC.

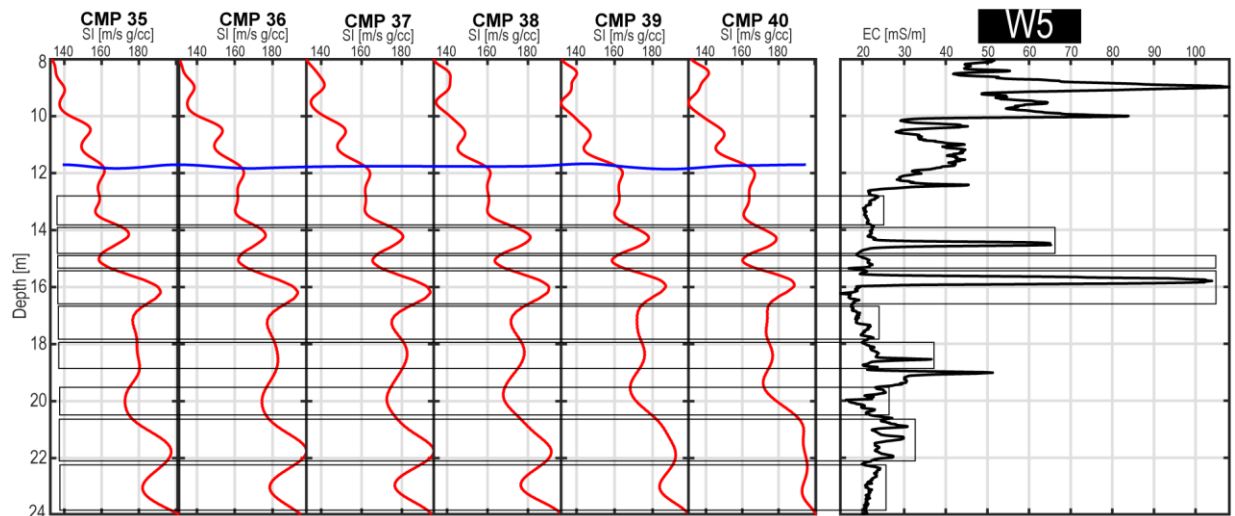


Figure 3.16. SI logs 35 – 40 (CMP 35 – 40) of the crossline SI profile juxtaposed to the W5 EC well-log measurements. All data at and above the solid blue corresponds to top-muted seismic data, therefore, there should be no similarity between SI and EC.

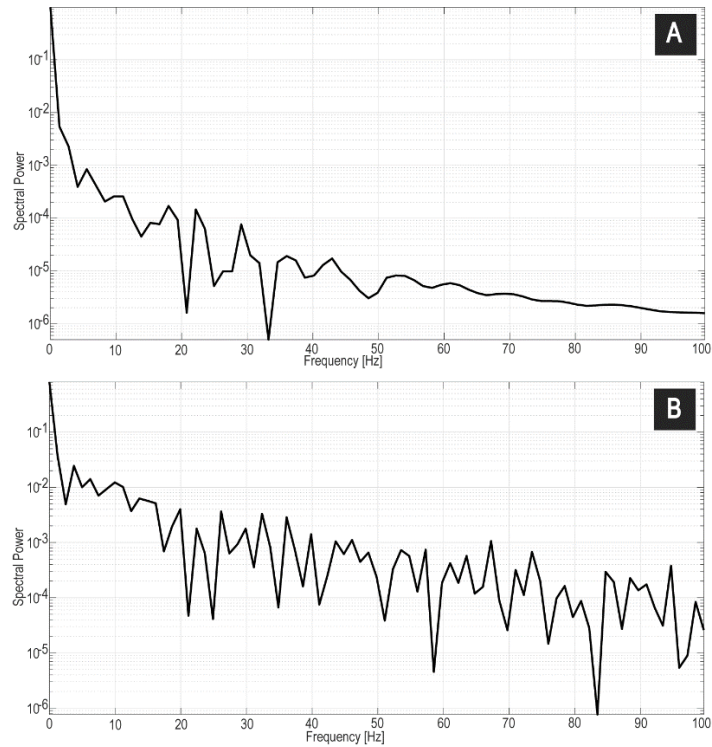


Figure 3.17. Plot A displays power spectra corresponding to crossline SI logs 35 – 40. Plot B shows power spectra properties of filtered EC log from W5.

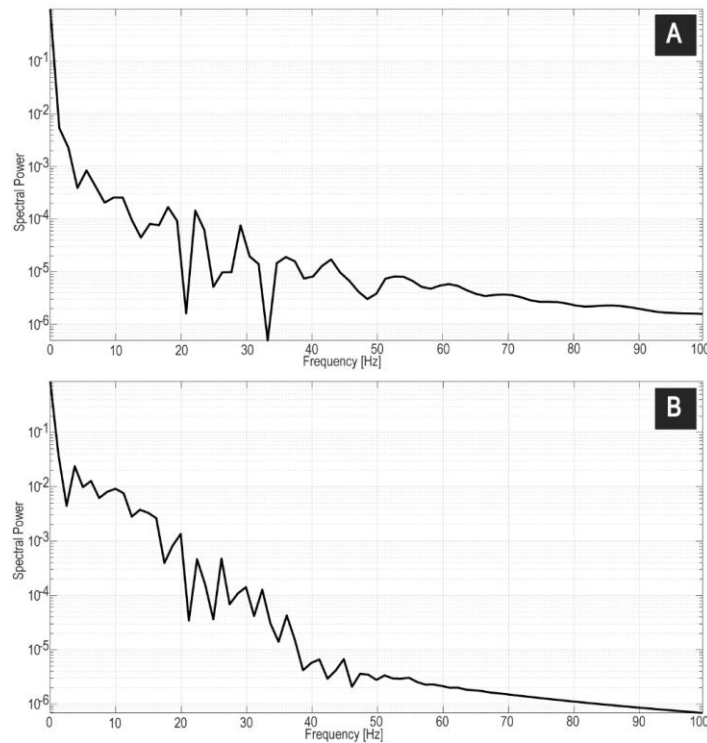


Figure 3.18. Plot A displays power spectra corresponding to crossline SI logs 35 – 40. Plot B shows power spectra properties of filtered EC log from W5.

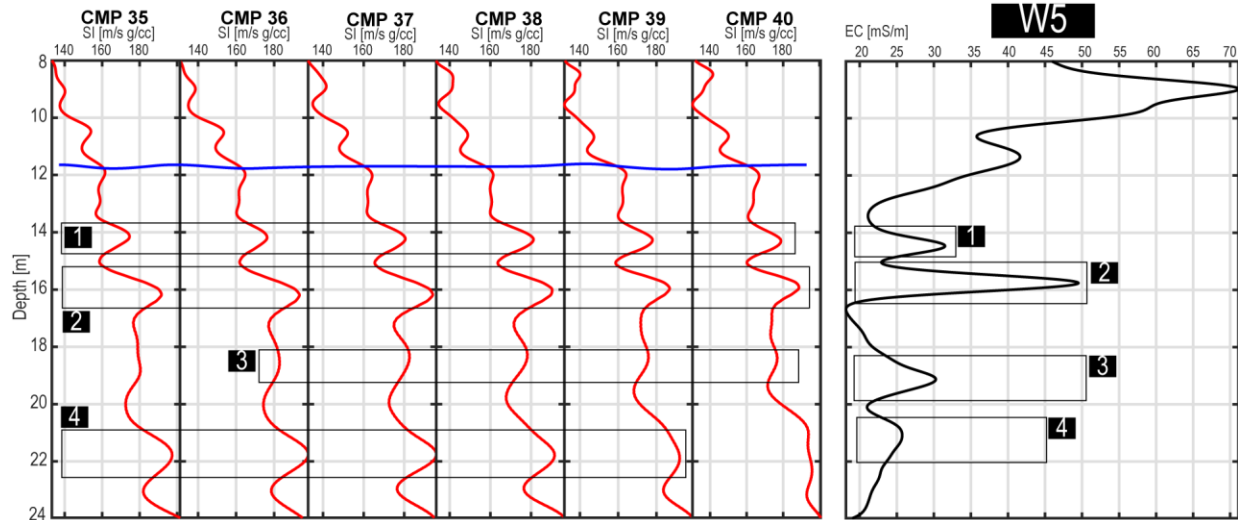


Figure 3.19. Filtered EC well-log juxtaposed to crossline SI logs 35 – 40. Comparisons 1 – 4 shown increase of SI correlating to increases of EC. All data at and above the solid blue corresponds to seismic data characterized by poor reflectivity, therefore, there should be little to no similarity between SI and EC.

(3.2) Interpretations

Interpretations of inline and crossline seismic cross-sections and SI profiles are divided into two sections. The first section explains seismic sections from both the inline and crossline surveys. The second and last section infers from results provided via inline and crossline SI profiles as well as EC well-log data.

(3.2.1) Seismic Cross-Sections & Sediment Package Architecture

I interpret the dipping seismic reflectors of the inline cross-section indicates the presence of inclined sediment packages dipping from close to the top of a near-surface point-bar (~NW) towards palaeochannel thalweg (~SE) (Figure 3.2). The dipping behavior of both continuously and semi-continuously dipping seismic reflectors is expected as the inline survey is situated approximately orthogonal to paleochannel (Bridge et al., 1995b; Durkin et al., 2017). For the crossline section, the presence of little to no dip of mapped seismic reflectors indicates comparatively less architectural change both vertically and laterally relative to the inline section (Figure 3.3). Indeed, the lack of dip of crossline seismic reflectors is also expected as this survey is situation (~SW – NE) parallel to paleochannel (Bridge et al., 1995a; Ghinassi et al., 2016). I believe this is a result of fluvial sediments being deposited parallel to palaeochannel, which results in less variability in both architecture and physical properties both laterally and vertically to an extent (Choi et al., 2004; Ghinassi et al., 2015).

The dipping and relatively non-dipping character of inline and crossline seismic reflectors is indeed consistent with ideal downstream point-bar models (Ghinassi et al., 2015; Ghinassi et al., 2016; Ielpi et al., 2014; Miall 2014; Pranter et al., 2007). As seismic reflectors are representative of near-surface geology, the overall architecture of near-surface point-bar packages may be inferred from the dipping and/or non-dipping behavior of crossline and inline reflectors.

(3.2.2) SI Profiles, EC Well-Logs, & Physical Properties of Sediment Packages

Relative increases of SI generally correspond to relative increases of EC (Figure 3.11, 3.15, & 3.19), which indicates that clay-rich sediment packages retain greater SI compared to sand-rich sediment packages.

EC is highly influenced by the presence of clays (Bowling et al., 2007). Specifically, clay-rich sediments show a relative increase of EC, and sand-rich sediments result in a decrease of EC (Inazaki et al., 2011). As such, I generalize relative increases of EC to indicate clay-rich sediments and decreases to sand-rich sediments (Solberg et al., 2012). Since there is a general trend of increasing SI correlating to relative increases of EC and relative decreases of SI correlating to decreases of EC, I infer that clay-rich sediment packages retain a greater SI than sand-rich sediment packages. The difference of SI between the two sediment packages is mainly a result of early-stage diagenetic processes such as compaction and dewatering, which variably alters physical properties associated with sediment packages such as pressure, porosity, volumetric water content, and rigidity (Holland 1980; Odum et al., 2004).

The apparent misalignment or lacking correlation of SI to EC may be attributable to multiple factors. These factors include dipping sediment packages, pinch-outs, tuning, wavelet effects, and depth conversion process (Section 5.3).

CHAPTER 4: ERROR ANALYSIS

(4.1) Error of Time-to-Depth Conversion

The V_{INT} model I use for depth-converting seismic cross-sections and SI profiles is an average of the raw V_{INT} model (Figure 3.59). The average of the raw V_{INT} model is generated via calculating the arithmetic mean of each row of the velocity model (Table 2.10, Step 5). As a result, the new velocity model retains identical values for a given sample of each column but vary with time. The process of averaging the raw V_{INT} model is required as the `suttopz` module `depthing.sh` (Section 8.8.2) calls cannot accept a velocity model where TWT/V_{INT} pairs vary for each trace (i.e. column).

I calculate the absolute percent difference of the raw V_{INT} model relative to the averaged V_{INT} model and infer the subsequent error associated with the depth-conversion process (Figure 4.1). The absolute percent error associated with both the inline and crossline averaged velocity models exhibits left-skewedness, thus indicating that the averaged V_{INT} models I use for time-to-depth conversion of the seismic cross-sections and SI profiles retains velocity values that are relative higher than those of the raw V_{INT} models.

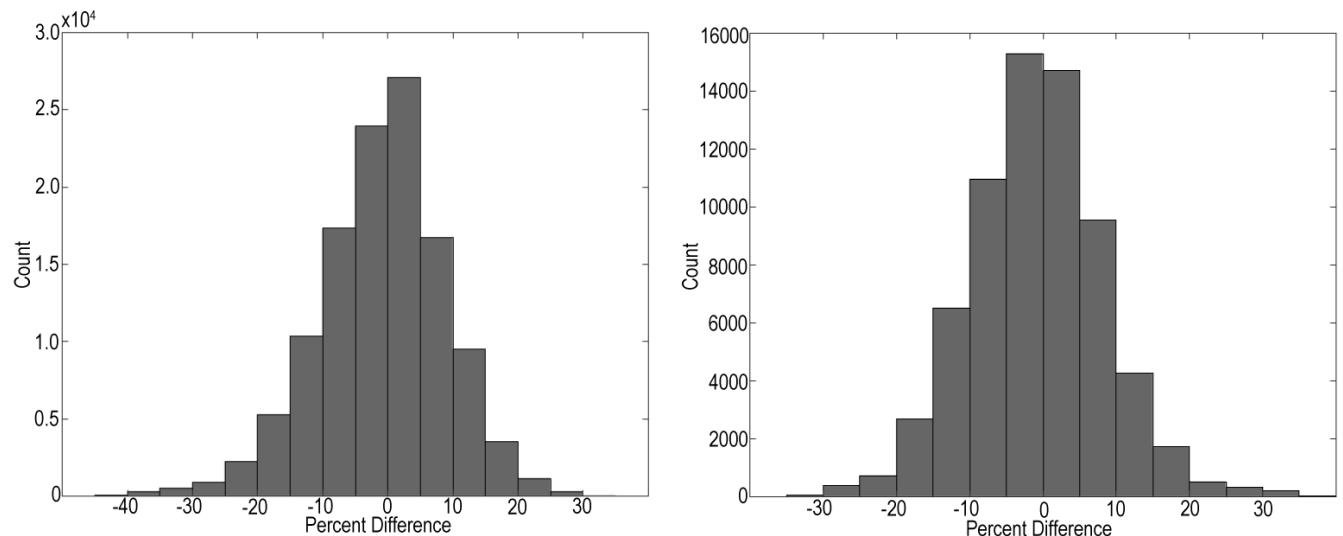


Figure 4.1 (left). Histogram of absolute percent error of the averaged V_{INT} relative to the raw inline V_{INT} model. The percent difference and count distribution shows a normal distribution. The overall error is slightly left-skewed. Approximate 95% of error count is within the percent difference range of -15% to 15%. Histogram of absolute percent error (right) of the averaged V_{INT} relative to the raw crossline V_{INT} model. Similar to data displayed in Figure 4.1[left], the overall error is normally distributed and is slightly left-skewed. Also, ~95% of error count is within the percent difference range of -15% to 15%

(4.2) Error of BLIMP Inversion & Sensitivity of Input Parameters

The input parameters for BLIMP include conditioned amplitudes from seismic cross-sections and low-frequency impedance models as well as user-defined high and low pass filter values. I evaluate the overall effect of BLIMP parameters from previous work and with tests applied to my data (Ferguson 1996; Ferguson et al., 1997; Lloyd

2013; Lloyd et al., 2012; Maulana et al., 2016). Each parameter is separately altered for a separate BLIMP inversion and subsequently compared to the accepted crossline and inline time-domain SI profiles in order to quantify and visualize the differences.

(4.2.1) Low-Cut Filter

I examine the frequency spectrum associated with processed cross-sections and low-frequency SI logs to determine the optimal low-cut filter value to use for BLIMP inversion. Also, I establish an acceptable bandwidth range associated with a 30-Hz geophone as this will assist the process of determining the lowest useable and reliable seismic frequencies.

Selecting an optimal low-cut filter for BLIMP inversion serves a dual purpose. First and foremost, it is the low-cut parameter that each seismic trace is filtered according to. Secondly, it also serves as the high-cut filter value for the low-frequency SI log. It is important to consider the bandwidth of both the seismic (Figure 4.2, 4.3, 4.4, & 4.5) and SI logs (Figure 4.6 & 4.7) to determine an optimal low-cut parameter.

The spectral power of processed seismic data corresponding to the inline and crossline sections is present from 0 – 100 Hz (Figure 4.2 & 4.3). Since all seismic data were acquired with 30-Hz geophones, I conclude that power residing within 0 – 10 Hz corresponds to coherent low-frequency noise (Mougenot 2005). I low-pass and band-pass both seismic cross-sections to confirm that the lower frequency bandwidth of seismic amplitudes included for BLIMP inversion primarily consists of usable reflection signal and thereby is indicative of subsurface geology rather than coherent noise (Figure 4.4 & 4.5). The frequency range of ~15 – 30 Hz of both cross-sections retains signal with minor interference of noise (Figure 4.4[B] & 4.5[B]). I confirm this observation via band-passed filtering cross-sections. I incorporate frequencies below 30 Hz for SI inversion because exploiting bandwidth below the natural frequency of a geophone is often performed and this analysis confirms that useable reflection signal is present below 30 Hz (Lloyd 2013; Maxwell et al., 2012; Roux* et al., 2014).

I examine the bandwidth of low-frequency SI logs set from the inline and crossline low-frequency SI model (Figure 4.6 & 4.7). The normalized amplitude spectra of each log is similar and shows that most amplitude is concentrated within 1 – 5 Hz range. Lower amplitude content extends into relatively higher frequency bandwidth (~5 – 15 Hz) (Figure 4.6 & 4.7). Altogether, I incorporate a low-frequency range (1 – 15 Hz) from the low-frequency impedance logs for BLIMP inversion to compensate for the lack of low-frequency content that is either absent or noisy in processed seismic data.

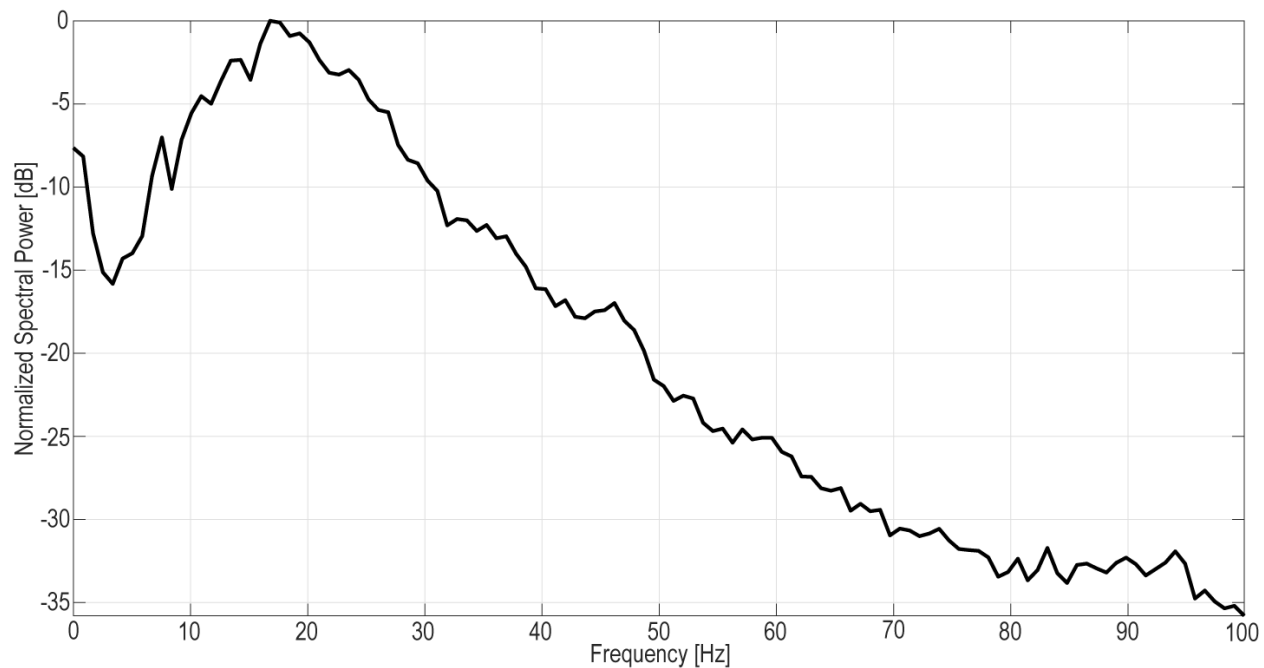


Figure 4.2. Power spectra of inline processed cross-section.

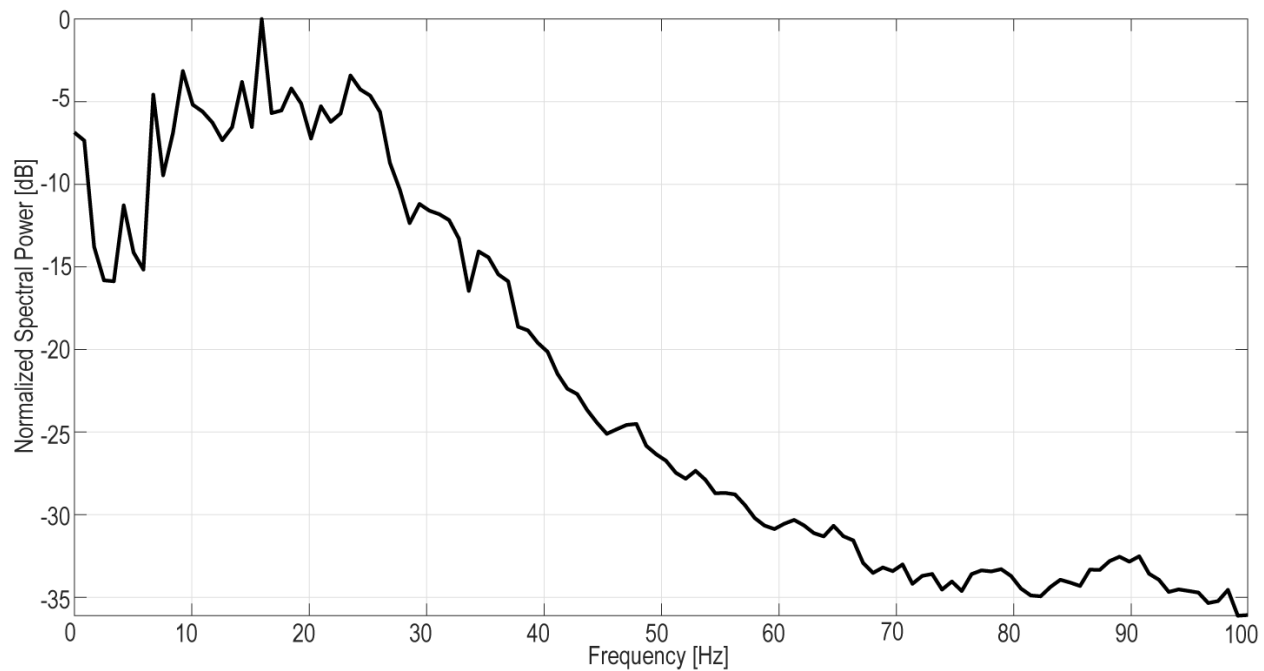


Figure 4.3. Power spectra of crossline processed cross-section.

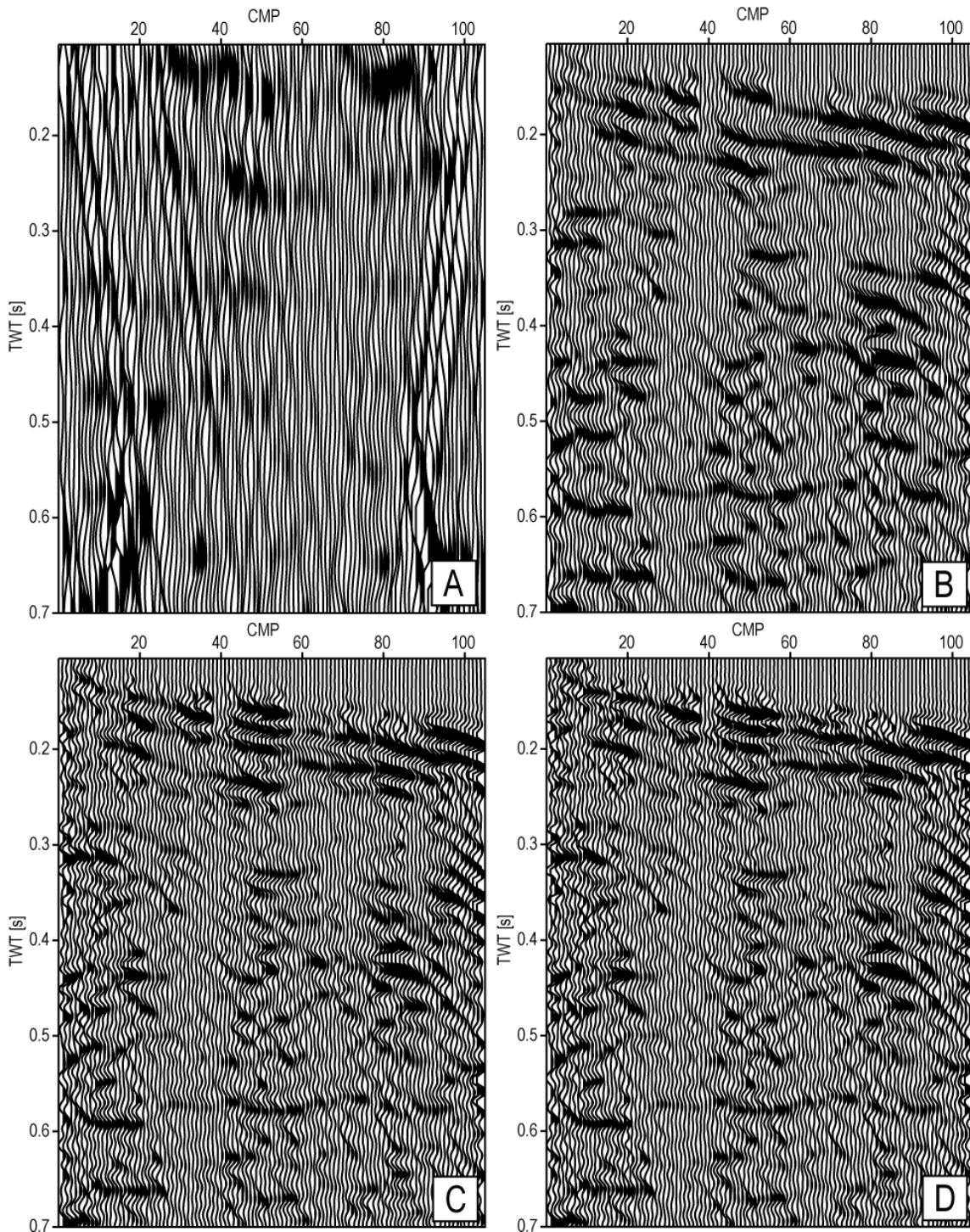


Figure 4.4. Low-pass filtered inline seismic cross-section ($f=0,10,12$ | $amps=1,1,0$). Seismic data are gained ($tpow=1.8$) and clipped ($perc=97$) (A). Band-passed filtered inline seismic cross-section ($f=10,15,30,50$ | $amps=0,1,1,0$). Seismic data are gained ($tpow=1.8$) and clipped ($perc=97$) (B). Band-passed filtered inline seismic cross-section ($f=10,15,50,70$ | $amps=0,1,1,0$). Seismic data are gained ($tpow=1.8$) and clipped ($perc=97$) (C). Band-passed filtered inline seismic cross-section ($f=10,15,70,90$ | $amps=0,1,1,0$). Seismic data are gained ($tpow=1.8$) and clipped ($perc=97$) (D).

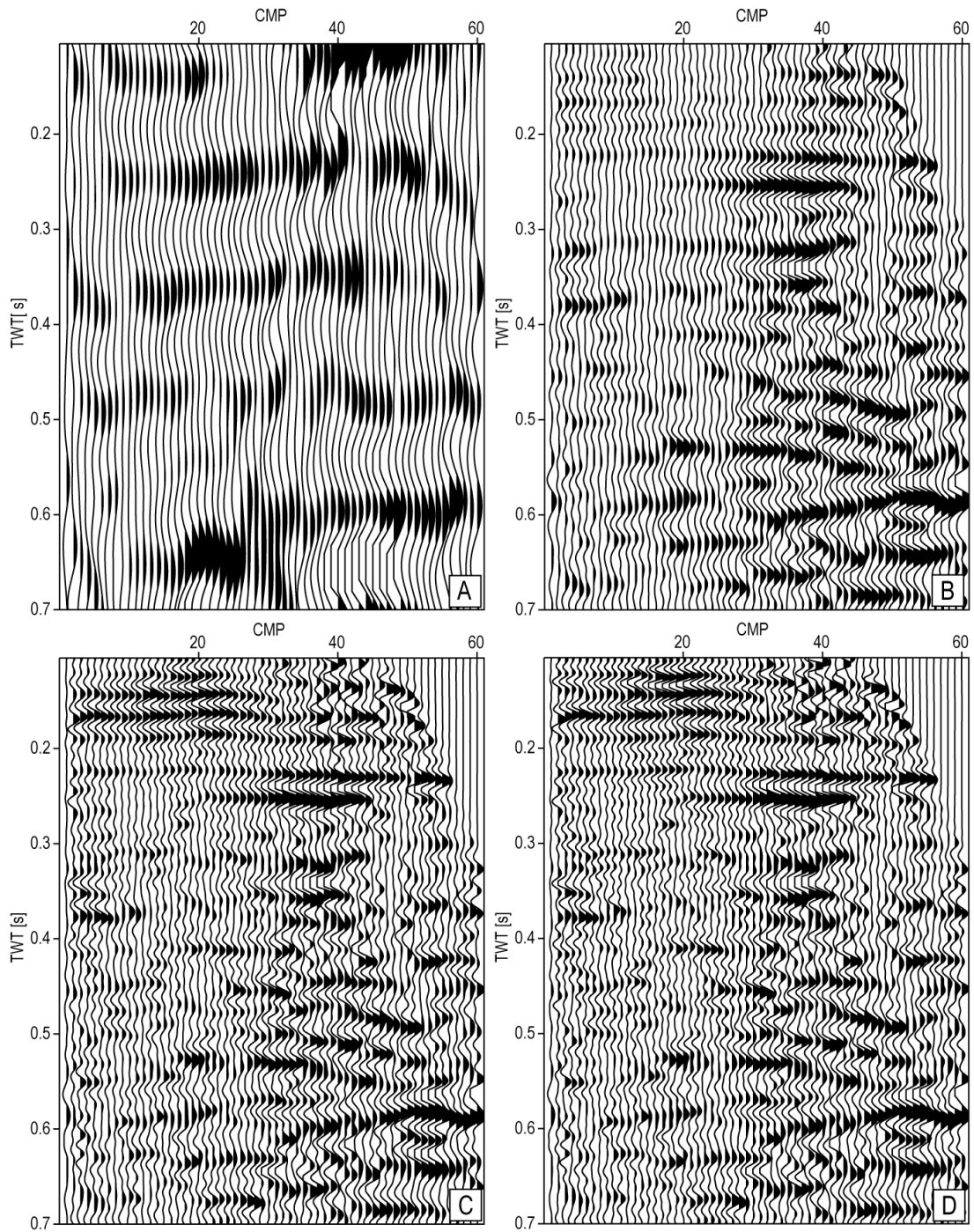


Figure 4.5. Low-pass filtered crossline seismic cross-section ($f=0,10,12$ | $amps=1,1,0$). Seismic data are gained ($tpow=1.8$) and clipped ($perc=97$) (A). Band-passed filtered crossline seismic cross-section ($f=10,15,30,50$ | $amps=0,1,1,0$). Seismic data are gained ($tpow=1.8$) and clipped ($perc=97$) (B). Band-passed filtered crossline seismic cross-section ($f=10,15,50,70$ | $amps=0,1,1,0$). Seismic data are gained ($tpow=1.8$) and clipped ($perc=97$) (C). Band-passed filtered crossline seismic cross-section ($f=10,15,70,90$ | $amps=0,1,1,0$). Seismic data are gained ($tpow=1.8$) and clipped ($perc=97$) (D).

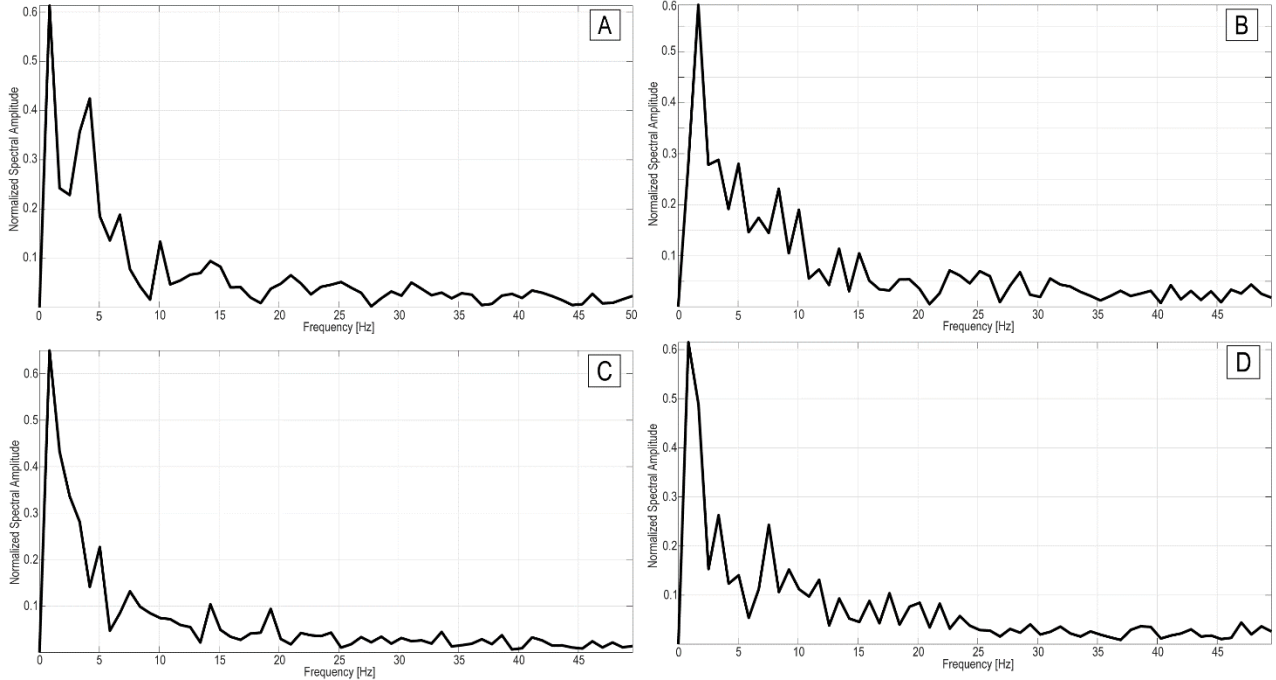


Figure 4.6. Low-frequency SI log 20 from the inline low-frequency SI model (A). Low-frequency SI log 40 from the inline low-frequency SI model (B). Low-frequency SI log 60 from the inline low-frequency SI model (C). Low-frequency SI log 80 from the inline low-frequency SI model (D).

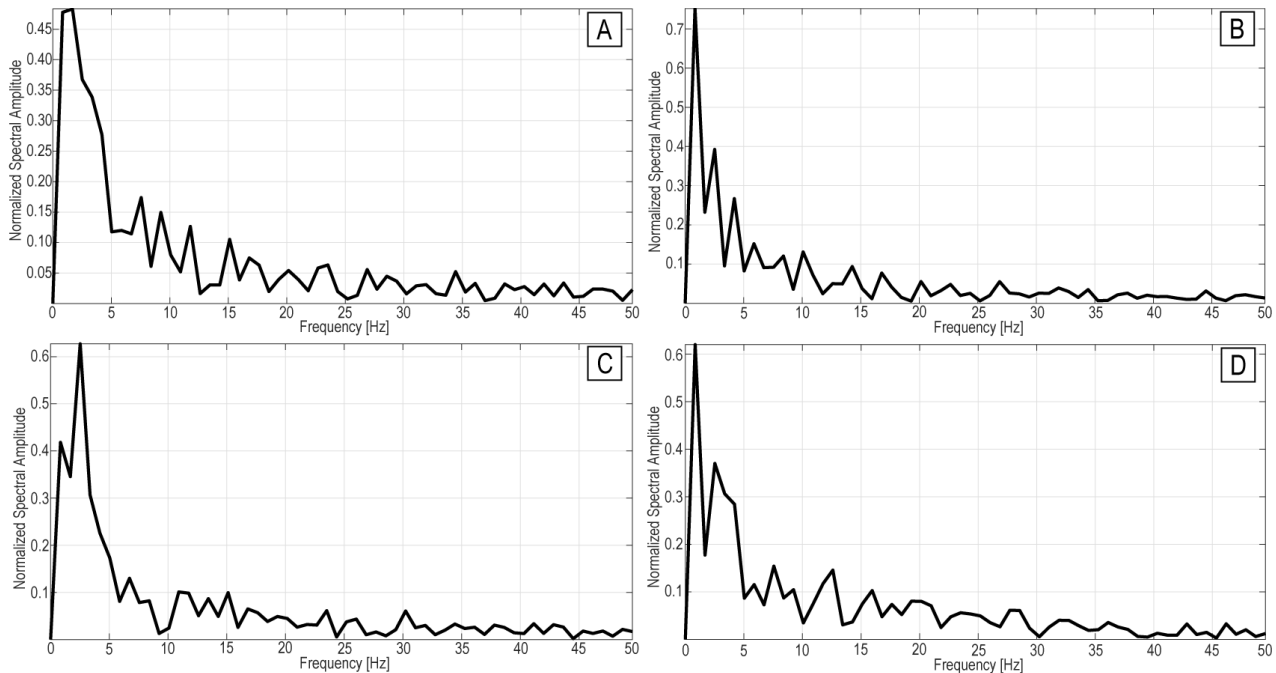


Figure 4.7. Low-frequency SI log 10 from the crossline low-frequency SI model (A). Low-frequency SI log 25 from the crossline low-frequency SI model (B). Low-frequency SI log 40 from the crossline low-frequency SI model (C). Low-frequency SI log 55 from the crossline low-frequency SI model (D).

(4.2.2) High-Cut Filter

High-frequencies are not present in low-frequency SI models, thus the only supplier of relatively higher frequency content is processed seismic data (Ferguson et al., 1997; Huck et al., 2010; Kroode et al., 2013).

I use the inline and crossline processed seismic cross-sections to provide mid to high-frequency data for BLIMP inversion. For the inline and crossline SI inversions, I set the cut-off filter for high frequency data at 90 Hz. Although power consistently decreases by orders of magnitude past 35 Hz (Figure 4.4 & 4.5), I still include bandwidth of low-power higher frequency data so as to capture as much detail as possible for the subsequent SI inversion (Lloyd 2013).

(4.2.3) Low-Frequency Impedance Model

Any low-frequency impedance model is naturally band-limited, therefore, the impedance values calculated from a model with limited frequency range is consequently band-limited (Cerney et al., 2007; Gholami 2016; Hendrick et al., 1993; Kroode et al., 2013).

The non-uniqueness associated with the low-frequency impedance models I use are identical to their corresponding V_{INT} model. Consequently, an error estimation for both the V_{INT} and low-frequency impedance models cannot be determined unless sonic well-log measurements are available (Cerney et al., 2007; Huck et al., 2010; Oldenburg et al., 1984).

Since error cannot be accurately calculated, I only evaluate the stability of BLIMP inversion with low-frequency impedance models by perturbing inline and crossline models. I evaluate the overall effect of low-frequency impedance models by testing their effect on BLIMP inversion output by applying constant perturbations to the inline and crossline models.

Each low-frequency impedance log from both the inline and crossline low-frequency impedance models are perturbed by $\pm 10.0\%$ (Figure 4.8) and subsequently incorporated for BLIMP inversion. Altogether, I perform separate tests whereby perturbed inversion results are compared to unperturbed results.

Perturbed inversion results are qualitatively similar to previously shown and accepted inversion results (Figure 4.9 & 4.10). Specifically, previously mapped SI horizons are still discernable and there is an overall increase of SI magnitude with time.

Comparing SI magnitudes confirms that there are large differences associated with perturbed inversion results (Figures 4.9 & 4.10) relative to unperturbed ones from the inline and crossline profiles. However, these large differences – whether comparatively smaller or larger – are expected. Indeed, BLIMP inversion results derived from an impedance model perturbed by -10% show a relative decrease in SI magnitude. Likewise, the 10% perturbed low-frequency impedance model results in a relative increase of SI magnitude in both the inline and crossline profiles. Both these expectations relate to the low-frequency impedance models associated with both the inline and crossline models.

Testing perturbed models confirms the stability of BLIMP inversion with different low-frequency model inputs.

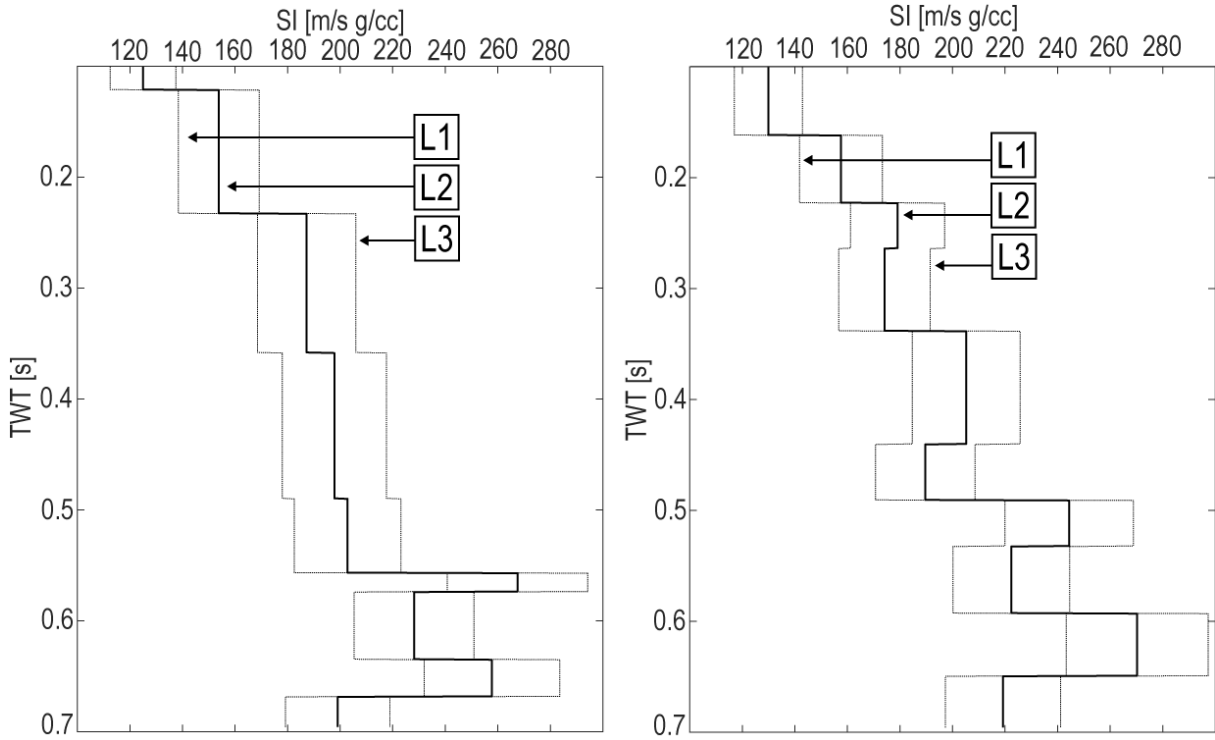


Figure 4.8. Low-frequency impedance logs that are perturbed by $\pm 10\%$. L2 is the original, unperturbed low-frequency impedance log 47 from the inline impedance model. L1 and L3 correspond to the -10% and $+10\%$ perturbed logs, respectively. Low-frequency impedance logs (right) that are perturbed by $\pm 10\%$. L2 is the original, unperturbed low-frequency impedance log 39 from the crossline impedance model. L1 and L3 correspond to the -10% and $+10\%$ perturbed logs, respectively.

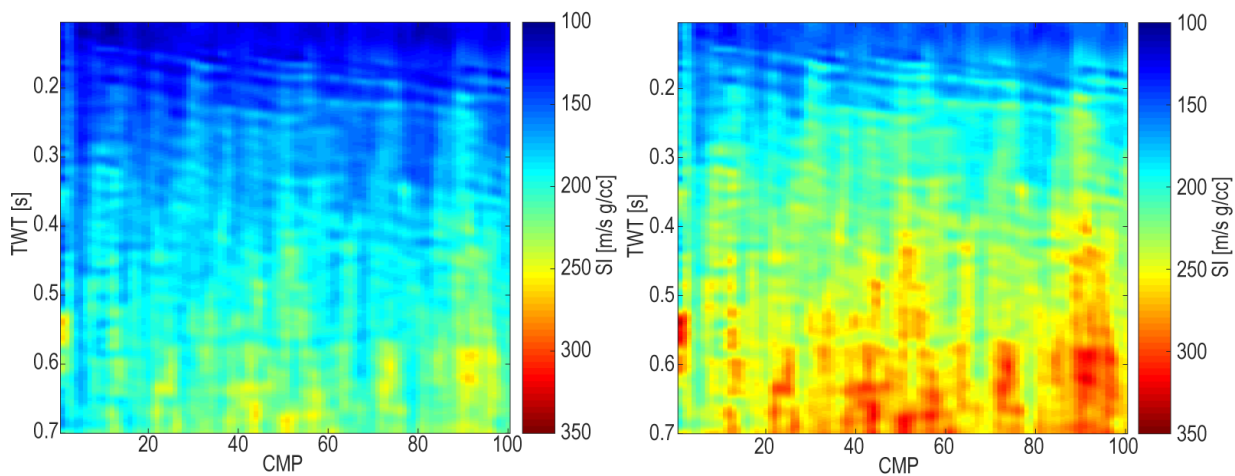


Figure 4.9. Inline inversion result (left) using a -10% perturbed low-frequency impedance model. Inline inversion result (right) using a $+10\%$ perturbed low-frequency impedance model.

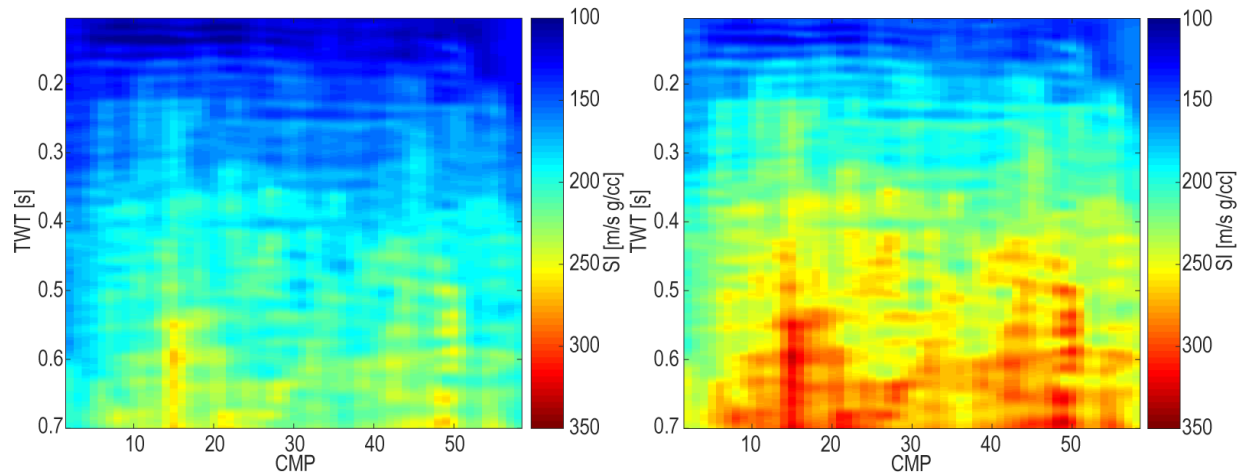


Figure 4.10. Crossline inversion result (left) using a -10% perturbed low-frequency impedance model. Crossline inversion result (right) using a +10% perturbed low-frequency impedance model.

(4.2.4) Seismic Amplitudes

I condition seismic amplitudes for inversion with gaining and a scalar wave equation divergence correction. The gain operation applied to seismic data is a $A(t)=A_0t^x$ (Section 8.7.5) algorithm whereby t is TWT and the x is the variable exponent assign by a user, A_0 is the initial seismic amplitude, and $A(t)$ is the modified amplitude. Most values of x range between 1.0 and 2.0 (Stockwell 1999). Also, performing the gaining operation is required for the subsequent divergence correction (Stockwell 1999). The scalar wave equation divergence correction (Section 8.8.1) modifies seismic amplitudes with respect to both time and velocity using V_{RMS} models. Seismic amplitude sensitivity analysis of the BLIMP algorithm is only tested by perturbing the t^x gaining function.

I perturb gaining parameters (Figure 4.11 – 4.12) to test the sensitivity of BLIMP to alterations of seismic amplitudes by comparing perturbed SI inversion results to those of benchmark SI results corresponding to amplitudes gained by $t^{1.8}$ and subsequently divergence-corrected by the raw V_{RMS} model.

Error analysis confirms that perturbing amplitudes by only the t^x function (i.e. $t^{1.3}$ and $t^{1.6}$) while keeping the divergence correction parameters (i.e. V_{RMS} model) unchanged results in negligible error (-6% – 5%) with an associated Gaussian distribution.

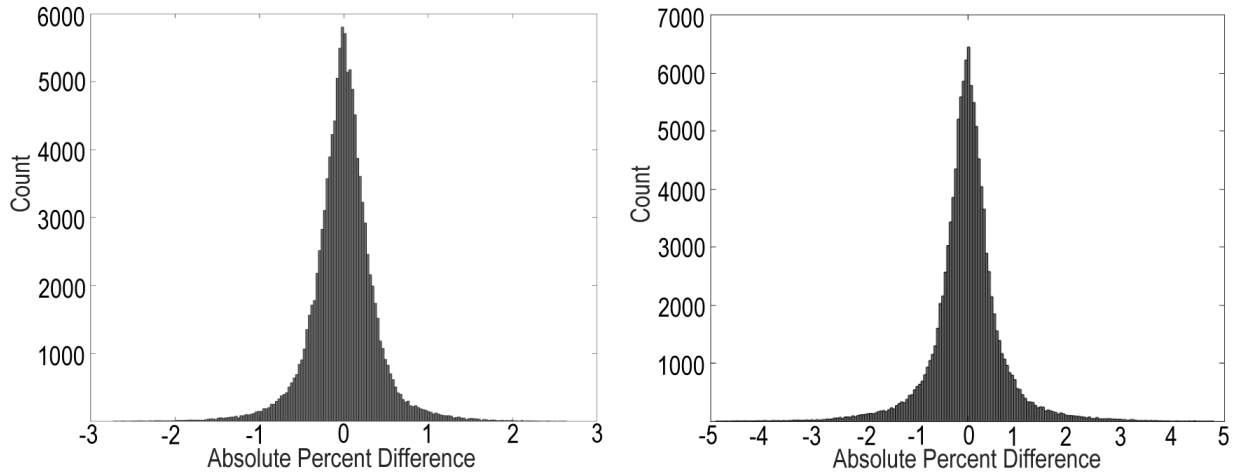


Figure 4.11. Histogram (left) displaying absolute percent difference of benchmark crossline SI inversion results compared to inline inversion results corresponding to amplitudes perturbed by $t^{1.3}$. Histogram (right) displaying absolute percent difference of benchmark inline SI inversion results compared to inline inversion results corresponding to amplitudes perturbed by $t^{1.6}$.

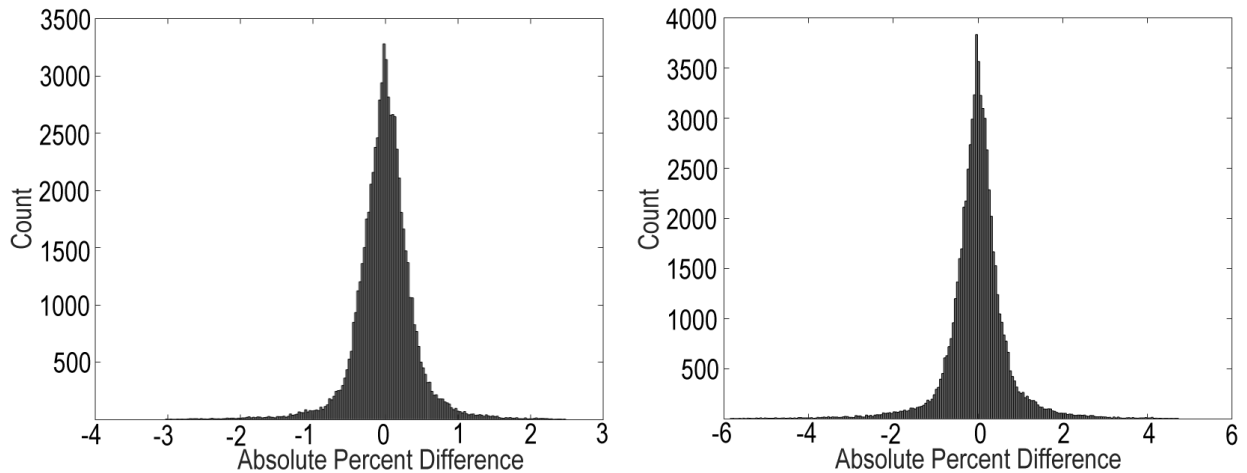


Figure 4.12. Histogram (left) displaying absolute percent difference of benchmark crossline SI inversion results compared to crossline inversion results corresponding to amplitudes perturbed by $t^{1.3}$. Histogram (right) displaying absolute percent difference of benchmark crossline SI inversion results compared to crossline inversion results corresponding to amplitudes perturbed by $t^{1.6}$.

CHAPTER 5: DISCUSSION

(5.1) The Architecture of a Near-Surface Point-Bar: Confirmation of Ideal Models

This study presents the first successful high-resolution SH-wave seismic reflection images of a near-surface downstream point-bar. Dipping seismic horizons of the inline cross-section are consistent with previous remote sensing studies and idealized point-bar models (Bridge et al., 1995b; Corbeanu et al., 2004; Ghinassi et al., 2015; Ghinassi et al., 2016). Likewise, the non-dipping character of most crossline section seismic horizons is also observed to other studies (Bridge et al., 1995b; Corbeanu et al., 2004; Musial et al., 2012). A previous investigation near our study area attempts to image an upstream point-bar with SH-wave seismic reflection surveying (Morrison 2017). No continuous reflectors are observed for that study. Despite the complexities associated with ancient fluvial erosional and depositional processes, this study succeeds in providing two high-resolution seismic images of architectural features associated with a downstream point-bar. This accomplishment is accentuated by the fact that the near-surface environment I analyze via seismic SH-waves is characterized by conductive, saturated, and unconsolidated sediments (Fisk 1944; Lechnowskyj 2015). In such a subsurface environment, both GPR and P-wave seismic reflection surveying would likely perform poorly (Bachrach et al., 1998b; Hildebrand et al., 2002).

Our seismic results confirm the expected dipping and non-dipping architecture of a near-surface downstream point-bar as well as demonstrate the usefulness of SH-wave seismic reflection surveying. To date, near-surface fluvial remote sensing studies have constrained their analyses to one that is purely qualitative. Namely, only the architectural image provided by either GPR or seismic surveying is interpreted. I use our seismic and inversion results to provide both qualitative and quantitative (i.e. SI) information to understand the architectural as well as physical properties associated with sediment packages associated with a near-surface downstream point-bar.

(5.2) Comparison of SI Between Sand & Clay-Rich Sediment Packages: Compaction/Dewatering Model

I observe an overall pattern of clay-rich sediment packages retaining a comparatively greater SI magnitude relative to sand-rich sediment packages.

Notable subsurface physical properties of sediments include pressure, grain size, density, packing, porosity, pore shape, pore pressure, pore fluid, volumetric water content, permeability, and rigidity (Crane 2013; Holland 1980; Santamarina et al., 2001; Yilmaz 1987). Although bulk density is an intrinsic material property and thereby affects seismic wave propagation to some extent, this study (Section 2.5.1) as well as others set bulk density as a unitary constant because seismic velocities are assumed to change more frequently and with greater magnitude than bulk density (Jarvis et al., 2002; Yilmaz 1987). Moreover, this study also proposes that the overall effect of packing, pressure, porosity, volumetric water content, and rigidity overshadows all other aforementioned physical properties in terms of influence on a dependent seismic property – seismic shear-impedance (SI).

The process of early-stage diagenesis alters many of the physical properties associated with saturated and unconsolidated sediments (Avseth et al., 2001; Holland

1980). I propose that early-stage diagenetic processes such as compaction and dewatering facilitate the change of pressure, porosity, volumetric water content, and rigidity of sand and clay-rich sediments (Avseth et al., 2005b; Holland 1980). As an overall effect of these early-stage diagenetic physical processes, the SH-wave seismic velocity of clay-rich sediments is greater relative to sand-rich sediments.

Previous studies report that clay-rich sediments can retain a greater S-wave seismic velocity compared to sand-rich sediments owing to both compaction and dewatering (Odum et al., 2004; Solberg et al., 2012). Compaction models set in the context of early-stage diagenesis have existed for decades (Englehardt 1977; Holland 1980). In these models, the overall behavior of sand- and clay-rich sediments during compaction and subsequently dewatering is different mainly due to initial packaging (Holland 1980). The initial packing of clay-rich sediments leads to a comparatively rapid and continual drop of porosity compared to sand-rich sediments, which experience minimal particle re-orientation in near-surface environments during compaction (Figure 5.1) (Holland 1980). Indeed, this cause and effect phenomenon is referred to as collapsing the "house of cards" (Englehardt 1977). An effect such as this must greatly affect seismic S-wave propagation (Hunter et al., 1998). The relatively lower porosity and increase of stable grain-to-grain contacts results in near-surface (~1 – 30 m) clay-rich sediments retaining a greater rigidity compared to sand-rich sediments (Englehardt 1977; Holland 1980; Mondol et al., 2008). Moreover, because near-surface (~1 – 30 m) sand-rich sediments are saturated, unconsolidated, and likely have undergone little to no diagenesis, the rigidity at grain-to-grain contacts is significantly low (Avseth et al., 2005a).

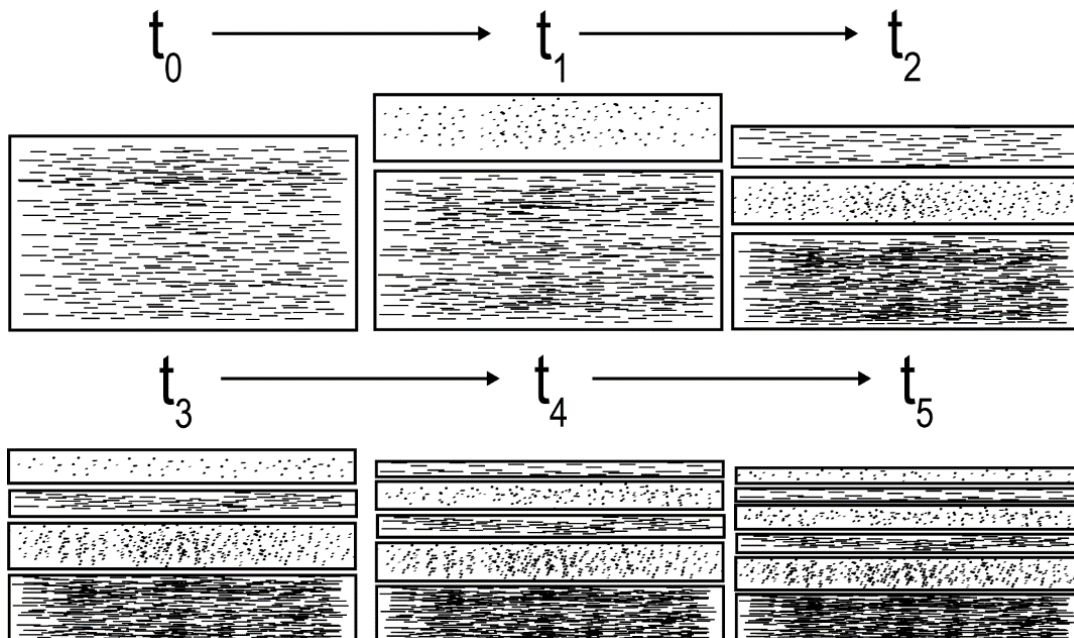


Figure 5.1. The process of compaction occurring at six arbitrarily discrete time intervals. The first (t_0) shows the initial deposition of a clay-rich sediment package. In t_1 , a sand-rich sediment package is deposited atop the clay and compaction begins. Overall, the thickness of each package is reduced with an accompanied increase of grain-to-grain contact, especially for clay-rich sediment packages.

During compaction and the corresponding increase of pressure, dewatering of sediment packages occurs (Lambe et al., 1969; Odum et al., 2004). As long as expelled fluids (i.e. water) can migrate vertically and/or laterally, dewatering leads to partial reduction of volumetric water content (Figure 5.2) (Burst 1976; Holland 1980). Alternating sand-rich sediment packages above and/or below clay-rich sediments allow for migration of water from the clays. To a degree, water saturation may increase the rigidity of clay (Figure 5.3) (Andrade et al., 2011). I assume that water saturation associated with clay-rich sediment packages resides between the plastic limit (PL) and the liquid limit (LL) (Figure 5.3). I also assume that clay-rich sediment packages retain enough water to reside within the plasticity index (PI) and retain a higher shear resistance (i.e. rigidity) compared to sand-rich sediment packages (Andrade et al., 2011; Mainsant et al., 2012). The argument can be made that these assumptions are based on high-strain theory, so they cannot be reasonably connected to this study as seismics usually involve low-strain regimes (Ikelle et al., 2005b). However, previous seismic laboratory research refers to such terms as PL, LL, and PI to study fluid saturation and pressure effects on rigidity of clay (Mainsant et al., 2012).

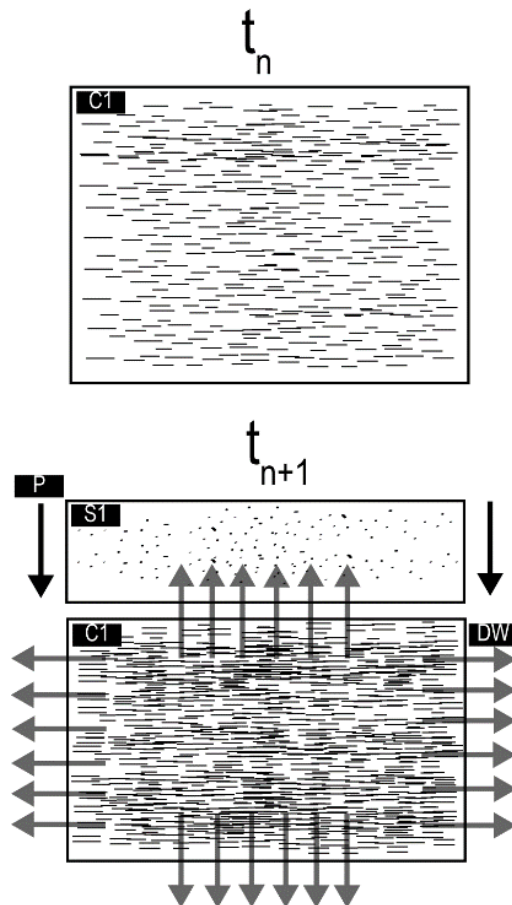


Figure 5.2. The process of compaction (increase of pressure P) facilitates dewatering (DW) and the corresponding reduction of volumetric water content. The laterally and vertically emanating arrows on all sides of C1 represent fluid flow paths. S1 is an abbreviation for sand-rich sediment package one, and C1 is an abbreviation for clay-rich sediment package one.

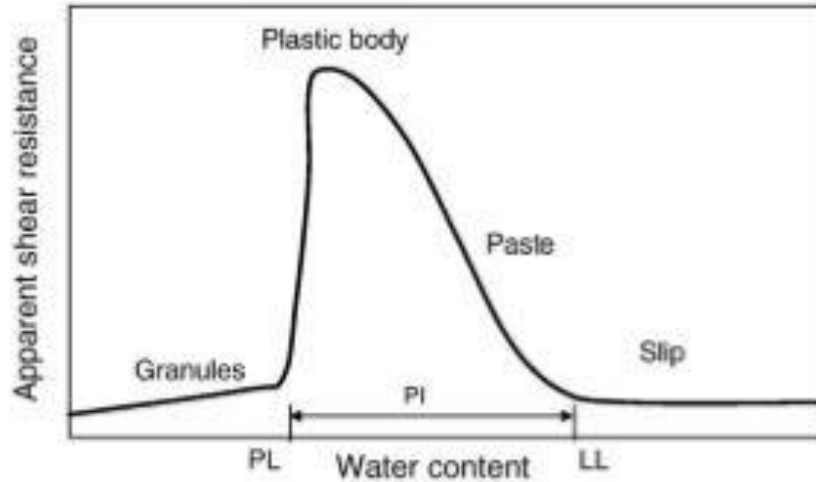


Figure 5.3. Within the range defined by the plasticity index (PI), relative increases of water content increases the apparent shear resistance (or rigidity) of clay until it reaches a paste state. This figure is adopted from Andrade et al. (2011).

In summary, due to initial packing, the process of compaction facilitates an increase of pressure and thereby reduces the porosity of near-surface clay-rich sediments more so compared to sand-rich sediments. Moreover, as compaction occurs, dewatering transpires and subsequently results in residual water content in near-surface clay-rich sediments. Both the porosity reduction and residual water content jointly develop the comparatively greater rigidity associated with clay-rich sediment packages. This results in a relatively higher SH-wave seismic velocity compared to sand-rich sediment packages, which also translates to a greater SI.

(5.3) Dominant Causes & Implications of Well-Log Misalignments

I observe that some SI curves do not correspond well to EC data. This observation may be slightly attributable to ubiquitous seismic physical phenomenon including tuning, wavelet effects, and focusing/defocusing (Khaidukov et al., 2004; Widess 1973; Yilmaz 1987). However, I believe the aforementioned causes are comparatively minor relative to three other causes: time-to-depth conversion as well as lateral stratigraphic variability and uncertainty.

During time-to-depth conversions, I compute the arithmetic mean of each V_{INT} model with respect to each sample (row) for all traces (columns). As a result, an overall error ranging from -35 – 30% was generated throughout each of the averaged inline and crossline depth-conversion models (Section 4.1).

There is always some degree of misalignment of well data to seismic and consequently impedance data due to the error associated with depth-conversion model (Etris et al., 2002). This unavoidable error combined with limitations of our tools (Section 8.8.2) and its detrimental effects results in slight bulk shift (~0.5 – 1.3 m) of SI curves relative to EC data.

CHAPTER 6: CONCLUSIONS & RECOMMENDATIONS

(6.1) Conclusions

Two SH-wave seismic reflection surveys are conducted atop a near-surface downstream point-bar at False River (Pointe Coupee Parish, Louisiana). The inline survey is orientated approximately parallel to the nearby well locations but orthogonal to paleochannel. However, the crossline survey is situated parallel to paleochannel. Seismic data are acquired and processed to provide high-resolution imagery of sand- and clay-rich sediment packages within the point-bar as well as to condition seismic amplitudes for the purposes of band-limited impedance inversion, which deterministically calculates SI. Depth-converted SI profiles are subsequently compared to nearby EC well-logs so as to facilitate a seismic-to-geology connection.

The inline seismic section shows dipping strata associated with sand- and clay-rich sediment packages extending towards paleochannel thalweg. However, the crossline seismic section exhibits little to no dip as this survey is oriented parallel to paleochannel. Indeed, the crossline seismic section offers a new and better perspective of point-bar architecture set parallel to paleochannel. These results confirm ideal downstream point-bar models and thereby demonstrate that using SH-wave seismic reflection imaging is advantageous compared to other remote surveying methods for near-surface environments characterized by conductive, saturated, and/or unconsolidated sediments.

Inline and crossline SI profiles show similarity to their corresponding seismic cross-sections. Namely, positive seismic amplitudes of sections match relative increases of SI on both profiles. Likewise, negative amplitudes match decreases of SI on both the inline and crossline profiles.

Comparing the geology (i.e. sand- and clay-rich sediments) inferred from EC well-logs to depth-converted inline and crossline SI profiles confirms that increases of SI usually correspond to clay-rich sediment packages. Likewise, relative decreases of SI generally indicates sand-rich sediment packages.

The overall pattern between SI and clay/sand-rich sediments may be rationalized via an early-stage diagenesis model. Physical properties corresponding to sand- and clay-rich sediment packages such as pressure, porosity, volumetric water content, and rigidity are variably altered during early-stage diagenetic processes such as compaction and dewatering. Compaction increases pressure and reduces porosity of clay-rich sediments significantly more compared to sand-rich sediments. Moreover, compaction facilitates the process of dewatering, which reduces the degree of volumetric water content in clay-rich sediments. Both the volumetric water content and reduction of porosity subsequently increases the overall rigidity of clay-rich sediments more than sand-rich sediments. The rigidity increase facilitates a comparatively greater SH-wave seismic velocity, and therefore a higher SI magnitude of clay-rich sediment packages.

This study demonstrates that SH-wave seismic reflection surveying can provide high-resolution imagery of near-surface environments where other remote sensing methods poorly perform. Seismic results corresponding to the crossline survey provide a new and useful perspective of point-bar architecture. Also, our results confirm ideal downstream point-bar models, and rationalize how early-stage diagenetic processes such as compaction and dewatering are likely the primary casual mechanisms that

develop the seismic impedance properties associated with downstream near-surface point-bars sediment packages. Incorporating an early-stage diagnosis model may be advantageous for other studies attempting to both qualitatively and quantitatively assess near-surface fluvial point-bars.

(6.2) Recommendations

1. Extend the inline seismic survey to examine the lateral extent of deeper dipping point-bar architecture towards paleochannel thalweg and to possibly analyze via SI profiles how shear impedance for a given sediment package changes with depth.
2. Employ more sophisticated seismic inversion algorithms and workflows that compensate for wavelet effects (i.e. probabilistic/stochastic methods). Wavelet in this context refers to the seismic source signature and not a type of spectral analysis
3. Develop better means of time-to-depth conversion by automating a trace-by-trace resampling algorithm for depth-converted traces that equalizes all number of samples (ns) for each trace in a section.
4. Configure work for the purposes of assessing geohazards for civil and geotechnical applications.

CHAPTER 7: REFERENCES

- Aki, K., and P. G. Richards. 1980, Quantitative seismology. Edited by A. Cox. 2 vols. Vol. 1, A series of books in Geology: W. H. Freeman and Co.
- Andrade, F. A.; H. A. Al-Qureshi, and D. Hotza. 2011, Measuring the plasticity of clays: A review. *Applied Clay Science*, **51**, no. 1-2,1-7. doi: 10.1016/j.clay.2010.10.028.
- Arya, V. K., and H. D. Holden. 1978, Deconvolution of seismic data-an overview. *IEEE Transactions on Geoscience Electronics*, **16**, no. 2,95-98.
- Avseth, P., and R. Bachrach. 2005a, Seismic properties of unconsolidated sands: Tangential stiffness, V_p/V_s ratios and diagenesis. Houston: Society of Exploration Geophysicists.
- Avseth, P.; G. Mavko; J. Dvorkin, and T. Mukerji. 2001, Rock physics and seismic properties of sands and shales as a function of burial depth. In *SEG Technical Program Expanded Abstracts 2001*.
- Avseth, P.; T. Mukerji, and G. Mavko. 2005b, *Quantitative seismic Interpretation: Applying rock physics tools to reduce interpretation risk*: Cambridge.
- Bachrach, R.; J. Dvorkin, and A. Nur. 1998a, High-resolution shallow-seismic experiments in sand, Part II: Velocities in shallow unconsolidated sand. *Geophysics*, **63**, no. 4,1234-1240.
- Bachrach, R., and T. Mukerji. 2001, Fast 3D ultra shallow seismic reflection imaging using portable geophone mount. *Geophysical Research Letters*, **28**, no. 1,45-48. doi: 10.1029/2000gl012020.
- Bachrach, R., and A. Nur. 1998b, Same wavelength GPR and ultra shallow reflection on a river point bar: Sand stratigraphy and water table complexity.
- Bachrach, R., and A. Nur. 1998c, Ultra Shallow Seismic Reflection in Unconsolidated Sediments: Rock Physics base for data acquisition.
- Bachrach, R., and A. Nur. 1998d, Ultra shallow seismic reflection in unconsolidated sediments: Rock physics base for data acquisition, *SEG Technical Program Expanded Abstracts 1998*: Society of Exploration Geophysicists. 866-869.

- Becquey, M.; M. Lavergne, and C. Willm. 1979, Acoustic impedance logs computed from seismic traces. *Geophysics*, **44**, no. 9.
- Beilecke, T.; C. M. Krawczyk; J. Ziesch, and D. C. Tanner. 2016, Near-surface fault detection using high-resolution shear wave reflection seismics at the CO2CRC Otway Project site, Australia. *Journal of Geophysical Research: Solid Earth*, **121**, no. 9,6510-6532. doi: 10.1002/2015jb012668.
- Berteussen, K. A., and B. Ursin. 1983, Approximate computation of the acoustic impedance from seismic data. *Geophysics*, **48**, no. 10,1315-1358.
- Bleistein, N.; J. K. Cohen, and J. W. Stoackwell. 2001, *Mathematics of Multidimensional Seismic Imaging, Migration, and Inversion* Edited by J. E. Marsde, L. Sirovich and S. Wiggins: Springer-Verlag.
- Bowling, J. C.; D. L. Harry; A. B. Rodriguez, and C. Zheng. 2007, Integrated geophysical and geological investigation of a heterogeneous fluvial aquifer in Columbus Mississippi. *Journal of Applied Geophysics*, **62**, no. 1,58-73. doi: 10.1016/j.jappgeo.2006.08.003.
- Bridge, J. S.; J. Alexander; R. E. Collier; R. L. Gawthorpe, and J. Jarvis. 1995a, Ground-penetrating radar and coring used to study the large-scale structure of point-bar deposits in three dimensions. *Sedimentology*, **42**,839-852.
- Bridge, J. S.; J. Alexander; R. E. Collier; R. L. Gawthorpe, and J. Jarvis. 1995b, Ground-penetrating radar and coring used to study the large-scale structure of point-bar deposits in three dimensions. *Sedimentology*, **42**, no. 6,839-852.
- Brown, A. R. 2001, Calibrate yourself to your data! A vital first step in seismic interpretation. *Geophysical Prospecting*, **49**,729-733.
- Büker, F.; A. G. Green, and H. Horstmeyer. 1998, Shallow 3-D seismic reflection surveying: Data acquisition and preliminary processing strategies. *Geophysics*, **63**, no. 4,1434-1450.
- Burger, H. R. 1992, *Exploration geophysics of the shallow subsurface*: Prentice Hall.
- Burst, J. F. 1976, Argillaceous sediment dewatering *Ann. Re. Earth Planet. Sci.*, **4**,293-318.

- Cardarelli, E.; M. Cercato, and G. D. Donno. 2014, Characterization of an earth-filled dam through the combined use of electrical resistivity tomography, P- and SH-wave seismic tomography and surface wave data. *Journal of Applied Geophysics*, **106**,87-95.
- Carr, B. J.; Z. Hajnal, and A. Prugger. 1998, Shear-wave studies in glacial till. *Geophysics*, **63**, no. 4,1273-1284.
- Cerney, B., and D. Bartel. 2007, Uncertainties in low-frequency acoustic impedance models. *The Leading Edge*, **26**, no. 1,74-87.
- Cha, M.; J. C. Santamarina; H.-S. Kim, and G.-C. Cho. 2014a, Small-Strain Stiffness, Shear-Wave Velocity, and Soil Compressibility. *Journal of Geotechnical and Geoenvironmental Engineering*, **140**, no. 10,06014011. doi: 10.1061/(asce)gt.1943-5606.0001157.
- Cha, M.; J. C. Santamarina; H.-S. Kim, and G.-C. Cho. 2014b, Small-Strain Stiffness, Shear-Wave Velocity, and Soil Compressibility. *Journal of Geotechnical and Geoenvironmental Engineering*, **140**, no. 10. doi: 10.1061/(asce)gt.1943-5606.0001157.
- Choi, K. S.; R. W. Dalrymple; S. S. Chun, and S.-P. Kim. 2004, Sedimentology of modern, inclined heterolithic stratification (IHS) in the macrotidal Han River delta, Korea. *Journal of Sedimentary Research*, **74**, no. 5,677-689.
- Clift, P. D. 2016, Facies Variability in a Large-Scale Mississippi River Point Bar, False River, Louisiana, USA.
- Cooke, D., and J. Cant. 2010, Model-based Seismic Inversion: Comparing deterministic and probabilistic approaches. *CSEG Recorder*.
- Corbeanu, R. M.; M. C. Wizevich; J. P. Bhattacharya; X. Zeng, and G. A. McMechan. 2004, Three-dimensional architecture of ancient lower delta-plain point bars using ground-penetrating radar, Cretaceous Ferron Sandstone, Utah. *The Fluvial-Deltaic Ferron Sandstone: Regional-to-Wellbore-Scale Outcrop Analog Studies and Applications to Reservoir Modeling*.
- Cox, M. 1999, *Static Corrections for Seismic Reflection Surveys*. Vol. 9: Society of Exploration Geophysicists.

- Crane, J. M. 2013, Effects of stress and water saturation on seismic velocity and attenuation in near-surface sediments
- Davidson, A. T. 1985, The Historical Geomorphology of Active Point Bars on the Lower Mississippi River From Red River Landing to Plaquemine, Louisiana The University of Louisiana
- Davies, D. K. 1966, Sedimentary structures and subfacies of a Mississippi River point bar. *The Journal of Geology*, **74**, no. 2,234-239.
- Deidda, G. P., and R. Balia. 2001, An ultrashallow SH-wave seismic reflection experiment on a subsurface ground model. *Geophysics*, **66**, no. 4,1097-1104.
- Durkin, P. R.; R. L. Boyd; S. M. Hubbard; A. W. Shultz, and M. D. Blum. 2017, Three-Dimensional Reconstruction of Meander-Belt Evolution, Cretaceous McMurray Formation, Alberta Foreland Basin, Canada. *Journal of Sedimentary Research*, **87**, no. 10,1075-1099. doi: 10.2110/jsr.2017.59.
- Englehardt, W. V. 1977, *The Origin of Sediments and Sedimentary Rocks* Halstead Press.
- Etris, E. L.; N. J. Crabtree, and J. Dewar. 2002, True Depth Conversion: More Than a Pretty Picture. *Recorder*, **26**, no. 9.
- Farrell, K. M. 1987, Sedimentology and facies architecture of overbank deposits of the Mississippi River, False River region, Louisiana.
- Ferguson, R. J. 1996, *P-S Seismic Inversion: Modeling, Processing, and Field Examples*, University of Calgary.
- Ferguson, R. J., and G. Margrave. 1997, A simple algorithm for band-limited impedance inversion. *CREWES Res. Rep.*, **8**.
- Fisk, H. N. 1944, Geological investigation of the alluvial valley of the lower Mississippi River, Mississippi River Commission: War Dept.
- Frazier, D. E., and A. Osanik. 1961, Point-bar deposits, Old River Locksite, Louisiana.

- Fustic, M.; S. M. Hubbard; R. Spencer; D. G. Smith; D. A. Leckie; B. Bennett, and S. Larter. 2012, Recognition of down-valley translation in tidally influenced meandering fluvial deposits, Athabasca Oil Sands (Cretaceous), Alberta, Canada. *Marine and Petroleum Geology*, **29**, no. 1,219-232. doi: 10.1016/j.marpetgeo.2011.08.004.
- Gawthorpe, R. L.; R. E. Collier; J. Alexander; J. S. Bridge, and M. R. Leeder. 1993, Ground penetrating radar: application to sand body geometry and heterogeneity studies. *The Geological Society of London* 421-432.
- Ghinassi, M., and A. Ielpi. 2015, Stratal Architecture and Morphodynamics of Downstream-Migrating Fluvial Point Bars (Jurassic Scalby Formation, U.K.). *Journal of Sedimentary Research*, **85**, no. 9,1123-1137. doi: 10.2110/jsr.2015.74.
- Ghinassi, M.; A. Ielpi; M. Aldinucci, and M. Fustic. 2016, Downstream-migrating fluvial point bars in the rock record. *Sedimentary Geology*, **334**,66-96. doi: 10.1016/j.sedgeo.2016.01.005.
- Gholami, A. 2016, A fast automatic multichannel blind seismic inversion for high-resolution impedance recovery. *Geophysics*, **81**, no. 5,357-364.
- Gray, S. H. 1997, True-amplitude seismic migration: A comparison of three approaches. *Geophysics*, **62**, no. 3,929-936.
- Grote, K.; S. Hubbard, and Y. Rubin. 2003, Field-scale estimation of volumetric water content using ground-penetrating radar ground wave techniques. *Water Resources Research*, **39**, no. 11. doi: 10.1029/2003wr002045.
- Guevara, S.-E.; D. Rueda; N. García; C. Becerra; Y. Figueredo, and A. Plata. 2010, Seismic and lithological near surface characteristics of an area in north-east Colombia. *CT&F-Ciencia, Tecnología y Futuro*, **4**, no. 1,7-21.
- Guy, E. 2006, High-resolution P-and S-wave seismic reflection investigation of a shallow stratigraphic sequence. *Electronic Journal of Geotechnical Engineering*, **11**,37.
- Haines, S. S., and K. J. Ellefsen. 2010, Shear-wave seismic reflection studies of unconsolidated sediments in the near surface. *Geophysics*, **75**, no. 2,B59-B66.

- Hanahan, P. M. 1948, Explosives Accidents on Geophysical Crews. *Geophysics*, **13**, no. 3,421-427.
- Harms, J. C.; J. B. Southard, and R. G. Walker. 1982, Fluvial deposits and facies models.
- Hasbrouck, W. P. 1991, Four shallow-depth, shear-wave feasibility studies. *Geophysics*, **56**, no. 11,1875-1885.
- Hendrick, N., and S. Hearn. 1993, Evaluation of Seismic Trace Inversion Techniques. *Explor. Geophys.*, **24**,549-560.
- Hildebrand, J. A.; S. M. Wiggins; P. C. Henkart, and L. B. Conyers. 2002, Comparison of seismic reflection and ground-penetrating radar imaging at the controlled archaeological test site, Champaign, Illinois. *Archaeological Prospection*, **9**, no. 1,9-21. doi: 10.1002/arp.177.
- Holland, H. D. 1980, *Early Diagenesis: A Theoretical Approach*: Princeton University Press
- Huck, A.; G. Quiquerez, and P. de Groot. 2010, Improving Seismic Inversion through Detailed Low Frequency Model Building. In 72nd EAGE Conference and Exhibition incorporating SPE EUROPEC 2010.
- Hunter, J. A.; S. E. Pullan; R. A. Burns; R. M. Gagne, and R. L. Good. 1984, Shallow seismic reflection mapping of the overburden-bedrock interfaces with the engineering seismograph - Some simple techniques. *Geophysics*, **49**, no. 8,1381-1385.
- Hunter, J. A.; S. E. Pullan; R. A. Burns; R. L. Good; J. B. Harris; A. J. M. Pugin; A. Skvortsov, and N. N. Goriainov. 1998, Downhole seismic logging for high-resolution reflection surveying in unconsolidated overburden. *Geophysics*, **63**, no. 4,1371-1384.
- Ielpi, A.; M. Ghinassi, and N. Mountney. 2014, Planform architecture, stratigraphic signature and morphodynamics of an exhumed Jurassic meander plain (Scalby Formation, Yorkshire, UK). *Sedimentology*, **61**, no. 7,1923-1960. doi: 10.1111/sed.12122.

- Ikelle, and Amundsen. 2005a, Introduction to Petroleum Seismology. Vol. 12, Investigations in Geophysics.
- Ikelle, L. T., and L. Amundsen. 2005b, Introduction to Petroleum Seismology. Edited by M. Cooper. 1 ed. 1 vols. Vol. 12, Investigations in Geophysics: Society of Exploration Geophysicists.
- Inazaki, T., and K. Hayashi. 2011, Utilization of Integrated Geophysical Surveying for the Safety Assessment of Levee Systems. Society of Exploration Geophysicists,370-378.
- Jarvis, K. D., and R. J. Knight. 2002, Aquifer heterogeneity from SH-wave seismic impedance inversion. Geophysics, **67**, no. 5,1548-1557.
- Julien, P. Y. 2002, River Mechanics Edited by Pierre Y. Julien: Cambridge University Press
- Kasvi, E.; M. Vaaja; P. Alho; H. Hyyppä; J. Hyyppä; H. Kaartinen, and A. Kukko. 2013, Morphological changes on meander point bars associated with flow structure at different discharges: MORPHOLOGICAL CHANGES ON MEANDER POINT BARS. Earth Surface Processes and Landforms, **38**, no. 6,577-590. doi: 10.1002/esp.3303.
- Khaidukov, V.; E. Landa, and T. J. Moser. 2004, Diffraction imaging by focusing-defocusing: An outlook on seismic superresolution. Geophysics, **69**, no. 6,1478-1490. doi: 10.1190/1.1836821.
- Knight, R. J., and A. L. Endres. 2005, An Introduction to Rock Physics Principles for Near-Surface Geophysics, in Dwain K. Butler, ed., Investigations in Geophysics No. 13 - Near-Surface Geophysics Society of Exploration Geophysics 756.
- Krawczyk, C.; U. Polom, and T. Beilecke. 2013a, Shear-wave reflection seismics as a valuable tool for near-surface urban applications. The Leading Edge, **March 2013**.
- Krawczyk, C. M.; U. Polom, and T. Beilecke. 2013b, Shear-wave reflection seismics as a valuable tool for near-surface urban applications. The Leading Edge.

- Krohn, C. E., and T. J. Murray. 2016, Shallow near-surface effects. *Geophysics*, **81**, no. 5, T221-T231.
- Kroode, F. t.; S. Bergler; C. Corsten; J. W. Maag; F. Strijbos, and H. Tjihof. 2013, Broadband seismic data — The importance of low frequencies. *SEG*, **78**, no. 2, WA3-WA14.
- L'Heureux, J.-S., and M. Long. 2017, Relationship between Shear-Wave Velocity and Geotechnical Parameters for Norwegian Clays. *Journal of Geotechnical and Geoenvironmental Engineering*, **143**, no. 6, 04017013. doi: 10.1061/(asce)gt.1943-5606.0001645.
- Labrecque, P. A.; S. M. Hubbard; J. L. Jensen, and H. Nielsen. 2011, Sedimentology and stratigraphic architecture of a point bar deposit, Lower Cretaceous McMurray Formation, Alberta, Canada. *Bulletin of Canadian Petroleum Geology*, **59**, no. 2, 147-171.
- Lambe, T. W., and R. V. Whitman. 1969, *Soil Mechanics* Edited by T. William Lambe and Robert V. Whitman, Series in Soil Engineering John Wiley & Sons.
- Latimer, R. B.; R. Davidson, and P. Van Riel. 2000, An interpreter's guide to understanding and working with seismic-derived acoustic impedance data. *The Leading Edge*, **19**, no. 3, 242-256.
- Lavergne, M., and C. Willm. 1977, INVERSION OF SEISMOGRAMS AND PSEUDO VELOCITY LOGS. *European Association of Geoscientists and Engineers*, **25**, no. 2, 231-250.
- Lechnowskyj, A. N. 2015, THE STRATAL ARCHITECTURE OF THE FALSE RIVER POINT BAR (LOWER MISSISSIPPI RIVER, LA), Louisiana State University.
- Lindseth, R. O. 1976, Seislog process uses seismic reflection traces. *The oil and gas journal*, **74**, no. 43, 67-71.
- Lindseth, R. O. 1979, Synthetic sonic logs—A process for stratigraphic interpretation. *Geophysics*, **44**, no. 1, 3-26.
- Liner, C. 2004, *Elements of 3D Seismology* Edited by Marla Patterson. Vol. 2: PennWell Corporation

- Lloyd, H. J. E. 2013, An Investigation of the Role of Low Frequencies in Seismic Impedance Inversion, University of Calgary.
- Lloyd, H. J. E., and G. Margrave. 2012, Acoustic impedance inversion using stacking velocities: Hussar example. In CREWES Research Report. Calgary, Canada: University of Calgary.
- Mainsant, G.; D. Jongmans; G. Chambon; E. Larose, and L. Baillet. 2012, Shear-wave velocity as an indicator for rheological changes in clay materials: Lessons from laboratory experiments. *Geophysical Research Letters*, **39**, no. 19, n/a-n/a. doi: 10.1029/2012gl053159.
- Maulana, Z. L.; O. D. Saputro, and F. D. E. Latief. 2016, New Modified Band Limited Impedance (BLIMP) Inversion Method Using Envelope Attribute. *IOP Conference Series: Earth and Environmental Science*, **29**, 012009. doi: 10.1088/1755-1315/29/1/012009.
- Mauring, E., and J. S. Ronning. 1995, Combined use of common depth point and common offset techniques in shallow reflection seismics. NGU.
- Maxwell, P., and M. Lansley. 2012, What receivers will we use for low frequencies? CGGVeritas.
- Mayne, W. H. 1962, Common reflection point horizontal stacking techniques. *Geophysics*, **27**, no. 6, 927-938.
- McCann, D. M.; P. D. Jackson, and P. J. Fenning. 1988, Comparison of the seismic and ground probing radar methods in geological surveying. *IEEE Transactions on Geoscience Electronics*, **135**, no. 4.
- Mestan, J. 2015, Land Seismic Sources in Exploration Seismology, Ludwig-Maximilians-University of Munich.
- Miall, A. 2014, The Facies and Architecture of Fluvial Systems, *Fluvial Depositional Systems*: Springer International Publishing. 9-68.
- Michaels, P. 1996, The anomalous behavior of SH-waves across the water table In *Symposium on the Application of Geophysics to Engineering and Environmental Problems* Environmental and Engineering Geophysical Society

- Miller, R. D.; S. E. Pullan; D. W. Steeples, and J. A. Hunter. 1989, Field Comparison of Shallow Seismic Sources near Chino, California. Society of Exploration Geophysicists.
- Miller, R. D.; S. E. Pullan, and J. S. Waldner. 1986, Field comparisons of shallow seismic sources. *GEOPHYSICS*, **51**, no. 2,2067-2092.
- Miller, R. D.; D. W. Steeples; C. Somanas, and P. B. Myers. 1988, Detecting voids in a 0.6 m coal seam, 7 m deep, using seismic reflection. *SEG Technical Program Expanded Abstracts*,298-301.
- Missiaen, T.; E. Slob, and M. E. Donselaar. 2008, Comparing different shallow geophysical methods in a tidal estuary, Verdronken Land van Saeftinge, Western Scheldt, the Netherlands. *Netherlands Journal of Geosciences*, **87**, no. 2,151-164.
- Moldoveanu, N., and W. Abriel. 2006, Over/under towed-streamer acquisition: A method to extend seismic bandwidth to both higher and lower frequencies. *The Leading Edge*, no. January,41-58.
- Mondol, N. H.; J. Jahren; K. Bjørlykke, and I. Brevik. 2008, Elastic properties of clay minerals. *The Leading Edge*, **27**, no. 6,758-770.
- Monrigal, O. J., and M. E. Vardy. 2016, Inversion of Ultra High Resolution 3D to Derive Sediments Properties. doi: 10.3997/2214-4609.201602148.
- Morrison, M. 2017, SHALLOW SHEAR-WAVE SEISMIC ANALYSIS OF POINT BAR DEPOSITS OF FALSE RIVER, LOUISIAN, Louisiana State University.
- Mougenot, D. 2005, Pushing towards lower frequencies. *World Oil*, no. September.
- Mowbray, T. D. 1983, The genesis of lateral accretion deposits in recent intertidal mudflat channels, Solway Firth, Scotland. *Sedimentary*, **30**,425-435.
- Musial, G.; J.-Y. Reynaud; M. K. Gingras; H. Fénies; R. Labourdette, and O. Parize. 2012, Subsurface and outcrop characterization of large tidally influenced point bars of the Cretaceous McMurray Formation (Alberta, Canada). *Sedimentary Geology*, **279**,156-172. doi: 10.1016/j.sedgeo.2011.04.020.

- Nanson, G. C. 1980, Point bar and floodplain formation of the meandering Beatton River, northeastern British Columbia, Canada. *Sedimentology*, **27**, no. 1,3-29.
- Noah, J. T.; G. S. Hofland, and K. Lemke. 1992, Seismic interpretation of meander channel point-bar deposits using realistic seismic modeling techniques. *The Leading Edge*, **11**, no. 8,13-18.
- Odum, J. K.; W. J. Stephenson; K. Goetz-Troost; D. M. Worley; A. D. Frankel; R. A. Williams, and J. Fryer. 2004, Shear – and Compressional- Wave Velocity Measurements from Two 150-m- Deep Boreholes in Seattle, Washington, USA. U.S. Geological Survey, Reston, Virginia 200.
- Oldenburg, D. W.; S. Levy, and K. Stinson. 1984, Root-mean-square velocities and recovery of the acoustic impedance. *Geophysics*, **49**, no. 10,1653-1663.
- Pelton, J. 2005, Near-surface seismology: Surface based methods., in D.K. Butler, ed., *Near Surface Geophysics: Society of Exploration Geophysicists*. 219-263.
- Peterson, R. A.; W. R. Fillipone, and E. B. Coker. 1955, The synthesis of seismograms from well log data. *Geophys.*, **20**,516.
- Pranter, M. J.; A. I. Ellison; R. D. Cole, and P. E. Patterson. 2007, Analysis and modeling of intermediate-scale reservoir heterogeneity based on a fluvial point-bar outcrop analog, Williams Fork Formation, Piceance Basin, Colorado. *AAPG Bulletin*, **91**, no. 7,1025-1051. doi: 10.1306/02010706102.
- Pugin, A. J. M.; T. H. Larson, and A. C. Phillips. 2002, Shallow high-resolution shear-wave seismic reflection acquisition using a land-streamer in the Mississippi River floodplain: potential for engineering and hydrogeologic applications. In *Society of Exploration Geophysicists*.
- Pugin, A. J. M.; T. H. Larson; S. L. Sargent; C. E. Bexfield, and J. H. McBride. 2004, Near-surface mapping using SH-wave and P-wave seismic land-streamer data acquisition in Illinois, US *The Leading Edge*, **23**, no. 7,677-682.
- R. G., F.; Z. Haijnal; D. Schmitt, and A. Zaja. 2007, High Resolution Seismic Reflection Imaging of Complex Stratigraphic Features in Shallow Aquifers. *Mem. Descr. Carta Geol. d'It.*, **LXXVI**,175-192.

- Robinson, C., and K. Larner. Datuming and layer replacement: When are static corrections sufficient? : Colorado School of Mines.
- Robinson, E. A. 1999, Seismic Inversion and Deconvolution Part B: Dual Sensor Technology Edited by Sven Treitel and Klaus Helbig, Handbook of Seismic Exploration: Elsevier Science Ltd.
- Roden, R., and H. Sepulveda. 1999, The significance of phase to the interpreter: Practical guidelines for phase analysis. Interpreter's Corner.
- Ronen, J., and J. Claerbout. 1985, Surface-consistent residual statics estimation by stack-power maximization. Geophysics, **50**, no. 12,2759-2767.
- Roth, M.; K. Holliger, and A. G. Green. 1998, Guided waves in near-surface seismic surveys. Geophysical Research Letters, **25**, no. 7,1071-1074. doi: 10.1029/98gl00549.
- Roux*, P.-F.; B. de Cacqueray, and C. Maisons. 2014, Conventional sensors: Is there anything useable below their natural frequency? In SEG Technical Program Expanded Abstracts 2014.
- Santamarina, C.; K. A. Klenk; Fam, and M. A. 2001, Soils and Waves: John Wiley & Sons Ltd.
- Santamarina, J. C.; V. A. Rinaldi; D. Fratta; K. A. Klein; Y.-H. Wang; G. C. Cho, and G. Cascante. 2005, A Survey of Elastic and Electromagnetic Properties of Near-Surface Soils in Dwain K. Butler, ed., Investigations in Geophysics No. 13 - Near-Surface Geophysics Society of Exploration Geophysics 756.
- Saucier, R. T. 1969, GEOLOGICAL INVESTIGATION OF THE MISSISSIPPI RIVER AREA ARTONISH TO DONALDSONVILLE, LA.: U. S. Army Engineer Waterways Experiment Station.
- Sentenac, S. U. R. C. A. G. a. P. 2015, Novel Approach for Health Monitoring of Earthen Embankments. Journal of Geotechnical & Geoenvironmental Engineering.
- Sheriff, R. E. 1981, Encyclopedic dictionary of exploration geophysics: Society of Exploration Geophysicists.

- Sheriff, R. E. 1991, Encyclopedic Dictionary of Exploration Geophysics. 3rd ed. Vol. 1, Geophysical References Series: Society of Exploration Geophysicists.
- Simm, R., and R. White. 2002, Phase, polarity, and the interpreter's wavelet. *First Break*, **20**.
- Simmons, J., and M. Backus. 2001, Shear waves from 3-D–9-C seismic reflection data: Have we been looking for signal in all the wrong places? : *The Leading Edge*, **20**, no. 6,604-612.
- Simons, D. B.; S. A. Schumm, and M. A. Stevens. 1974, *Geomorphology of the Middle Mississippi River* Colorado State University
- Sloan, S. D.; D. W. Steeples, and G. P. Tsoflias. 2008, Imaging a Shallow Paleo-Channel Using 3D Ultra-Shallow Seismic Reflection Methods.568-576. doi: 10.4133/1.2963298.
- Sloan, S. D.; G. P. Tsoflias; D. W. Steeples, and P. D. Vincent. 2007, High-resolution ultra-shallow subsurface imaging by integrating near-surface seismic reflection and ground-penetrating radar data in the depth domain. *Journal of Applied Geophysics*, **62**, no. 3,281-286. doi: 10.1016/j.jappgeo.2007.01.001.
- Sloan, S. D.; J. Tyler Schwenk, and R. H. Stevens. 2016, An example of extreme near-surface variability in shallow seismic reflection data. *Interpretation*, **4**, no. 3,SH1-SH9. doi: 10.1190/int-2015-0215.1.
- Solberg, I.-L.; L. Hansen; J. S. Rønning; E. D. Haugen; E. Dalsegg, and J. F. Tønnesen. 2012, Combined geophysical and geotechnical approach to ground investigations and hazard zonation of a quick clay area, mid Norway. *Bulletin of Engineering Geology and the Environment*, **71**, no. 1,119-133. doi: 10.1007/s10064-011-0363-x.
- Spikes, K.; D. Steeples; M. Ralston; J. Blair, and G. Tian. 2005, *Common Midpoint Seismic Reflection Data Recorded with Automatically Planted Geophones*. Lawrence, Kansas: The University of Kansas Department of Geology.
- Steeple, D. W. 1998, A review of shallow seismic methods.

- Steeple, D. W., and R. W. Knapp. 1982, Reflections from 25 feet or less. Engineering and Groundwater.
- Steeple, D. W., and R. D. Miller. 1998, Avoiding pitfalls in shallow seismic reflection surveys. Geophysics, **63**, no. 4,1213-1224.
- Steeple, D. W.; C. M. Schmeissner, and B. K. Macy. 1995, The evolution of shallow seismic exploration methods. Journal of Environmental and Engineering Geophysics, **1**, no. A,15-24.
- Sternberg, H. O. R. 1956, A contribution to the geomorphology of the False River area, Louisiana, Louisiana State University.
- Stockwell, J. W. 1999, The CWP/SU: Seismic Unix package. Computers & Geosciences, **25**, no. 4,415-419. doi: citeulike-article-id:4838882.
- Stone, D. G. 1998, Designing Seismic Surveys in Two and Three Dimensions. Translated by -. Edited by Charles A. Meeder. 3 ed. Vol. 5: Society of Exploration Geophysics
- Vardy, M. E.; M. Vanneste; T. J. Henstock; E. C. Morgan, and L. Pinson. 2015, Can high-resolution marine geophysical data be inverted for soil properties?
- Veeken, P. C. H., and M. Da Silva. 2004, Seismic inversion methods and some of their constraints. First break, **22**, no. 6,47-70.
- Wang, Z.; R. L. Street; E. W. Woolery, and I. P. Madin. 2000, SH-Wave Refraction/Reflection and Site Characterization. American Society of Civil Engineers,126-140.
- Waters, K. H. 1981, Reflection seismology: A tool fo energy resource exploration Wiley-Interscience
- Widess, M. B. 1973, How thin is a thin bed? : Geophysics, **38**, no. 6,1176-1180.
- Wiederhold, H. 2006, Seismic Methods.

Wolman, M. G., and L. B. Leopold. 1957, River Flood Plains: Some Observations On Their Formation. PHYSIOGRAPHIC AND HYDRAULIC STUDIES OF RIVERS.

Wolz, S. 2003a, From low to high fidelity geophysics: 3-D multi-component shallow seismic surveying in the Lion's Harbour of Miletus (Turkey).

Wolz, S. 2003b, From Low to High Geophysics: 3-D Multi-component Shallow Seismic Surveying in the Lions' Harbour of Miletus (Turkey).

Xia, J.; R. D. Miller; C. B. Park; E. Wightman, and R. Nigbor. 2002, A pitfall in shallow shear-wave refraction surveying. Journal of Applied Geophysics, **51**,1-9.

Yilmaz, O. 1987, Seismic data processing. Edited by E. B. Neitzel, Investigations in Geophysics: Society of Exploration Geophysicists.

Yilmaz, O. 2001, Seismic data processing. Edited by E. B. Neitzel. 2 ed. 2 vols, Investigations in Geophysics: Society of Exploration Geophysicists.

Young, R. A., and J. Hoyos. 2001, Near-surface, SH-wave surveys in unconsolidated, alluvial sediments. The Leading Edge, **20**, no. 9,936-948.

Zhang, S. 1990, Shallow SH-wave Seismic Exploration for Subway Construction in Shanghai, in Stanley H. Ward, ed., Geotechnical and Enviromental Geophysics Society of Exploration Geophysicists 175-179.

CHAPTER 8: APPENDIX

(8.1) List & Definition of Terms

Keywords and processing terms I use throughout seismic data processing and post-processing are presented below (Table 8.1, 8.2, & 8.3).

Table 8.1. The keywords are used accessing, managing, and processing seismic data.

Seismic Unix Keywords	Definition
tracl	Trace sequence number within a line
tracr	Trace sequence number within a SEG-Y file
tracl	Trace number within original field record
offset	Distance from the center of the source point to the center of the receiver group
cdp	Ensemble number for a common-depth-point
ns	Number of samples in a given trace
dt	Sampling rate/interval in microseconds
sx	Source coordinate in the x-direction
sy	Source coordinate in the y-direction
gx	Receiver coordinate in the x-direction
gy	Receiver coordinate in the y-direction
clip	Clip used to determine bclip and wclip
perc	Percentile used to determine clip

Table 8.2. Processing terms I use for filtering and gaining.

Seismic Unix Processing Terms	Definition
wagc	Time window over which AGC is calculated
f	Frequency [Hz] value for filtering purposes
amps	Scalar value assigned to each designated frequency value for filtering

Table 8.3. Terms I use throughout data processing and post-processing.

Processing/Post-Processing Terms	Definition
CMP	Common-mid-point
CDP	Common-depth-point
SP	Shotpoint
WASP	Walk-Away Survey Shotpoint
ILSP	Inline Survey Shotpoint
CLSP	Crossline Survey Shotpoint
Vrms	Root-mean-square velocity
Vint	Interval velocity
Left/Right-Shotgather	Another term for opposite polarity shotgather
Shotgather	Single collection of seismic data corresponding to a single seismic source
Shotpoint	Position of seismic source
2-D	Two-dimensional
Cross-Section	A 2-D depth or time slide of the earth
Profile	Display of shear-impedance
SI	Shear-Impedance
TWT	Two-Way-Time
f-k	Frequency-Wavenumber
F-X	Frequency-Offset
Fold	Number of traces associated with a single CDP or CMP
SNR	Signal-To-Noise Ratio
m	Meter
s	Second(s)

(8.2) A Disclosure of Seismic Data Processing/Post-Processing & Image/Wiggle Plots

For the process of seismic data acquisition, processing, and post-processing, great care is taken to preserve the initial amplitude and frequency characteristics of our data. Multiple wiggle/image plots and figures in this thesis display gained, clipped, and/or band-passed seismic data. These processes are only applied for the sake of visualization. No alteration to frequency or amplitude characteristics is permanently applied to our seismic data until the final stage of processing and subsequent post-processing steps.

(8.3) Description & Effect of Clipping Seismic Data

I clip seismic data by way of using one of two Seismic Unix parameters in both `suxwigb` and `suximage`. The two parameters are `perc` and `clip`. The difference of these parameters are outlined in `ximage` documentation.

I clip (0.5) a raw shotgather from ISP3 to visualize and quantify the overall effect of clipping on seismic data (Figure 8.1). The overall results of clipping seismic data is the apparent amplification of comparatively low-magnitude seismic amplitudes. This phenomenon occurs because amplitude values greater than 0.5 and less than -0.5 are truncated and subsequently added to existing samples of 0.5 magnitude.

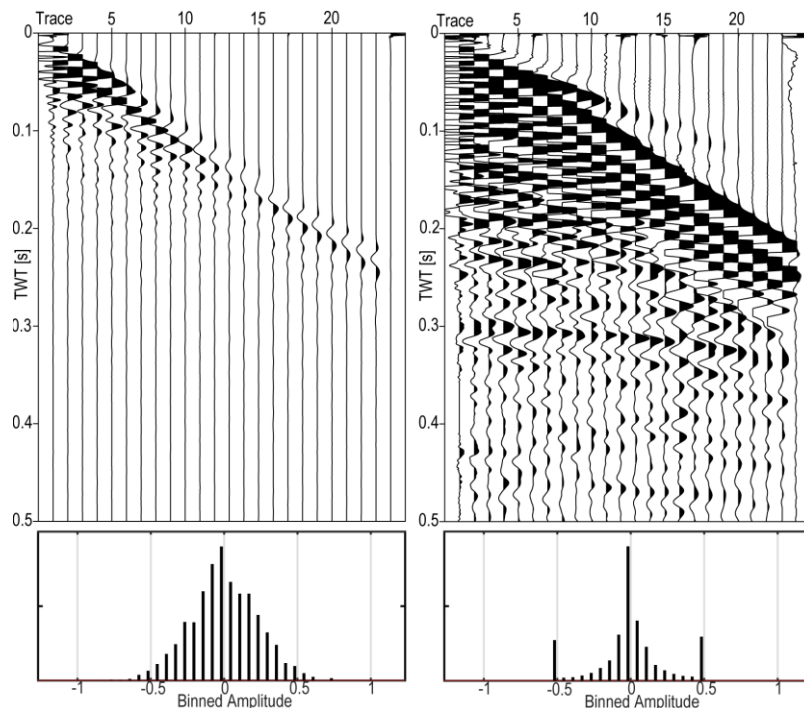
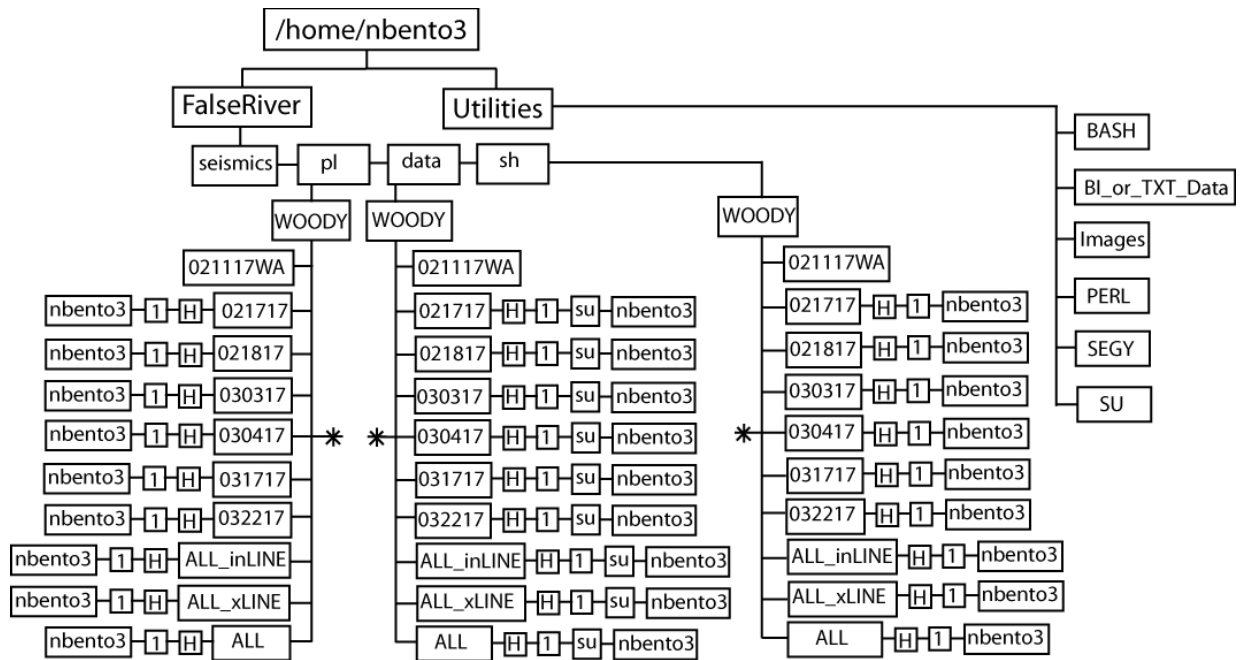


Figure 8.1. Raw shotgather of ILSP3 (left). A histogram of the seismic amplitudes of the unclipped shotgather is immediately below it. The histogram exhibits a normal distribution of binned amplitudes. Seismic data are clipped (`perc=99`). Clipped shotgather of ILSP3 (right) and its corresponding histogram of seismic amplitudes immediately below it. Clipping has truncated the initial normal distribution of amplitudes. Clip value is 0.5. Seismic data are clipped (`perc=99`).

(8.4) Zamin Directory Structure & Copying/Moving Data

Zamin is server used to store and process seismic data for this study (Table 8.4). Moving and/or copying any data from Zamin to another machine is accomplished via a software called FileZilla®.

Table 8.4. Director structure and tree of all directories with content used for seismic data storage and processing tools. The asterisks adjacent to 030417 denotes a day where data acquisition occurred but is completely disregarded for this study due to poor quality.



(8.5) Seismic Data Upload & Conversion Workflow

Transferring seismic data from the Geometrics R-24 to a processing machine requires several steps. The steps are outlined below (Table 8.5).

Table 8.5. Steps 1 – 15 *must* be performed sequentially with Step 1 being the start of the data upload/conversion workflow. After Step 5, all copied seismic data reside in the floppy disk. All steps thereafter pertain to copying the floppy disk data to a flash drive. Before commencing Step 9, you must supply a login username and passcode. The **X** character is a variable that represents the directory name (and all seismic data therein) that is to be copied and converted.

Step	Operation
1	Attach "SCSI ONLY" floppy drive to Geometrics
2	Insert floppy disk into "SCSI ONLY"
3	Turn on Geometrics
4	Exit to DOS
5	Type: <i>xcopy E:\X D:\X /S</i>
6	Attach "parallel port" floppy drive to laptop
7	Insert floppy disk into the "parallel port" drive
8	Turn on laptop
9	Type : <i>/sbin/modprobe ppa</i>
10	Type : <i>mount -t vfat /dev/sda4 /mnt/zip</i>
11	Type: <i>cd /mnt/zip</i>
12	Attach USB to laptop
13	Type: <i>mount -t vfat /dev/sdb /mnt/flash</i>
14	Type: <i>/mnt/flash</i>
15	Type: <i>cp -r /mnt/zip/X ./</i>

(8.6) Main Seismic Data Output Files

Multiple images and the source seismic data from which they are derived appear throughout this document. Details below outline directions as to how to access certain data sets from processing. Absolute paths and file names are provided from the walk-away, inline, and crossline surveys.

If an image shows and/or explicitly notes a specific type of gather or stacked section, be sure to record that information and refer to the data presented below. For example, if an image shows CMP 35 from the inline survey, you can access that data via */home/nbento3/FalseRiver/seismics/data/WOODY/ALL_inLINE/H/1/su/nbento3* in file *ALL_inLINE_D2_GEOM_CMP_headers.su* or *All_CMP_inLINE_D2_sorted_ep_offset.su*.

Walk-Away Survey

- 1) Total Walk-Away Shotgather (Shear-Gun Source)
 - Path: /home/nbento3/FalseRiver/seismics/data/WOODY/021117WA/su
 - File: all_gun_geom.su
- 2) Total Walk-Away Shotgather (Shear-Gun Source)
 - Path: /home/nbento3/FalseRiver/seismics/data/WOODY/021117WA/su
 - File: all_hit_geom.su

Inline Survey

- 1) (Pre/Post-Top Mute & Pre-NMO) Geometry & CMP-Sorted
 - Path:
/home/nbento3/FalseRiver/seismics/data/WOODY/ALL_inLINE/H/1/su/nbento3
 - File: All_CMP_inLINE_D2_sorted_ep_offset.su
- 2) (Pre-fk Filter) Stacked Seismic Cross-Section
 - Path: /home/nbento3/FalseRiver/seismics/data/WOODY/ALL/H/1/su/nbento3
 - File: All_CMP_inLINE_D2_stacked.su
- 3) (Post-fk Filter) Stacked Seismic Cross-Section
 - Path: /home/nbento3/FalseRiver/seismics/data/WOODY/ALL/H/1/su/nbento3
 - File: All_CMP_inLINE_D2_stacked_FK_t-muted.su

Crossline Survey

- 1) (Pre/Post Top-Mute & Pre-NMO) Geometry & CMP-Sorted
 - Path:
/home/nbento3/FalseRiver/seismics/data/WOODY/ALL_xLINE/H/1/su/nbento3
 - File: ALL_xLINE_D2_GEOM_CMP_headers.su
- 2) (Pre-fk Filter) Stacked Seismic Cross-Section
 - Path: /home/nbento3/FalseRiver/seismics/data/WOODY/ALL/H/1/su/nbento3
 - File: All_CMP_xLINE_D2_stacked.su
- 3) (Post-fk Filter) Stacked Seismic Cross-Section
 - Path: /home/nbento3/FalseRiver/seismics/data/WOODY/ALL/H/1/su/nbento3
 - File: All_CMP_xLINE_D2_stacked_FK.su

(8.7) Non-Scripted Seismic Unix Commands for Processing/Post-Processing

Each of the following Seismic Unix modules are used during seismic data processing. If more information is needed for any of the listed modules, refer to sudoc for details.

(8.7.1) sustatic

For this study, this module is used for both elevation statics and residual statics corrections. This section only focuses on how sustatic is used to calculate elevation static correction. Refer to Section 8.8.4 to view how this module is handled for residual statics corrections.

(8.7.2) **suphase**

This module is used to apply a constant phase rotation to the inline and crossline seismic cross-sections. I provide a simple example with synthetic seismic data to show how `suphase` works (Figure 8.2).

I use `suphase` to apply a +90 constant phase rotation to a synthetic data set (via `suphase a=90 < data.su > data_ppr90.su`).

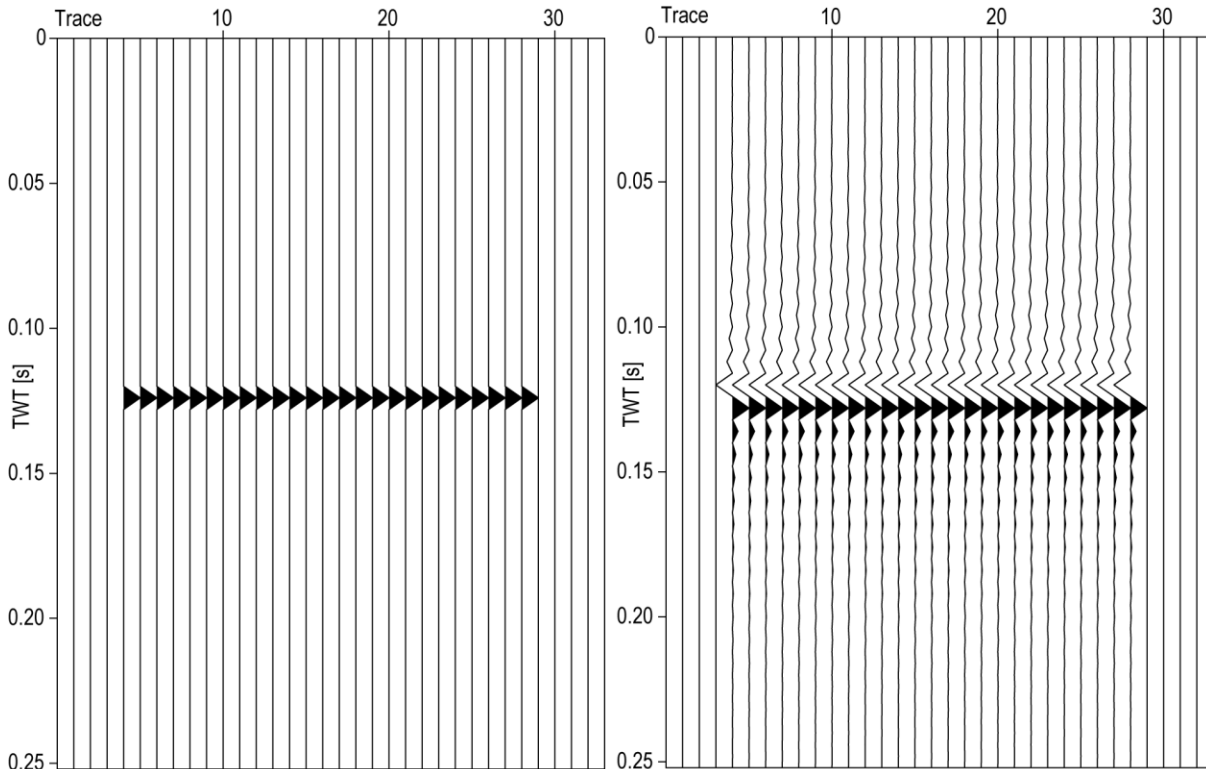


Figure 8.2. Synthetic seismogram (left) showing a single seismic reflector. No phase rotation is applied. Data displayed in Figure 8.4 with a constant phase rotation of +90° (right).

(8.7.3) **sukeycount**

I use `sukeycount` to calculate the fold count for each CMP gather from both the inline and crossline surveys (Figure 8.3).

Before using this module, make sure input seismic data retains a primary sort by CMP (i.e. `susort cdp offset < cmp_data.su > cmp_sorted_data.su`). CMP-sorted seismic data have their fold count evaluated with `sukeycount` (via `sukeycount < cmp_sorted_data.su key=cdp > fold_count.txt`).

(8.7.4) **suwind**

This module is used numerous times throughout processing and post-processing. However, I describe here how to use `suwind` to window depth-converted

seismic data. Using a depth-converted crossline seismic cross-section, I provide a step-by-step workflow to window these type of seismic data.

Immediately after depth-converting a given seismic file (Section 8.8.2), use *surange* to read the non-zero keys for the file (via *surange < TVD_data.su*) (Figure 8.4). Also, use *suximage* to view the non-windowed, depth-converted seismic file (via *suximage < TVD_data.su*) (Figure 8.5 & Equation 8.1).

```

cdp = 1      has  1  trace(s)
cdp = 2      has  3  trace(s)
cdp = 3      has  5  trace(s)
cdp = 4      has  7  trace(s)
cdp = 5      has  9  trace(s)
cdp = 6      has 11  trace(s)
cdp = 7      has 13  trace(s)
cdp = 8      has 15  trace(s)
cdp = 9      has 17  trace(s)
cdp = 10     has 19  trace(s)
cdp = 11     has 21  trace(s)
cdp = 12     has 23  trace(s)
cdp = 13     has 24  trace(s)
cdp = 14     has 24  trace(s)
cdp = 15     has 24  trace(s)

```

Figure 8.3. The output of the command above should appear similar to the text imaged here.

```

60 traces:
tracl  1 60 (1 - 60)
tracr  1 1152 (1 - 1152)
fldr   1 48 (1 - 48)
tracf  1 24 (1 - 24)
ep     1 48 (1 - 48)
cdp    1 60 (1 - 60)
trid   130
nhs    1 24 (1 - 1)
sx     1 48 (1 - 48)
gx     2 72 (2 - 72)
delrt  105
mutss  80 300 (81 - 300)
ns     2378
dt     500
dl     0.030039
fl     6.308215

Shot coordinate limits:
      North(1,0) South(1,0) East(48,0) West(1,0)

Receiver coordinate limits:
      North(2,0) South(2,0) East(72,0) West(2,0)

Midpoint coordinate limits:
      North(1.5,0) South(1.5,0) East(60,0) West(1.5,0)

```

Figure 8.4. *Surange* output for a depth-converted file. The three important keys to note from this output are *ns*, *d1*, and *f1*.

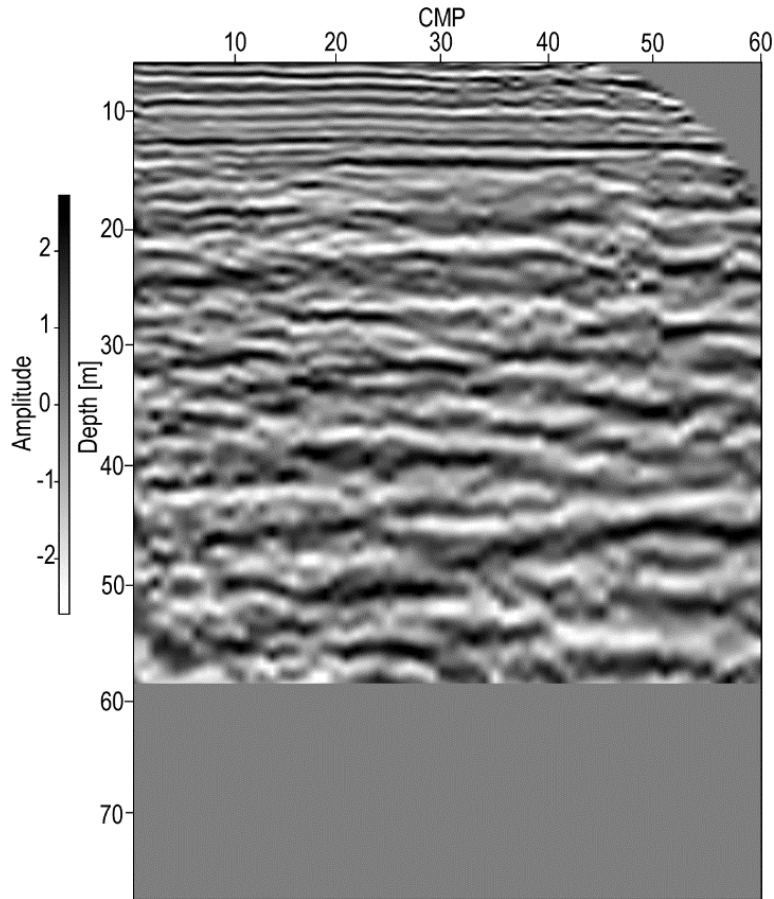


Figure 8.5. Depth-converted seismic file. This process will always yield a greyed region at the bottom of the seismic file. The grey section is the part of region I window out.

Record three specific parts of the surange output (ns, d1, & f1) and determine the maximum depth of windowing. For this example, I window from shallowing depth to 50 m. An equation is used to determine an ns value that is subsequently used for windowed depth-converted seismic data.su.

$$ns = \frac{MWD - f1}{d1} = \frac{50 - 6.308215}{0.030039} \equiv 1455$$

Equation 8.1. MWD is the maximum window depth selected by the user, f1 is provided by surange output. For this example, it is 6.308215. This value is actually the shallowest calculated depth. The d1 key value is 0.030039.

The calculated ns value is used to window the seismic data with suwind with respect to depth (via *suwind key=ns itmin=1 itmax=ns < TVD_data.su > TVD_data_windowed.su*). Check the windowed, depth-converted seismic data by viewing the file with suximage (Figure 8.6). The data are windowed from the shallowest depth (~6.4 m) to 50 m.

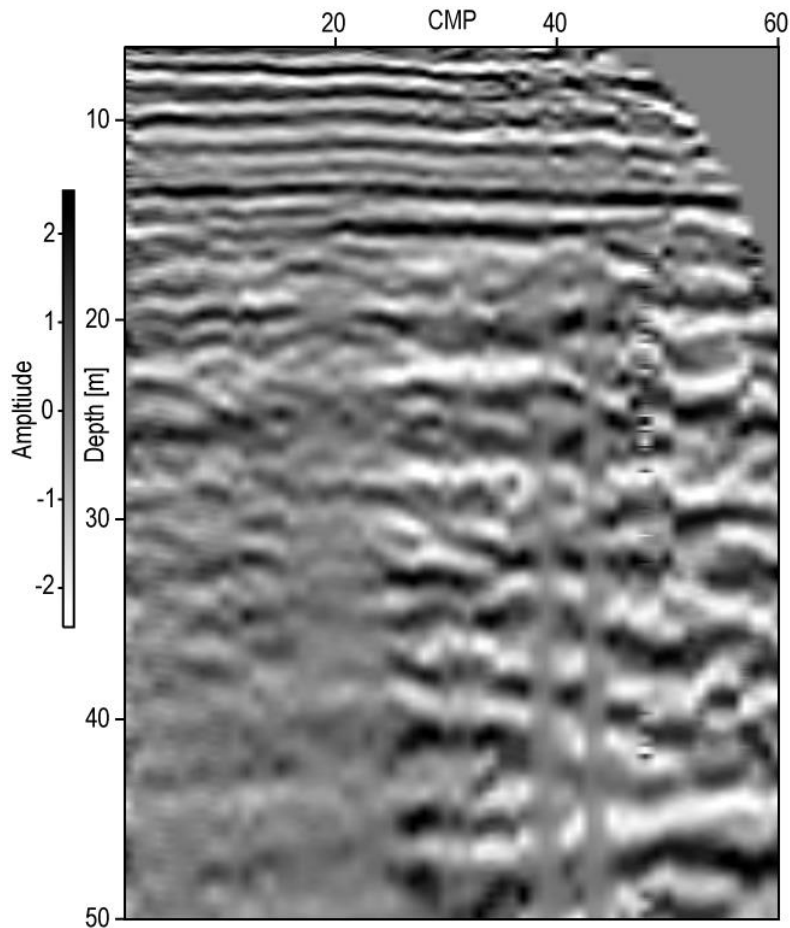


Figure 8.6. Windowed, depth-converted seismic data.

(8.7.5) sugain

Seismic data are gained for viewing and amplitude conditioning purposes throughout this study. I use automatic gain control (AGC) (Section 8.1) and a velocity-invariant, time-dependent divergence correction. To apply AGC to any seismic data, I use *sugain* (e.g. *sugain agc=1 wagc=0.08 < input_data.su > output_agc_data.su*). The parameter *wagc* is the TWT window over which AGC is applied to seismic data. To apply a velocity-invariant, time-dependent divergence correction, I also use *sugain* (e.g. *sugain tpow=1.8 < input_data > output_dc_data.su*).

(8.8) BASH Scripts

All BASH scripts written for this study are original and are incorporated throughout seismic data processing and post-processing.

(8.8.1) ample_recov_2.sh & input_mod.awk

Explanation

Both *ample_recov_2.sh* and *input_mod.awk* are used in conjunction to apply a time and velocity-variant divergence correction (via *sudivcor*) to processed and post-

stack seismic data. For this process to work, there must be RMS velocity (Figure 8.7) info from velocity analysis corresponding to each stacked trace.

Required Input

1.) TWT/RMS Velocity File Format

0.1	100	120	90
0.2	150	150	100
0.3	200	170	120
0.4	300	320	200
0.5	500	400	300

Figure 8.7. The input TWT/ V_{RMS} text file is formatted according to the text imaged here. Column 1 must comprise only of TWT data. All columns thereafter must be populated with V_{RMS} data. For example, Column 2 shows V_{RMS} data that corresponds to velocity information acquired from velocity analysis for a given CMP or stacked trace. The same applies to all other columns except for Column 1.

2.) Post-Stack Seismic Data

ample_recov_2.sh

```
#!/bin/bash
```

```
#Builder: Nathan Benton
```

```
#Description: recovers amplitude via sudivcor from
```

```
#velocity/TWT input txt data in a trace-by-trace
```

```
#manner
```

```
#Date Created: 09/29/2017
```

```
#Date Modified: NA
```

```
#-----
```

```
#Section 0=====
```

```
echo
```

```
echo "---Make sure previous output .su file is deleted---";
```

```
echo "Enter TWT/Velocity File: ";
```

```
read tvdata; #Input TWT/velocity file
```

```
echo "Enter Seismic File: ";
```

```
read sdata; #Input seismic data
```

```
echo "Enter Total Number of CMP/CDPs: ";
```

```
read max_cmp; #Total number of trace/CMPs
```

```
counter=1;
```

```
while [ $counter -le $max_cmp ]
```

```
do
```

```

#Section 1=====
gawk -f input_mod.awk n=1 $tvdata > zcolA.txt;      #Takes input TWT data,
                                                    #and sends column-formatted
                                                    #data to separate file
gawk -f input_mod.awk n=${counter+1} $tvdata > zcolB.txt; #Takes velocity data from
                                                    #input file and sends to
                                                    #separate file as column-
                                                    #formatted text data

#Section 2=====
i1=0; i2=0;
declare -a F1; declare -a F2;

#Field 1 (read and assign data from two-way-time [TWT] file)
while read line;
do
    F1[$i1]="$line";
    i1=${i1+1};
    #echo "Value of element $i1: ${F1[$i1-1]}.";    QC
done < zcolA.txt;

#Field 2 (read and assign data from velocity column)
while read line;
do
    F2[$i2]="$line";
    i2=${i2+1};
    #echo "Value of element $i2: ${F2[$i2-1]}.";    QC
done < zcolB.txt;

#Section 3=====
F1="${F1[*]}";
F1=$(echo $F1 | sed s'/.$/');
F2="${F2[*]}";
F2=$(echo $F2 | sed s'/.$/');
#echo "Content of F1: $F1.";    QC
#echo "Content of F2: $F2.";    QC

#Section 4=====
#Organize seismic data and apply divergence correction
current_cdp=$counter;
suwind key=cdp min=$current_cdp max=$current_cdp \
< $sdata > sdata_temp_1.su
sudivcor trms=$F1 vrms=$F2 < sdata_temp_1.su > sdata_temp2.su
cat sdata_temp2.su >> ${sdata}_1_ampt.su

echo "Trace $counter Complete.";
counter=${counter+1};

```

```
#Section 5=====
rm -rf zcolA.txt, zcolB.txt, sdata_temp_1.su, sdata_temp2.su;      #Removes files
```

done

```
echo "New File: ${sdata}_1_ampt.su"
echo Done.
```

input_mod.awk

```
#Builder: Nathan Benton
#Description: single line awk command iteratively called by ample_recov_2.sh
#Date Created: 09/29/2017
#Date Modified: NA
#-----
```

```
{print $n","} #Places comma next to every row element of input file
```

(8.8.2) depthing.sh

Explanation

Time-to-depth conversion is performed via depthing.sh. There are three inputs required for the depth-conversion process: seismic, TWT, and V_{INT} data. The TWT and V_{INT} data is calculated and provided by a MATLAB script (Section 8.9.1.14).

In depthing.sh, the bolded T variable represents the TWT string that must be copied and pasted where the T resides (e.g. $t=0.1,0.2,0.3,\dots$). Likewise, the V variable indicates where a single V_{INT} must be copied and pasted (e.g. $v=100,200,300,\dots$).

The limitation of this tool is that the input velocity model (Figure 8.8) must be identical across rows. This requires that the V_{INT} model be averaged (Section 8.9.1.14) before depth conversion.

Required Input

1.) Input V_{INT} String from V_{INT} Model

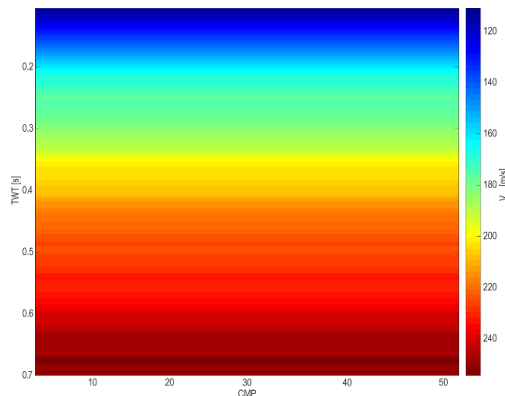


Figure 8.8. Arithmetic mean of the original V_{INT} model. Values are identical across rows but vary with TWT. To access a V_{INT} string, refer to Section 8.9.1.14.

2.) Input TWT String

To access a TWT string, refer to Section 8.9.1.14.

3.) Post-Stack Seismic Data

depthing.sh

```
#!/bin/bash

#Builder: Nathan Benton
#Description: depth-converts post-stack seismic data
#Date Created: 03/25/2017
#Date Modified: NA
#-----

echo "Enter TWT Seismic File: ";
read sinput;

verbose=1

suttoz \
<${sinput} \
${sinput}_TVD.su \
t=T
v=V
echo "New TVD File: ${sinput}_TVD.su"

echo Done.
```

(8.8.3) kill_interp_repair.sh

Explanation

Trace interpolation is almost always applied to seismic data to mitigate spatial aliasing issues before migration. However, for the purpose of this study, I use it to repair corrupted/null traces (Figure 8.9).

The limitation of this process is that the first and last traces of a given seismic data set cannot be interpolated. The reason for this is that there must be a trace on either side of the trace that is to be interpolated for this process to function accordingly.

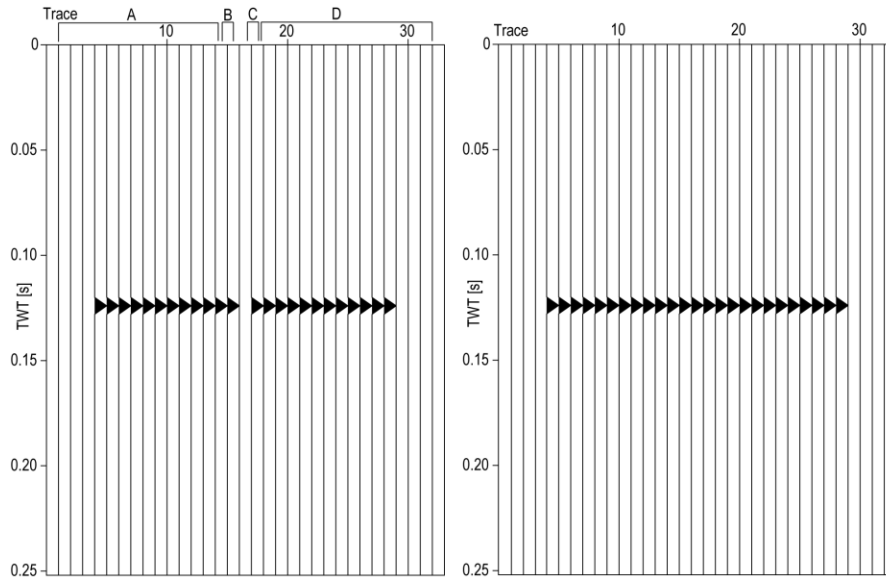


Figure 8.9. Synthetic seismic data (left) with trace 16 nulled. I use interpolation to repair this trace by using traces directly adjacent to it. The process of interpolation is performed in four steps: A, B, C, and D. Step A and D separates a range of trace into separate temporary files. Steps B and C take single trace on either side of the null/corrupted trace and then build/repair a given trace via interpolation. Trace 16 is repaired via interpolation (right).

Required Input

1.) Seismic Data

kill_interp_repair.sh

```
#!/bin/bash

#Author: Nathan Benton
#Description: kills (nulls) a single corrupted
#trace and then interpolates it
#by considered the traces directly
#adjacent to the null trace
#on the left and right side
#Created: 03/02/17
#Modified: NA
#-----

ls;

echo "Enter .su File to Mute and Interpolate: ";
read seis_input;

suxwigb<$seis_input clip=0.5 &

echo "Enter trac trace number to mute: ";
```

```

read tracf_kill;

echo "Enter Left File MIN: ";
read lfmin;
echo "Enter Left File MAX: ";
read lfmax;

echo "Enter Middle-L (1) File MIN: ";
read mlfmin;
echo "Enter Middle-L (1) File MAX: ";
read mlfmax;

echo "Enter Middle-R (2) File MIN: ";
read mrfmin;
echo "Enter Middle-R (2) File MAX: ";
read mrfmax;

echo "Enter Right File MIN: ";
read rfmin;
echo "Enter Right File MAX: ";
read rfmax;

sukill<${seis_input}>${seis_input}_KIS.su \
    key=cdp min=$tracf_kill count=1

#For the left side
suwind<${seis_input}_KIS.su>left.su \
    key=cdp min=$lfmin max=$lfmax

#For the middle(1) [left]
suwind<${seis_input}_KIS.su>middle_1.su \
    key=cdp min=$mlfmin max=$mlfmax

#For middle(2) [right]
suwind<${seis_input}_KIS.su>middle_2.su \
    key=cdp min=$mrfmin max=$mrfmax

#For the right side
suwind<${seis_input}_KIS.su>right.su \
    key=cdp min=$rfmin max=$rfmax

#Cat middle files and then interpolate between
#the two traces directly adjacent two on
#the left and right side of the null trace
cat middle_1.su middle_2.su > middle_all.su
suinterp<middle_all.su>middle_all_interp.su \

```

```

ninterp=1 freq1=2 freq2=1000

#Now, cat all properly modified files together
cat left.su middle_all_interp.su right.su \
> ${seis_input}_interp.su

#Delete unneeded files
rm -rf ${seis_input}_KIS.su \
    left.su \
    middle_1.su \
    middle_2.su \
    right.su \
    middle_all.su \
    middle_all_interp.su

echo Done.

```

(8.8.4) MNSatics.sh

Explanation

Comparatively small-scale seismic wavelength corrections are applied to our data before stacking. The first part of MNSatics.sh calculates the residual statics correction values via suresstat. Subsequently, the corrections are applied to input seismic data via sustatic.

Using residual static corrections for this study did not appear to notably improve a given stack. Also, using this type of static correction is limited to comparatively small-scale wavelength misalignments and should not be used larger-scale seismic wavelength corrections related to large-scale velocity heterogeneity corresponding to the weathered zone and/or elevation static corrections.

Required Input

1.) Sorted Input Seismic Data

MNSatics.sh

```

#!/bin/bash

#Author: Nathan Benton
#Description: computes and applies residual statics correction
#Created: 05/05/17
#Modified: NA
#-----

echo "Enter File Name: ";
read sd;

SU_DATA=$sd;

```

```

#Sort the incoming file
susort fldr tracf < $SU_DATA > temp

#SECTION 1
#Compute residual statics (output to be used in Section 2)
suresstat fn=temp \
  ssol=sstats \
  rsol=rstats \
  ntpick=50 \
  niter=25 \
  imax=10000 \
  sub=1 \
  mode=0

#SECTION 2
#Apply the statics corrections
sustatic < $SU_DATA > ${SU_DATA}_static.su \
  hdrs=3 \
  sou_file=sstats \
  rec_file=rstats \
  ns=104 \
  nr=2220 \
  no=24

echo Done.

```

(8.8.5) segy_to_su.sh

Explanation

For this study, seismic data are transferred and reformatted from MATLAB to Seismic Unix for processing. I use segy_to_su.sh to convert SEG-Y formatted seismic data to SU (Seismic Unix) format.

Some operating systems may fail to convert seismic data. Sometimes, this issue may be attributable to a machine endian configuration.

Required Input

1.) SEG-Y Formatted Input Seismic Data.

seggy_to_su.sh

```

#!/bin/bash

#Author: Nathan Benton
#Description: converts .seggy to .su data
#Created: 04/01/17
#Modified: NA
#-----

```

```

verbose=1

echo Provide Input File Name: ;
read sdata;

segyread tape=${sdata} verbose=1 endian=0 \
segyclean > ${sdata}.su

echo "New File: ${sdata}.su";

rm -rf binary header;

echo Done.;

```

(8.8.6) header_input.sh

Explanation

Setting trace header information can be simplified and optimized by generating text files, converting them to binary format, and subsequently applying header values to seismic data via sushw. An example of inputting elevation and UTM coordinates into the crossline seismic cross-section is presented.

Required Input

- 1.) Text Files with Trace Header Information
- 2.) Input Seismic Data

header_input.sh

```

#!/bin/bash

#Author: Nathan Benton
#Description: sets trace header info via sushw
#Created: 06/13/17
#Modified: NA
#-----

echo "Enter .su File: ";
read sinput;
echo "Enter Header .txt File: ";
read tinput;

a2b<${tinput} n1=4>hfile.bin

sushw<${sinput} key=ep,tracr,tracl,tstat infile=hfile.bin>${sinput}_headers.su

echo Done.

```

(8.8.7) su_to_segy.sh

Explanation

Similar to Section 8.8.5, seismic data are transferred and reformatted from Seismic Unix to MATLAB for processing. I use su_to_segy.sh to convert SU (Seismic Unix) formatted seismic data to SEG-Y format.

Required Input

Some operating systems may fail to convert seismic data. Sometimes, this issue may be attributable to a machine endian configuration.

su_to_segy.sh

```
#!/bin/bash

#Author: Nathan Benton
#Description: converts .su to .segy data
#Created: 04/01/17
#Modified: NA
#-----

echo Provide Input File Name: ;
read var1;

segyhdrs < $var1
segywrite tape=${var1}.sgy < $var1
verbose=1;

echo "New File: ${var1}.sgy"

rm -rf binary header;

echo Done.;
```

(8.8.8) cat_oddOReven.sh

Explanation

Each shotgather for a given shotpoint from both the inline and crossline surveys is organized into separate “odd” or “even” files. For example, a file named 1003 and 1004 for some given shotpoint indicates that seismic data corresponding to file 1003 is of opposite polarity to seismic data from 1004. The bolded X variable in the for-loop represents a single-line list of odd/even file names that must be supplied in order for the concatenation process to execute properly (e.g. *1001.su 1003.su 1005.su ...* or *1002.su 1004.su 1006.su ...*).

Before differencing shotgathers, I concatenate all odd shotgather files into a single file. Likewise, I also combine all even shotgather files into a single file.

Required Input

1.) Single-Line List of All Odd/Even Seismic File Names

cat_oddOReven.sh

```
#!/bin/bash
```

```
#Author: Nathan Benton  
#Description: cats all even or odd numbered  
#shotgathers into single .su file for later  
#processing and viewing  
#-----
```

```
echo "Supply the absolute path to the data directory: ";  
read path;  
echo "Supply the absolute path to the current sh directory: ";  
read current;
```

```
cd $path;
```

```
for var1 in X; do
```

```
#cat $var1 >> all_even_IR_1.su; un-comment if catting even files  
cat $var1 >> all_odd_IR_1.su; #comment this line if catting even files
```

```
done;
```

```
cd $current;
```

```
echo Done.;
```

(8.8.9) suDiff.sh

Explanation

The odd/even concatenated seismic files are subsequently differenced via suDiff.sh. This process is performed separately for both the inline and crossline odd/even seismic files.

Required Input

1.) Concatenated Odd/Even Input Seismic Data File

suDiff.sh

```
#!/bin/bash
```

```
#Author: Nathan Benton  
#Description: accepts the two different  
#odd/even lines and then 'subtracts' the two  
#in order to improve SNR
```


(8.8.11) SET_p2_GEOM.sh

Explanation

The inline survey acquisition and subsequent geometry setting is divided by two stages: part 1 (p1) and part 2 (p2). Part 2 of the inline surveys extends from SP82 to SP104.

Each successive shotgather from SP82 to SP104 loses a trace (i.e. SP82=23 traces, SP83=22 traces,...,SP104=1 trace). For every shotgather corresponding to part of the inline survey, SET_p2_GEOM.sh is executed and used to process each shotgather from SP82 to SP104.

To configure input parameters accordingly for each shotgather, the gs and ep variables must be set correctly. For example, the parameters set for SET_p2_GEOM.sh for SP83 are gs=23 and ep=83. Likewise, the parameters set for SET_p2_GEOM.sh for SP82 are gs=22 and ep=82. This process is repeated for each shotgather until SP104, where gs=1 and ep=104.

Required Input

1.) Input Seismic Data (i.e. SP2-SP104 of the inline survey)

SET_p2_GEOM.sh

```
#!/bin/bash

#Author: Nathan Benton
#Description: sets geometry of part 2 of the inline survey
#-----

echo
echo "Enter Seismic File to Set Geometry: ";
read sinput;

echo "Enter Single EP to Set Geometry: ";
read ep;

gs=23;      #gather size
ep=82;      #shotpoint number

suwind key=ep min=$ep max=$ep \
< $sinput > ${sinput}_${ep}.su

sushw < ${sinput}_${ep}.su > \
${sinput}_${ep}_geom.su \
key=fldr,tracl,tracl,tracl,offset,ep,sx,gx \
a=$ep,2220,1,1,1,$ep,$ep,105 \
b=0,1,1,1,1,0,0,1 \
c=1,0,0,0,0,1,1,1 \
j=$gs,276,$gs,$gs,$gs,$gs,$gs,$gs
```

```
surange<${sinput}_${ep}_geom.su
```

echo Done.

(8.9) MATLAB

MATLAB is used extensively in this study for processing and post-processing of seismic data. Although many scripts and subroutines are original and multiple scripts/subroutines are borrowed from other users. If MATLAB script or subroutine is not original, a disclosure and citation are provided for that given code.

(8.9.1) MATLAB Subroutines

(8.9.1.1) wiggle.m

This script and documentation are located at the following URL:
https://www.mathworks.com/matlabcentral/mlc-downloads/downloads/submissions/38691/versions/2/previews/wiggle.m/index.html?access_key= (MATLAB, 2017). This MATLAB script is written by Rodrigo Portugal (<https://www.mathworks.com/matlabcentral/fileexchange/38691-wiggle?requestedDomain=www.mathworks.com>) (Portugal, 2016).

Note that this script is incorporated for Section 2.4.12 for displaying seismic data and is used in the MATLAB script listed in Section 8.9.1.13.

(8.9.1.2) vrms2vint.m

The following script is written by contributors of the Consortium for Research in Elastic Wave Exploration Seismology (CREWES) at the University of Calgary (Canada). Access to this subroutine and others are located at the following URL:
<<https://www.crewes.org/ResearchLinks/FreeSoftware/>> (CREWES, 2018).

This script is used in Section 8.9.1.4 to convert (column-by-column) V_{RMS} data into V_{INT} data.

vrms2vint.m

```
function vint=vrms2vint(vrms,t,flag)
% VRMS2VINT: convert rms to interval velocity
%
% vint=vrms2vint(vrms,t,flag)
% vint=vrms2vint(vrms,t);
%
% flag=0 ... return nonphysical interval velocities as NaN
%   =1 ... interpolate interval velocities from neighbors to
%         replace non-physical results
% ***** default = 0 *****
%
% NOTE: This SOFTWARE may be used by any individual or corporation for any
purpose
```

```
% with the exception of re-selling or re-distributing the SOFTWARE.  
% By using this software, you are agreeing to the terms detailed in this software's  
% Matlab source file.
```

```
% BEGIN TERMS OF USE LICENSE
```

```
%
```

```
% This SOFTWARE is maintained by the CREWES Project at the Department  
% of Geology and Geophysics of the University of Calgary, Calgary,  
% Alberta, Canada. The copyright and ownership is jointly held by  
% its 'AUTHOR' (identified above) and the CREWES Project. The CREWES  
% project may be contacted via email at: crewesinfo@crewes.org
```

```
%
```

```
% The term 'SOFTWARE' refers to the Matlab source code, translations to  
% any other computer language, or object code
```

```
%
```

```
% Terms of use of this SOFTWARE
```

```
%
```

```
% 1) This SOFTWARE may be used by any individual or corporation for any purpose  
% with the exception of re-selling or re-distributing the SOFTWARE.
```

```
%
```

```
% 2) The AUTHOR and CREWES must be acknowledged in any resulting publications  
or
```

```
% presentations
```

```
%
```

```
% 3) This SOFTWARE is provided "as is" with no warranty of any kind  
% either expressed or implied. CREWES makes no warranties or representation  
% as to its accuracy, completeness, or fitness for any purpose. CREWES  
% is under no obligation to provide support of any kind for this SOFTWARE.
```

```
%
```

```
% 4) CREWES periodically adds, changes, improves or updates this SOFTWARE  
without
```

```
% notice. New versions will be made available at www.crewes.org .
```

```
%
```

```
% 5) Use this SOFTWARE at your own risk.
```

```
%
```

```
% END TERMS OF USE LICENSE
```

```
if(nargin<3)
```

```
    flag=0;
```

```
end
```

```
%force column vectors
```

```
vrms=vrms(:);
```

```
t=t(:);
```

```
%compute interval velocity squared
```

```

vint=zeros(size(vrms));
nt=length(t);
i1=1:nt-1;i2=2:nt;
vrms2=vrms.^2;
vint(i1)= (vrms2(i2).*(t(i2)-t(1))-vrms2(i1).*(t(i1)-t(1)))/(t(i2)-t(i1));
%find and process non-physical ones
ind=find(vint<0);
if(~isempty(ind))
    if(flag)
        ilive=find(vint>0);
        vint(ind)=interpextrap(t(ilive),vint(ilive),t(ind));
    else
        vint(ind)=nan*ones(size(ind));
    end
end
end
%compute interval velocity
vint=sqrt(vint);
vint(nt)=vint(nt-1);

```

(8.9.1.3) Vint_populate.m

This script uses output from Section 8.9.1.2 and resamples it. Let us assume the output from vrms2vint.m is the following file (Table 8.6). In order to interpolate point beyond these TWT/ V_{INT} values, Vint_populate.m needs to be used (Figure 8.10). Note that this interpolation is performed with respect to the sampling rate.

Table 8.6. Input text file to be resampled.

TWT [s]	V_{INT} [m/s]
0.4	120
0.6	270
0.8	150

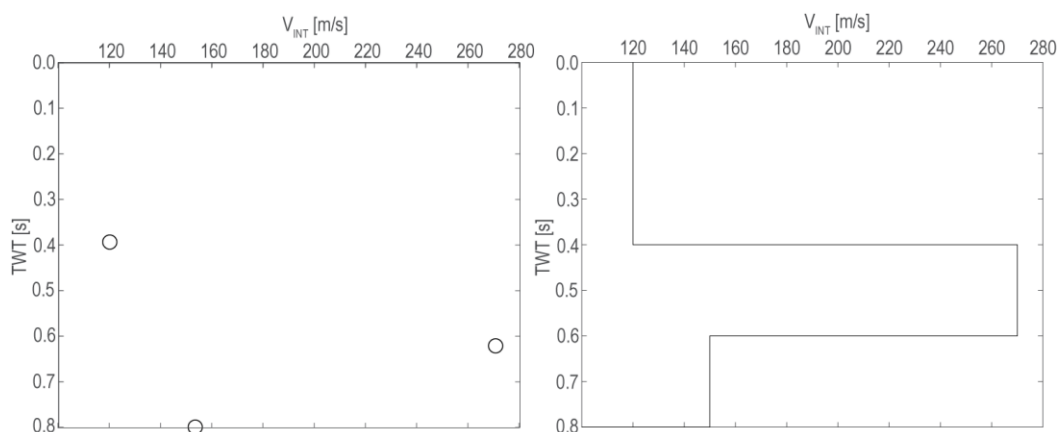


Figure 8.10. Sparse data (left) provided by vrms2int.m (Section 8.9.1.2). Vint_populate.m output (right) given the input provided by the table above.

Vint_populate.m

```
% % Builder: Nathan Benton
% % Description: accepts V_int vector and modifies it for full time
% % Date Created: 10/11/2017
% % Date Modified: NA
% -----

function Vint=Vint_populate(twt_vint)

dt=0.0005; %sampling rate (0.0005 s) – check this with your data
full_time=[0:dt:1]'; %full time vector with respect to defined dt (0.0 – 1.0 s) – check this

all_twt_vint=twt_vint; %assign function argument
interp_TWT_V=zeros(size(full_time,1),2); %later to be populated with final TWT/V pairs
interp_TWT_V(:,1)=full_time; %assign full time array to TWT column
rc=size(interp_TWT_V,1); %calculate and assign total number of rows

%stage 1: populate sparse matrix with initial V_int picks
for i1=1:size(all_twt_vint,1),
    for i2=1:rc,
        if(isalmost(full_time(i2),all_twt_vint(i1,1),dt)) %TWT matching with testing
            interp_TWT_V(i2,2)=all_twt_vint(i1,2);
        end
        if(i2~=1 && interp_TWT_V(i2,2)==interp_TWT_V(i2-1,2) ...
            && interp_TWT_V(i2,2)~=0)
            interp_TWT_V(i2,2)=0; %replace repeated values with zero
        end
    end
end

%stage 2: fill sparse matrix with "vertical" values of V_int
[rL,cL]=find(interp_TWT_V(:,2)); %calc. row/column location of non-zero values
interp_TWT_V_FULL(:,1)=interp_TWT_V(:,1); %assign full time vector

for i1=1:size(all_twt_vint,1),
    if(i1==size(all_twt_vint,1)-1) %for last two rows of all_twt_vint
        interp_TWT_V_FULL(rL(i1):rL(end),2)=all_twt_vint(i1,2);
        break;
    end

    interp_TWT_V_FULL(rL(i1):rL(i1+1),2)=all_twt_vint(i1,2);
end

Vint=interp_TWT_V_FULL;
```

(8.9.1.4) model_builder.m

The following script uses the TWT/ V_{RMS} files that are generated from velocity analysis (Section 8.10.7). After velocity analysis, each CMP retains a unique TWT/ V_{RMS} file. I use these data to resample each file, calculate TWT/ V_{INT} , and subsequently concatenate each 1-D TWT/ V_{RMS} and TWT/ V_{INT} data to generate 2-D V_{RMS} and V_{INT} models for later post-processing.

This script calculates the 2-D V_{RMS} and V_{INT} models separately for each survey. For example, to generate both models corresponding to the crossline survey, comment-out the line

```
all_input=dir('C:\Users\Nathan\Desktop\Seis\RESEARCH\Software_Code\MATLAB\NB\vpicks_inline'); %velocity data from inline survey. Next, set the trace_size variable to the total number of CMPs in the given seismic cross-section. For this study, the crossline section retains 60 CMP traces, so I set trace_size to 60.
```

model_builder.m

```
% % Builder: Nate B.
% % Description: accepts input file containing selected velocity and
% % corresponding two-way-time (TWT) from velocity analysis and then
% % (linearly) interpolates the velocity values - finally, the
% % interpolated data is then mapped to an approximate TWT corresponding
% % to the true recorded time series (which means that the time ranges
% % from zero time [or some other selected starting time] to a
% % designated end time with respect to the sampling rate)
% % Created: 05/23/17
% % Modified: (v.2)-> 06/13/17, (v.3)->06/19/17
% -----

% % *Make sure all input seismic data and velocity picks only range from
% % 0.0 s TWT to 1.0 s TWT - also, this entire script is formatted to for
% % time series data that has been acquired with sampling rate (dt) of
% % 0.0005 seconds

tic

% % % SECTION 1 [below] % % %
%-----
addpath('C:\Users\Nathan\Desktop\Seis\RESEARCH\Software_Code\MATLAB\NB\ivpic
ks_old');
addpath('C:\Users\Nathan\Desktop\Seis\RESEARCH\Software_Code\MATLAB\NB\ivpic
ks_inline');
addpath('C:\Users\Nathan\Desktop\Seis\RESEARCH\Software_Code\MATLAB\NB\ivpic
ks_xline');
addpath('C:\Users\Nathan\Desktop\Seis\RESEARCH\Software_Code\MATLAB\NB');
%-----
%purpose: input processing
```

```

% %
all_input=dir('C:\Users\Nathan\Desktop\Seis\RESEARCH\Software_Code\MATLAB\NB\i
vpicks_old'); %extra dir for input data
all_input=dir('C:\Users\Nathan\Desktop\Seis\RESEARCH\Software_Code\MATLAB\NB\i
vpicks_xline'); %velocity data from xline survey
% %
all_input=dir('C:\Users\Nathan\Desktop\Seis\RESEARCH\Software_Code\MATLAB\NB\i
vpicks_inline'); %velocity data from inline survey
trace_size=60; %set to max number of CMP processed - go to the velocity dir to
determine how many files/trace need to be interpolated

for A_i1=1:(trace_size+2), %set the second number to max number (or desired)
number of files/iterations

if(A_i1==1 || A_i1==2) %this is for the first two fields of the struct [all_input] - they are dir
names, so we don't want to use those
    continue; %go back to control for first two fields of struct (mentioned above)
end

inFile_1=dlmread(all_input(A_i1).name); %file name from seismic dir
TWT=inFile_1(:,1); %two-way-time data from current file
ivpicks=inFile_1(:,2); %corresponding V_rms values from current file

dt=0.0005; %sampling rate – check this
total_time=[0:dt:1]; %total time vector with respect to dt – check this
total_time=total_time'; %transpose to make vertical (time) vector
TV_pair=zeros(size(total_time,1),1); %zeros array that is later populated with
TWT/V_rms pairs

tt_size=size(total_time,1); %number of rows calc. and assigned
inFile_size=size(inFile_1,1); %row size of input file

                %%% SECTION 2 [below] %%%
%-----
%purpose: calc. V_int and build full V_int model via Vint_populate

v_int=vrms2vint(ivpicks,TWT); %calculates V_int from V_rms
int_twt_v=[TWT,v_int]; %builds partially complete V_int model
TWT_V_INT=Vint_populate(int_twt_v); %calc. full V_int model

interp_Vrms=vel_interp(inFile_1); %interpolates sparse V_rms picks
anchor_point=inFile_1(1); %first TWT in inFile_1 to act as anchor point
i1=1; %counter/index for loop
while('true') %to find index location in total_time of anchor point match
    if(isalmost(total_time(i1),anchor_point,dt))
        index_location=i1;

```

```

        break;
    end
    i1=i1+1;
end

TWT_V_RMS=zeros(tt_size,2);
TWT_V_RMS(:,1)=total_time; %assign first column the total TWT vector
TWT_V_RMS(index_location:size(interp_Vrms,1)+index_location-1,2)=interp_Vrms;
%assign V_rms to matrix

                    %%% SECTION 3 [below] %%%
%-----
%purpose: evaluates current input file via regular expressions and
%organizes the file in the vel_model matrix according to its cdp/cmp number
% - that is, our files end with "..._cdp123 or ..._cdp12 or ..._cdp1"
%the statements below basically asks one question and then proceeds to
%modify the file name in the following summarized workflow: 1) is there 1, 2, or 3
%integers at the end of the file name (which is a string) and 2) delete
%the prefix "cdp", save the integer identifier (123, 12, or 1) and then
%use that as a reference of where to be placed in the vel_model matrix

if (A_i1==3)
    vel_model_RMS=zeros(tt_size,trace_size); %build zeros matrix to be later
iteratively populated with velocity model (below)
    vel_model_INT=zeros(tt_size,trace_size);
end

    current_file_name=all_input(A_i1).name; %current file name for given iteration

if(any(cell2mat(regexp(current_file_name,'\d\d\d$', 'match')))) %for cdp files >=100
    mod_file=regexprep(current_file_name,'cdp','');
    index=cell2mat(regexp(mod_file,'\d\d\d$', 'match'));
    index=str2num(index);
    vel_model_RMS(:,index)=TWT_V_RMS(:,2); %V_rms model
    vel_model_INT(:,index)=TWT_V_INT(:,2); %V_int model
    fprintf('Interpolating/Assigning CMP Trace: %d\n', index);
    continue;
end

if(any(cell2mat(regexp(current_file_name,'\d\d$', 'match')))) %for cdp files >=10<100
    mod_file=regexprep(current_file_name,'cdp','');
    index=cell2mat(regexp(mod_file,'\d\d$', 'match'));
    index=str2num(index);
    vel_model_RMS(:,index)=TWT_V_RMS(:,2); %V_rms model
    vel_model_INT(:,index)=TWT_V_INT(:,2); %V_int model
    fprintf('Interpolating/Assigning CMP Trace: %d\n', index);
end

```

```

    continue;
end

if(any(cell2mat(regexprep(current_file_name,'d$','match')))) %for cdp files<10
    mod_file=regexprep(current_file_name,'cdp','');
    index=cell2mat(regexprep(mod_file,'d$','match'));
    index=str2num(index);
    vel_model_RMS(:,index)=TWT_V_RMS(:,2); %V_rms model
    vel_model_INT(:,index)=TWT_V_INT(:,2); %V_int model
    fprintf('Interpolating/Assigning CMP Trace: %d\n', index);
    continue;
end

end

fprintf('\n\nV_{RMS} Data is Stored in Matrix: "vel_model_RMS"\n');
fprintf('\n\nV_{INT} Data is Stored in Matrix: "vel_model_INT"\n\n');

                %%% SECTION 4 [below] %%%
%-----

%purpose: building model and txt file for subdivcor purposes
% % vel_model_subdivcor=[total_time,TWT_V_RMS]; %needed for subdivcor (we use
v_rms only)
% % vel_model_subdivcor_w=vel_model_subdivcor(210:1400,:); %window data as
neccessary
% % dlmwrite('xline_twt_vel.txt',vel_model_subdivcor_w,'delimiter','\t'); %write txt file to
export

toc

```

(8.9.1.5) vel_interp.m

The following script is extremely similar to the one presented in Section 8.9.1.3. The only difference is that instead of resampling TWT/ V_{INT} data, vel_interp.m resamples TWT/ V_{RMS} data (Table 8.7) trace-by-trace.

An example of using this script is given by a single TWT/ V_{RMS} file generated from velocity analysis. Assume the table below represents the TWT/ V_{RMS} pairs in a given text file.

With respect to the total recorded time (0.0 – 0.5 s) and the sampling rate (0.0005 s), these data are sparse (Figure 8.11[*left*]). The script below (vel_interp.m) accepts data formatted as shown in the table directly above, performs a linear interpolation with respect to the sampling rate and anchor points, and generates a continuous line from the first TWT/ V_{RMS} pick/anchor point (0.1 s, 90 m/s) to the last TWT/ V_{RMS} pick/anchor point (0.5 s, 280 m/s) (Figure 8.11[*right*]).

Table 8.7. Input text file to be resampled.

TWT [s]	V_{RMS} [m/s]
0.1	90
0.2	130
0.3	170
0.4	200
0.5	280

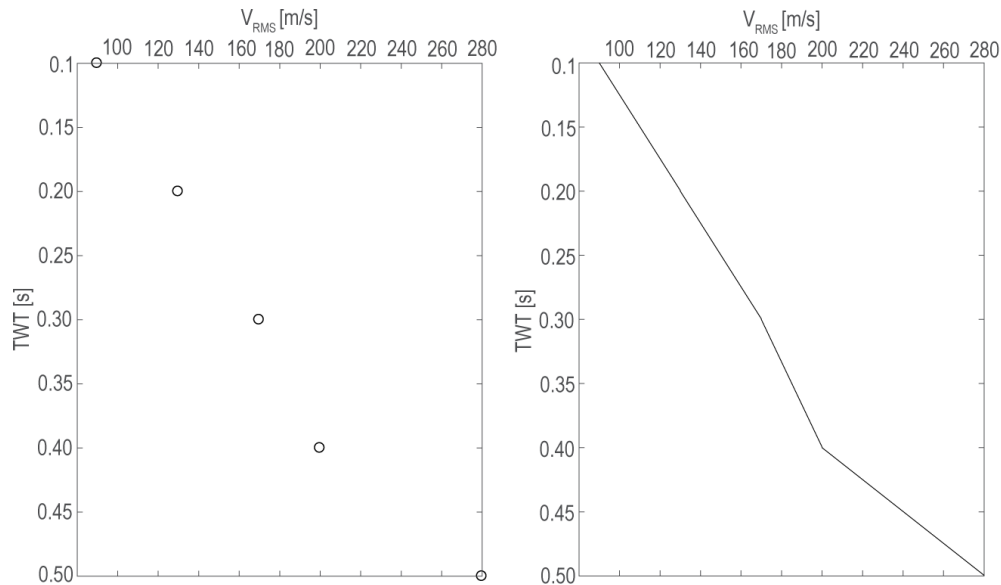


Figure 8.11. Sparse TWT/ V_{RMS} (left) generated from velocity analysis. Resampled and interpolated TWT/ V_{RMS} (right) data to provide continuous data.

vel_interp.m

```

%% % Builder: Nate B.
%% % Description: linearly interpolates and resamples TWT/V_rms
%% % picks from IVA
%% % Created: 06/17/17
%% % Modified:
%% -----

function interp_array=vel_interp(var1)

%input section
inFile_1=var1; %assignment of var1 (input file) to inFile_1
[row_size,col_size]=size(inFile_1);
TWT=inFile_1(:,1); %two-way-time data from current file
V=inFile_1(:,2); %corresponding V_rms values from current input file

%(linear) interpolation section
dt=0.0005; %sampling rate (verify this with notes/machine - Nate B.)

```

```

%[below] time intervals from 0 - 1 seconds (this MUST be modified if you
%are using (or interpolating) data that extends beyond 1 second)
total_interp_size=round((TWT(row_size)-TWT(1))/dt); %used below
counter1=1; %counter for loop (below)

```

```

interval_v_cell=cell((row_size-1),1); %zeros (cell) matrix for velocity

```

```

for i1=1:row_size,
    if(i1==row_size)
        break; %when i1 equals the last row, no interpolation occurs
    end
    %[below] this statement calc. how many samples are between two
    %selected points (which is then used by the following statement
    %to perform the correct amount of interpolation step calculations)
    interval_step=round((TWT(i1+1)-TWT(i1))/dt);
    interval_v_cell(Sentenac4)=linspace(V(i1),V(i1+1),interval_step);

    counter1=counter1+1;
end

```

```

%[below] initially declares and populates a zeros vector that of the same
%demension corresponding to the number of samples between first time and
%last time of the input file
interp_array_initial=zeros(total_interp_size,1);
row_sum=0;

```

```

for i1=1:size(interval_v_cell,1),
    if(i1==1)
        interp_array_initial(1:size(interval_v_cell(Sentenac4),2))=...
            interval_v_cell(Sentenac4);
        row_sum=size(interval_v_cell(Sentenac4),2);
        continue;
    end

```

```

    last_size=row_sum;
    current_size=size(interval_v_cell(Sentenac4),2);
    interp_array_initial((last_size+1):(last_size+current_size))=...
        interval_v_cell(Sentenac4);
    row_sum=row_sum+current_size;
end

```

```

interp_array=interp_array_initial;

```

(8.9.1.6) utm_interpolation.m

For each data acquisition day, I record the first and last geophone position. Because the location of each receiver and/or geophone is not noted, I use a linear

interpolation algorithm to estimate the position between the two GPS points recorded for a given day.

Suppose two UTM GPS measurements (p1 & p2) are acquired on a given acquisition day (e.g. p1=(3389410 [Northing], 654576 [Easting]) & p2=(3389379 [Northing], 654602 [Easting])). Given these two points, the number of even spaces between the two points (i.e. number of spacing between geophones separating the anchor points) must be supplied (i.e. *step* variable). With these three data sets as input, `utm_interpolation.m` calculates and graphs the interpolated and anchor points (Figure 8.12)

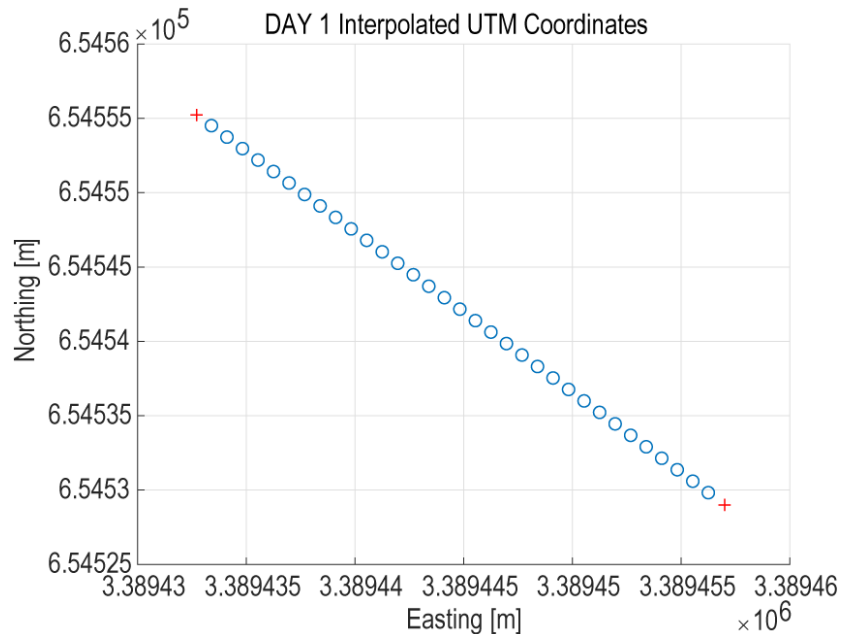


Figure 8.12. Red crosses are anchor points (i.e. p1 & p2) and circles are the interpolated UTM positions.

utm_interpolation.m

```

%% Author: Nathan Benton
%% Description: accepts two UTM coordinates for point 1 and 2 - then,
%% using a linear step between the two points, the script calculates the
%% relative position of the points between points 1 and 2
%% Created: 04/06/17
%% Modified: v.1->04/06/17
% -----

%clear current memory and command window
clc; clear all;

%define the two UTM points below
%special note: make sure to know whether the easting or northing values
%are decreasing - why? Because not knowing will possibly negatively
%affect the correct position of the interpolated points - that is,

```

```
%the UTM values will be flipped upside down, so all that will need to be
%done is to change point 1 to point 2, vice versa
```

```
p1=[3389410,654576]; %the first value is northing and the second easting
p2=[3389379,654602]; %the first value is northing and the second easting
pX=[p1(1),p2(1)]; %take the x-values of points and put into a single array
pY=[p1(2),p2(2)]; %take the y-values of points and put into a single array
```

```
DX=p2(1)-p1(1); %total x-distance between the two points
DY=p2(2)-p1(2); %total y-distance between the two points
```

```
step=39; %total evenly spaced spatial steps between point 1 and 2
dx=DX/step;
dy=DY/step;
```

```
%this loop calculates and assigns x and y values of interpolated points
%to a single array
for i1=1:(step-1),
    iP_x=((i1/step)*DX)+pX(1);
    iP_y=((i1/step)*DY)+pY(1);
    iP_xy(i1,:)=[iP_x,iP_y];
end
```

```
%plotting and QC
figure; hold on; grid on;
scatter(iP_xy(:,2),iP_xy(:,1)); %plot only the interpolated values
scatter(pY,pX,'+r'); %plot only the original two UTM points
title('Inline (Day 3) Interpolated UTM Coordinates');
xlabel('Easting [m]');
ylabel('Northing [m]');
```

(8.9.1.7) blimp.m

The following script is written by contributors of the Consortium for Research in Elastic Wave Exploration Seismology (CREWES) at the University of Calgary (Canada). Access to this subroutine and others are located at the following URL: <https://www.crewes.org/ResearchLinks/FreeSoftware/>.

This script is used to perform band-limited impedance (BLIMP) inversion. This script is executed for each trace of given processed seismic cross-section with its corresponding low-frequency impedance model.

blimp.m

```
function imp=blimp(trin,implog,t,flow,fhigh,delf)
% imp=blimp(trin,implog,t,flow,fhigh,delf)
%
```

```

% BLIMP estimates acoustic impedance from a seismic trace
% using a well log to provide the low frequency component.
% The algorithm is described in Ferguson and Margrave (1996 CREWES
% annual report). This used to be called SEISINV2. Blimp is an
% acronym for band limited impedance.
%
% trin ... input seismic trace
% implog ... input impedance log (in time)
% t ... time coordinate vector for trin
% flow ... lowest frequency in trin to keep
% fhigh ... highest signal frequency in trin
% delf ... width of Gaussian rolloff filter to be applied to
%   log at flow and trin at flow+delf
%   ***** default min([5 flow/5]) *****
%
% G.F. Margrave, CREWES Project, U of Calgary, 1995-96
%
% NOTE: This SOFTWARE may be used by any individual or corporation for any
% purpose
% with the exception of re-selling or re-distributing the SOFTWARE.
% By using this software, you are agreeing to the terms detailed in this software's
% Matlab source file.

% BEGIN TERMS OF USE LICENSE
%
% This SOFTWARE is maintained by the CREWES Project at the Department
% of Geology and Geophysics of the University of Calgary, Calgary,
% Alberta, Canada. The copyright and ownership is jointly held by
% its 'AUTHOR' (identified above) and the CREWES Project. The CREWES
% project may be contacted via email at: crewesinfo@crewes.org
%
% The term 'SOFTWARE' refers to the Matlab source code, translations to
% any other computer language, or object code
%
% Terms of use of this SOFTWARE
%
% 1) This SOFTWARE may be used by any individual or corporation for any purpose
%   with the exception of re-selling or re-distributing the SOFTWARE.
%
% 2) The AUTHOR and CREWES must be acknowledged in any resulting publications
%   or
%   presentations
%
% 3) This SOFTWARE is provided "as is" with no warranty of any kind
%   either expressed or implied. CREWES makes no warranties or representation
%   as to its accuracy, completeness, or fitness for any purpose. CREWES

```

```

% is under no obligation to provide support of any kind for this SOFTWARE.
%
% 4) CREWES periodically adds, changes, improves or updates this SOFTWARE
without
% notice. New versions will be made available at www.crewes.org .
%
% 5) Use this SOFTWARE at your own risk.
%
% END TERMS OF USE LICENSE

%-----

%%%%%%%%%%%%%%%%%%%%%%%%%%%%%%%%%%%%%%%%%%%%%%%%%%%%%%%%%%%%%%%%%%%%%%%%
%%%%%%%%%%%%%%%%%%%%%%%%%%%%%%%%%%%%%%%%%%%%%%%%%%%%%%%%%%%%%%%%%%%%%%%%
% check for row vectors and transpose if needed
nsamps=length(t);
aa=size(trin);
bb=size(t);
cc=size(implog);

if aa(1)==1
    trin=trin';
end

if bb(1)==1
    t=t';
end

if cc(1)==1
    implog=implog';
end

if(length(trin)~=nsamps || length(implog)~=nsamps)
    error('trin,implog, and t must all have the same length')
end

%%%%%%%%%%%%%%%%%%%%%%%%%%%%%%%%%%%%%%%%%%%%%%%%%%%%%%%%%%%%%%%%%%%%%%%%
%%%%%%%%%%%%%%%%%%%%%%%%%%%%%%%%%%%%%%%%%%%%%%%%%%%%%%%%%%%%%%%%%%%%%%%%
%integrate
if(nargin<6)
    delf=min([5 flow/5]); %gaussian on low end
end

impbl=racs2impbl(trin,t,flow+delf,fhigh,delf);

%zero pad to impbl

```

```

impbl=padpow2(impbl);

%%%%%%%%%%%%%%%%%%%%%%%%%%%%%%%%%%%%%%%%%%%%%%%%%%%%%%%%%%%%%%%%%%%%%%%%
%%%%%%%%%%%%%%%%%%%%%%%%%%%%%%%%%%%%%%%%%%%%%%%%%%%%%%%%%%%%%%%%%%%%%%%%
%remove linear trend of log
p=polyfit(t,implog,1); %FIGURE 4(B)
implog=implog-polyval(p,t); %FIGURE 4(C) [FFT TO GENERATE 4(D), TOO]
%%%%%%%%%%%%%%%%%%%%%%%%%%%%%%%%%%%%%%%%%%%%%%%%%%%%%%%%%%%%%%%%%%%%%%%%
%%%%%%%%%%%%%%%%%%%%%%%%%%%%%%%%%%%%%%%%%%%%%%%%%%%%%%%%%%%%%%%%%%%%%%%%
implog=pad_trace(implog,impbl); %zero pad

t2=xcoord(t(1),t(2)-t(1),implog);
%%%%%%%%%%%%%%%%%%%%%%%%%%%%%%%%%%%%%%%%%%%%%%%%%%%%%%%%%%%%%%%%%%%%%%%%
%%%%%%%%%%%%%%%%%%%%%%%%%%%%%%%%%%%%%%%%%%%%%%%%%%%%%%%%%%%%%%%%%%%%%%%%
%merge log and bandlimited impedance
imp=mergetrcs(implog,impbl,t2,flow,delf,fhigh); %FIGURE 5(A-B)
%%%%%%%%%%%%%%%%%%%%%%%%%%%%%%%%%%%%%%%%%%%%%%%%%%%%%%%%%%%%%%%%%%%%%%%%
%%%%%%%%%%%%%%%%%%%%%%%%%%%%%%%%%%%%%%%%%%%%%%%%%%%%%%%%%%%%%%%%%%%%%%%%
imp=imp(1:length(trin)); %FIGURE 5(C) & FIGURE 5(D)

imp=imp+polyval(p,t);

```

(8.9.1.8) auto_blimp.m

The script below completely automates the process of blimp.m (Section 8.9.1.7). auto_blimp.m allows users to input a time-windowed seismic cross-section and low-frequency impedance model and subsequently inverts the entire seismic data set.

To configure parameters accordingly, users need to set the lower time-limit (*ITL*) and upper time-limit (*uTL*) equal to that of the windowed seismic cross-section. Also, the *highpass* (i.e. *fhigh*) and *lowpass* (i.e. *flow*) variables must be properly set. Lastly, ensure that the columns of the input seismic data (*sdata*) match that of the low-frequency impedance model (*INT_LOWF_V_MODEL*).

auto_blimp.m

```

% % Builder: Nate B.
% % Description: uses the BLIMP inversion algorithm in a stream-line/automated
% % way - also, some input conditioning of both the seismic and low-freq.
% % models is performed
% % Created: 07/01/17
% % Modified: NA
% -----

```

```
tic
```

```

%add main path
addpath('C:\Users\Nathan\Desktop\Seis\RESEARCH\Software_Code\MATLAB\NB');

```

```

window input velocity model
INT_LOWV_V_MODEL=vel_model_INT(ISL:uSL+dt,2:58);

>load and configure input seismic
sdata_input=sdata.traces; %assings seismic data from sdata structure built via
'load_plot_seismic.m'
Input_Seismic=sdata_input(:,2:58); %only accept useable/neccesary parts (or window)
of seismic to invert

lowpass=15; %low-pass freq. for seismic trace for BLIMP
highpass=90; %high-pass freq. for seismic trace for BLIMP

>assign to impedance model
const_rho=ones(size(INT_LOWV_V_MODEL,1),size(INT_LOWV_V_MODEL,2));
LOWF_IMP_MODEL=INT_LOWV_V_MODEL.*const_rho;

>build/configure calculated impedance matrix
[sample_count,trace_count]=size(Input_Seismic);
INV_IMP=zeros(sample_count,trace_count);

>perform inversion (via BLIMP) trace-by-trace
for i1=1:trace_count,
    INV_IMP(:,i1)=blimp(Input_Seismic(:,i1),LOWF_IMP_MODEL(:,i1),time,lowpass,
highpass);
end

fprintf('\n\nInversion Complete -> The final output matrix is called "INV_IMP."\n\n');

toc

```

(8.9.1.9) load_plot_seismic.m

In order to load converted SEG-Y files into MATLAB for processing, load_plot_seismic.m must be used. Output from Section 8.8.7 (su_to_segy.sh) provides the SEG-Y files that is subsequently read by the script below.

This script automates two SeisLab functions: read_segy_file_legacy (Section 8.9.2.3) and s_cplot (Section 8.9.2.8).

load_plot_seismic.m

```
% % Builder: Nathan Benton
% % Description: uploads and plots seismics/impedance data and saves
% % uploading data as a structure (sdata or idata)- note that this is all
% % done via SeisLab
% % Date Created: 07/10/2017
% % Date Modified: 08/27/2017
% -----

tic

%SEGY data may also be uploaded via SeisLab reader
addpath('C:\Users\Nathan\Desktop\Seis\RESEARCH\Software_Code\MATLAB\NB');
addpath('C:\Users\Nathan\Desktop\Seis\RESEARCH\Software_Code\MATLAB\NB\seis
mic_data'); %seismic data location
addpath('C:\Users\Nathan\Desktop\Seis\RESEARCH\Software_Code\MATLAB\SeisLab
\SeisLab 3.02\S4M\Geophysics_3.0');

%load seismic data into struct
[sdata,ebcdic_header,binary_header]=read_segy_file_legacy('1005_clean_rev_twind_0
5clipped.su.sgy.su.sgy'); %for seismic data

%plot seismic data
s_cplot(sdata,{'limits',-1.0,1.0},{'colormap','gray'},{'shading','interp'});

toc
```

(8.9.1.10) isalmost.m

This script is used in both Vint_populate.m and model_builder.m. I use this script to match the TWT values provided by velocity analysis to defined time vectors that range from the beginning of a recording time to the end with respect to the sampling rate (Table 8.8 & 8.9). For example, three discrete picks are made during velocity analysis. The table below shows TWT picks that are not multiples of the sampling rate (this is almost always the case). Because of this, a time vector must be defined by a start time (e.g., 0.0 s) and an end time (e.g., 0.45 s) with respect to the sampling rate (e.g., 0.05).

Table 8.8. Input text data to be resampled and compared.

TWT [s]	V _{RMS} [m/s]
0.1239	110
0.2113	220
0.4333	330

By comparing the TWT values of the table directly above and those below via `isalmost.m`, a time comparison and V_{RMS} assignment is performed. The zeros populated with real velocity values with later post-processing via `Vint_populate.m` and `model_builder.m`. This script may be accessed at:

<https://www.mathworks.com/matlabcentral/fileexchange/15816-isalmost?requestedDomain=www.mathworks.com> (James, 2017).

Table 8.9. Resampled text file with compared values assigned to new times.

TWT [s]	V _{RMS} [m/s]
0	0
0.05	0
0.1	110
0.15	0
0.2	220
0.25	0
0.3	0
0.35	0
0.4	0
0.45	330

isalmost.m

```
function test = isalmost(a,b,tol)
%
% usage: test = isalmost(a,b,tol)
%
% tests if matrix a is approximately equal to b within a specified
% tolerance interval (b-tol <= a <= b+tol)
%
% note: if b is given as a scalar, all values in a are compared against
%       the scalar value b
%
% calls: none
%
% inputs:
%
% a(nr,nc) = matrix of data values to test
```

```

% b(nr,nc) = matrix of data values for comparison (or a single scalar value)
%   tol = tolerance used in computation
%
% outputs:
%
% test(nr,nc) = matrix of test results:
%
%   test(i,j) = 0 -> a(i,j) is not equal to b(i,j) (or is NaN)
%   test(i,j) = 1 -> a(i,j) is approximately equal to b(i,j)
%
% author : James Crawford
% created 01/08/2007
%
% history: v1.0 (01/08/2007)
%

% get length of input matrix a
[nr,nc] = size(a);

% check input for consistency
if ~all(size(a) == size(b))
    if all(size(b) == [1 1])
        % convert scalar value b to a matrix of size(a)
        b = b*ones(size(a));
    else
        disp('error: input arguments are inconsistent (isalmost.m)')
        disp('(b) must be a matrix of same size as (a) or a single value')
    end
end
one = ones(size(b));

% perform test
test = (a <= b+tol*one)&(a >= b-tol*one);

```

(8.9.1.11) phase_estimator.m

This script is used to estimate the phase of processed post-stack seismic data by establishing a 1-D time gate along a relatively flat and continuous seismic reflector and cumulatively summing amplitudes along the gate. The script `phase_estimator.m` accepts user input to set the gate. Each phase rotation is performed in MATLAB via `s_phase_rotation` (Section 8.9.2.9) and seismic data is plotted with `wiggle.m` (Section 8.9.1.1).

After uploading seismic data with `load_plot_seismic.m` (Section 8.9.1.9), this script can be executed. For the initial run of `phase_estimator.m`, the gate is established by a user. After the first run, the line including `[apprx_CMP,apprx_sample]=ginput();` must be commented out.

phase_estimator.m

```
% % Builder: Nate B.
% % Description: estimates phase of seismic by phase rotation along a
% % single, continuous reflection event (note that this work is inspired
% % by Roden and Sepulveda, 1999 [The significance of phase to the
% % interpreter: Practical guidelines for phase analysis])
% % Date Created: 08/04/17
% % Date Modified: NA
% -----

tic

%path for SeisLAB utilities
addpath('C:\Users\Nathan\Desktop\Seis\RESEARCH\Software_Code\MATLAB\SeisLab
\SeisLab 3.02\S4M\Geophysics_3.0');

%wiggly plot input seismic data set
sdata_traces=sdata.traces; %change this for each file (or phase rotation)
figure;
wiggly(sdata_traces,'5+'); hold on;
[apprx_CMP,apprx_sample]=ginput();
plot(apprx_CMP,apprx_sample,'r--','LineWidth',1.7);
hold off;

%print and cat result
fprintf('\n\n*The following points were selected for phase analysis: \n');
rounded_CMP_samples=round([apprx_CMP,apprx_sample]) %rounding and printing
selected points from ginput
[cmp_count,sample_count]=size(rounded_CMP_samples); %dimensions calculations
(from above)
amp_holder=zeros(1,size(sdata_traces,2)); %define zeros array with 1 row and columns
equal to the number traces in the input seismic (sdata)

%parse catted result of defined points for selection from input seismic
for i1=1:cmp_count,
    if(i1==1)
        amp_holder(1)=...
            sdata_traces(rounded_CMP_samples(1,2));
        continue;
    end

    amp_holder((rounded_CMP_samples(i1-1)+1):rounded_CMP_samples(i1))=...
        sdata_traces(rounded_CMP_samples(i1,2),rounded_CMP_samples(i1));
```

```
end %end of loop
```

```
%sum amplitudes along selected point
```

```
energy_sum=sum(abs(amp_holder)); %change for each phase rotation  
fprintf('\nApproximate Energy: %f\n',energy_sum);
```

```
toc
```

(8.9.1.12) vmodel_avg.m

The script below is used to average the initial and true velocity models for depth conversion purposes. Also, it generates two strings for `depthing.sh` (Section 8.8.2). One string holds TWT data (i.e. `time_string` variable), and the other holds corresponding V_{INT} data (i.e. `vel_string` variable). These data are directly copied from MATLAB to the `depthing.sh`. Note that `model_builder.m` (Section 8.9.1.4) must be run first before this script can be used.

vmodel_avg.m

```
% % Builder: Nathan Benton
```

```
% % Description: averages velocity models by rows for SU depthing
```

```
% % Date Created: 08/25/2017
```

```
% % Date Modified: 08/25/2017
```

```
% -----
```

```
%enter model - this needs to be the Dix calculated model for input
```

```
depthing_model=vel_model_INT(210:1400,1:100); %make sure v-model is windowed  
the same as time
```

```
[rs,cs]=size(depthing_model);
```

```
%average model (with respect to ROWS)
```

```
depthing_model_main=mean(depthing_model,2);
```

```
depthing_model_main_copy= repmat(depthing_model_main,[1 cs]);
```

```
%incorporate appropriate time vector to cat with averaged model
```

```
%note that time vector already exists and is defined in
```

```
%auto_blimp
```

```
time=[0.105:0.0005:0.7]'; %check this
```

```
depthing_model=[time,depthing_model_main];
```

```
%convert both arrays to strings delimited by commas
```

```
time_string = sprintf('%0.7f,' , depthing_model(:,1));
```

```
time_string = time_string(1:end-1); %strip final comma
```

```
vel_string = sprintf('%0.7f,' , depthing_model(:,2));
```

```
vel_string = vel_string(1:end-1); %strip final comma
```

```
%special
time_string = sprintf('%0.7f,' , inline_cdp_45(:,1));
time_string = time_string(1:end-1); %strip final comma
vel_string = sprintf('%0.7f,' , inline_cdp_45(:,2));
vel_string = vel_string(1:end-1); %strip final comma
```

(8.9.1.13) imp_smoother.m

After SI is calculated with auto_blimp.m (Section 8.9.1.8), this script is used to smooth with SI profile with a Gaussian filter. I set the sigma value to one for this study.

imp_smoother.m

```
% % Builder: Nate B.
% % Description: smooths SI profiles
% % Date Created: 10/02/17
% % Date Modified: NA
% -----
```

```
IMP_smoothed=imgaussfilt(INV_IMP,1);
```

(8.9.1.14) gaussfilt.m

I filter EC logs via a 1-D Gaussian smoothing filter. The script used for this purpose in this study was not written by the author of this thesis. It may be accessed via the following URL: <https://www.mathworks.com/matlabcentral/fileexchange/43182-gaussian-smoothing-filter?focused=3839183&tab=function>.

gaussfilt.m

```
function [ zfilt ] = gaussfilt( t,z,sigma)
%Apply a Gaussian filter to a time series
% Inputs: t = independent variable, z = data at points t, and
%        sigma = standard deviation of Gaussian filter to be applied.
% Outputs: zfilt = filtered data.
%
% written by James Conder. Aug 22, 2013
% convolution for uniformly spaced time time vector (faster) Sep 4, 2014

n = length(z); % number of data
a = 1/(sqrt(2*pi)*sigma); % height of Gaussian
sigma2 = sigma*sigma;

% check for uniform spacing
% if so, use convolution. if not use numerical integration
uniform = false;
```

```

dt = diff(t);
dt = dt(1);
ddiff = max(abs(diff(diff(t))));
if ddiff/dt < 1.e-4
    uniform = true;
end

if uniform
    filter = dt*a*exp(-0.5*((t - mean(t)).^2)/(sigma2));
    i = filter < dt*a*1.e-6;
    filter(i) = [];
    zfilt = conv(z,filter,'same');
    length(filter)
else
    %%% get distances between points for proper weighting
    w = 0*t;
    w(2:end-1) = 0.5*(t(3:end)-t(1:end-2));
    w(1) = t(2)-t(1);
    w(end) = t(end)-t(end-1);

    %%% check if sigma smaller than data spacing
    iw = find(w > 2*sigma, 1);
    if ~isempty(iw)
        disp('WARNING: sigma smaller than half node spacing')
        disp('May lead to unstable result')
        iw = w > 2.5*sigma;
        w(iw) = 2.5*sigma;
        % this correction leaves some residual for spacing between 2-3sigma.
        % otherwise ok.
        % In general, using a Gaussian filter with sigma less than spacing is
        % a bad idea anyway...
    end

    %%% loop over points
    zfilt = 0*z; % initialize output vector
    for i = 1:n
        filter = a*exp(-0.5*((t - t(i)).^2)/(sigma2));
        zfilt(i) = sum(w.*z.*filter);
    end

    %%% clean-up edges - mirror data for correction
    ss = 2.4*sigma; % distance from edge that needs correcting

    % left edge
    tedge = min(t);
    iedge = find(t < tedge + ss);

```

```

nedge = length(iedge);
for i = 1:nedge;
    dist = t(iedge(i)) - tedge;
    include = find( t > t(iedge(i)) + dist);
    filter = a*exp(-0.5*((t(include) - t(iedge(i))).^2)/(sigma2));
    zfilt(iedge(i)) = zfilt(iedge(i)) + sum(w(include).*filter.*z(include));
end

% right edge
tedge = max(t);
iedge = find(t > tedge - ss);
nedge = length(iedge);
for i = 1:nedge;
    dist = tedge - t(iedge(i));
    include = find( t < t(iedge(i)) - dist);
    filter = a*exp(-0.5*((t(include) - t(iedge(i))).^2)/(sigma2));
    zfilt(iedge(i)) = zfilt(iedge(i)) + sum(w(include).*filter.*z(include));
end
end % uniform vs non-uniform

end

```

(8.9.2) SeisLab Commands

The SeisLab package is used extensively in data processing and post-processing for this study. To date, the most recent version is SeisLab 3.02 (all built by Eike Rietsch) and may be accessed and downloaded via the following URL: <https://www.mathworks.com/matlabcentral/fileexchange/53109-seislab-3-02> (Rietsch, 2007).

For any documentation of the following SeisLab functions refer to either the manual (*SeisLab for Matlab: MATLAB Software for the Analysis of Seismic and Well-Log Data*) or use the command `s_tools` (for seismic tools) or `l_tools` (for well-log tools) to list complete register of all available data tools as well as a brief description of each. If a user seeks more detail/information concerning a particular SeisLab function, type `help` followed by the function name (e.g. `help s_convert`)

I do not provide the source code of any functions. However, an example using each is provided.

(8.9.2.1) s_convert

Most MATLAB data types handled by SeisLab are structures. I use `s_convert` to convert matrix data (e.g. SI profile) into a structure for processing.

Example: `IMP_SCT=s_convert(INV_IMP);`

After converting a matrix data type into a structure, it can be managed and processed via SeisLab functionality.

(8.9.2.2) write_segy_file

I use `write_segy_file` to convert structure data types in SeisLab into SEG-Y files for post-processing.

Example: `write_segy_file(IMP_SCT)`

(8.9.2.3) read_segy_file_legacy

To read and process SEG-Y files in MATLAB, I use `read_segy_file_legacy`. The seismic data is stored in the `sdata` structure. To access the matrix of seismic data, use `sdata.traces`. Note that this function is used by `load_plot_seismic` (Section 8.9.1.9)

Example: `[sdata, ebcdic_header, binary_header]=read_segy_file_legacy('data.segy')`

(8.9.2.4) s_phase_rotation

I apply constant phase rotation in MATLAB via `s_phase_rotation`. This is used before each iteration of `phase_estimator.m` (Section 8.9.1.11). The variable `data` is the input seismic data (structure data type). The data are phase-rotated by +35°.

Example: `pr_data=s_phase_rotation(data,35);`

(8.9.2.5) read_las_file

The EC well-logs and SI curves I use for this study are read and processed in MATLAB via `read_las_file`. The input file must be formatted for LAS 2.0 or 3.0. Generating an LAS file is outlined in Section 8.11.2.

Example: `well_log1=read_las_file('well1.las');`

(8.10) Perl Scripts

Perl scripts are used extensively for seismic data processing from sorting to stacking.

(8.10.1) Sseg2su

This script may be accessed via the following path on the Zamin server: `/media/data1/nbento3`. Be sure to view the configuration file before using `Sseg2su` (`Sseg2su.config`).

(8.10.2) Reverse_polarity.pl

This script may be accessed via the following path on the Zamin server: `/home/nbento3/FalseRiver/seismics/pl/WOODY/ALL_xLINE/H/1/nbento3`.

(8.10.3) Suclean_geom.pl

This script may be accessed via the following path on the Zamin server: `/home/nbento3/FalseRiver/seismics/pl/WOODY/ALL_xLINE/H/1/nbento3`.

(8.10.4) Make_cmp.pl

This script may be accessed via the following path on the Zamin server:
/home/nbento3/FalseRiver/seismics/pl/WOODY/ALL_xLINE/H/1/nbento3.

(8.10.5) iTop_Mute3 & iTop_Mute3.config

This script may be accessed via the following path on the Zamin server:
/home/nbento3/FalseRiver/seismics/pl/WOODY/ALL_xLINE/H/1/nbento3.

(8.10.6) Sumute2.pl

This script may be accessed via the following path on the Zamin server:
/home/nbento3/FalseRiver/seismics/pl/WOODY/ALL_xLINE/H/1/nbento3.

(8.10.7) iVA2 & iVA2.config

This script may be accessed via the following path on the Zamin server:
/home/nbento3/FalseRiver/seismics/pl/WOODY/ALL_xLINE/H/1/nbento3.

(8.10.8) suCatpar.pl

This script may be accessed via the following path on the Zamin server:
/home/nbento3/FalseRiver/seismics/pl/WOODY/ALL_xLINE/H/1/nbento3.

(8.10.9) Sustack.pl

This script may be accessed via the following path on the Zamin server:
/home/nbento3/FalseRiver/seismics/pl/WOODY/ALL_xLINE/H/1/nbento3.

(8.10.10) Sudipfilt & Sudipfilt.config

This script may be accessed via the following path on the Zamin server:
/home/nbento3/FalseRiver/seismics/pl/WOODY/ALL_xLINE/H/1/nbento3.

(8.10.11) estat_calc.pl

This script is used to calculate elevation statics correction and generate a text file to be later encoded to binary and inputted into trace headers via sustatic (Section 8.7.1).

estat_calc.pl

```
#!/bin/perl
```

```
#Builder: Nate Benton
```

```
#Description: desinged to calculate elev. static correction
```

```
#for each trace of each shotgather and assign values to text
```

```
#file for subsequent geometry input and static correction assignment
```

#Created: 05/03/2017

#Modified: NA

#-----

```
use strict;
use warnings;
use POSIX;
use IO::Handle;
```

```
#calc. elevation statics correction for each trancel key - note that
#each correction is in seconds (s)
```

```
#scalar declarations
```

```
my $inFile='RS_Elev.txt'; #input txt file (with gps info of elevation of receivers and
sources)
my $i1=1; #index/counter for while-loop below
my $total_shots=104; #total number of ep's or fldr's for the entire pre-NMO gather
my $gather_size=24; #24 traces for each shotgather - this isn't always valid
my $Wv=105.26; #weathering velocity layer or velocity at and above the defined
datum
my $trancel_count=1; #used for for-loop, each trace of each shotpoint retains a
unique trancel value
my $update_size=0;#needed for for-loop to +1 for each successive shotpoint
my $gather_count=1; #QC for for-loop to make sure 24 trace per shotgather
my $flag=0; #needed for section 2 in both for-loops
```

```
#array declarations
```

```
my @elems;
my @RelevDiff; #array to hold difference of receiver elevation relative to the datum

#my @SelevDiff; #array to hold difference of source elevation relative to the datum
my @SelevDiff; #array to hold difference of source elevation relative to the datum
my @elev_statics; #finaly elevation static correction of each shot/receiver
```

###SECTION 1###

```
#the looping below serves to only extract the elevation of
#recievers and sources relative to the datum
```

```
open(my $fh0, '<', $inFile) or die "Cannot open file: $!"; #open/read input file
while(my $current_line=$fh0->getline()){
    @elems=split(' ', $current_line); #splits input into two seperate columns
    $RelevDiff[$i1]=$elems[0]; #column 0 holds reciever elevation difference
    $SelevDiff[$i1]=$elems[1]; #column 1 holds source elevation difference
    print("Row $i1: Rec. Elev -> $RelevDiff[$i1] | "); #QC
    print("S. Elev -> $SelevDiff[$i1] \n"); #QC
    $i1++;
}
```

```

close $fh0; #close input file handle

print("\n\n~File Input Complete~\n\n");

#####SECTION 2###
my @all_keys;      #this array will hold all data to be assigned to file handle below
my $outFile='ep_tstats.txt'; #only output file to hold ep, tracl, and tstats data

open(my $fh1, '>', $outFile) or die "Output Process Terminated: $!"; #declare/open
outfile

#takes data extracted from section 1 and assigns it to an array (elev_statics)
for(my $i1=1; $i1<=$total_shots; $i1++){
    for(my $i2=(1+$update_size); $i2<=($gather_size+$update_size); $i2++){

        $elev_statics[$tracel_count]=ceil((($SelevDiff[$i1]+$RelevDiff[$i2])/$Wv)*1000);
        #elevation statics correction
        print("Shotpoint: $i1 / Tracef: $gather_count / Tracel: $tracel_count ->
Statics Value: $elev_statics[$tracel_count] ms.\n");
        #QC printing of currently assigned value to elev-statics matrix for each
iteration

        @all_keys[$tracel_count]=$i1."\t".$gather_count."\t".$tracel_count."\t".$elev_stati
cs[$tracel_count];
        #assign all necessary data from line above to element of array as called
string

        print $fh1 $all_keys[$tracel_count]."\n";
        #print current element of all_keys to output file

        $tracel_count++; #increment for each successive trace of every gather
$gather_count++; #QC

        if($i1==81){ #beyond shotpoint 81, every shotgather incrementally
decreases by 1
            $flag=1;      #set to 'true' to skip back to control in loop 1
        }
    } #end of loop 2

    $gather_count=1; #QC

    if($flag){
        $gather_size--; #decreases gather size by 1 for each successive shotpoint
beyond 81
        $update_size++;
    }
}

```

```

#printf("Gather Size=%d | Update Size=%d\n", $gather_size, $update_size);
#QC
next; #skip statement below and go back to control of loop 1
}

$update_size++; #updates by +1 for each new/successive shotpoint (unless
flag=1 aka 'true')
} #end of loop 1

print("\n\nDone.\n\n");

```

(8.11) Software

(8.11.1) Opendtect

I use Opendtect only for visualization purposes for seismic and SI data. This software may be downloaded from the following URL: <https://dgbes.com/> (dGB, 2018).

(8.11.2) LasApps

The LasApps software is used to generate LAS files from text files. Both EC and some SI data are converted to LAS for plotting. After downloading the LasApps, view tutorial videos on how to create and format LAS files.

The software may be downloaded from the following URL: <http://www.cwls.org/las/> (Canadian Well Log Society, 2018).

VITA

Nathan Benton was born in Little Rock, Arkansas, in 1993. He attending Baylor University for undergraduate studies and earned a Bachelor's of Science degree which included a major in geophysics and a minor in mathematics in 2016. He anticipates graduating from Louisiana State University in May of 2018 with a Master of Science in geology, with a specialization in geophysics.